The Effects of Aging on the Mechanical Behavior of Lead Free and Mixed Formulation Solder Alloys

by

Yifei Zhang

A dissertation submitted to the Graduate Faculty of
Auburn University
in partial fulfillment of the
requirements for the Degree of
Doctor of Philosophy

Auburn, Alabama
August 9, 2010

Keywords: solder, aging, lead-free, mixed formulation,
mechanical property, creep, microstructure

Copyright 2010 by Yifei Zhang

Approved by

Jeffrey C. Suhling, Chair, Quina Distinguished Professor of Mechanical Engineering
Pradeep Lall, Thomas Walter Professor of Mechanical Engineering
R. A. Tony Overfelt, Professor of Mechanical Engineering
John L. Evans, Professor of Industrial and Systems Engineering

Abstract

The microstructure, mechanical response, and failure behavior of lead free solder joints in electronic assemblies are constantly evolving when exposed to isothermal aging and/or thermal cycling environments. In this work, the effects of isothermal aging on solder mechanical behavior has been investigated using a carefully-designed test matrix of aging temperatures, aging times, and Sn-Ag-Cu (SAC) solder alloys. Stress-strain and creep tests have been performed on four "standard" SAC alloys (SAC105, SAC205, SAC305, SAC405) with varying silver content. For the alloys studied, five different aging conditions have been used including room temperature (25 °C), and four elevated temperatures (50, 75, 100, and 125 °C). Variations of the mechanical and creep properties (elastic modulus, yield stress, ultimate strength, creep compliance, etc.) have been observed as a function of aging. In addition, mathematical models have been developed to predict the variation of the stress-strain and creep properties with aging time, aging temperature, and SAC alloy composition. The existence of creep cross-over points between the SAC alloys and eutectic 63Sn-37Pb under various aging conditions has been investigated in detailed.

In a second portion of this work, the mechanical behavior and physical properties of several mixed formulation solder alloys have been investigated. Seven mixed solders with different mixture ratios of 63Sn-37Pb and SAC305 solder materials have been formed. For the various percentage mixtures, the melting point, pasty range, stress-strain curves, mechanical properties and creep behavior have been characterized. The variations of the mechanical

properties and creep rates with aging at room temperature (25 °C) and elevated temperature (100 °C) have also been measured. Finally, the microstructures of these mixtures have been examined and correlated to their mechanical properties. The results for the mechanical and physical properties show a very complicated nonlinear dependence on the mixture ratio.

Acknowledgements

I would like to express wholehearted gratitude to my advisor Dr. Jeffrey C. Suhling, for his support, guidance and mentorship throughout this work. Sincere appreciation is sent to members of my advisory committee including Dr. Pradeep Lall, Dr. Ruel A. Overfelt and Dr. John L. Evans for their insightful instruction and precious time in the course of this research. Special thanks are extended to Dr. Michael J. Bozack for his assistance and creative discussions regarding the lead-free and mixed formulation solder projects. Thanks are also given to my colleagues and friends, Dr. Chang Lin, Zijie Cai, Safina Hussain, Jordan Roberts, John Marcell and Huihua Shu for their constant encouragement and invaluable friendship.

I am heartily grateful to my parents and my sister for their unremitting support to my study and life in the United States. I am truly in debt to my beautiful wife, Huan Peng for her taking care of my family, her perseverance and love, and her understanding of my decisions. Finally, I solemnly dedicate this dissertation and all achievements in pursuit of doctoral degree to my grandparents, Qingying Zhang and Yanqiu Dang, who taught me the first step in my life, gave me endless love and protection, and encouraged me to move on toward a better tomorrow.

Table of Contents

Abstract ii

Acknowledgements iv

List of Tables viii

List of Figures ix

Chapter 1
General Introduction 1
1.1 Introduction of Soldering Materials 1
1.2 Performance Characteristics of Solder Alloys 2
1.3 Development of Pb-free Solders 4
1.3.1 Choice of Pb-free Solders 4
1.3.2 Pb-free Candidates 4
1.4 Sn-Ag-Cu (SAC) Series Alloys 7
1.4.1 SAC Characteristics and Applications 7
1.4.2 SAC Phase Diagram 8
1.4.3 SAC Metallography 10
1.5 Pb-free Challenges in Electronic Packaging 13
1.5.1 Pb-free Process Challenges 13
1.5.2 Pb-free Reliability Challenges 14
1.6 Transition from Sn-Pb to Pb-free Solder Alloys 15
1.6.1 The Existence of an Interim Stage 15
1.6.2 Mixed Formulation Metallurgy and Technical Challenges 16
1.7 Mechanical Properties of Soldering Materials 20
1.7.1 CTE Mismatch Stress/Strain 21
1.7.2 Tensile Properties 23
1.7.3 Shear Properties 26
1.7.4 Creep 28
1.7.5 Fatigue 32
1.8 Objectives of This Research 35
1.9 Organization of the Dissertation 36

Chapter 2
Literature Review 37
2.1 Introduction 37
2.2 Aging Effects on Solder Materials 38

2.2.1 Aging Effects on Bulk Solder Alloys 39
2.2.2 Aging Effects on Solder Joints 43
2.3 Metallurgical Approaches in Mitigating Aging Effects 57
2.4 Constitutive Modeling of Soldering Materials 60
2.4.1 Stress-Strain Curve Modeling 61
2.4.2 Constitutive Modeling of Creep Deformation 63
2.4.3 Anand Viscoplastic Constitutive Model 66
2.5 Life Prediction of Solder Joints 72
2.6 Summary 78

Chapter 3
Specimen Preparation and Uniaxial Tensile Testing 81
3.1 Introduction 81
3.2 Uniaxial Test Specimen Preparation Procedure 82
3.3 Mechanical Testing and Testing system 87
3.4 Empirical Modeling of Tensile Stress-Strain Test Results 90
3.5 Microstructure Observation 95

Chapter 4
Effects of Aging on Mechanical Properties
and Microstructure of Lead-free SAC Solder Alloys 98
4.1 Introduction 98
4.2 Aging Effects on Stress-Strain Response of SAC Solder Alloys 99
4.3 Effects of Aging on Young's Modulus 110
4.4 Effects of Aging on Yield Stress 116
4.5 Effects of Aging on Ultimate Tensile Strength 122
4.6 Microstructure Evolution during Aging 128
4.7 Fractography Analysis of Failed Specimens 140
4.8 Summary and Conclusions 140

Chapter 5
Effects of Aging on the Creep Behavior of Lead-free SAC Solder Alloys 146
5.1 Introduction 146
5.2 Aging Effects on Creep Response of SAC Solder Alloys 146
5.3 Creep Strain Rate Evolution and Modeling with Aging 158
5.4 Comparison of Aging Effects on SAC Alloys and Eutectic 63Sn-37Pb 164
5.5 Influence of Silver Content on the Creep Strain Rate and Aging Effects 168
5.6 Influence of Stress Level on Creep Strain Rate 172
5.7 Discussion and Conclusions 181

Chapter 6
Preparation, Microstructure and Application of Mixed Formulation Solders 183
6.1 Introduction 183
6.2 Preparation of Mixed Formulation Solders 184
6.3 Physical Properties of Mixed Formulation Solders 185
6.4 Microstructure Evolution of Mixed Formulation Solders 187

6.5 Application of Mixed Formulation Solders ... 193
6.6 Discussion and Conclusion ... 200

Chapter 7
Effects of Aging on Mechanical Properties
and Creep Behavior of Mixed Formulation Solders ... 201
7.1 Introduction ... 201
7.2 Aging Effects on Stress-Strain Response of Mixed Formulation Solders ... 202
7.3 Effects of Aging on Elastic Modulus ... 210
7.4 Effects of Aging on Yield Strength ... 212
7.5 Effects of Aging on Ultimate Tensile Strength ... 214
7.6 Fractography Analysis of Failed Specimens ... 216
7.7 Effects of Aging on Creep Behavior ... 220
7.8 Discussion and Conclusions ... 232

Chapter 8
Conclusions ... 235
8.1 Literature Review ... 235
8.2 Specimen Preparation and Experimental Procedures ... 237
8.3 Aging Effects on Mechanical Properties of SAC Alloys ... 237
8.4 Aging Effects on the Creep Behavior of SAC Alloys ... 239
8.5 Preparation and Microstructure of Mixed Formulation Solders ... 240
8.6 Aging Effects on the Tensile and Creep Behavior of Mixed Formulation Solders ... 241

References ... 243

Appendix I ... 260

Appendix II ... 266

Appendix III ... 269

List of Tables

1.1 Performance Characteristics of Solder Alloys 3

1.2 Eutectic and Homologous Temperatures of Binary Pb-free Solders 6

2.1 Nomenclature Used for the Anand Constitutive Model 69

2.2 Anand Model Constants Defined in ANSYS 70

2.3 Summary of Solder Joint Fatigue Models 73

2.4 Effects of Design Parameters on the Fatigue Life of BGA Solder Joints 77

4.1 Aging Matrix for Stress-Strain Tests 99

4.2 Values of Elastic Modulus after 60-days of Aging 115

4.3 Values of Yield Stress after 60-days of Aging 119

4.4 Values of UTS after 60-days of Aging 125

4.5 Quantitative Analysis of IMCs in SAC105 139

4.6 Quantitative Analysis of IMCs in SAC405 139

5.1 Aging Matrix for Creep Tests of SAC Alloys 147

5.2 Increases in Creep Strain Rate with Aging 164

5.3 Comparison of Stress Level Influence (R.T. Aging) 180

5.4 Comparison of Stress Level Influence (125 °C Aging) 180

6.1 Composition of Mixed Formulation Solders (in wt.%) 184

6.2 Elemental Solubility in Binary System at Room Temperature 192

7.1 Aging Matrix for Tensile Tests of Mixed Formulation Solders 202

7.2 Increase in Creep Strain Rate with Aging (60-days at 100 °C) 231

List of Figures

1.1 The Market Share of Different Pb-free Solders 8
1.2 Typical 3-D Ternary Phase Diagram 9
1.3 Top View of Sn–Ag–Cu Ternary Phase Diagram 10
1.4 SEM Micrographs of Eutectic SAC Structure 11
1.5 “Backwards” Mixed Assembly Process 17
1.6 Micrographs of Typical Mixed Formulation Solder Joints 18
1.7 Failure Mechanisms in Microelectronic Packaging 21
1.8 Cyclic Stress Induced by CTE Mismatch 22
1.9 Solder Joints Subjected to Tensile Loading due to Substrate Flexing 23
1.10 Stress-Strain Curve (Engineering vs. True) 24
1.11 Typical Stress-Strain Curve of Pb-free Alloys 25
1.12 Solder Joints Subjected to Shear Strain due to CTE Mismatch 27
1.13 Typical Shear Stress-Strain Diagram 27
1.14 Creep Curve under Constant Stress/Load and Temperature 29
1.15 Creep Deformation Map for Solder Alloys 30
2.1 Room Temperature Aging Effects on Sn-Pb Solder 39
2.2 Coarsening of Intermetallic Phases in Eutectic SAC Alloy under Aging 42
2.3 Fracture Modes of Solder Joints in Ball Shear Test 44
2.4 IMCs Formed in SAC387 Solder Joint on Bare Cu Pad 50
2.5 IMCs at the Interface of Cu Pad and SAC405 Solder Ball 52
2.6 Sequential Reactions Occurred at SAC357/ENIG/Cu Interface at 200 °C 53
2.7 Formation of Kirkendall Voids with Aging Time and Temperature 55
2.8 Schematic Illustration of Kirkendall Voiding (Sn-3.0Ag-0.5Cu-1.0Zn/bare Cu) 56
2.9 Refinement of Sn Dendrite Size and Spacing with La Addition 60
2.10 Flowchart for Absolute Fatigue Life Prediction Methodology 75

3.1 Setup for Uniaxial Test Specimen Preparation 82
3.2 Illustration of Specimen Making Procedure 83
3.3 Water Quenching Profile 84
3.4 Heller 1800EXL Reflow Oven 84
3.5 Solder Reflow Temperature Profiles 85
3.6 Uniaxial Test Specimens........ 86
3.7 X-Ray Inspection of the Test Specimens 86
3.8 MT-200 Testing System with Environmental Chamber 88
3.9 Typical Solder Stress-Strain Curve and Labeled Mechanical Properties 88
3.10 Definition of "Steady State" Creep Strain Rate 91
3.11 A Set of Typical Stress-Strain Curves for Solder 92
3.12 Truncated Solder Stress-Strain Curves 93
3.13 Empirical Model Fit to Solder Stress-Strain Curves........ 95
3.14 Nikon ECLIPSE L150/L150A Optical Microscope 97
3.15 JEOL JSM-7000F Field Emission SEM 97
4.1 Stress-Strain Curves for SAC105 Aged for 0-60 Days 101
4.2 Stress-Strain Curves for SAC205 Aged for 0-60 Days 103
4.3 Stress-Strain Curves for SAC305 Aged for 0-60 Days 105
4.4 Stress-Strain Curves for SAC405 Aged for 0-60 Days 107
4.5 Stress-Strain Curves for 63Sn-37Pb Aged for 0-60 Days 109
4.6 Change of Elastic Modulus with Aging for SAC105 111
4.7 Change of Elastic Modulus with Aging for SAC205 111
4.8 Change of Elastic Modulus with Aging for SAC305 112
4.9 Change of Elastic Modulus with Aging for SAC405 112
4.10 Effects of Silver Content on the Evolution of the Elastic Modulus with Aging........ 114
4.11 Change of Elastic Modulus with Aging for 63Sn-37Pb 115
4.12 Change of Yield Stress with Aging for SAC105 117
4.13 Change of Yield Stress with Aging for SAC205 117
4.14 Change of Yield Stress with Aging for SAC305 118
4.15 Change of Yield Stress with Aging for SAC405 118
4.16 Change of Yield Stress with Aging for 63Sn-37Pb 119

4.17 Effects of Silver Content on the Evolution of the Yield Stress with Aging 121
4.18 Change of UTS with Aging for SAC105 123
4.19 Change of UTS with Aging for SAC205 123
4.20 Change of UTS with Aging for SAC305 124
4.21 Change of UTS with Aging for SAC405 124
4.22 Change of UTS with Aging for 63Sn-37Pb 125
4.23 Effects of Silver Content on the Evolution of the UTS with Aging 127
4.24 Microstructure of SAC105 Test Specimens (SEM).. 129
4.25 Microstructure of SAC205 Test Specimens (SEM).. 130
4.26 Microstructure of SAC305 Test Specimens (SEM).. 131
4.27 Microstructure of SAC405 Test Specimens (SEM).. 132
4.28 Microstructure of 63Sn-37Pb Test Specimens (SEM).. 133
4.29 Microstructure Evolution of SAC105 Microstructure during Aging................................ 136
4.30 Microstructure Evolution of SAC405 Microstructure during Aging................................ 137
4.31 Microstructure Evolution of 63Sn-37Pb during Aging 138
4.32 Fracture Surfaces of the Failed Specimens (No Aging) 141
4.33 Fracture Surfaces of the Failed Specimens (60-days Aging at R.T.)................................ 142
4.34 Fracture Surfaces of the Failed Specimens (60-days Aging at 100 °C) 143
5.1 Creep Curves for SAC105 Aged for 0-6 Months 149
5.2 Creep Curves for SAC205 Aged for 0-6 Months 151
5.3 Creep Curves for SAC305 Aged for 0-6 Months 153
5.4 Creep Curves for SAC405 Aged for 0-6 Months 155
5.5 Creep Curves for 63Sn-37Pb Aged for 0-6 Months 157
5.6 Empirical Model for the Creep Strain Rate Evolution.. 159
5.7 Evolution of the Creep Strain Rate with Aging (SAC105)... 160
5.8 Evolution of the Creep Strain Rate with Aging (SAC205)... 161
5.9 Evolution of the Creep Strain Rate with Aging (SAC305)... 161
5.10 Evolution of the Creep Strain Rate with Aging (SAC405) 162
5.11 Evolution of the Creep Strain Rate with Aging (63Sn-37Pb).. 162
5.12 Creep Strain Rate Range for 63Sn-37Pb 165
5.13 Creep Strain Rate Comparison (SAC105 vs. 63Sn-37Pb).. 165

5.14 Creep Strain Rate Comparison (SAC205 vs. 63Sn-37Pb) 166
5.15 Creep Strain Rate Comparison (SAC305 vs. 63Sn-37Pb) 166
5.16 Creep Strain Rate Comparison (SAC405 vs. 63Sn-37Pb) 167
5.17 SACN05 Creep Rate Comparison (Aging at 25 °C) 169
5.18 SACN05 Creep Rate Comparison (Aging at 50 °C) 169
5.19 SACN05 Creep Rate Comparison (Aging at 75 °C) 170
5.20 SACN05 Creep Rate Comparison (Aging at 100 °C) 170
5.21 SACN05 Creep Rate Comparison (Aging at 125 °C) 171
5.22 Creep Curves for SAC305 173
5.23 Creep Curves for SAC405 174
5.24 Creep Curves for 63Sn-37Pb 175
5.25 Influence of Stress Level on the Creep Rate of SAC305 177
5.26 Influence of Stress Level on the Creep Rate of SAC405 178
5.27 Influence of Stress Level on the Creep Rate of 63Sn-37Pb 179
6.1 DSC Analysis of Mixed Formulation Solders 185
6.2 Melting Temperature vs. 63Sn-37Pb Content 186
6.3 Pasty Range vs. 63Sn-37Pb Content 186
6.4 Microstructure Evolution of Mixed Formulation Solders 188
6.5 EDX Analysis of Mixed Formulation Solders 192
6.6 Mixed Formulation Microstructure in Real BGA Solder Joints 198
7.1 Stress-Strain Curves for SAC305 Aged for 0-60 Days 203
7.2 Stress-Strain Curves for MIX10-90 Aged for 0-60 Days 204
7.3 Stress-Strain Curves for MIX30-70 Aged for 0-60 Days 205
7.4 Stress-Strain Curves for MIX50-50 Aged for 0-60 Days 206
7.5 Stress-Strain Curves for MIX70-30 Aged for 0-60 Days 207
7.6 Stress-Strain Curves for MIX90-10 Aged for 0-60 Days 208
7.7 Stress-Strain Curves for 63Sn-37Pb Aged for 0-60 Days 209
7.8 Elastic Modulus Variation with 63Sn-37Pb Content 211
7.9 Change of Elastic Modulus under R.T. Aging 211
7.10 Change of Elastic Modulus under 100 °C Aging 211
7.11 Yield Strength Variation with 63Sn-37Pb Content 213

7.12 Change of Yield Strength under R.T. Aging 213
7.13 Change of Yield Strength under 100 °C Aging 213
7.14 UTS Variation with 63Sn-37Pb Content 215
7.15 Change of UTS under R.T. Aging 215
7.16 Change of UTS under 100 °C Aging 215
7.17 Fracture Surface of Failed Tensile Specimens (as Water Quenched) 217
7.18 Fracture Surface of Failed Tensile Specimens (60-day Aging at R.T.) 218
7.19 Fracture Surface of Failed Tensile Specimens (60-day Aging at 100 °C) 219
7.20 Creep Curves for SAC305 for Aging from 0-60 Days 221
7.21 Creep Curves for MIX 10-90 for Aging from 0-60 Days 222
7.22 Creep Curves for MIX 30-70 for Aging from 0-60 Days 223
7.23 Creep Curves for MIX 50-50 for Aging from 0-60 Days 224
7.24 Creep Curves for MIX 70-30 for Aging from 0-60 Days 225
7.25 Creep Curves for MIX 90-10 for Aging from 0-60 Days 226
7.26 Creep Curves for 63Sn-37Pb for Aging from 0-60 Days 227
7.27 Evolution of Creep Response with 63Sn-37Pb Content (No Aging) 228
7.28 Comparison of Creep Strain Rates of Mixed Formulation Solders 230

Chapter 1
General Introduction

1.1 Introduction of Soldering Materials

Soldering, by definition, is a metallurgical process in which two or more metallic surfaces are joined together by melting a filler metal at the joint. The filler metal, which has a relatively low melting point, usually below 425 °C [1], is called solder.

In the ever-developing electronics world, there are two primary soldering techniques used for the mass-production of printed circuit boards (PCBs), namely, wave soldering and reflow soldering [2]. Wave soldering is a process in which electronic components are temporarily adhered to the PCB with small dabs of adhesive, then the whole assembly passes over flowing solder in a bulk container. Reflow soldering is a process in which parts are attached to their designated pads on PCB by using a sticky mixture of powdered solder and flux, i.e. solder paste, and then the whole assembly passes through a carefully-controlled oven in which the solder joints between parts and bonding pads are formed.

As the joining material, solder provides electrical, thermal and mechanical continuity in electronics assemblies. Its properties are crucial to the integrity of a solder joint, which in turn determines the overall functioning of the assembly.

Throughout the history of electronics packaging, 63Sn-37Pb (a eutectic composition) and 60Sn-40Pb (a near eutectic composition) have been the most widely used soldering alloys. The Sn-Pb binary system features a melting eutectic temperature as low as 183 °C and provides material compatibility with most substrate materials and devices. As the primary

component of Sn-Pb solders, Pb has many technical advantages over other alloying elements, [3, 4]:

(1) Pb facilitates wetting by reducing the surface tension of Sn-Pb solders.

(2) Pb prevents the allotropic transformation of Sn, i.e. from white or β-tin to gray or α-tin upon cooling below 13 °C, which results in a 26% increase in volume and causes loss of structural integrity once it occurs.

(3) Pb enhances the diffusion of other joint constituents such as Sn and Cu in the liquid state to help with the formation of intermetallic bonds by serving as a solvent metal.

(4) Pb is inexpensive and readily available.

Based on these factors, the application of eutectic and near eutectic Sn-Pb solders in the electronic packaging industry has been well developed and refined over decades of experience. Moreover, the scientific knowledge base about the physical metallurgy, mechanical properties, flux chemistries, manufacturing processes and reliability of Sn-Pb solders has been established.

However, despite the outstanding advantages of Sn-Pb solders, rising concerns over the human health dangers of Pb exposure is driving a current push forward Pb-free soldering materials and techniques on a global scale [5-14].

1.2 Performance Characteristics of Solder Alloys

In order to be used in electronics packaging, solder alloys must meet strict performance requirements (see Table 1.1). First, the solder alloy must have desired (low) melting temperature that is important to all aspects of electronics manufacturing process. Second, it must meet the expected levels of electrical and mechanical performance. Third, it is required to adequately to wet common PCB lands. Fourth, it is expected to form inspectable solder joints, allow high volume soldering and rework of defective joints, and provide reliable solder joints under service

conditions. Last, it must be economical and not significantly increase assembly cost. A summary of performance characteristics of solder alloys is listed in Table 1.1 [15]. Manufacturability describes the suitability of a solder alloy for current electronics packaging practices. Reliability refers to how dependable the solder joint is under service condition.

In searching for Pb-free alternative soldering materials, it is important to insure that the properties of the alternative solders are comparable or superior to Sn-Pb solders. Here are some established criteria for ‘‘perfect’’ lead-free alternatives [16]:

(1) Similar melting temperature to Sn–Pb solders to maintain a similar reflow profile;

(2) Good wettability to ensure good metallization in the manufacturing process;

(3) Similar or better electrical properties to efficiently transmit the electrical signals;

(4) Adequate mechanical properties to ensure the reliability of the electronic products;

(5) Nontoxic and relatively inexpensive.

Table 1.1 Performance Characteristics of Solder Alloys

Manufacturability	Reliability
Melting/liquidus temperature	Electrical conductivity
Wettability (of copper)	Thermal conductivity
Cost	Coefficient of thermal expansion
Environmental friendliness	Shear properties
Availability and number of suppliers	Tensile properties
Manufacturability using current processes	Creep properties
Ability to be made in balls	Fatigue properties
Copper pick-up rate	Corrosion resistance
Recyclability	Oxidation resistance
Ability to be made into paste	Intermetallic compound formation

1.3 Development of Pb-free Solders

A relatively large number of Pb-free solder alloys have been proposed so far, including binary, ternary and even quaternary alloys. More than 70 alloys have been identified in the literature [15]. The great majority of the candidates are Sn-rich alloys with Sn serving as the primary or major constituent.

1.3.1 Choice of Pb-free Solders

The choice of Sn as the principal component of most lead free solders results from its unusual ability to wet and spread over a wide range of substrates. Elemental Sn has a melting temperature of 231 °C and an allotropic transformation temperature of 13 °C. White or β-tin has a body-centered tetragonal crystal structure and is stable at room temperature. Gray or α-tin, which has a diamond cubic crystal structure, is thermodynamically stable below 13 °C. The transformation from β-tin to α-tin at 13 °C is referred to as "tin pest" or "tin disease" [17], which is accompanied by a large increase in volume and may induce cracking in the tin structure. Some elements (e.g. Bi and Sb) are reportedly effective in suppressing the phase transformation [18]. Hence, as a solution to tin pest, they are added as alloying agents to ameliorate the negative effect. Sn-rich solders are also prone to growth of fine wire shaped single crystals called tin whiskers [19-21], which are a danger to the reliability of electronic circuitry.

1.3.2 Pb-free Candidates

There are several Pb-free solder candidates that have been considered for replacing Sn-Pb solders. The candidates primarily originate from a group of adequate binary alloy systems, which are further developed by adding small quantity of third or fourth elements in order to (1) lower the solder melting temperature and (2) increase its wettability and reliability [22].

1.3.2.1 Sn-Zn System

The eutectic composition of Sn-Zn binary system is Sn-9 wt.% Zn [23] with a melting temperature of 198 °C, which is near that of eutectic Sn-Pb (183 °C). The lamellar microstructure consists of alternating Sn-rich and Zn-rich phases. The Sn-Zn system is fairly reactive since both constituents interact with Cu to form intermetallic phases. However, Zn reacts with flux to form hard paste and it also causes oxidation and corrosion problems due to the high oxidation potential of Zn.

1.3.2.2 Sn-Cu System

The Sn-Cu binary system has a eutectic composition of Sn-0.7 wt.% Cu and a eutectic temperature of 227 °C. This alloy is preferably used in wave soldering due to its low material cost. In air reflow, it has unsatisfactory wetting, which results in rough and textured fillets. Moreover, Sn-Cu alloys have poor mechanical properties [23].

1.3.2.3 Sn-Bi System

The eutectic Sn-Bi alloy has been recommended as a promising replacement for Sn-Pb solders. The eutectic composition is Sn-57 wt.% Bi and the eutectic temperature is 139 °C. This alloy has equivalent, even better properties than 63Sn-37Pb and is suitable for low temperature applications [24]. The room temperature equilibrium phases are Bi and Sn with about 4 wt.% Bi in solid solution. Cracking in the alloy may occur at slow cooling rate since Bi, which has a maximum solubility of 21 wt.% in Sn, will precipitate in the Sn phase as the alloy cools [25].

1.3.2.4 Sn-Ag System

The eutectic composition of the Sn-Ag binary system is Sn-3.5 wt.% Ag, with a eutectic temperature of 221 °C. The solidified microstructure of the eutectic alloy features β-tin phase with dendritic globules and inter-dendritic regions with a eutectic dispersion of Ag_3Sn

precipitates within β-tin matrix [26]. Although there is a long experience of using Sn-Ag alloys, its poor wetting in reflow soldering applications significantly prohibits widespread use.

1.3.2.5 Sn-In System

The eutectic point of Sn-In binary system is Sn-50.9 wt.% In and the most commonly used stoichiometry for SMT applications is near eutectic Sn-52 wt.% In. The eutectic temperature is 117 °C. There are two phases in the eutectic microstructure: an In-rich, psudo-body-centered tetragonal phase, β, which has 44.8 wt.% Sn, and a hexagonal Sn-rich phase, γ, with 77.6 wt.% Sn [27]. Despite its low melting temperature and limited tendency to scavenge gold compared to Sn-Pb solders, the high material cost and low availability greatly handicaps its application in the electronics packaging industry.

The eutectic and homologous temperatures of several binary Pb-free solder alloys are given in Table 1.2 [28]. The homologous temperature (T_H) of a solder alloy is obtained by dividing the alloy's desired service temperature (room temperature in Table 1.2) by its melting temperature (both in degrees Kelvin). It measures activation state of the atoms within an alloy. When $T_H > 0.5$, the atoms within the metallic alloy will gain sufficient kinetic energy and are able to participate in thermally activated processes such as creep and grain growth.

Table 1.2 Eutectic and Homologous Temperatures of Binary Pb-free Solders

Lead free solders	T_e (°C)	T_H (R.T.)
Sn-37Pb (Ref.)	183	0.654
Sn-9Zn	198	0.633
Sn-0.7Cu	227	0.596
Sn-57Bi	139	0.723
Sn-3.5Ag	221	0.603
Sn-52In	117	0.764

1.4 Sn-Ag-Cu (SAC) Series Alloys

The search for Pb-free replacements for Sn-Pb solders has been carried on for more than a decade. Even though a number of viable candidates have been identified, there is still no "drop-in" alternative that is suitable for all applications. However, the Sn–Ag–Cu (SAC) series, a ternary system that derives from Sn-Ag and/or Sn-Cu binary systems, has become the most promising replacement and many SAC alloys have been adopted by major electronics manufacturers. The alloy 96.5Sn–3.0Ag–0.5Cu (SAC305) has been widely accepted in Japan, 95.5Sn–3.8Ag–0.7Cu (SAC387) is now the leading lead-free choice in the EU, and 95.5Sn–3.9Ag–0.6Cu (SAC396) has gained its popularity with the U.S. companies.

1.4.1 SAC Characteristics and Applications

The advantages of SAC series over other Pb-free systems include relatively low melting temperatures, superior mechanical and solderability properties, and good tolerance for Pb contamination [29, 30]. These characteristics give SAC alloys good compatibility with existing electronics packaging infrastructure. In fact, there is a long history of using 95.5Sn–4.0Ag–0.5Cu (SAC405) to form solder joints for BGA packages. The high market share (≈ 70%) by SAC series alloys on a global scale (as illustrated in Fig.1.1) [31] provides strong evidence of its world-wide acceptance. However, despite the benefits and high market share, SAC series alloys are not a perfect Pb-free solder replacement choice due to several shortcomings:

(1) SAC alloys have higher melting points than eutectic Sn–Pb, and therefore higher reflow temperatures are needed;

(2) SAC alloys are prone to excessive growth of intermetallic compounds at the interface between solder joints and copper pad, which can cause reliability problems [32-34];

(3) SAC alloys have higher material costs [35].

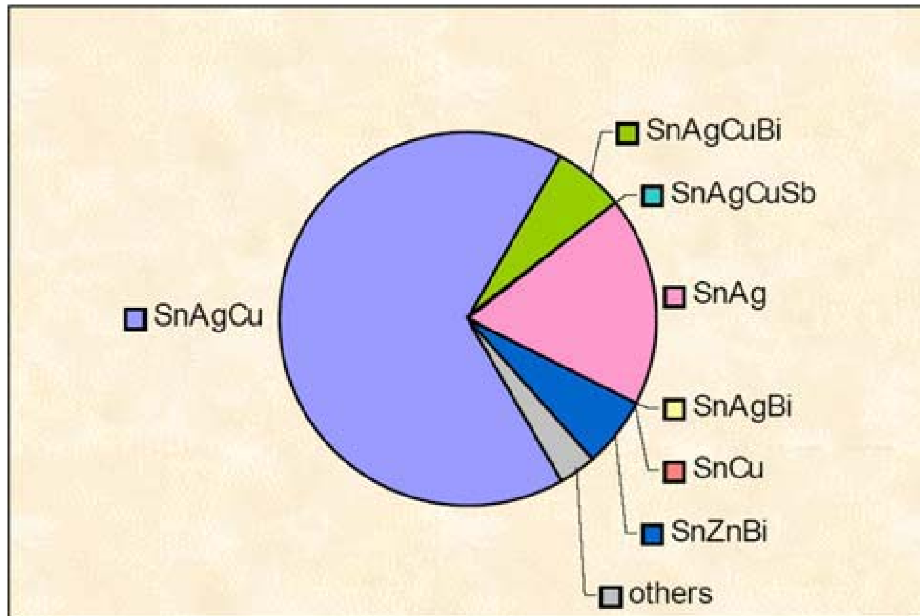

Figure 1.1 The Market Share of Different Pb-free Solders

1.4.2 SAC Phase Diagram

Since SAC series alloys are currently used to replace traditional Sn-Pb solders, the eutectic melting temperature of this ternary system is of great importance and interest. The development of ternary SAC alloys is based on the Sn-rich Sn-Cu and/or Sn-Ag binary eutectics. In the SAC system, the addition of Cu both lowers the melting temperature and improves the wettability [36]. It is known that the melting point of near eutectic SAC alloys is 217 °C, which is lower than the melting temperature of the binary eutectic 96.5Sn–3.5Ag at 221 °C.

The eutectic composition of SAC series alloys was first discovered by Miller, et al. in 1994 using DTA [37]. The eutectic point was 4.7 wt.% Ag and 1.7 wt.% Cu in the ternary system with a melting temperature of 217°C. In the year 2000, this composition was refined to 3.5 wt.% Ag and 0.9 wt.% Cu by Loomans and Fine [38], who used thermal analysis of

monovariant Sn-Cu and Sn-Ag binary eutectics. Their work was then confirmed by Moon, et al. [39] by using thermal analysis, simulated DTA curves and thermodynamic calculations. The melting point of the ternary system was relocated to 217.2 ± 0.2 °C with 2σ standard deviation. The resulting 3-D ternary phase diagram of SAC system is illustrated in Figure 1.2.

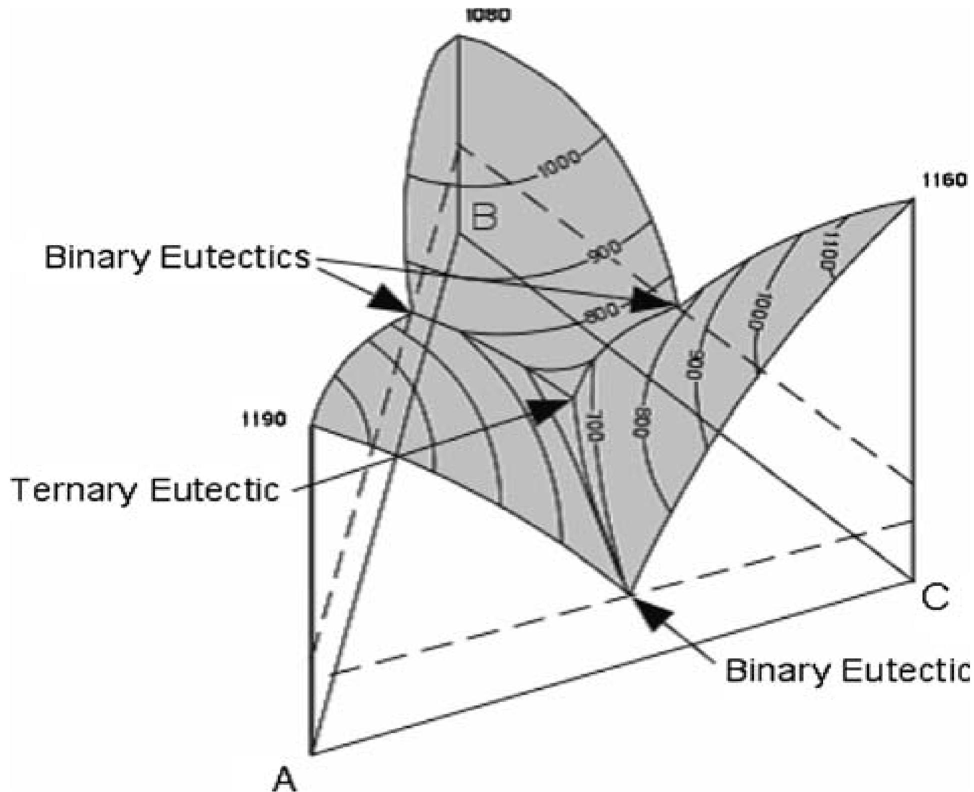

Figure 1.2 Typical 3-D Ternary Phase Diagram
(http://www.tulane.edu/*sanelson/geol212/ternaryphdiag.htm)

The contours on the top surface in Figure 1.2 (shaded area) represent isothermal lines. The lowest point on the diagram, where the isothermal lines converge, is the eutectic point of the ternary system. The eutectic reaction is formulated as:

$$L \rightarrow Ag_3Sn + Cu_6Sn_5 + Sn \text{ (Matrix)}$$

The three sectors in the diagram, demarcated by three binary eutectic points and the ternary eutectic point, represent the binary phase diagrams of Sn-Ag, Sn-Cu and Ag-Cu.

Even though there are three constituent elements in SAC series, the concentration of each element (especially Ag and Cu) has to fall into a certain region on the ternary phase diagram to form the alloys that can be used as potential replacement for Sn-Pb solders. This region (termed the near eutectic composition) is indicated by a red box on the top (2-D) view of the ternary phase diagram of SAC system, as shown in Figure 1.3.

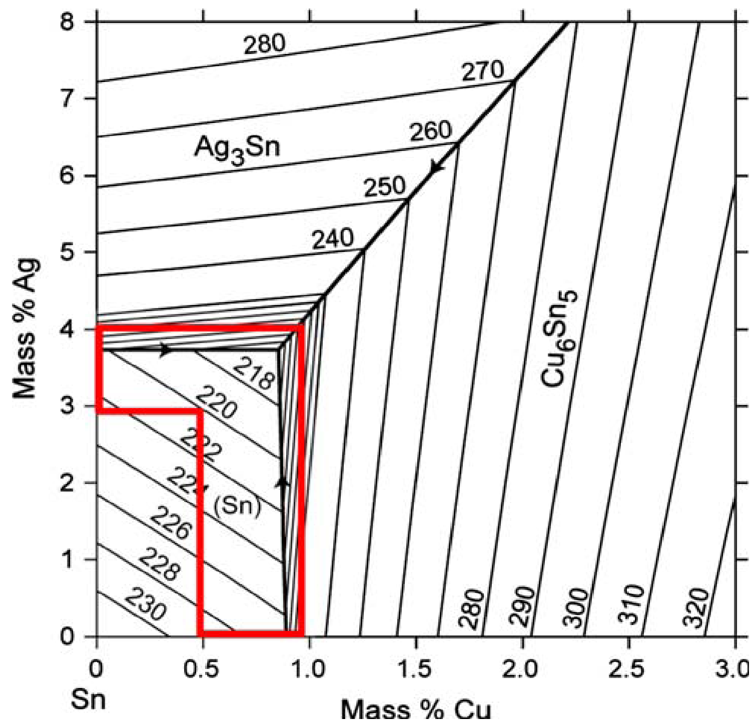

Figure 1.3 Top View of Sn–Ag–Cu Ternary Phase Diagram
(http://www.metallurgy.nist.gov/phase/solder/solder.html)

1.4.3 SAC Metallography

The solidification of SAC solders from a fully liquid state undergoes two stages: nucleation and growth. The development of the SAC microstructure depends on undercooling of the constituent phases for nucleation and kinetics for growth [40]. The ternary eutectic

microstructure of SAC solders consists of primary dendrites of β-Sn, and a eutectic micro-constituent comprising fine Ag_3Sn and Cu_6Sn_5 particles in β-Sn. The uniform dispersion of fine precipitates over the β-Sn matrix can be found in Figure 1.4, in which Ag_3Sn assumes a needle shape and Cu_6Sn_5 takes a disk-like morphology. Due to variation in cooling rate, two phase regions, i.e. $Sn+Cu_6Sn_5$ and $Sn+Ag_3Sn$, may co-exist and distribute around β-Sn dendrite arms [39]. Several Studies [40-42] show that in near-eutectic SAC alloys, the cooling rate has a large effect on the number, size and distribution of dispersed intermetallic precipitates.

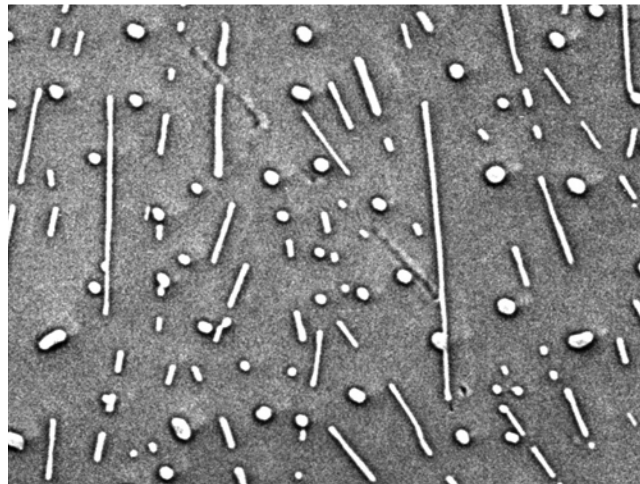

(a) Ternary Eutectic Microstructure

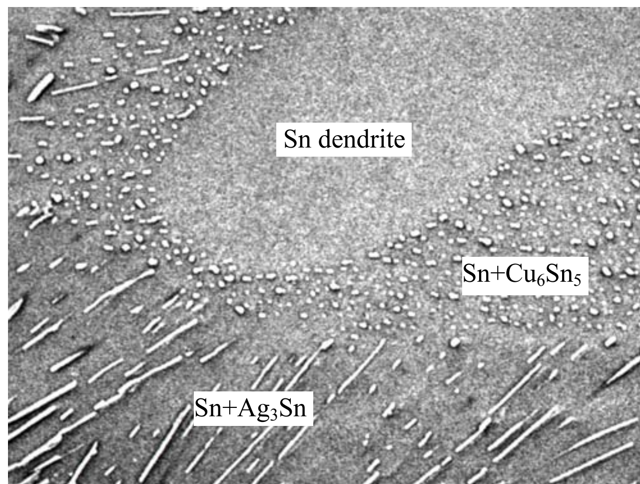

(b) Sn Dendrite Arm and Fine Intermetallic Compounds

Figure 1.4 SEM Micrographs of Eutectic SAC Structure

Swenson [42] has observed that in a typical solder joint, Ag_3Sn and Cu_6Sn_5 IMC phases need a minimum undercooling for nucleation while β-Sn phase requires a temperature range anywhere from 15 to 30°C below the melting point. Due to the relatively lower undercooling, the IMC phases nucleate first and grow with further cooling. In contrast, the significant undercooling required for the β-Sn phase results in rapid solidification, which in turn gives rise to a rapid growth of β-Sn dendrites from multiple nucleation sites. The latent heat of fusion associated with the solidification process inhibits further nucleation by raising the temperature of the solder alloy system. Nonetheless, the formation of β-Sn dendrites accelerates the growth of intermetallic phases near the saturated impingement zones, which are considered to be the sites of nucleation and subsequent growth of the Ag_3Sn and Cu_6Sn_5 phases. As a result, a honeycomb network of intermetallic compounds is formed throughout bulk solder joint along the impingement zones.

The addition of Cu and Ag to pure Sn increases the flow stress, which is a strong function of the alloy cooling rate. Fast cooling rates (e.g. water quenching) result in much higher flow stress compared to pure Sn, while low cooling rates (e.g. furnace cooling) increase the strength modestly. The strengthening effect is largely due to Ag and determined by the size of Ag_3Sn intermetallic plates and Ag content in the Sn-rich matrix phase [43, 44]. In general, the intermetallic compound particles possess much higher strength than the Sn matrix [45, 46]. It has been reported that the fatigue resistance of SAC alloys is 3~4 times greater than Sn–Pb eutectic solder. The higher fatigue resistance is ascribed to the interspersed Ag_3Sn and Cu_6Sn_5 particles, which pin and block the movement of dislocations [47].

1.5 Pb-free Challenges in Electronic Packaging

Although there are many Pb-free solder candidates available today as a result of the decade-long R&D investment, no "one-fits-all" Pb-free solder has arisen to supplant eutectic Sn-Pb in meeting all the rigorous technology requirements for electronic packaging today.

From a manufacturing point of view, the melting temperature or the liquidus temperature (the temperature at which non-eutectic solder alloy is completely molten) is considered the first and most important factor. As shown in Table 1.2, the majority of Pb-free candidates have a melting point over 200 °C, whereas the electronics assembly equipment in use today is designed to operate at 183 °C. Hence, the higher melting temperatures of SAC alloys mean higher processing temperatures, which in turn, greatly increases solder joint reliability risk and may cause damage to components and package during assembly.

1.5.1 Pb-free Process Challenges

In flip chip packages, the soldering process and the materials in use are designed and optimized for Sn-Pb solder alloys, including underfill and flux chemistries. Underfill is primarily used to reduce the shear load carried by solder joints and reduce the inelastic strain sustained by the solder, ultimately to enhance the life of solder joints. As use of Pb-free solders increases, a new database of underfill and flux information needs to be generated and optimized due to the high melting temperature and increased stiffness of Pb-free solder joints. Further, potential cracking in the low-K ILD (Inner Layer Dielectric) caused by large stress loading in flip chip packages (due to CTE mismatch of Si die and substrate) needs to be better understood [48].

Similarly, as the demand for fine pitch BGA packages soars in the electronics market, the assembly of BGA packages has become more challenging. This situation further escalates during the transition from Pb-containing to Pb-free solders, especially in the case of mixed

metallurgy, i.e. mixed Sn-Pb/Pb-free solder joints. In BGA assembly processes, the most widely used Pb-free solders are the eutectic Sn-Ag-Cu alloys, which have melting temperatures in the range of 217-221 °C, which is 34-38 °C higher than eutectic Sn-Pb solder. When SAC solder balls are used in assembling packages to PCBs under higher reflow temperatures, problems such as underfill-to-die interfacial delamination and "pop corning" are expected to be more serious.

1.5.2 Pb-free Reliability Challenges

Solder joint reliability is of uppermost concern in the electronics packaging industry and attracts substantial research effort to develop testing methods and mathematical models to accurately predict the life span and failure mode of solder joints. The stress experienced and sustained by solder joints is the critical factor, which goes into prediction models for both BGA and flip chip package configurations. Hua [48] has categorized the stresses in package operation as (1) mechanical stress due to the thermal expansion coefficient difference (CTE) of package materials; (2) chemical stress due to interface chemical reaction; and (3) current stress from high current density.

Most of the current reliability prediction models only deal only with one of the three stresses based on the assumption that a clear understanding of the dominant stress at operation is available. This approach is valid for Sn-Pb packages, however, for Pb-free packages, as melting temperature and/or current density increases, solder joint failure can be caused by each or a combination of these stresses. Thus, it is impossible to accurately predict solder joint reliability without understanding the interaction of these stresses.

1.6 Transition from Sn-Pb to Pb-free Solder Alloys

Since the European Union (EU) initiated the ban of lead, the Pb-free revolution in soldering technique has taken place at every corner of the world and draws on tremendous efforts in scientific research and technological innovation to meet the requirements. Even though there is a strong demand for the completion of this Sn-Pb to Pb-free transition, many critical issues have not been resolved yet due to the incomplete infrastructure for Pb-free soldering technology and the timing and technical readiness in the wide variety of sectors of the electronics manufacturing industry. In the meanwhile, the industry is currently experiencing an interim stage marked by mixture of Pb-free solder with Pb-coated components and vice-versa. This interim period has been well acknowledged within the industry and considered an effective approach in bridging the gap between Sn-Pb and Pb-free soldering.

1.6.1 The Existence of an Interim Stage

The necessity of the interim stage originates from the complexity of the Pb-free implementation. First, as mentioned above, the infrastructure for Pb-free soldering technology is still evolving. The industry is still striving for fine-tuned Pb-free substitute alloys and relevant technical protocols for Pb-free soldering. Second, electronic product manufacturers desire to use Sn-Pb components and Pb-free solder paste as a compromise between the ever growing demand for Pb-free assembly and the large inventory of Pb-containing components. Third, as the industry moves toward Pb-free technology, it will benefit both component suppliers and OEMs to avoid having production lines solely for Pb-free components. Finally, a few electronic products designed to meet long-term field reliability or survive harsh environments (telecommunications, avionics and high-end servers) are exempted from the requirement for Pb-free solder alloys (indicated in the EU RoHS Directive) [49, 50]. Before Pb containing

components become unavailable in the market, these products will continue to be built with Sn-Pb solder and assembly processes, or with a combination of Sn-Pb solder paste and Pb-free solders used in the same assembly.

1.6.2 Mixed Formulation Metallurgy and Technical Challenges

Several important materials and reliability challenges exist when Sn-Pb and Pb-free materials and processes are mixed. For example, mixed Sn-Pb and SAC alloys in area array packages has caused compatibility concerns, which result from the 34 °C difference between the eutectic temperature of the Sn-Ag-Cu system of 217 °C and the eutectic temperature of Sn-Pb of 183 °C [51]. Two kinds of assembly compatibilities arise when alloys and processes are mixed. When Sn-Pb pastes and processes are mixed with SAC surface finishes and solder balls on components or boards, it is referred to as "backward compatibility", as shown in Figure 1.5 [52]. Likewise, when SAC pastes and processes are mixed with Sn-Pb surface finishes and solder balls on components or boards, it is referred to as "forward compatibility" [51, 53, 54].

The metallurgical reaction of SAC alloys and Pb is a secondary alloying process and two different microstructural scenarios may be formed during reflow soldering: (1) a fully mixed joint and (2) a partially mixed joint. These options are shown in Figure 1.6 [55, 56]. The homogeneity of a mixed Pb and SAC structure is driven by Pb diffusion in the solder joint and determined by such factors as Pb concentration, peak reflow temperature and time, soldering environment, and Pb-free solder composition [57].

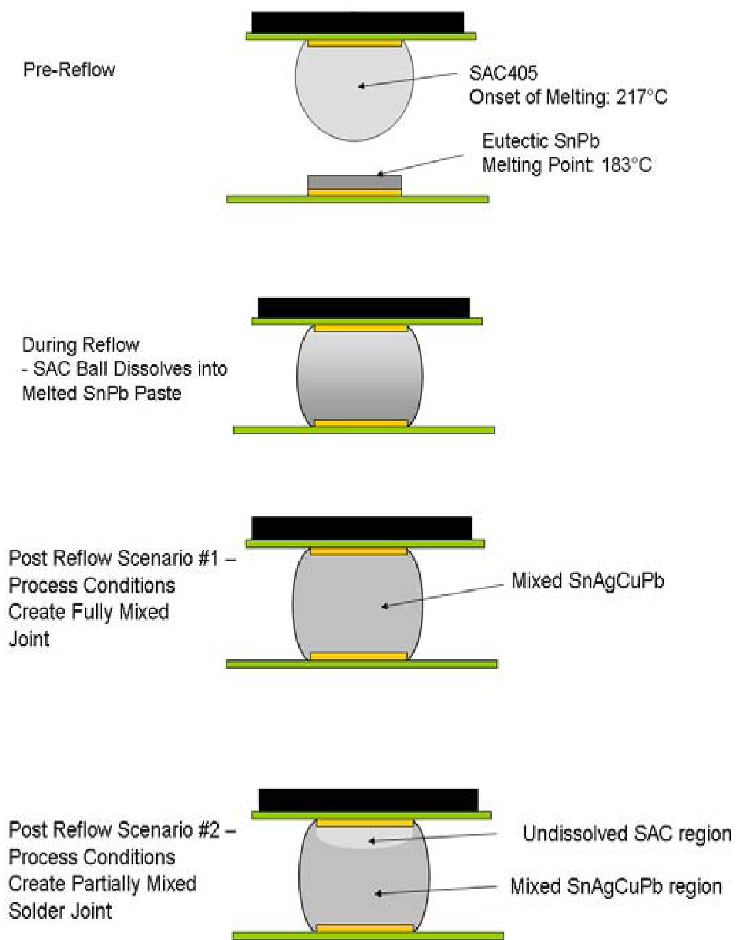

Figure 1.5 "Backwards" Mixed Assembly Process

(a) Fully Mixed BGA Solder Joint

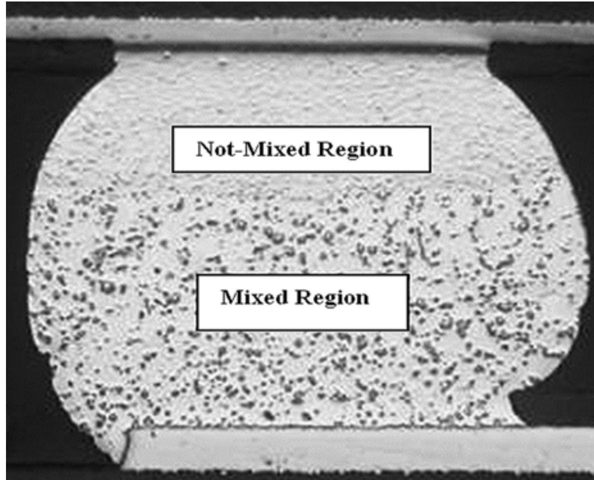

(b) Partially Mixed BGA Solder Joint

Figure 1.6 Micrographs of Typical Mixed Formulation Solder Joints

The literature currently reports contradictory results regarding mixed soldering [55]. Some studies show enhanced mechanical properties and reliabilities in solder joints formed by mixing SAC and Pb, whereas other studies report deteriorated performance. Two major topics in the debate are: (1) what are the minimum peak temperature and time above liquidus (TAL) for backward assembly, and (2) how to achieve the desired mixed-alloy homogeneity and reliability. High peak temperatures are usually used in reflowing Pb-free solder joints to obtain a homogenous microstructure. However, high reflow temperature results in reliability concerns to packages. Hua, et al.[53, 58] found that reliability and process risks are high for backward solder joints formed with a reflow profile of peak temperature less than 217 °C due to the inhomogeneous microstructure resulting from the partially collapsed SAC solder ball. The same phenomenon was observed by Zbrzezny and coworkers [56]. Theuss, et al. [59] further noted that a peak temperature of at least 235 ºC is needed to obtain acceptable reliability of backward solder joints. On the contrary, Nandagopal, et al. [49, 60] reported that backward solder joints with fully mixed microstructure can be achieved with a peak reflow temperature of about 210 °C within 20 to 30 seconds for certain paste-to-ball weight ratios. Therefore, uniform microstructures of backward compatible solder joints formed either below or above the Pb-free ball melting point may be considered equivalent. In addition, Sun [61] reported good reliability and relatively homogenous microstructure when using reflow peak temperatures between 183-220 ºC.

Additional research topics on mixed assemblies include the influence of Pb concentration on the mechanical strength of mixed solder joints [57], Pb diffusion in backward assembly processes and the phases formed in solder mixtures containing Sn-Pb and SAC alloys [62, 63], the reliability of backward solder joints under multiple accelerated thermal cycling (ATC) test conditions for various kinds of electronic components and board finishes [50, 52, 54,

64, 65], and the different failure modes of mixed solder joints under mechanical shock environments (drop, shear, and bending) [64, 66].

1.7 Mechanical Properties of Soldering Materials

As a bonding material, solder alloys provide electrical, thermal and mechanical continuity in electronics assemblies. The relevant solder properties are crucial to the paramount issue in electronics packaging --- solder joint reliability, or SJR in short, which is the ability of solder joints to remain in conformance to their mechanical and electrical specifications over a given period of time, under specified operating conditions. There are two levels of SJR with different interconnection methods:

(1) Component Level: Wire Bonding or Flip Chip Connection

(2) Board Level: Pin-Through-Hole (PTH) or Surface Mount Technology (SMT)

Correspondingly, failures of solder joints in microelectronic devices can be classified into three categories: electrical, mechanical, and corrosion failures. A summary of the various failure mechanisms is shown in Figure 1.7 [67]. Most failures that occur in electronics packages are caused by fatigue and/or fracture, which leads to the loss of device functionality prior to any visible breaking of the device. This type of failure, since it is associated with the mechanical behavior of solder alloys under certain thermal environments, is usually called thermo-mechanical failure of solder joints.

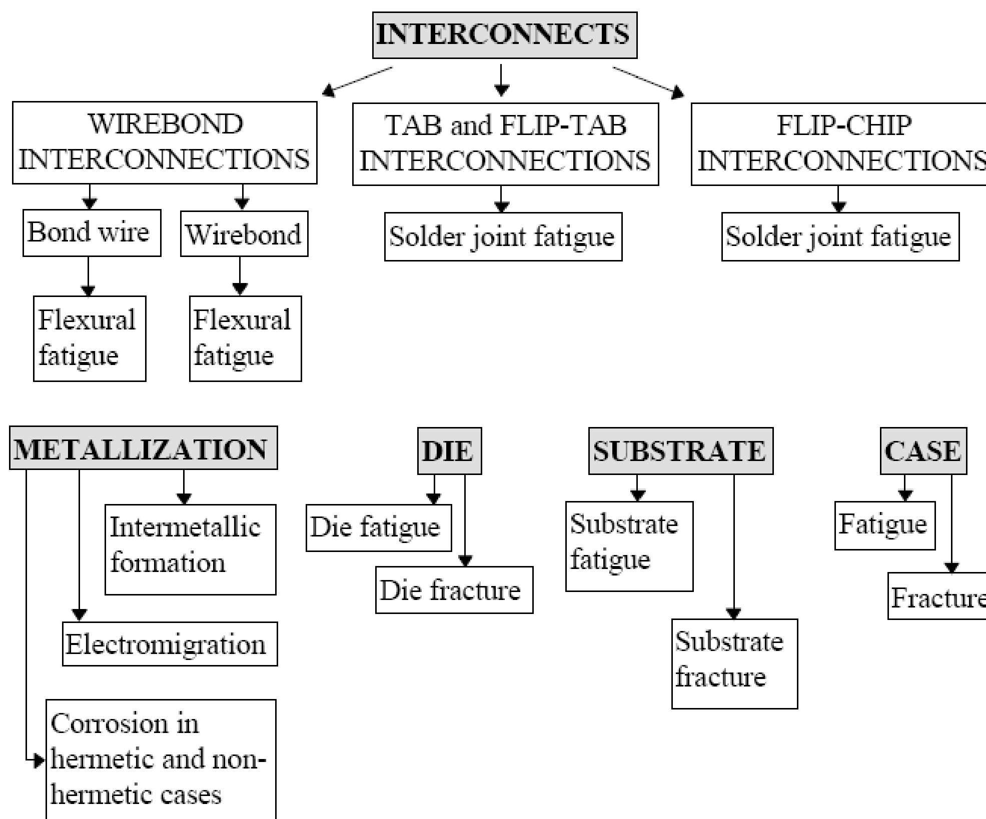

Figure 1.7 Failure Mechanisms in Microelectronic Packaging

1.7.1 CTE Mismatch Stress/Strain

Thermally induced stresses inevitably exist in electronic devices due to CTE (coefficient of thermal expansion) mismatches between the various metals, polymers, composites and sometimes ceramics, used to construct the assembly. Heat is generated every time an electronic product is powered on. If all of the materials within the assembly have identical CTEs, they will expand and contract together if there is good heat transfer in the assembly. In this case, there will be no net thermal stress. However, this circumstance is highly unrealistic since CTE mismatches always exist due to wide array of materials used in modern electronic packaging.

When an electronic assembly is subjected to temperature change, the CTE mismatch within the system results in cyclic stresses in solder joints, as shown in Figure 1.8. From the reliability point of view, it is important to attain thorough knowledge of the spatial and temporal distribution of the cyclic stress, which usually takes the form of solder joint shearing. The governing factors have been identified as the CTE mismatch, the range of the temperature variation, the component configuration and solder joint distribution, the solder joint geometry, and the solder alloy elastic-plastic and creep constitutive relationships.

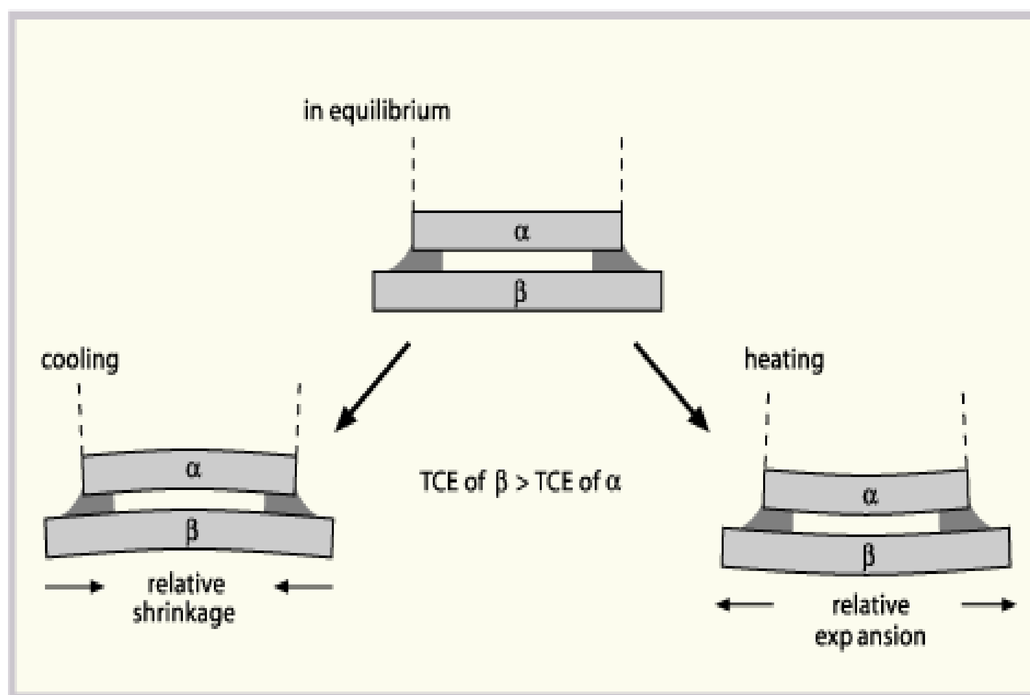

Figure 1.8 Cyclic Stress Induced by CTE Mismatch
http://www.ami.ac.uk/courses/topics/0162_sctm/index.html

1.7.2 Tensile Properties

It is often the case that the solder connection in electronic assembly experiences tensile loading. For example, extensive solder joint deformations occur when the substrate is flexed, as shown in Figure 1.9 [15]. Therefore, the tensile properties of a solder alloy such as yield strength, ultimate tensile strength and elastic modulus are very important in determining the extent of tensile deformation to which solder joint can sustain prior to failure.

The strength of a material is its ability to withstand a load without undue deformation or failure. This property is usually determined by a tensile test, where the results are generally plotted in the form of a stress-strain diagram, as shown in Figure 1.10. There are two types of stress-strain diagrams (deemed "engineering" and "true") in common use. The differences appear in the strain-hardening range, where the magnitude of strain becomes significant. The engineering stress-strain diagram has a significant advantage since it provides the means for obtaining data about a material's tensile strength without regard for the material's physical size or shape [68]. Moreover, most engineering designs are carried out within the elastic range of a material, where distortion is not severe and the errors in using engineering values of stress and strain are very small compared with the true values. Therefore, engineering stress-strain diagrams are more convenient to use and employ.

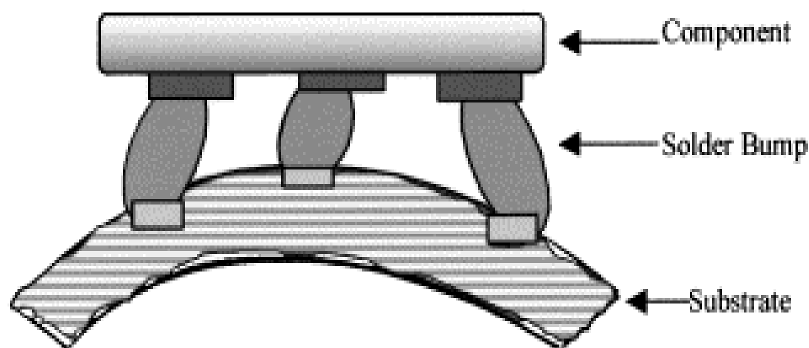

Figure 1.9 Solder Joints Subjected to Tensile Loading due to Substrate Flexing

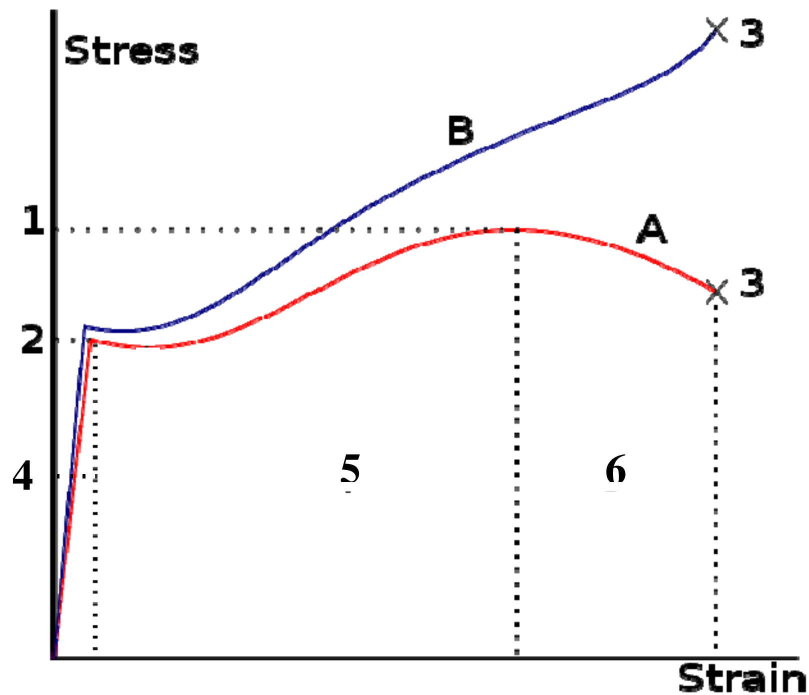

Figure 1.10 Stress-Strain Curve (Engineering vs. True)
http://en.wikipedia.org/wiki/File:Stress_v_strain_A36_2.svg

A. Engineering Stress-Strain Curve; B. True Stress-Strain Curve
1. Ultimate tensile strength (UTS), 2. Yield strength,
3. Rupture, 4. Elastic region
5. Strain hardening (plastic) region
6. Necking (plastic) region

In the elastic region in Figure 1.10, the engineering stress is linear, with the engineering strain obeying Hooke's law [68]:

$$\sigma_{eng} = E\varepsilon_{eng} \tag{1.1}$$

where E is the elastic modulus (Young's modulus), which can be determined from the slope of the elastic portion of the stress-strain curve. The value of E obtained in this way is generally referred to as the apparent or effective elastic modulus. It is generally smaller than the dynamic modulus measured by the acoustic or ultrasonic wave method, which largely eliminates the inelastic deformation due to rapid wave propagation [69-71].

After the engineering stress-strain curve enters the plastic region, the material will experience permanent plastic deformation. Specimens subject to plastic deformation will simultaneously elongate and decrease in diameter, and such behavior is called yielding. The stress that causes yielding is defined as the yield stress (YS). It is usually determined by drawing a parallel line to the elastic portion of the engineering stress-strain curve but offset from the origin by a certain fixed amount. The yield strength is then determined as the intersection between the stress-strain curve and the offset line. This value is usually defined as the 0.2% offset yield strength [68]. The ultimate tensile stress (UTS) is defined as the maximum load divided by the initial cross-sectional area of the specimen. It indicates the maximum stress level a material can withstand before failure under uniaxial loading. A typical engineering stress-strain curve of Pb-free solders is shown in Figure 1.11, which shows the definitions of all important mechanical properties of solder materials.

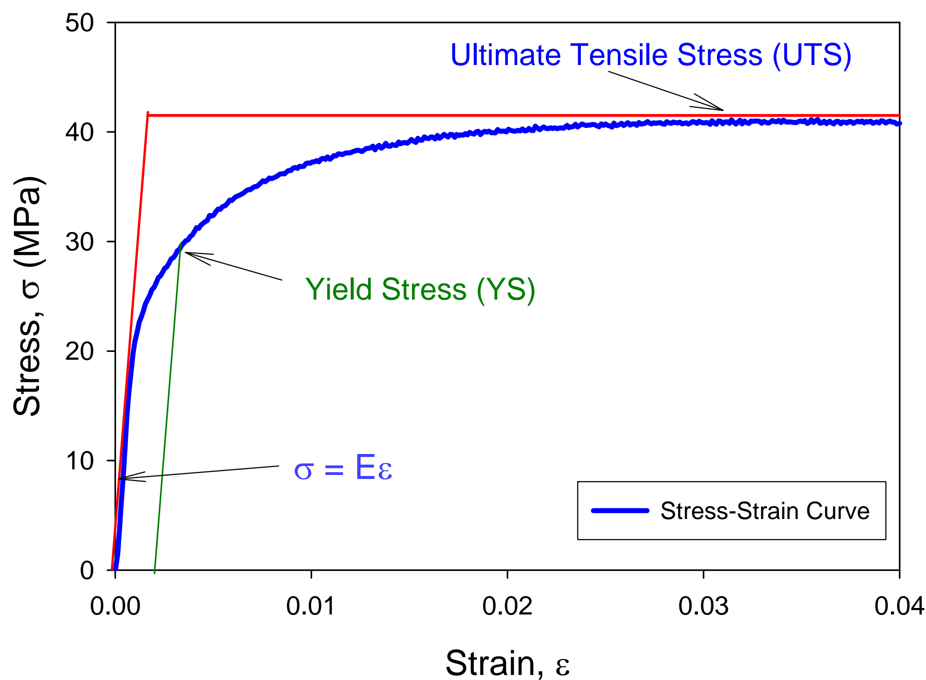

Figure 1.11 Typical Stress-Strain Curve of Pb-free Alloys

1.7.3 Shear Properties

Cyclic shear stresses in solder ball connections are generated by CTE mismatches as an electronic assembly is subjected to thermal cycling conditions. An example of the shear stress generated between a silicon die and the substrate in a flip chip package is shown in Figure 1.12 [15]. In this case, the shear properties of the solder alloy such as the shear modulus and shear strength become important.

A typical shear stress-strain diagram is shown in Figure 1.13 [72]. Similar to tension (Figure 1.10), when a material is subjected to shear loading, it will behave in a linear-elastic manner and exhibit a proportional limit τ_{pl}. Strain hardening will take place from this point to the ultimate share stress τ_u. Then, shear strength will start to decline until it reaches the material's fracture strength τ_f.

For most engineering materials, Hooke's law also holds for the linear elastic behavior in shear:

$$\tau_{eng} = G\gamma_{eng} \tag{1.2}$$

where G is called the shear modulus of elasticity or the modulus of rigidity, measured as the slope of the linear portion on the $\tau - \gamma$ diagram. The shear modulus is also related to the elastic modulus and Poisson's ration by the equation [68]:

$$G = \frac{E}{2(1+\nu)} \tag{1.3}$$

Due to CTE mismatches and thermal gradients (caused by either power switching or the ambient environment), electronic assemblies often undergo combined shear deformation, warpage, and distortion. Under such circumstances, solder joints are usually subjected to a combination of shear and tensile loading.

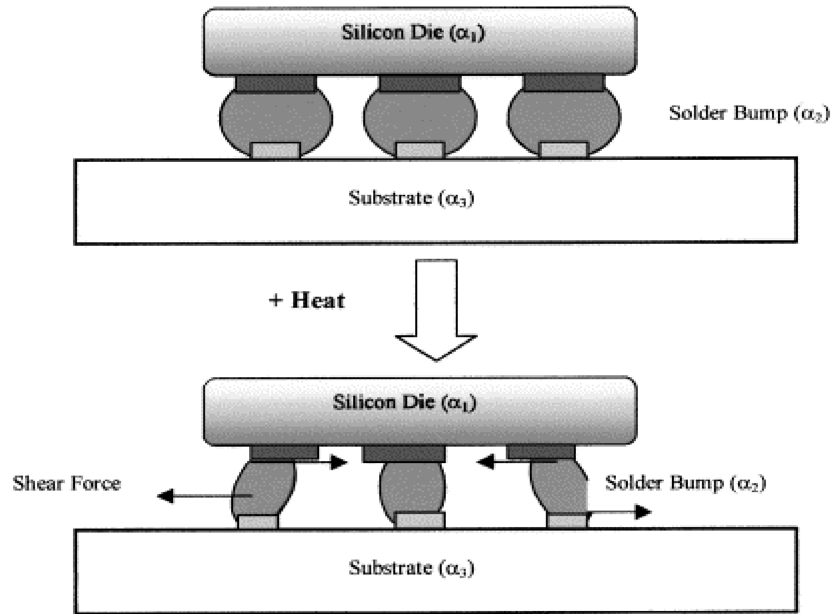

Figure 1.12 Solder Joints Subjected to Shear Strain due to CTE Mismatch

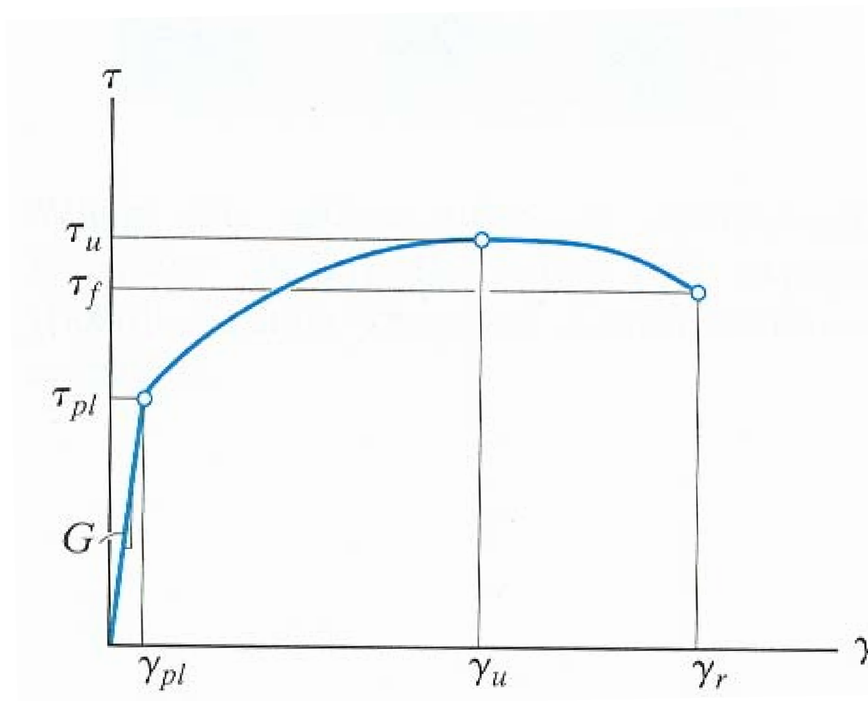

Figure 1.13 Typical Shear Stress-Strain Diagram

1.7.4 Creep

Electronic assemblies are often subjected to long periods of constant elevated temperatures. Under such environments, the solder joints are susceptible to creep. Creep deformation is one of the major failure modes of solder joints for electronic packaging modules [73].

1.7.4.1 The Creep Phenomenon

Creep is a time-dependent permanent deformation that occurs when a material supports a constant load for a very long period of time at a constant temperature. Creep is a measure of the time required for a material to fail when it is under constant loading at an elevated temperature [72]. The level of load/stress and the temperature are dominant factors in creep.

For most materials, creep develops in three stages, namely, primary, secondary and tertiary creep. A typical creep curve for solder is shown in Figure 1.14. The creep response begins with an initial instantaneous strain, which consists of the elastic or time-independent plastic deformation as soon as the constant load is applied [74, 75]. The creep deformations then occur. They are typically divided into three regions or stages as discussed below:

Stage I: Primary Creep

In this stage, the creep strain rate ($d\varepsilon/dt$) decreases rapidly over time due to strain hardening, which restricts the deformation.

Stage II: Secondary Creep or Steady-State Creep

In this stage, the creep strain rate is relatively stable (linear part of the curve) as strain hardening and recovery softening reach a dynamic balance. For metals, if the homologous temperature is greater than 0.5 T_m, most plastic deformation during creep will occur in this stage. At elevated temperature, strain hardening is associated with subgrain formation caused by the rearrangement of dislocations. On the contrary,

recovery and/or recrystallization softening are related to thermally activated cross-slip and edge dislocation climb [68].

Stage III: Tertiary Creep

Tertiary creep is characterized by an accelerated creep rate, which may be caused by various weakening metallurgical instabilities such as localized necking, corrosion, intercrystalline fracture, formation of microvoids, dissolution of strengthening second phases, etc. [68]. Eventually, at the end of this stage, rupture occurs.

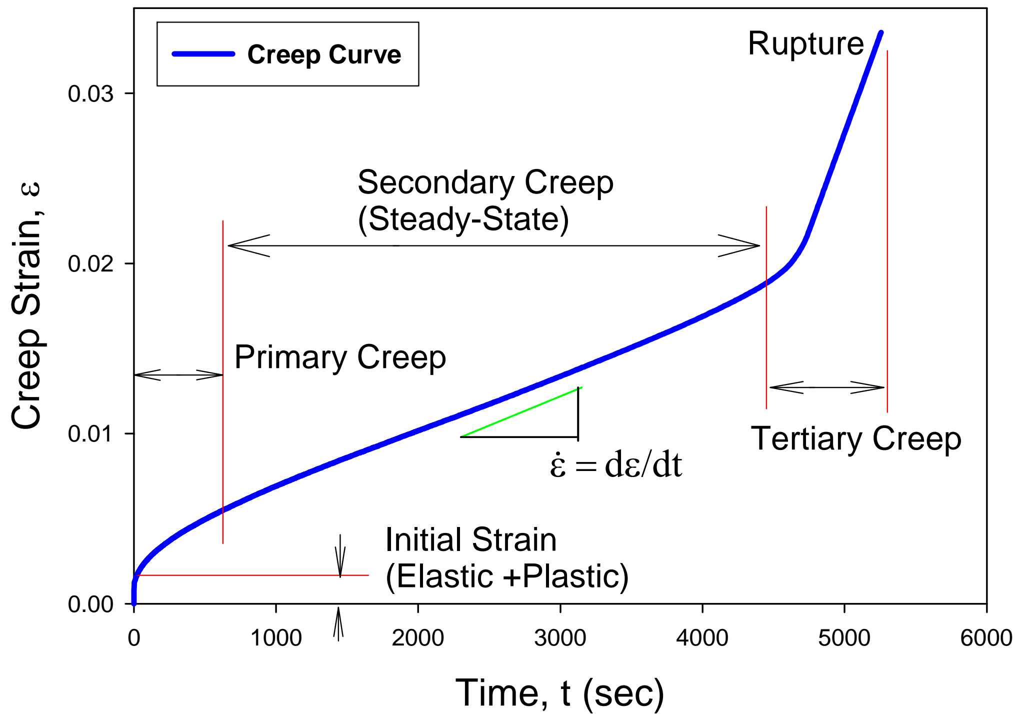

Figure 1.14 Creep Curve under Constant Stress/Load and Temperature

1.7.4.2 Creep Mechanism

Creep deformation becomes critical when the temperature exceeds one-half the melting temperature (°K) of the material. This is the case for most soldering alloys at room temperature. Therefore, creep is considered the most important solder deformation mechanism in SMT [76]. Several creep mechanisms have been proposed such as dislocation glide, dislocation creep, grain boundary diffusion, and lattice diffusion. A widely accepted deformation mechanism map of the dominant creep mechanisms is shown in Figure. 1.15 [75, 77, 78]. This deformation map was first constructed by Ashby and his coworkers [78], based on the idea that plastic deformation is a kinetic process occurring on the atomic scale. The kinetic processes include mechanical twinning, glide and/or climb of dislocations, the diffusive flow of individual atoms, and the relative displacement of grains by grain boundary sliding (involving diffusion and defect-motion in the boundaries). These are the underlying atomistic processes that cause plastic flow or deformation and contribute to deformation and depend on factors as strain, strain-rate, and temperature.

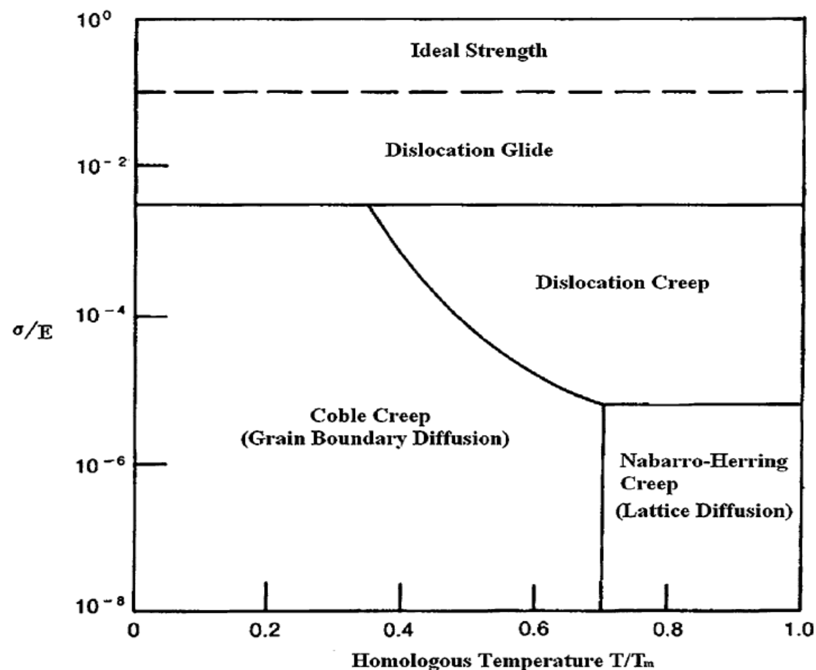

Figure 1.15 Creep Deformation Map for Solder Alloys

In the deformation map show in Figure 1.15, the abscissa is the homologous temperature and the ordinate is normalized tensile or shear stress. Five zones are defined on the map, each of which corresponds to a particular deformation mechanism. These zones are:

Zone 1: Ideal Strength. Plastic flow occurs when the ideal shear strength is exceeded.

Zone 2: Dislocation Glide. This occurs at high stress levels over the entire homologous temperature range. The dislocations move along the slip planes [77].

Zone 3: Dislocation Creep. This is characterized by a high-temperature deformation mechanism with homologous temperatures greater than $0.5T_m$ and requiring intermediate high stress [79]. The deformation results from diffusion controlled dislocation movement, with dislocations climbing away from barriers.

Zone 4: Grain Boundary Diffusion – Coble Creep. This is a grain boundary based diffusion mechanism involves atomic or ionic diffusion along the grain boundaries [80]. The deformation occurs at intermediate low stress levels over a low to intermediate temperature range.

Zone 5: Lattice Diffusion – Nabarro-Herring Creep. This occurs at low stress level and high temperature. Interstitial atoms and lattice vacancies along the gradient of a grain boundary migrate in reversed directions in the presence of tension or compression pressure. Lattice or bulk diffusion becomes the primary deformation mechanism under this circumstance [68, 81, 82].

In Nabarro-Herring creep, if there is no pressure, interstitial atoms and lattice vacancies will migrate in proportion to the gradient of their concentrations. Under pressure, the lattice defects tend to move in directions to relieve the imbalance of pressure. The movement will eventually cause creep deformation [82].

Grain-boundary sliding is another possible creep deformation mechanism at high temperatures and is caused by applied stress [68]. However, this mechanism is not independent, and is associated with other deformation mechanisms aforementioned.

Due to the high homologous temperature (> $0.5T_m$) of most solder alloys under normal operating conditions, the stress level determines the creep deformation mechanism. At low stress levels, the controlling mechanism is lattice diffusion and grain-boundary diffusion. As the stress rises to intermediate levels, dislocation creep takes over, and at high stress level, dislocation gliding becomes dominant. Additionally, the contribution of grain boundary gliding to creep deformation should be taken in account at all stress levels.

1.7.5 Fatigue

Solder joints in electronic assemblies are often subjected to cyclic loadings due to CTE mismatches. The operational life span of an electronic product will typically depend upon the solder joint fatigue life, defined as the number of cycles before fatigue failure occurs.

1.7.5.1 Fatigue Phenomena

When a material is subjected to high cyclic stress, which causes its structure to break down and finally fracture, the material undergoes a deformation process called fatigue. This phenomenon usually occurs at stress levels lower than the material's yield stress. Fatigue is responsible for a large percentage of failures of engineering materials.

Fatigue failure results from localized stress concentrations. The surface of materials contains microscopic regions, where the localized stress becomes much greater than the average stress acting over the cross section. As the increased stress is cycled, micro-cracks will initiate and lead to stress concentrations at crack tips or boundaries. Higher stresses consequently cause

crack extensions into the material. As the process continues, the reduced cross-sectional area will no longer be able to withstand the applied load and fatigue fracture occurs.

Fatigue failure is sudden, catastrophic, and involves relatively little plastic deformation. When subjected to fatigue, ductile materials often behave as if they were brittle. The fatigue damage is cumulative, and the materials will not recover when load is removed. There are three stages for a fatigue failure to fully develop and occur [68]:

Stage 1: Crack nucleation

Cracks initiate at the sites of stress concentration (micro-cracks, scratches, indents, interior corners, dislocation slip steps, etc.).

Stage 2: Crack propagation occurs in two steps:

Step I: Initial slow propagation along crystal planes with high resolved shear stress. Fracture formed in this step features flat surface.

Step II: Faster propagation perpendicular to the applied stress. Cracks grow by repetitive blunting and sharpening process at crack tip. Fractures have a rough surface.

Stage 3: Ultimate failure, where cracks eventually reach critical dimension and propagates very rapidly.

It is notable that competition occurs during the process of fatigue crack growth [83]:

(1) Intrinsic, crack growth promoting mechanism: cracks advancing ahead of the crack tip, including alternating crack-tip blunting and resharpening, etc.

(2) Extrinsic, crack growth impeding mechanism: crack-tip shielding behind the tip, including crack closure and bridging, etc.

1.7.5.2 Fatigue Life

The American Society for Testing Materials (ASTM) [84] defines fatigue life by N_f, the number of cycles to fail at specified stress level. The length of a material's fatigue life depends on such factors as surface finish, load amplitude and direction, residual stress, grain size, internal defect distribution, notch sensitivity, geometry and size, as well as temperature and environment.

1.7.5.3 High Cycle Fatigue

Fatigue caused by low stress, which occurs at relatively large cycle numbers ($N > 10^5$) is usually defined as high cycle fatigue. The incurred deformation is primarily elastic and fatigue strength can be described by stress-based parameters.

A number of cumulative damage theories exist to understand the relationship between stress interactions and the amount of damage. Miner's rule or the Palmgren-Miner linear damage law [85], which attempts to determine the proportion of life consumed by stress reversal at each magnitude and form a linear combination of their aggregate, has been widely utilized:

$$\sum_{i=1}^{k} \frac{n_i}{N_i} = C \tag{1.4}$$

where k is the number of stress levels in the loading spectrum; σ_i is the i_{th} stress level; n_i is the number of cycles applied at σ_i; N_i is the fatigue life at σ_i; and C is usually assumed to be 1 for design purposes and is experimentally found to be somewhere between 0.7 and 2.2.

1.7.5.4 Low Cycle Fatigue

Fatigue caused by high stress, which occurs at relatively small cycle numbers ($N < 10^3$) is usually defined as low cycle fatigue. Since the stress is high, plastic deformation occurs. Therefore, strain-based parameters are normally used to predict fatigue life. The most widely accepted theory for low cycle fatigue is the Coffin-Manson relation [86]:

$$\frac{\Delta\varepsilon_p}{2} = \varepsilon'_f \left(2N_f\right)^c \tag{1.5}$$

where $\frac{\Delta\varepsilon_p}{2}$ is the plastic strain amplitude; ε'_f is an empirical constant known as the fatigue ductility coefficient; $2N_f$ is the number of strain reversals to failure; and C is an empirical constant known as the fatigue ductility exponent.

1.8 Objectives of This Research

The objective of this research is to systematically study isothermal aging effects on the mechanical behavior and microstructure evolution of Pb-free SAC alloys as well as a series of mixed formulation solders. The steps to achieve this objective are:

- Develop test specimen preparation procedures that produce uniaxial test specimens with consistent microstructure comparable to the Pb-free solder materials used in commercial electronic assemblies.
- Design and prepare mixed formulation solder alloys that are mixtures of pure SAC305 and pure eutectic 63Sn-37Pb with different mixing ratios.
- Measure isothermal aging effects on the uniaxial tensile and creep properties of 63Sn-37Pb, Pb-free, and mixed formulation solders over a wide range of aging temperatures and times.
- Investigate the influence of chemical composition (Ag content for SAC alloys and 63Sn-37Pb content for mixed formulation alloys), and applied stress level on the tensile stress-strain and creep behaviors under various aging conditions.
- Study the microstructure evolution as a function of aging conditions and chemical compositions, as well as the transition to failure by fractography analysis.

- Examine the physical properties of mixed formulation solders and explore their potential application in real electronic packages.
- Establish constitutive models and a mechanical property database of Pb-free SAC and mixed formulation solders for use in finite element reliability simulations.

1.9 Organization of the Dissertation

This dissertation is divided into the following chapters:

- Chapter 1: Introduction to Pb-free soldering technology and alloys, the rationale for mixed formulation solders, and key mechanical properties of solders.
- Chapter 2: Literature survey on solder thermal aging effects with respect to mechanical properties and microstructure evolution, and on constitutive modeling of solder material behavior and life prediction of solder joints.
- Chapter 3: Description of the experimental procedures used in specimen preparation and the uniaxial tests conducted on the micro-tensile testing machine.
- Chapter 4: Study on aging effects on the stress-strain behavior, mechanical tensile properties, and microstructure evolution of Pb-free SAC alloys.
- Chapter 5: Study on aging effects on the creep behavior of Pb-free SAC alloys.
- Chapter 6: Study on preparation and microstructure of mixed formulation solders.
- Chapter 7: Study on aging effects on the mechanical properties and creep behavior of mixed formulation solders.
- Chapter 8: Summary and conclusions of the dissertation.

Chapter 2
Literature Review

2.1 Introduction

As the world transitions to Pb-free soldering, great efforts have been undertaken to develop desirable Pb-free solders and establish a corresponding database of material properties. Thousands of technical articles have attempted to measure the key mechanical properties of Pb-free solders, but large discrepancies remain in the reported values [87].

There are a variety of causes for the discrepancies. First, mechanical properties obtained from bulk solder specimens are usually substantially different from those of solder joints in real electronic assembly. Second, specimen preparation methods will directly affect the experimental results to a considerable degree. A consistent starting microstructure is necessary to ensure reproducible and consistent results [88-102]. Third, the test methods (e.g. direct loading [103-106] or solder joint indenting [107, 108]) and test conditions may vary between researchers, which results in data sets that cannot be easily compared. Finally, the lack of standardization in the data acquisition and processing of mechanical properties makes it difficult to obtain good laboratory-to-laboratory comparisons.

One critical factor that has been neglected in most previous literature on solder alloys is isothermal aging. For solder materials, aging is especially important because most solder alloys have high homologous temperatures even in room temperature environments. During the service life of an electronic device, solder joints undergo continuous aging, which affects not only the mechanical properties of the solder but also its microstructure. The study of aging effects on

soldering materials will thus help reduce the discrepancies in the current mechanical property database, explain the change in microstructure and mechanical behavior of solder alloys over time, and provide information on failure mode of solder joints at various working conditions.

In surface mounted electronic components, solder joints provide not only electrical connections but also mechanical support on the printed circuit board (PCB). The CTE mismatches between the PCB and the IC components generate large cyclic deformations, which in turn produce complex stress/strain conditions and eventually lead to solder joint failure. In order to improve solder joint reliability, and achieve ideal product design, it is helpful to have well-established, reliable constitutive models for solder alloys so that accurate solder joint stress/strain analysis can be performed and solder joint life can be predicted. Due to the high homologous temperatures solder joints experience during operation, solder alloys usually exhibit complicated creep-plasticity interactions and significant temperature-stain rate dependent material characteristics. It is for this reason that the constitutive modeling of material behavior of solder alloys is challenging and requires in-depth investigations.

2.2 Aging Effects on Solder Materials

Solder materials used in electronics packaging are supplied in three common forms: (a) bulk solder for operations such as wave soldering; (b) solder paste for operations such as surface mount reflow; and (c) solder balls or solder columns for applications such as ball grid array, column grid array and flip chip packages. As mentioned above, the mechanical properties of bulk solders are different from solders in solder joints in a number of important ways, including aging effects. An early example of room temperature aging effects on solder alloys was identified by Lampe [109] in 1976, as shown in Figure 2.1. He found that Sn-Pb and Sn-Pb-Sb

solder alloys experienced a loss up to 20% in their shear strength and hardness after 30-day storage at room temperature. As early as 1956, Medvedev [110] observed a 30% loss of tensile strength for bulk Sn-Pb solder stored for 450 days at room temperature, but a 23% loss of tensile strength for solder joints subjected to the same condition for up to 435 days. Optimally, the investigation of aging effects on solder materials should be carried out close to the specific operating conditions of the actual solder joints.

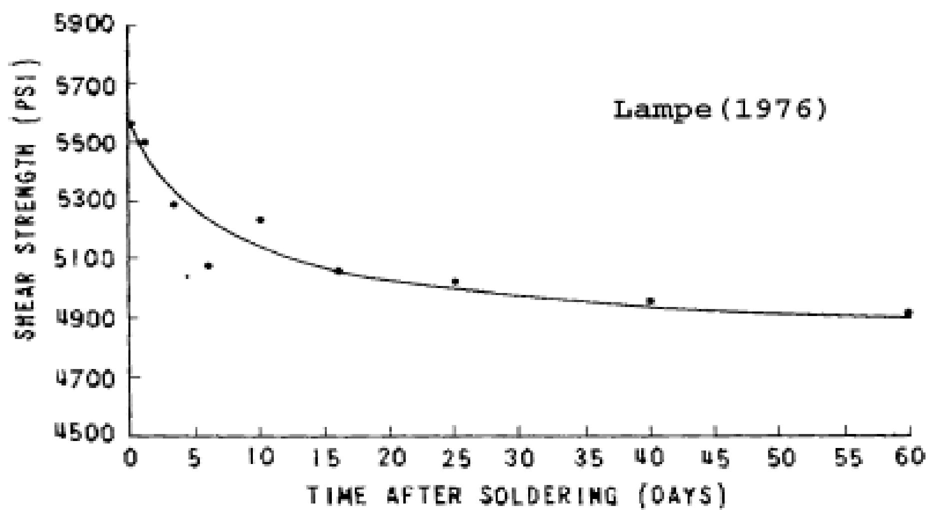

Figure 2.1 Room Temperature Aging Effects on Sn-Pb Solder

2.2.1 Aging Effects on Bulk Solder Alloys

2.2.1.1 Mechanical Behavior

The mechanical behavior of solder alloys under aging is influenced by such factors as applied mechanical loads, strain rate, temperature and time [111-113]. The specimen size [114] and cooling method [115, 116] can also be significant. In the case of SAC alloys, however, previous work has demonstrated that temperature and time are the most critical factors, which most strongly affect the solder aging performance [92, 100, 101, 109, 117-120]. At room temperature, Sn3.9Ag0.6Cu alloy continually age-softens, whereas at 180 °C, the alloy reaches

its minimum flow strength after only one day of aging [101]. Further aging at 180 °C leads to aging hardening of the alloy, an effect thought to be caused by the dispersion of Ag_3Sn particles into Sn-rich crystals which previously did not contain any intermetallic precipitates. Three SAC alloys (SAC432, SAC396 and SAC387) all exhibit a decrease in their flow strength with increasing test temperatures after being aged at 125 °C for 24 hours, and the degree of strength change is highly dependent on their composition [117].

Ma, et al. [118] have systematically observed the evolution and saturation of Young's modulus, yield strength, and ultimate strength of a series of SAC alloys under various aging conditions. A linear-exponential model was developed to describe the material property evolution. Aging effects on creep resistance in terms of secondary creep strain rate were also reported. Xiao, et al. [100] found that SAC396 showed much lower absolute creep rates compared with eutectic Sn-Pb and ascribed this increase in creep resistance to the finely dispersed intermetallic compound (IMC) precipitates in the Sn matrix. Aging effects on primary creep were found to be more dramatic than on secondary creep [120]. This finding is correspondent with the finding of Plumbridge [121], in that ignoring the primary portion of creep can lead to significant under-prediction of solder joint life. Development of constitutive models that account for aging effects on both the primary and secondary creep responses of SAC385 was proposed for future study.

2.2.1.2 Microstructure Evolution

Mechanical behavior changes in solder alloys reflect the *extrinsic* response to aging for the material. For deepest understanding, it is necessary to understand their *intrinsic* response to the effects of aging, i.e. the evolution of solder microstructure under aging conditions. A vast body of

previous work on aging has focused on the growth of IMC layers at the solder-substrate interface. In contrast, only limited information exists on microstructure changes in bulk solders during aging.

Aging effects on microstructure include coarsening of IMC with increased temperature, IMC coalescing, and dispersing with increased aging duration [100, 120]. Ngoh, et al. [34] studied the effects of temperature on the microstructure of a SAC alloy (SAC387) by using a fixed aging time but various aging temperatures. They found that with increased aging temperature, IMCs became smaller in number, larger in size and rounder in shape, indicating the growth of large IMCs at the expense of the small ones. The effect of time was studied by using a fixed high aging temperature and various aging times. Evolution and saturation of IMC coarsening were found as aging time increased.

Allen, et al. [122, 123] investigated the coarsening kinetics of the ternary eutectic in cast SAC solder alloys and concluded that the process is governed by $r^3 \propto t$, where r is the rod radius of the dispersed phase and t is aging time. The two types of intermetallic rods (Cu_6Sn_5 and Ag_3Sn) in the eutectic structure coarsened at different rates due to different rate-controlling mechanisms: a Cu diffusion mechanism for the coarsening of Cu_6Sn_5 phase, and diffusion of Sn along the Ag_3Sn/(Sn) interface for the mechanism of the breakdown of the Ag_3Sn plates. A backscattered electron image (shown in Figure 2.2) on a boundary region in a cast ternary eutectic SAC sample after being aged at 201 °C for 4 weeks shows that both Cu_6Sn_5 (dark) and Ag_3Sn (light) intermetallic phases are present with coarsening of Cu_6Sn_5 being the dominant process [122]. They found that the SAC microstructure coarsened more slowly with aging than that of Sn-Pb. Research conducted by Reinikainen [124] also concluded that the microstructure evolution for SAC alloys is considerably slower than eutectic or near eutectic Sn-Pb solders.

Snugovsky, et al. [125] studied the microstructural changes occurring within SAC387 during aging for various times at 150 °C. They found that with aging, the Sn dendrite pattern became progressively less distinct due to the continuous coarsening of the Ag_3Sn and Cu_6Sn_5 phases. The Cu_6Sn_5 phase coarsened rapidly owing to the fast diffusion rate of Cu in Sn, while coarsening of the Ag_3Sn particles occurred more slowly because of the much slower diffusion rate of Ag atoms compared to Cu atoms. Estimates of particle size as a function of aging time indicated that the Ostwald ripening process (controlled by bulk diffusion of Cu and Ag in the Sn matrix) is the ruling phase coarsening mechanism in SAC alloys.

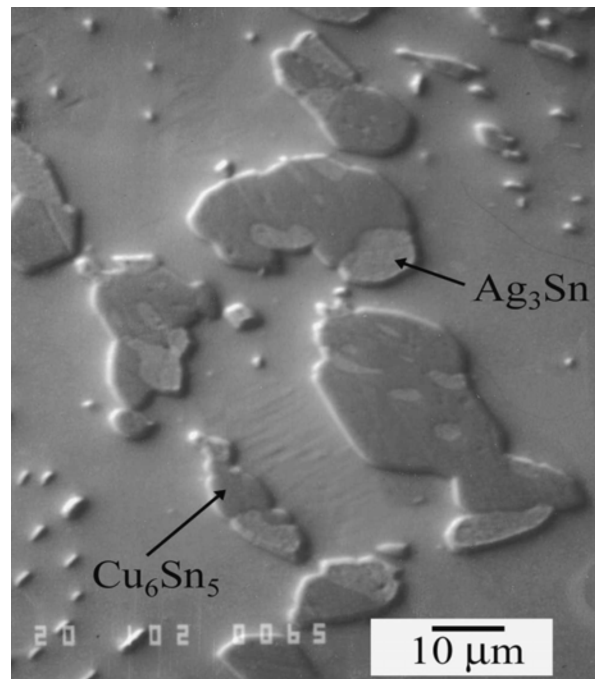

Figure 2.2 Coarsening of Intermetallic Phases in Eutectic SAC Alloy under Aging

2.2.2 Aging Effects on Solder Joints

2.2.2.1 Mechanical Behavior

The mechanical response of solder joints to external loading can be dramatically different from bulk solders due to the distinctive features of solder joints, including: interfacial intermetallic compounds, fine microstructure and mechanical constraint jointly imposed by substrate and bulk solder. Early experimental result shows that solder joints usually have higher strength than bulk solder specimens [126].

When studying the mechanical behavior of solder joints in area array packages, ball shear testing is considered to be the most suitable method for capturing the actual mechanical behavior of solder joints and to assess the integrity of solder ball attachment [105, 127]. During the ball shear test, the shear tool moves at a specified speed to exert a force on the solder balls. The fracture mode of a solder joint is determined by the relationship between bulk solder strength and joint interfacial strength, shown in Figure 2.3 [128]. Generally, when fracture occurs within the bulk solder ball, it is called good fracture mode or a solder ball fracture mode (Figure 2.3a), whereas if peeling takes place at the plating interface, it is called bad fracture mode or interfacial fracture mode (Figure 2.3b).

For a solder joint or an array of solder joints, aging affects the final solder joint reliability in two ways: (1) aging determines the bulk solder strength, and (2) aging determines the strength and structure of intermetallic compounds formed at the interface between the bulk solder and substrate through the reaction of the solder alloy with the bond-pad metallization. Aging effects on solder alloys as a function of substrate pad finishes (SMT package) and under bump metallurgies (UBM, flip chip technology) can be found in the substantial literature on this topic [104, 128-151].

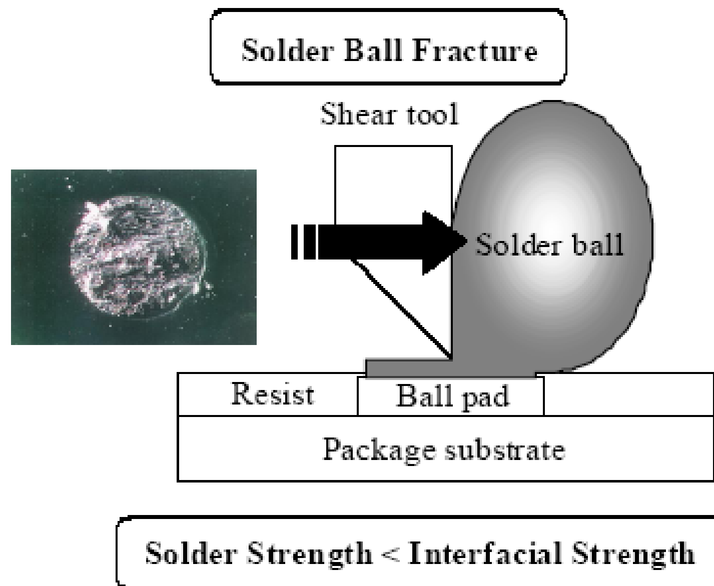

(a) Good Fracture or Solder Ball Fracture Mode

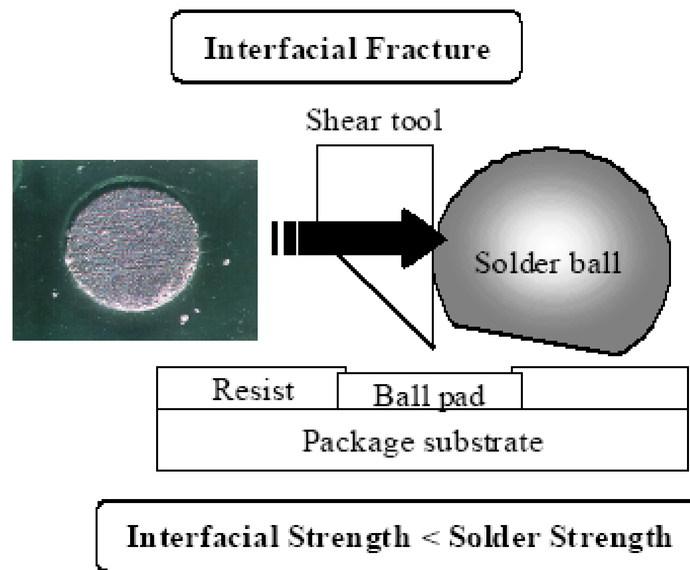

(b) Bad Fracture or Interfacial Fracture Mode

Figure 2.3 Fracture Modes of Solder Joints in Ball Shear Test

2.2.2.1.1 Room Temperature Aging Effects

Ball shear tests used to characterize 63Sn-37Pb solder ball shear strength of 5 commercial plastic ball grid array (PBGA) packages have showed that the solder ball shear strength can drop 10% within 3 days of room temperature aging after reflow [137, 139]. Room temperature aging experiments on eutectic 63Sn-37Pb, Sn-0.7Cu, Sn-3.5Ag, and SAC387 solder bumps with electroless Ni-P UBM and Cu UBM used for flip chip packaging applications have showed that after 51 days of aging, the shear strength of 63Sn-37Pb bumps dropped 25% and the shear strengths of the other Pb-free solder bumps experienced a 5–8% decrease [97, 129]. The shear strength was found to decrease most in the first 100 hours after reflow. Microstructure evolution with aging was thought to be the root cause for the shear strength change. Coyle, et al. [140] reached a similar conclusion by experimenting with 63Sn-37Pb and 62Sn-36Pb-2Ag solder alloys used for solder balls in area array IC packages. Room temperature aging effects on fatigue strength was studied by Chilton and coworkers [148] on a SMD test package with 60Sn-40Pb solder joints. A decrease of 10 to 15% in fatigue strength was observed after 60 to 120 days aging.

2.2.2.1.2 Elevated Temperature Aging Effects

Flip-chip devices with SAC387 solder on electroless Ni (EN) surface finish without immersion Au were studied after aging at elevated temperatures by Li, et al. [145]. The shear strength of solder bumps subjected to aging at 80 °C decreased gradually after 20 days. For those subjected to higher aging temperatures, e.g. 150 °C and 175 °C, the shear strength dropped much faster. The fracture mode of the solder bumps was found to be within bulk solder. Shear tests with SAC387 solder joints on electroless Ni with immersion Au (ENIG) showed that after aging at 80 °C and 150 °C for up to 440 hours, gradual decreases in the solder joint strength occurred [147].

The deformation behaviors of 5 solder alloys (63Sn-37Pb, Sn-3.5Ag, Sn-0.7Cu, SAC305 and SAC405) under aging were compared on 0.5 mm pitch wafer level chip scale packages (WLCSP) with Al/NiV/Cu pad metallization by Darveaux [104]. Shear tests indicated that after 24 hours of aging at 125 °C, all alloys showed a 10% to 30% reduction in solder joint strength. All of the solder joints failed within the bulk solder and exhibited high ductility. In addition, the ductility of all of the Pb-free solder joints decreased with increased aging [104].

Oliver, et al. [146] found the solder joint strength of Sn-3.5Ag and SAC325 on both Ni/Au and Sn/Pb pad metallizations remained unchanged after being aged for 1000 hours at R.T., 100 °C and 150 °C. In contrast, the solder joint strength of 63Sn-37Pb gradually became weaker than the two Pb-free alloys. Koo, et al. [141] found that 63Sn-37Pb solder joint strength on electroplated Ni/Au BGA substrate was significantly affected by aging at 170 °C for up to 21 days, while the deterioration of shear properties of Sn-3.5Ag was much smaller. Shear tests were carried out by Li, et al. [144] after aging at 150 °C for up to 1000 hours on two Pb-free solders joints (Sn-3.5Ag and SAC305) and one Pb-containing solder joint (62Sn-36Pb-2Ag) on Cu/Ni/Au BGA pad metallization. This work verified that the Pb-free solders had good resistance to thermal aging effects since the ball shear strengths of SnAg and SAC alloys almost remained constant, while the SnPbAg alloy experienced considerable reduction in ball shear strength with aging time.

Aging effects on the creep properties of SAC387 solder alloy were studied on flip-chip joints, PCB solder joints and bulk specimens by Wiese [150, 151]. It was found that short thermal storage times (24 hours at 125 °C) softened the SAC solder joints significantly, while longer thermal storage times (1176 hours at 125 °C) failed to change the creep behavior significantly. Longer aging times appeared to stabilize the creep behavior and alloy

microstructure. This agrees with the results from Sigelko and coworkers [152], who demonstrated the high temperature stability (up to 180 °C) of SAC. Age softening effects on the creep behavior of various Pb-free solder joints were also observed by Darveaux, et al. [132].

The mechanical properties and fatigue life of 63Sn-37Pb solder joint specimens were investigated under thermal cycling condition from -40 °C to 125 °C by Pang, et al. [143, 149]. The shear strength showed a significant reduction for specimens subjected to 1000 thermal cycles. Microstructure coarsening and intermetallic growth were connected to the deterioration in the solder joint strength. The fatigue life of specimens subjected to 1000 and 2000 thermal cycles dropped drastically (6 to 8 times) compared to non-cycled specimens.

Some researchers have studied the relationship between solder ball joint reliability and substrate pad finish under aging conditions. Hasegawa, et al. [128] evaluated the relationship of thermal aging at 150 °C on the reliability of both eutectic Sn-Pb and Pb-free SAC alloys on substrates with a variety of PBGA surface finishes. Little change was observed in the mechanical strength (shear strength and elastic modulus) and structure of SAC357 solder even after thermal aging as long as 1,000 hours. SAC showed very high joint reliability, especially for the electroless Ni-P/Pd/Au plating. In contrast, 63Sn-37Pb solder joints exhibited low joint reliability after aging regardless of the substrate pad finish. The deterioration in joint reliability was attributed to a decline in stress relaxation owing to the increase of elastic modulus after thermal aging. Zhou, et al. [153] compared the joint strengths of SAC387 on both Cu and Ag substrates at an aging temperature of 170 °C, and concluded that aging had little effect on the SAC/Ag interface, but dramatically softened the SAC/Cu joint. The softening difference was said to be due to lower residual stresses at the SAC/Ag joint interface.

2.2.2.2 Microstructure Evolution

Aging affects solder joints through changes in bulk solder and solder-pad reaction layer microstructures [124]. The solder bump and alloy compositions, the passivation technologies in use, and the reflow thermal profile are important factors. Moreover, due to the high homologous temperatures of solder alloys and the intrinsic thermal mismatch between the various materials that constitute the package, substantial mechanical stresses and strains will arise and under the influence of temperature, which will cause continuous changes in the solder joint microstructure.

2.2.2.2.1 As-reflowed Microstructure

During reflow solder processes, molten solder at joints contacts the substrate and causes a series of metallurgical reactions, including surface finish dissolution, substrate dissolution, intermetallic layer formation, and precipitation of second phases. These interactions change both the solder composition and solder properties.

In Sn-rich solders such as Sn-Ag and Sn-Ag-Cu on a Cu substrate, a double layer of intermetallics will be formed after reflow with Cu_3Sn (ε) on the Cu substrate side and Cu_6Sn_5 (η) on the bulk solder side [154]. The nucleation and growth of the IMCs take place when the molten solder reacts with the Cu substrate. The η phase forms first at low temperature (< 170 °C). Formation of the ε phase needs higher activation energy and requires higher temperature.

The cooling rate has a significant effect on solder joints microstructure by determining the initial interfacial IMCs which form (e.g.. Ag_3Sn and η-Cu_6Sn_5 phases) [155]. Fast cooling rates (e.g. water quenching) result in relatively thin and planar IMCs, while slow cooling rates (e.g. air or furnace cooling) lead to a relatively thick and scalloped IMC morphology. Fast cooling rates also result in a fine β-Sn primary grain structure in bulk solder, while slow cooling rates lead to relatively coarse β-Sn dendrites.

The thickness of intermetallic layers after reflow is a function of reflow temperature, reflow time, and number of reflows [129, 156]. Pandher [157] has studied the optimization of the reflow process for SAC solder alloys in order to achieve the highest solder joint reliability in BGA applications. He found that lower temperatures result in thinner IMC layers, which improves the mechanical integrity of the solder joint. Shorter periods of time above the liquidus (TAL) are thus preferred for reducing interfacial fractures. The solder volume/pad metallization area (V/A) ratio also has an effect on the thickness of the IMC formed during reflow [136]. Thicker IMC layers were associated with lower V/A ratios regardless of the surface finish [158].

Different substrate surface finishes cause IMC layers with different characteristics to form at solder joints. Nonetheless, the IMC layers formed on various surface finishes possess similar composition to Cu_6Sn_5. SAC/Ni is an example [144, 159]. Ni plating provides a good barrier to the excessive growth of Cu-Sn intermetallics. The reaction layer formed between Sn and Ni has a composition of $(Cu_{1-y}Ni_y)_6Sn_5$ with some Ni atoms substituted for the Cu atoms. Also, due to the consumption of Cu atoms in SAC/Cu system or SAC/Ni system during reflow, when the last portion of molten solder solidifies, there is a depletion of Cu in the system and Sn-Ag binary solder is left in bulk solder to form the Ag_3Sn/Sn eutectic structure. The morphology of Ag_3Sn is long needle-like phases in bulk solder, but after deep etching as shown in Figure 2.4. They appear to be lamella-like and may become crack initiation and propagation sites under stress [160]. With Ni/Au (ENIG) surface finishes, a thin layer (~0.1μm) of immersion Au is plated to promote wetting and protect the Ni finish from oxidation [144]. This layer of Au will totally dissolve in molten solder during reflow and precipitate out as the $(Au_xNi_{1-x})Sn_4$ phases inside the bulk solder upon cooling and thermal aging [161-165].

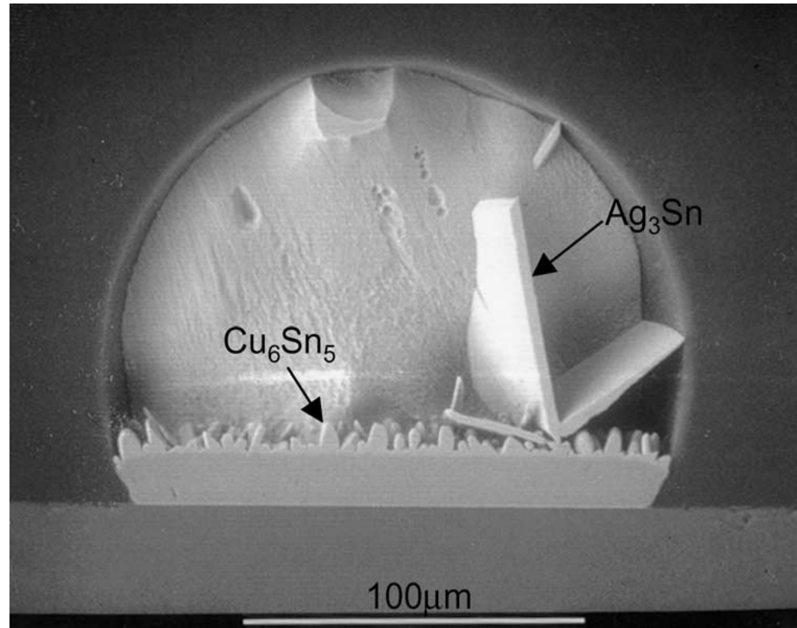

Figure 2.4 IMCs Formed in SAC387 Solder Joint on Bare Cu Pad

2.2.2.2.2 Thermally Aged Microstructure

Interfacial IMCs play an important role in determining the properties of Pb-free solder joints. Normally, aging will cause the IMC to grow thicker and have a negative effect on the interfacial strength. Many studies on aging have been performed in order to evaluate the microstructural changes and growth kinetics of the intermetallic layers formed between different solder alloys (SAC alloys in particular) and substrates (bare Cu pad [33, 129, 149, 156, 166-169], OSP [134, 135], ENIG [103, 136, 147, 170-172] and EN without immersion Au [145, 173]).

The microstructure evolution and growth kinetics of Cu_6Sn_5 (η) and Cu_3Sn (ε) layers in Sn-Ag solder/Cu joints during thermal aging were studied by Deng, et al. [156]. It was found that the growth of IMCs was governed by a mixed mechanism of grain-boundary and bulk diffusion. The growth of the η phase was controlled by its initial thickness and morphology,

which had little effect on the ε-phase growth kinetics. During aging, the ε phase formed and grew at the η phase/Cu interface, primarily at the expense of the η phase due to the interfacial reaction between the Cu and the η phase. This can be expressed by the reaction [174]:

$$Cu_6Sn_5 + 9Cu \rightarrow 5Cu_3Sn \quad (2.1)$$

The dominant growth mechanism for the ε phase is grain-boundary diffusion, while for the η phase, a bulk diffusion mechanism is dominant. A micrograph of the IMCs at the interface between Cu and SAC405 is shown in Figure 2.5 [167]. A study on thermal-mechanically induced phase coarsening of Sn-Ag alloys showed that the majority of fine Ag_3Sn particles present in bulk solder after reflow are replaced by a few coarse Ag_3Sn platelets during thermal mechanical cycling (TMC) [168]. The size and spacing of Ag_3Sn platelets increased in static aging, but more significantly in TMC, which was referred to as strain-enhanced coarsening.

Aging effects on the microstructures of 63Sn-37Pb, Sn-3.5Ag and SAC405 solder balls on Cu/Ni/Au surface finish were investigated by Fan and coworkers [171]. The IMC layers were identified to be Ni_3Sn_4+(Sn-Ni-Au) for 63Sn-37Pb, Ni_3Sn_4 for Sn-3.5Ag, and (Sn-Cu-Ni-Au) for SAC405. The thicknesses of the IMC layers all increased with increasing aging time and temperature, but at different rates due to different diffusion coefficients of the moving atomic species. The 63Sn-37Pb solder had thicker IMC layer than the Sn-3.5Ag and SAC405 solders due to the high sensitivity of its diffusion coefficient to temperature and its low melting point.

A detailed study on the interfacial reactions between SAC357 and ENIG plated Cu under high temperature storage was carried out by Chun, et al. [172]. A series of reactions took place as the aging time increased, as schematically illustrated in Figure 2.6. The final interfacial structure was identified to be Cu/Cu_3Sn/Cu_6Sn_5/Ni-Sn-P layer/$(Cu,Ni)_6Sn_5$/SAC357. Chou [170] also studied 63Sn-37Pb and near eutectic SAC BGA solder joints on Cu/Ni/Au substrates after thermal

aging. He found that the SAC alloy had fast interfacial IMC growth rate during reflow, but almost no interfacial IMC growth under solid state aging. Contrastingly, the IMC layer in eutectic 63Sn-37Pb solder grew faster during aging, with significant phase coalescence in the solder joints.

Flip-chip devices with SAC387 solder joints on electroless Ni (EN) without immersion Au surface finish were aged at different temperatures to study the change in joint microstructure [145, 173]. The facet-like morphology of interfacial IMC $(Cu,Ni)_6Sn_5$ remained unchanged during aging, but its thickness increased considerably by a volume diffusion mechanism. The Ag_3Sn IMCs existed as plate-like or lamella-like phases or as small particles around the β-Sn dendrites in the bulk solder. Two different Ag_3Sn coarsening processes took place under high temperature aging: (1) small Ag_3Sn particles directly coarsened into pebble-like phases and (2) the plate and lamella Ag_3Sn phases broke up into small parts and then coarsened into pebble-like phases.

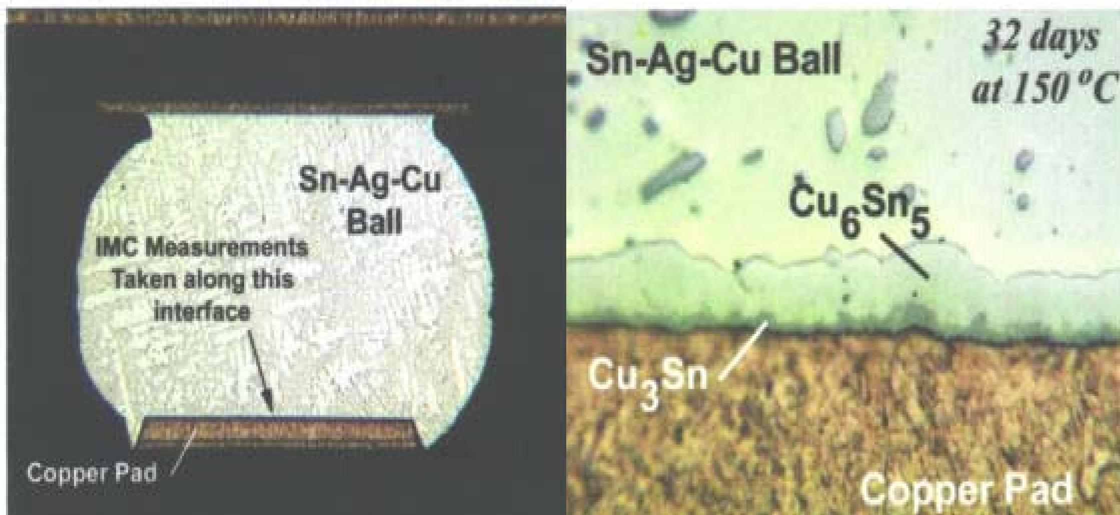

Figure 2.5 IMCs at the Interface of Cu Pad and SAC405 Solder Ball

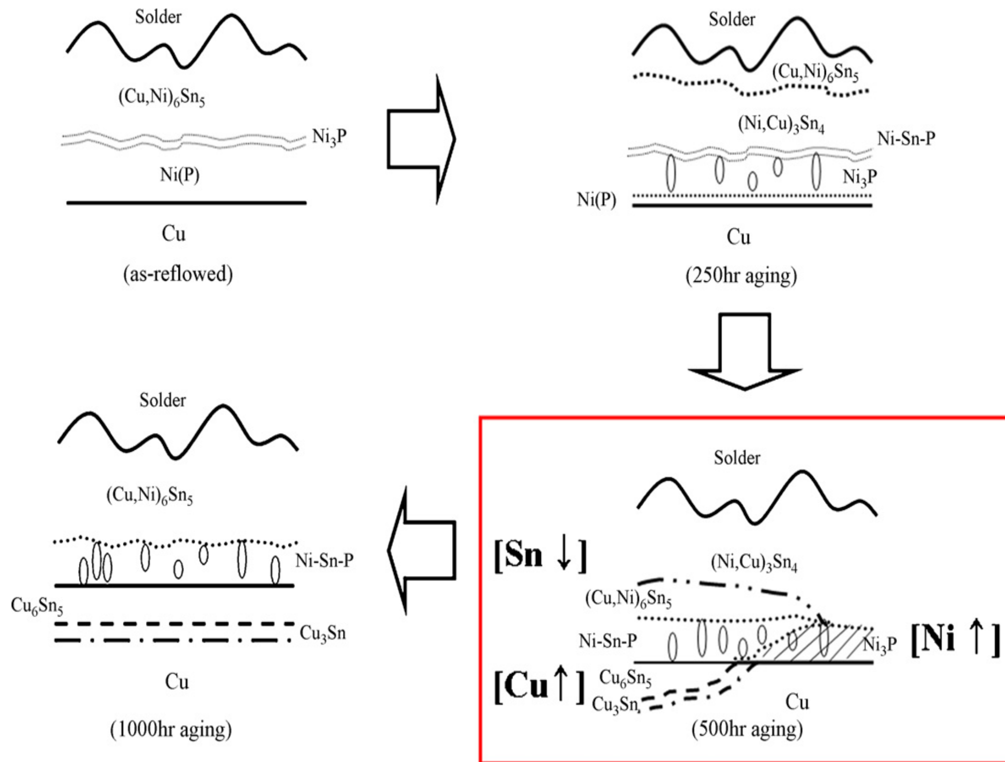

Figure 2.6 Sequential Reactions Occurred at SAC357/ENIG/Cu Interface at 200 °C

2.2.2.2.3 IMC Thickness Growth

The thicknesses of IMC layers depend on a number of factors such as temperature/time, solder volume, the nature of the solder alloy, and the morphology of the deposit. It is well documented that the growth of IMC layers can be modeled by parabolic growth kinetics (also called square root time law) regardless of the solder alloy and substrate surface finish [34, 143, 145, 153, 167, 171, 174, 175].

The mathematic expression of IMC thickness growth is:

$$d = d_0 + D\sqrt{t} \tag{2.2}$$

where d is the thickness of IMC layer at aging time t; d_0 is the initial IMC thickness after reflow;

D is the diffusion coefficient of a specific IMC atom species at a certain aging temperature; and t is the isothermal aging time. The diffusion coefficient D is given by an Arrhenius expression:

$$D = D_0 \exp(\frac{-Q}{kT}) \tag{2.3}$$

or by a linear logarithmic expression:

$$\ln(D) = \ln(D_0) - (\frac{Q}{k}).(\frac{1}{T}) \tag{2.4}$$

where D_0 is the diffusion constant of a specific IMC atom species (at infinite temperature); Q is the activation energy for the growth of a specific IMC layer; k is the Boltzman constant; and T is the absolute temperature.

The total thickness of IMC layer at solder joint is the sum of the thicknesses of the different IMC species. For example, there are usually two kinds of IMCs formed at SAC/Cu interface, namely Cu_6Sn_5 and Cu_3Sn, which grow at different rates. Therefore, the total thickness of the interfacial IMC layer will be the thickness of the Cu_6Sn_5 plus that of the Cu_3Sn.

2.2.2.2.4 Kirkendall Voiding

Formation of Kirkendall voids has been widely observed in solder joint interfaces on bare Cu pads or Cu pads with OSP under isothermal aging [131, 134, 135, 169, 174]. This phenomenon has also been found with EN (Electroless Ni without immersion Au) [145, 173].

Kirkendall voiding on Cu is unavoidable in solder joints because of the unbalanced interdiffusion of Cu and Sn. The process takes place in two steps [131, 174]. First, vacancies are generated near the Cu_3Sn layer after the Cu atoms leave the Cu pad and diffuse towards the solder. Second, the vacancies coalesce into voids. The density of Kirkendall voids is a function of aging time and temperature. The longer the time and the higher the temperature, the denser the voids (as illustrated in Figure 2.7).

Void formation in Cu_3Sn and at the Cu/Cu_3Sn interface indicates faster diffusion of Cu in Cu_3Sn than in Sn, although the diffusion flux of Sn through Cu_3Sn is still significant. Wang, et al. [169] studied Kirkendall voiding in a modified SAC alloy (SAC305 with addition of 1.0 wt% Zn) on Cu and provided a schematic illustration of the void formation process. In Figure 2.8, the vertical arrows with dashed lines indicate the diffusion of atoms, while the arrows with solid line indicate the moving directions of the boundaries during aging.

The mechanism of Kirkendall voiding on OSP is no different from that on bare Cu [134, 135], because during reflow, the OSP coating is vaporized and the Cu beneath is exposed to the solder. Therefore, bare Cu pads with OSP are basically the same as bare Cu in terms of the metallurgy of solder joints. In any case, the coalescence and growth of voids in the brittle Cu_3Sn phase will degrade the interfacial strength and negatively impact the solder joint reliability.

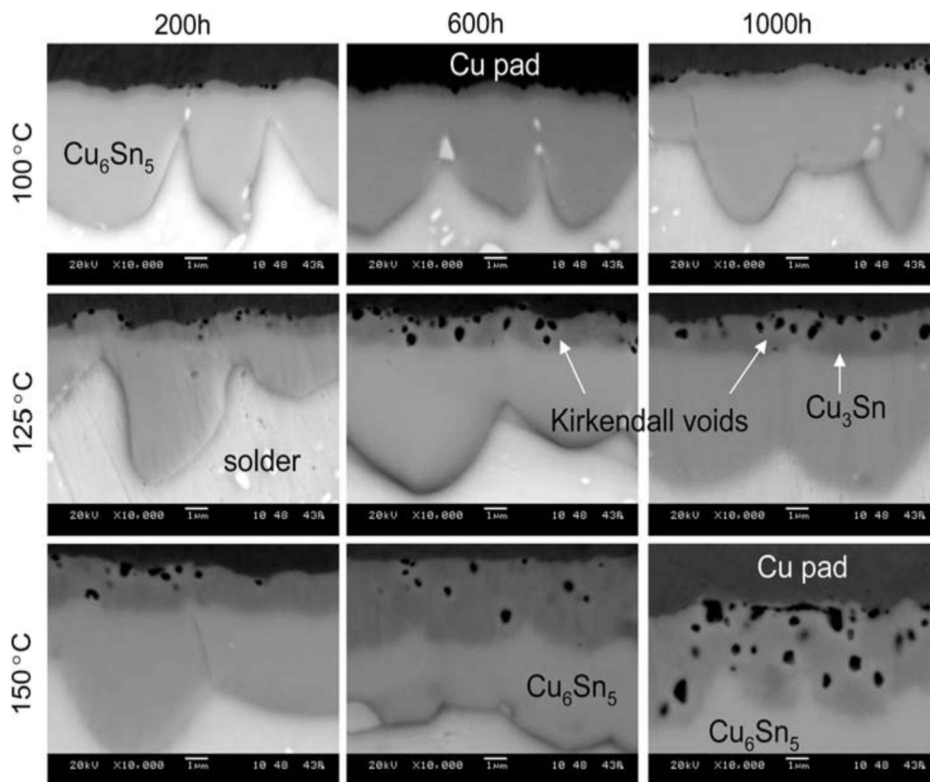

Figure 2.7 Formation of Kirkendall Voids with Aging Time and Temperature

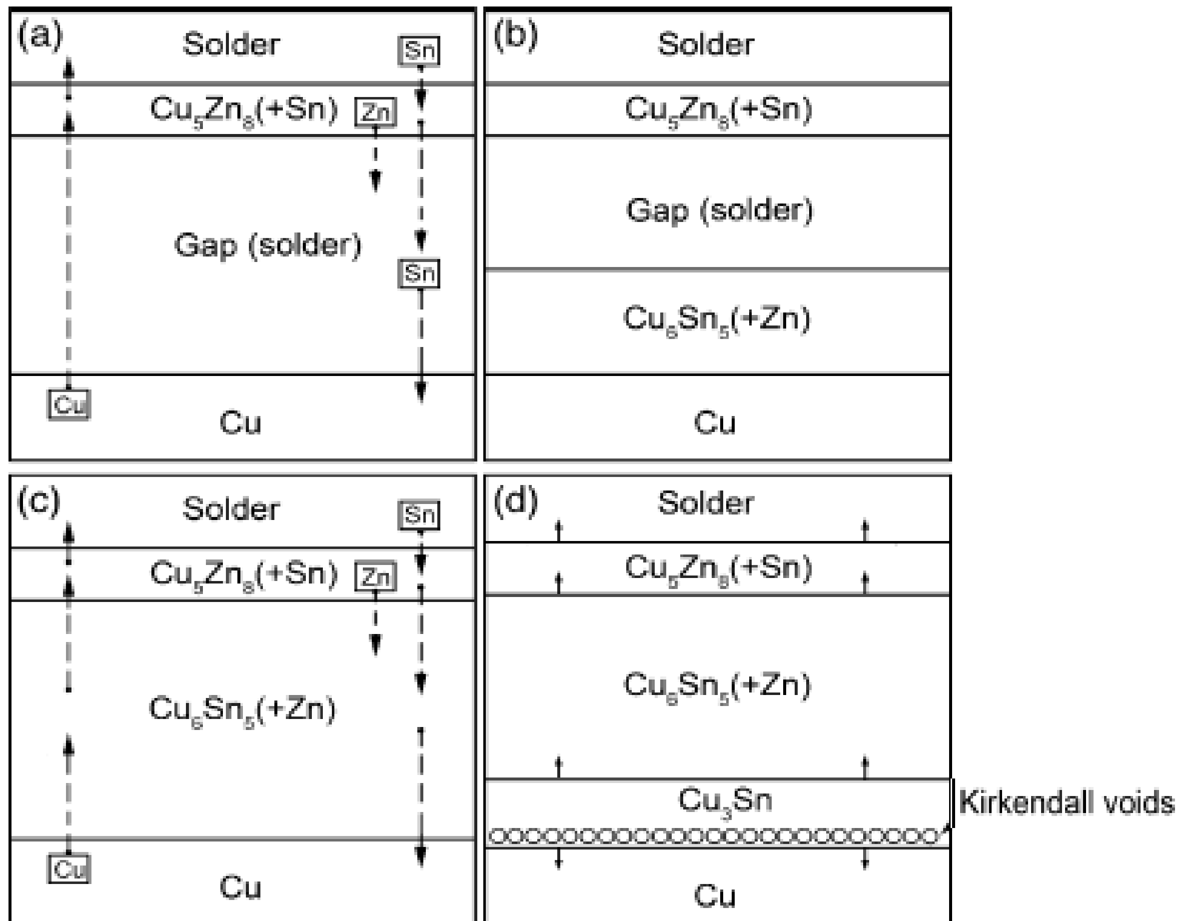

Figure 2.8 Schematic Illustration of Kirkendall Voiding (Sn-3.0Ag-0.5Cu-1.0Zn/bare Cu)
(a) after reflow (b-d) after aging

2.3 Metallurgical Approaches in Mitigating Aging Effects

Aging negatively impacts solder mechanical properties and changes solder microstructure at both the bulk solder and solder joint levels. The softening effects are unfavorable for electronics packaging and require countermeasures.

To increase the thermal aging resistance of solder joints, metallurgical strengthening approaches, which act to reinforce not only the solder matrix but also the matrix/intermetallic interface, offer an effective solution. For common solder joints (e.g. SAC), there are several aspects of the strengthening strategy [176]: (1) refine Sn dendrites and any pro-eutectic intermetallic phases; (2) increase the fraction of fine eutectic in the as-solidified joint; and (3) suppress the formation of interfacial Kirkendall voids and voids coalescence. According to the results of many recent studies, strengthening can be achieved by the addition of an alloying element, or in other words, by using a doping element in the solder alloys [33, 177-189].

A series of SAC+X alloys were investigated to determine how the addition of a fourth element X mitigates aging effects in solder joints [177]. The metallurgical modification provided microstructure and strength control of both the bulk solder and IMC layer. Further, SAC+X solders appeared effective at suppressing Kirkendall void coalescence and embrittlement after extensive aging of solder joints at high temperatures. Solder joints with X modified SAC solders on Cu substrate all retained good combination of strength and ductility for a long period of isothermal aging. The same conclusion was drawn in studying the failure mode of solder joints made from Co- and Fe-modified SAC alloys after aging at elevated temperature for 1,000 hours [33].

de Sousa, et al. [181] investigated the influence of low level doping (Co, Fe, In, Ni, Zn and Cu) on the thermal evolution of SAC305 solder joints on Cu. They found that all of the alloying elements had similar effects on the interfacial intermetallic compound formation, solidification

behavior, solder properties, and interfacial void formation. However, the use of Zn (0.64 wt.%) doping drastically reduced the rate of formation of Cu_3Sn and the rate of Cu pad consumption. Zn also dramatically lowered the Kirkendall void formation at the interface during thermal aging.

Che, et al. [182] used nickel as a doping element to modify SAC alloys. The effect of nickel (200 ppm and 500 ppm) on the mechanical properties of SAC solders was tested using tensile loading at room temperature. The results showed that higher doping concentrations had more effects on material properties. A lower modulus, yield stress and UTS, but higher elongation was found for SAC105-Ni0.05 compared to SAC105-Ni0.02. Related work by Guo, et al. [187] also reported the effects of mechanically incorporated Ni particles on the mechanical behavior and microstructure changes of Pb-free solders during aging.

The addition of boron dopant was found to alter the microstructure of SAC alloys [183]. In B modified SAC305, the Ag_3Sn phase changed from lamella-like to spherical and distributed homogeneously, but the grain size and distribution of the Cu_6Sn_5 phase remained unchanged. The introduction of B particles was believed to provide nucleation sites during solidification, and to refine the microstructure.

Rare-earth elements have been found to enhance the mechanical behavior of solder alloys. Law, et al. [185] measured the ball shear strength of Sn-3.5Ag and Sn-3.5Ag-0.5RE (RE = rare earth) solders alloys attached to Au/Ni ball grid array (BGA) pads after thermal aging at 150°C for up to 1000 hours. The RE modified solder was found to have higher shear strength with completely ductile fracture inside the bulk solder. Dudek and coworkers [186] observed more than a 150% increase in strain-to-failure compared to conventional SAC397 after the alloy was doped with relatively small amounts of lanthanum (La). The high ductility was obtained with a very small penalty in shear strength due to the ability of the $LaSn_3$ IMCs to nucleate and

grow voids in the solder interior, which redirected the fracture process and minimized crack growth along the brittle Cu_6Sn_5/solder interface.

The enhanced mechanical behavior of RE-modified solder alloys is caused by microstructure refinement. Hao, et al. [179] systematically investigated the evolution of microstructure and intermetallic compounds (IMCs) for SAC solder modified with trace amounts of the rare earth element Er (addition of 0.15 wt.% Er to SAC387) during isothermal aging. They found that $ErSn_3$ formed in the molten solder provided heterogeneous nucleation sites for the formation of other IMCs in the soldering and aging process. The increases in nucleation led to the refinement of Er-containing solder joints. As a result, the Cu-Sn IMCs and Ag-Sn IMCs were present in small uniform size, and evenly distributed throughout the solder matrix. An example of RE element refining SAC microstructure is shown in Figure 2.9 [186].

Doping effects on the drop impact reliability of SAC solder joints was studied by Liu and Lee [180]. Under impact loading, solder joints using SAC alloys in area array packages such as BGA and CSP are prone to premature interfacial failure. These authors added small amounts of doping elements (Mn, Ce, Ti, Bi, and Y) to a family of SAC alloys and measured the effects of doping on drop test performance, creep resistance, and microstructure. The solder joints with the modified alloys on electroplated Ni/Au all exhibited significantly higher impact reliability. Moreover, the doping was found to have negligible effect on the melting behavior of the original SAC solder alloys. This means that the doped SAC alloys can be used under the same processing conditions as conventional SAC alloys.

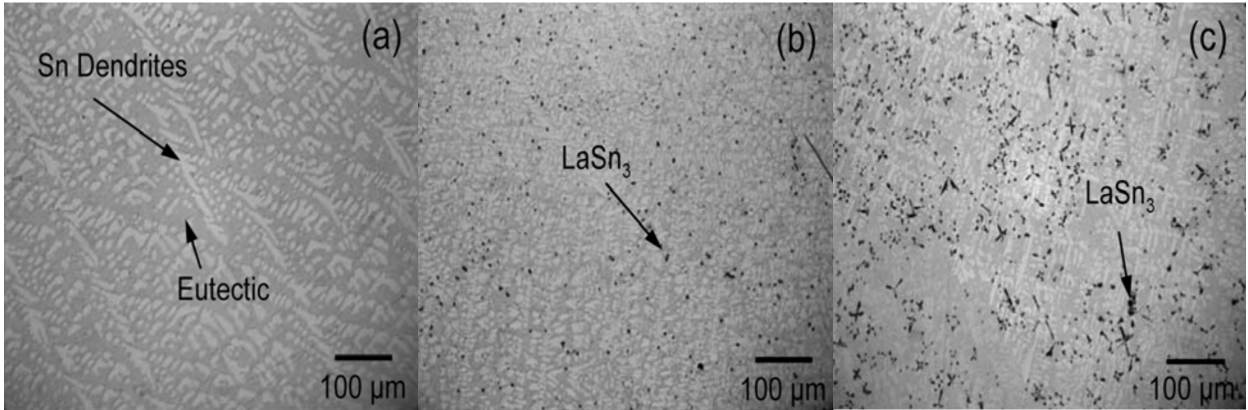

Figure 2.9 Refinement of Sn Dendrite Size and Spacing with La Addition
(a) SAC397, (b) SAC397 + 0.1 wt.% La, (c) SAC397 + 0.5wt.% La

2.4 Constitutive Modeling of Soldering Materials

In electronic packages, thermal mismatch induced stresses can result in extensive plastic deformation at solder joints, which is responsible for the low cycle thermal fatigue failure of solder materials. An expression for the strain was proposed by Yang, et al. [190]:

$$\varepsilon_t = \varepsilon_e + \varepsilon_p + \varepsilon_c \tag{2.5}$$

or more explicitly by:

$$\varepsilon_t = \frac{\sigma}{E} + C_1\sigma^m + \gamma_T(1 - e^{-B\dot{\varepsilon}_s t}) + C_2\dot{\varepsilon}_s t \tag{2.6}$$

where σ is the stress; ε is the strain; E is the modulus of elasticity; m is the reciprocal of the strain-hardening exponent; C_1 is the reciprocal of the strength coefficient; $\dot{\varepsilon}_s$ is the steady-state creep-rate which is a function of the applied stress; γ_T is the amplitude of primary creep strain; and B and C_2 are material (deformation mechanism) constants for the creep response.

The four terms on right-hand-side of equation (2.6) are the elastic, plastic, time-dependent primary creep, and steady-state creep strain components respectively. This relation is

also commonly known as the classical elastic-plastic-creep constitutive equation. It has been extensively investigated over the last two decades for electronic solders [73]. It serves as the basis for constitutive modeling of the material behavior of solder alloys, and covers both stress-strain curve modeling and constitutive modeling of creep deformation.

2.4.1 Stress-Strain Curve Modeling

Mechanical properties of solder alloys are necessary for the applications of finite element analysis to various aspects of electronics packaging. Tensile testing is usually used for this purpose, and the measured data are used to develop constitutive models to describe the stress-strain responses and the corresponding mechanical properties.

Tensile strength decreases significantly with decreasing strain rate and increasing test temperature as indicated by the two equations below [68, 113]:

$$\sigma = \mathrm{C}\dot{\varepsilon}^{m} \tag{2.7}$$

.

$$\sigma = -\alpha T + \beta \tag{2.8}$$

Grain size is the factor that has been primarily used in studying the effects of microstructure evolution on the mechanical properties of metallic materials. Its influence can be described by the well-known Hall-Petch equation, which states that the yield strength of a polycrystalline material is inversely proportional to its grain size [68]:

$$\sigma_y = \sigma_i + kd^{-0.5} \tag{2.9}$$

where σ_y is yield strength of the polycrystalline material; σ_i is a constant for the material, which represents the overall resistance of the lattice to dislocation movement; k is a constant which measures the contribution of hardening due to grain boundaries; and d is the grain size.

Nose, et al. [89] performed a parametric study of tensile strength in Sn-Pb solders as a function of chemical composition, strain rate and temperature. The tensile strength was described as:

$$\sigma = A_0 + m \log_{10} \dot{\varepsilon} + n \log_{10} T \tag{2.10}$$

where σ is the tensile strength; $\dot{\varepsilon}$ is the strain rate; T is the test temperature (°K); and A_0, m, and n are all functions of the weight percent ratio of Sn in the alloys. They found that both elastic modulus and yield strength increase with increasing Sn content.

Pang, et al. [191] developed a modified Ramberg-Osgood model to describe the temperature and strain rate dependent stress-strain curves for SAC387. The Ramberg-Osgood model for elastic-plastic behavior can be expressed as:

$$\varepsilon = \frac{\sigma}{\mathrm{E}} + \alpha \left(\frac{\sigma}{\sigma_0} \right)^n \tag{2.11}$$

The modified temperature and strain rate dependent Ramberg-Osgood Model is described as:

$$\varepsilon(\mathrm{T}, \dot{\varepsilon}) = \frac{\sigma}{\mathrm{E}} + \alpha \left(\frac{\sigma}{\sigma_0(T, \dot{\varepsilon})} \right)^{n(T, \dot{\varepsilon})} \tag{2.12}$$

The hardening exponent n and stress coefficient σ_0 are temperature and strain rate dependent:

$$\sigma(\mathrm{T}, \dot{\varepsilon}) = \sigma_0 + aT^* + b\dot{\varepsilon}^* \tag{2.13}$$

$$n(\mathrm{T}, \dot{\varepsilon}) = n_0 + cT^* + d\dot{\varepsilon}^* \tag{2.14}$$

where $T^* = \frac{T - T_r}{T_m - T_r}$ and $\dot{\varepsilon}^* = \ln(\frac{\dot{\varepsilon}}{\dot{\varepsilon}_r})$. In these relations, a and c are temperature coefficients; c and d are strain rate coefficients; T_r and $\dot{\varepsilon}_r$ are reference temperature and strain rate respectively; T_m is the melting temperature of SAC387 (217 °C); and n_0 and σ_0 are the hardening exponent and stress coefficient at the reference temperature and strain rate.

2.4.2 Constitutive Modeling of Creep Deformation

Constitutive modeling of creep deformation is needed to predict the end-of-life of electronic components by using finite element analysis. A constitutive creep model is established by conducting creep tests at different temperature and stress levels. Two constitutive creep models have received the highest acceptance, namely, the Dorn power law model [65, 70, 100, 150, 190, 192, 193] and Garofalo hyperbolic sine model [69, 126, 192, 194-198]. These relationships can be expressed as:

$$\dot{\varepsilon} = A\sigma^n \exp(-\frac{Q}{RT}) \tag{2.15}$$

$$\dot{\varepsilon} = C[\sinh(\alpha\sigma)]^n e^{(-\frac{Q}{RT})} \tag{2.16}$$

In these expressions, $\dot{\varepsilon}$ is the secondary creep strain rate; σ is the applied stress; α is a temperature independent parameter; R is the universal gas constant; T is temperature in Kelvin; A and C are material dependent constants; n is the stress exponent; and Q is the activity energy. It is important to note that these models are based solely on steady-state creep, and do not include aging effects or other phenomena. It is debatable whether the Dorn and Garofalo laws can be reasonably applied to actual solder joints.

Ma and Suhling [87] have evaluated the creep parameters in the two models for various Pb-containing and Pb-free solder alloys and found large discrepancies in the creep data for solder alloys of the same chemical composition. There are several reasons that could explain the differences, including the specimen design, variations in testing method and test conditions used by different researchers, and storage time and temperature before the creep test. Moreover, it is important to recognize that the creep behavior of bulk solder significantly differs from solder in a joint due to the effects of microstructure evolution, intermetallic compound formation, and

constraint due to different methods of assembly. Since creep modeling is supposed to be incorporated in finite element analysis to predict the end-of-life of electronic package, the discrepancies in material constants will directly affect the accuracy of prediction.

2.4.2.1 Influence of Stress Level

In logarithmic coordinates, the Dorn power law model yields a linear relationship between the creep strain rate and applied stress for a specified temperature. Nonlinear experimental curves for creep, however, have been found over the entire stress range [100, 192]. The high stress regime exhibits the largest stress exponent n, and the low stress regime exhibits the smallest n value for any given temperature. This phenomenon is referred to as "power law break down" and indicates that the Dorn model is not suitable for fitting data obtained over large stress ranges.

2.4.2.2 Influence of Temperature

The Garofalo hyperbolic sine law was established as a closed formula for matching creep behavior at both low and high stresses. At low and medium stresses, the creep strain rate depends on stress to the power n. At high stresses, the creep strain rate is an exponential function of stress [100]. The model is able to predict the creep deformation over intermediate temperature regimes for the entire stress range, but it underestimates the creep deformation at both low (-40 °C) and high (125 and 150 °C) temperatures. Also, it is unable to explain the temperature dependence of stress exponent n, which decreases as temperature increases [192].

2.4.2.3 Influence of Primary and Tertiary Creep

Total creep strain is defined as the sum of primary and secondary strains in the classical solder creep model (the last two terms in equation 2.6):

$$\varepsilon_{creep} = \varepsilon_{SAT}(1 - e^{-k\dot{\varepsilon}_{ss}t}) + \dot{\varepsilon}_{ss}t \tag{2.17}$$

where ε_{SAT} is the primary saturation strain; K is a rate constant for exponential decay of primary strains; and $\dot{\varepsilon}_{ss}$ is the steady-state strain rate for a given stress and temperature.

By differentiating equation (2.17), the instantaneous creep rate is:

$$\dot{\varepsilon}_{creep} = K\varepsilon_{SAT}\dot{\varepsilon}_{ss}e^{-K\dot{\varepsilon}_{ss}t} + \dot{\varepsilon}_{ss} \tag{2.18}$$

There are two potential issues in applying the classical creep model to constitutive modeling of Sn-based solders. First, time acts as a state variable in the instantaneous creep rate formulation. This is not recommended since the calculated rate would change under a simple translation in time. Second, the steady-state creep is assumed to last forever and the creep strain in the tertiary stage is not taken into account. In effect, even though most of Sn-based solders display a minimum creep rate, the steady-state stage is often not unambiguously evident on solder creep curves [199].

In order to address the limitations of the creep constitutive models, several modifications have been proposed by researchers. Shi, et al. [192] established a unified dislocation-controlled creep constitutive model that described the creep deformation of solder alloy over a wide temperature range (-40 to 150 °C) and explained the temperature dependencies of the stress exponent n and activation energy Q. For creep strain rates at very low stress levels, they further developed a unified diffusion-controlled creep constitutive model to describe low temperature Coble creep and high temperature Nabarro-Herring creep.

Clech [200] established obstacle-controlled creep models for both Pb-containing and Pb-free solder alloys. Creep deformation is impeded by discrete obstacles (phases, precipitates, grain boundaries, and other defects) distributed throughout the Sn-matrix in Sn-based solders. By taking these impeding elements into consideration, the rate-dependent obstacle-controlled

creep models are able to resolve the anomalies observed in the classical analysis of creep data including stress and/or temperature dependences of activation energies and stress exponents in the Power Law or Hyperbolic Sine models.

Clech also proposed an A-Ω model that includes both primary and tertiary creep deformation. It addresses the essential requirement for a constitutive model, which is that the strain rates should remain invariant under changes of time. More specifically, his model demonstrates that strain rates decay exponentially with strains in the primary creep region and increase exponentially with strains in the tertiary creep region [199].

$$\dot{\varepsilon} = ae^{-A \cdot \varepsilon} + be^{\Omega \cdot \varepsilon} \tag{2.19}$$

In this equation, there is no explicit time dependent variable. The first term on the right represents strain hardening in the primary creep region and the second term captures strain softening or creep damage accumulation in the tertiary creep region. The quantity A (alpha) is a hardening parameter for exponential decay of primary creep rates with increasing strains. The quantity Ω (omega) is a softening (or weakening) parameter for exponential growth of tertiary creep rates with increasing strains. The two coefficients "a" and "b" have units of strain rate and possess strong stress and temperature dependences. Comparatively, A and Ω represent the inverse of strains. They are dimensionless and have weak stress and temperature dependence.

2.4.3 Anand Viscoplastic Constitutive Model

Electronic solder alloys are utilized at high homologous temperatures due to their low melting points. Under such conditions, creep deformations are very significant. Classical constitutive models are largely divided into portions describing rate-independent plasticity (stress-strain response) and rate-dependent steady state creep (creep deformation developed as a function of strain rate or time). However, it is very difficult to separate the plastic strain from the

creep strain based on the mechanical tests of solder alloys. Therefore, a unified plastic/creep constitutive relation is highly desirable.

The Anand viscoplastic model, which was initially proposed by Anand [201] and subsequently developed by Brown, et al. [202] for the rate-dependent deformation of metals at high temperatures, has been applied often to describe the viscoplastic behavior of solder alloy. This constitutive model unifies both rate-dependent creep behavior and rate-independent plastic behavior occurring concurrently in solder alloys. The parameters in the unified constitutive model can be determined in a direct method by combining both rate-dependent and rate-independent plastic strains into viscoplastic strain and plastic flow terms. The Anand viscoplastic constitutive model embedded within the ANSYS finite element software has become a common tool for engineers performing electronic packaging reliability studies.

Several equations are used in the model for the purpose of unifying the rate-dependent creep and the rate-independent plastic behavior of solder alloys [203]. These include flow equation and evolution equations given by:

$$\dot{\varepsilon}_p = A\exp\left(-\frac{Q}{R\theta}\right)\left[\sinh\left(\xi\frac{\sigma}{s}\right)\right]^{1/m} \tag{2.20}$$

$$\dot{s} = \{h_0(|B|)^a \frac{B}{|B|}\}\dot{\varepsilon}_p \text{ and } B = 1-\frac{s}{s^*} \text{ and } s^* = \hat{s}[\frac{\dot{\varepsilon}_p}{A}\exp(\frac{Q}{R\theta})]^n . \tag{2.21}$$

The parameters in these equations, along with their definitions are listed in Table 2.1 [204].

The flow equation is similar to the Garofalo hyperbolic sine model used to describe steady-state creep but with the addition of an internal state variable defined as the deformation resistance s, which depends on the temperature- and rate-dependent strain history of the material. The evolution equation, in the context of solder behavior, mainly captures strain hardening effects through the hardening coefficient h_0. In the flow equation, the inelastic strain rate $\dot{\varepsilon}_p$ is the sum of time-dependent creep and time-independent plastic strain rates. The Arrhenius term captures the temperature dependence of the creep process. The hyperbolic sine term describes the stress dependence of the inelastic strain rate and includes state variable s. In general, the Anand constitutive model possesses two distinctive features [205]: (1) It needs no explicit yield condition and therefore no loading and unloading criterion; (2) It employs a single scalar as an internal variable, s, which expresses the average isotropic deformation resistance to macroscopic plastic flow.

As mentioned earlier, ANSYS finite element software offers the Anand model as a standard option. The application requires the input of nine material constants (summarized in Table 2.2), which have to be determined experimentally. In order to obtain the acquired data for the curve-fitting of the material parameters, a series of constant strain rate tensile tests and constant load creep tests must be conducted under isothermal conditions at different temperatures. Over the years, several efforts have been taken to determine the Anand model constants for various solder alloys by using different approaches [204-210]. The effect of aging can create large variations in the published constants, even for identical alloys.

Table 2.1 Nomenclature Used for the Anand Constitutive Model

Symbol	Description	Unit
α	Strain rate sensitivity of hardening coefficient	mm
A	Pre-exponential factor	1/s
h_0	Hardening Coefficient	MPa
k	Boltzman's constant	J/K
m	Strain rate sensitivity of stress	
n	Strain rate sensitivity of saturation value	
Q	Activation energy	J/mol
R	Universal gas constant	J/kgK
s	Deformation resistance	MPa
s_0	Initial value of deformation resistance	MPa
$\hat{s}$	Coefficient of deformation resistance	MPa
Greek Symbols		
ε	Strain	
σ	Stress	MPa
θ	Temperature	K
ξ	Stress multiplier	
Subscripts		
m	Melting point	K
p	Plasticity	

Table 2.2 Anand Model Constants Defined in ANSYS

Constant	Meaning	Material property	Units
C_1	s_0	Initial value of deformation resistance	MPa
C_2	Q/R	Q - activation energy	J/mol
		R - universal gas constant	J/kgK
C_3	A	Pre-exponential factor	1/s
C_4	ξ	Stress multiplier	---
C_5	m	Strain rate sensitivity of stress	---
C_6	h_0	Hardening coefficient	MPa
C_7	$\hat{s}$	Coefficient of deformation resistance	MPa
C_8	n	Strain rate sensitivity of saturation (deformation resistance) value	---
C_9	α	Strain rate sensitivity of hardening coefficient	---

Nie, et al. [211] have investigated the limitations of the Anand model. They pointed out that since the Anand model does not account for both primary and tertiary creep, it can only be expected to perform well under the conditions of high strain rate loading such as shock and drop testing, in which creep is not able to play a significant role. Also, the Anand model may not be effective in predicting the noticeable strain hardening observed in compression tests.

Modifications of Anand model have been proposed recently [205]][212]. The model parameter h_0 is supposed to have a close relationship with work hardening, but it is assumed to be constant in the original form of Anand constitutive model. Chen, et al. [205] have modified the Anand model by correlating the hardening coefficient h_0 with temperature and strain rate through the following equation:

$$h_0 = a_0 + a_1 T + a_2 T^2 + a_3 \dot{\varepsilon}_p + a_4 (\dot{\varepsilon}_p)^2 \tag{2.22}$$

The coefficients in this expression can be determined by nonlinear least square fitting of data obtained through experimental tests conducted at different temperatures and strain rates.

Pei and Qu [212] used the Anand model to study the deformation behavior of Pb-free solders and found that the formulation must be modified to be more temperature sensitive to better fit data for Pb-free solder alloys. They proposed a change where all of the nine Anand model constants are taken to be linearly dependent on temperature:

$$C_i = C_i^0 + C_i^{(1)} T \qquad i = 1 \text{ to } 9 \tag{2.23}$$

Together with two elastic constants (E_0 and E_1), there are a total of 20 constants in the revised model. Their results show that the modified temperature dependent Anand model fits the data for Pb-free solders much better than original version, at a price of adding 9 more constants.

2.5 Life Prediction of Solder Joints

The prevailing trend today in electronic packaging is for faster, cheaper and more robust electronic products. This makes it increasingly important for the packages to be evaluated at early design stages by simulation tools. Solder joint reliability models based on actual test data, accurate constitutive modeling, dominant damage mechanisms and appropriate simulation, are needed to perform this task [213].

Electronic packages often undergo thermal power cycling conditions throughout their service life. The CTE mismatch induced stresses/strains are the root cause of most solder joint failures. Accurate constitutive deformation models are necessary to understand the deformation behavior of solder joints in accelerated tests. The common failure mechanism for solder joints is joint fatigue, and two major steps are involved in solder joint reliability modeling [214]:

(1) Deploy a suitable solder constitutive equation into the finite element (FE) model. The stress–strain results from the FE model are then extracted by averaging the inelastic strain energy density as a failure parameter.

(2) Apply a solder fatigue model to calculate the number of cycles to fatigue failure using the failure parameter extracted from the FE model results.

Lee, et al. [215] have conducted a thorough review of solder fatigue models. They identified 14 models in the literature, which were developed based upon various assumptions, including the manner in which the physical and metallurgical aspects of fatigue are taken into account. According to the fundamental damage mechanisms, these models can be classified into such categories as stress-based, plastic strain-based, creep strain-based, energy-based, and damage-based. The characteristics of the 14 identified fatigue models are presented in Table 2.3.

Table 2.3 Summary of Solder Joint Fatigue Models [215]

Fatigue Model	**Model Class**	**Parameters**	**Coverage**	**Applicability**
Coffin-Manson	Plastic strain	Plastic strain	Low cycle fatigue	All
Total Strain	Plastic + elastic strain	Strain range	High and low cycle fatigue	All
Solomon	Plastic shear strain	Plastic shear strain	Low cycle fatigue	All
Engelmaier	Total shear strain	Total shear strain	Low cycle fatigue	Leaded & leadless, TSOP
Miner	Superposition (plastic and creep)	Plastic failure & creep failure	Plastic shear and matrix creep	PQFP, FCOB
Knecht & Fox	Matrix creep	Matrix creep shear strain	Matrix creep only	All
Syed	Accumulation of creep strain energy	gbs energy and mc energy	Implies all coverage	PBGA, SMD, NSMD
Dasgupta	Total strain energy	Energy	Joint geometry accounted for	LLCC, TSOP
Liang	Stress/strain energy density based	Energy	Constants from isothermal low cycle fatigue tests	BGA and leadless joints
Heinrich	Energy density based	Energy	Hysteresis curve	BGA
Darveaux	Energy density based	Damage + energy	Hysteresis curve	PBGA, leadless
Pan	Strain energy density	Strain energy density and plastic energy density	Hysteresis curve	LCCC
Stolkarts	Damage accumulation	Damage	Hysteresis curve & damage evolution	All
Norris & Landzberg	Temperature and frequency	Temperature frequency	Test condition vs. use conditions	All

Low cycle fatigue models are frequently used to predict fatigue life of solder joints. The most commonly used low cycle model is the Coffin-Manson strain-based model [197]:

$$N_f^m \Delta\varepsilon_{in} = C \tag{2.24}$$

where N_f is the total number of cycles to failure, $\Delta\varepsilon_{in}$ is the inelastic strain amplitude, C is the fatigue ductility coefficient, and n is the fatigue ductility exponent.

The modeling methodology shown in Figure 2.10 was proposed by Ng, et al. [216]. They refer to this approach as absolute fatigue life prediction, and have applied it to estimate the thermal cycling life of electronic packages with eutectic Sn-Pb solder. This methodology has also shown potential for making life predictions for Pb-free BGA packages and modules.

Numerous other studies have been performed on methods for predicting the creep-fatigue life of solder joints under complex thermal cycling conditions [112, 124, 213, 214, 216-225]. Che and Pang [217] conducted thermal fatigue reliability analyses for PBGA components with SAC387 solder joints. The viscoplastic Anand model and elastic-plastic-creep model, as well as energy based and strain based fatigue life models were employed in the FE simulations. The failure mode was found to be bulk solder fatigue failure with failure sites close to the solder/IMC interface. Yeo, et al. [214] studied flip chip solder joint reliability by using the viscoplastic Anand and elastic-plastic-creep constitutive models. They found that the calculated viscoplastic work was up to 25% higher than the total inelastic strain energy densities calculated from the corresponding elastic-plastic-creep analysis.

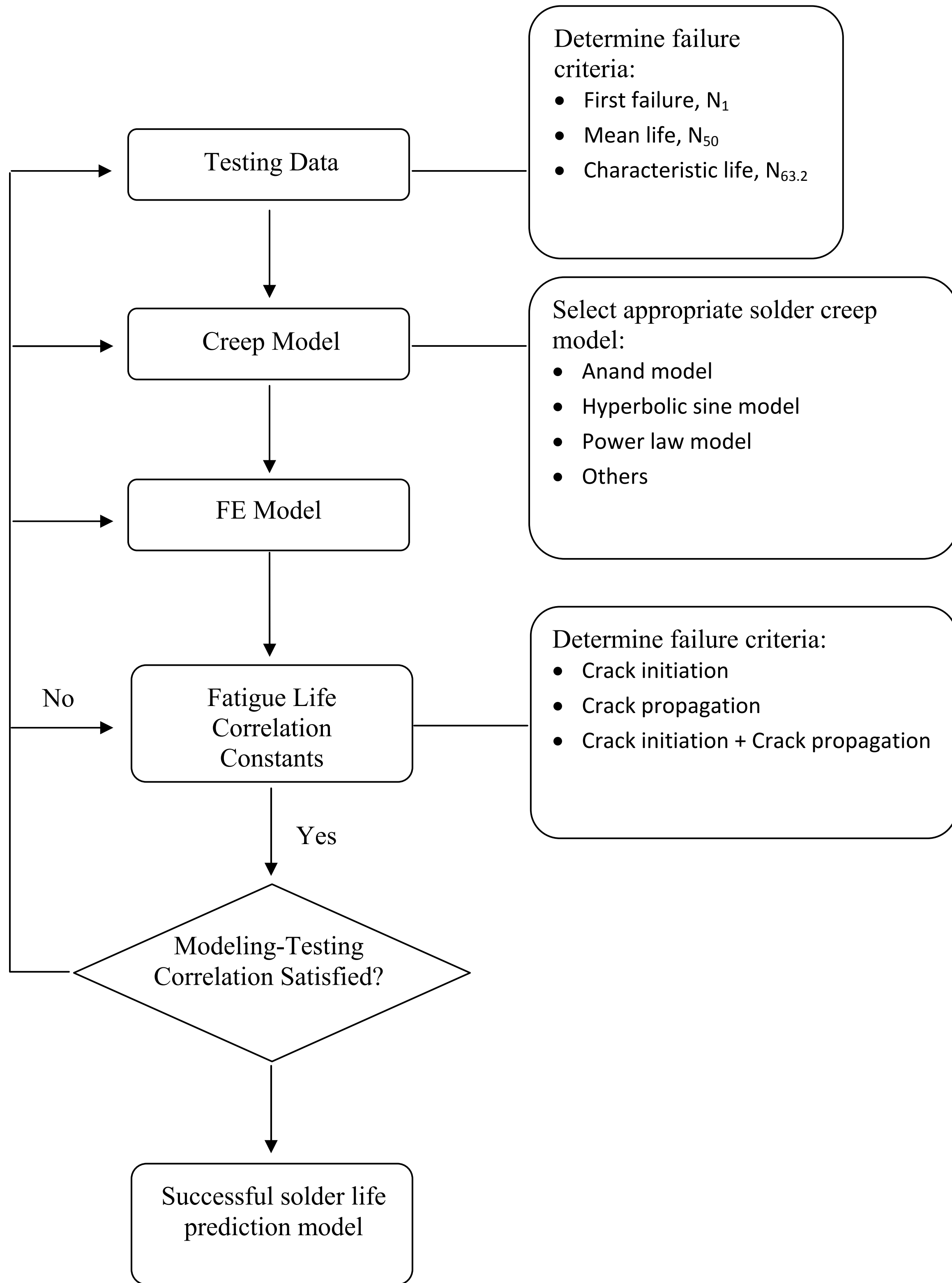

Figure 2.10 Flowchart for Absolute Fatigue Life Prediction Methodology

Pitarresi, et al. [223] estimated the thermal cycling reliability of chip scale packages by using a finite element based approach. The viscoplastic Anand constitutive creep model was used for the solder response, and the Darveaux crack growth rate model was used to predict the characteristic fatigue life of the solder joints. In a study of board level thermal cycling solder joint reliability on BGAs, Ng, et al. [216] employed the Anand constitutive model for different SAC solders and introduced a fatigue corrective factor (f_c) to integrate the different solder creep models and different modeling assumptions. Chen, et al. [218] investigated the reliability of solder joints in flip chip assemblies with both rigid and compliant substrates under accelerated temperature cycling conditions by using FE simulations. The Anand model was applied to describe the viscoplastic behavior of solder joints, and the results showed that the reliability was higher using the flexible substrates. This improvement might be ascribed to the higher energy dissipated by the flex substrates, which would otherwise be absorbed by the solder joints.

Pang and Low [222] compared the failure life of FCOB solder joints undergoing thermal cycling (TC) and thermal shock (TS) by using finite element modeling. Both the elastic-plastic-creep model and the viscoplastic Anand model, as well as solder joint fatigue models based on inelastic strain range and inelastic energy density were employed. It was found that solder joints under TC had shorter failure life cycles than in TS testing due to the lower ramp rate. Moreover, compared with the elastic-plastic-creep analysis method, the Anand viscoplastic method was more effective in modeling the ramp rate effects for both TS and TC conditions. Classe and Sitaraman [221] worked with microBGA assemblies on organic substrates to compare the differences between symmetric and asymmetric accelerated thermal cycles (ATCs) using numerical simulations. The asymmetric ATCs were found to emulate field-use conditions and have the potential to reduce the time for qualification testing. Several finite element models with different solder constitutive models including the

viscoplastic Anand model were applied. The numerical simulations showed little difference between symmetric and asymmetric cycles in predicting solder joint failures.

In closing, there are a number of factors that affect solder joint fatigue performance, including joint geometry, chip size, interface metallurgy, underfill and substrate materials. The microstructure of solder joints [124] and phase coarsening during thermal-mechanical deformation [225] not only affect the creep and fatigue failure of solder joints but also determine the stress levels at the joint interface. In an investigation on the design analysis of BGA packages conducted by Ng, et al. [216], there were eleven key parameters found to affect the life of BGA joints. Table 2.4 gives a list of these parameters.

Table 2.4 Effects of Design Parameters on the Fatigue Life of BGA Solder Joints

No.	Design Parameters	Effects (Life Improvement)
1	Die size	Smaller (significant)
2	Die thickness	Thinner (little)
3	Ball standoff	Higher (significant)
4	Max. ball diameter	Smaller (significant)
5	Solder mask opening	Bigger (significant)
6	Board size	Smaller (little)
7	Board thickness	Thinner (significant)
8	Substrate thickness	Thicker (little)
9	MC (Mold Compound) thickness	Thinner (little)
10	MC modules	Lower (little)
11	MC CTE	Higher (significant)

2.6 Summary

In this chapter, an extensive discussion has been presented on two major issues in the development and application of Pb-free solders, i.e. aging effects and constitutive modeling. Aging is perhaps the main cause of the discrepancies in the mechanical property databases for soldering materials. Due to the high homologous temperatures at which solder alloys operate, aging affects not only their mechanical properties but also their microstructure. The mechanical response of solder joints to external loading can be dramatically different from bulk solders under the same aging conditions. This is due to the distinctive feature that solder joints have interfacial intermetallic compounds (interfacial IMCs), fine microstructure and mechanical constraints jointly imposed upon substrate and solder. Usually, solder joints also have higher strength than bulk solder.

In contrast to the IMC coarsening, coalescing, and dispersing observed in bulk solder, the microstructure evolution of solder joints under aging can be much more complicated and requires consideration of solder bump/solder compositions, the passivation technology or bond-pad metallization in use and the thermal profile of reflow soldering process. The thickness of the interfacial IMC layer at solder joints is found to increase according to a square root time law regardless of the solder type and substrate surface finish. Formation of Kirkendall voids is widely observed in solder joint interfaces on Cu pads with various surface finishes under solid state thermal aging conditions. Additionally, the thermal mismatch between the various materials that constitute a package may result in substantial mechanical stresses/strains and thereby, continuous changes in solder joint microstructure.

Generally speaking, aging causes a reduction in mechanical properties and change of microstructure on both the bulk solder and the solder joint level. The softening effects are

unfavorable for electronics packaging and require effective countermeasures. To increase the thermal aging resistance of bulk solder and solder joints, metallurgical strengthening approaches, which aim to reinforce not only the solder matrix but also the matrix/intermetallic interface, are able to offer a solution and can be achieved by adding an alloying element such as Bi, Ti, Cr, Mn, Ni, B, or rare earth elements.

The CTE mismatches between the PCB and IC components can generate complex stress/strain conditions and eventually lead to the cyclic fatigue failure of the solder joints. Therefore, it is necessary to establish reliable constitutive models to describe solder mechanical behavior, in order to accurately analyze solder joint stress/strain states and predict solder joint life.

The classical elastic-plastic-creep constitutive model consists of four components, namely, elastic, plastic, time-dependent primary (transient) creep, and steady-state creep strain components. Starting from this approach, studies of constitutive modeling of solder alloys has been pursued and various stress-strain and creep curve models have been proposed.

The Anand viscoplastic model, which was developed for the rate-dependent deformation of metals at high temperatures, has been often adopted to model the viscoplastic behavior of solders alloys. This constitutive model unifies both rate-dependent creep behavior and rate-independent plastic behavior occurring concurrently. Moreover, the Anand model possesses two distinctive features: it needs no explicit yield or loading/unloading criteria and it employs a single scalar as an internal variable, s, which expresses the averaged isotropic deformation resistance to macroscopic plastic flow. The parameters in the unified model can be determined in a direct method by combining both rate-dependent and rate-independent plastic strains into viscoplastic strain and plastic flow terms. The Anand viscoplastic

constitutive model is embedded in the ANSYS finite element software, and is the frequent choice for electronic packaging reliability studies.

Solder joint reliability modeling and life prediction are very important in evaluating electronic packages at an early stage of product design. Two major steps are involved in solder joint reliability modeling: (1) Deploy a suitable solder constitutive equation into the finite element (FE) model; (2) Apply a solder fatigue model to calculate the number of cycles to fatigue failure. Over the past two decades, efforts have been undertaken to predict solder joints lifetimes with different solder alloys and various packaging techniques. A number of modeling methods have resulted, which are able to estimate the creep-fatigue life of solder joints under complex thermal cycling conditions.

Chapter 3
Specimen Preparation and Uniaxial Tensile Testing

3.1 Introduction

In this chapter, the specimen preparation method used in this work is presented. It has the advantages of eliminating specimen variation and ensuring microstructure uniformity. Compared with other specimen making approaches, this method has two unique features: (1) Small specimen dimensions that minimize the waste of solder alloys; (2) Net shape technique that requires no further machining operations on specimen.

All solder test specimens were formed in Pyrex glass tubes with high precision rectangular cross-section using an induction melting + vacuum suction specimen preparation system. The typical specimen dimensions were length (80) x width (3) x thickness (0.5) mm. Water quenching and controlled reflow oven cooling were used before aging treatment and test.

Uniaxial tension and creep tests were carried out on a multifunctional tension/torsion thermo-mechanical test system to determine the material properties of solder alloys of interest. Moreover, a two-function empirical mathematical model based on truncated stress-strain curves was developed to characterize the stress-strain response of solder alloys.

Microstructure analysis was conducted on Epoxy potted specimens. Various techniques such as OM, SEM, EPMA, were employed in order to obtain high quality micro-images of solder alloys. Other analytical methods used were DSC, EDX, etc.

3.2 Uniaxial Test Specimen Preparation Procedure

In the current study, a novel specimen preparation procedure was developed where solder uniaxial test specimens were formed in high precision rectangular cross-section glass tubes using a vacuum suction process. These tubes were made of Pyrex glass that has high thermal shock resistance due to its very low CTE (about $5x10^{-6}$ at 20 °C).

The raw solder material was first melted in a quartz crucible using a pair of heating coils. This approach was an induction melting process in nature and a thermocouple was attached to the crucible to monitor the temperature of molten alloy. A temperature control module that modulated the power input was used to direct the melting process. After the solder reached its designated temperature (melting point + superheating for later solidification process), one end of the glass tube was inserted into the molten solder and a suction force was applied to the other end via a rubber tube connected to a mechanical vacuum pump. A regulator was installed on the vacuum system in order to generate an adequate vacuum force so that a desired amount of molten solder was drawn into the tubes. The specimen making system and animated procedure are shown in Figures 3.1 and 3.2 [227].

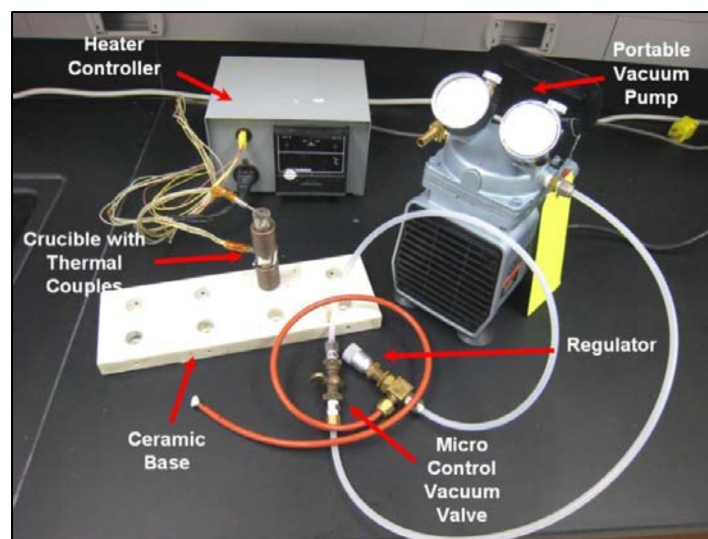

Figure 3.1 Setup for Uniaxial Test Specimen Preparation

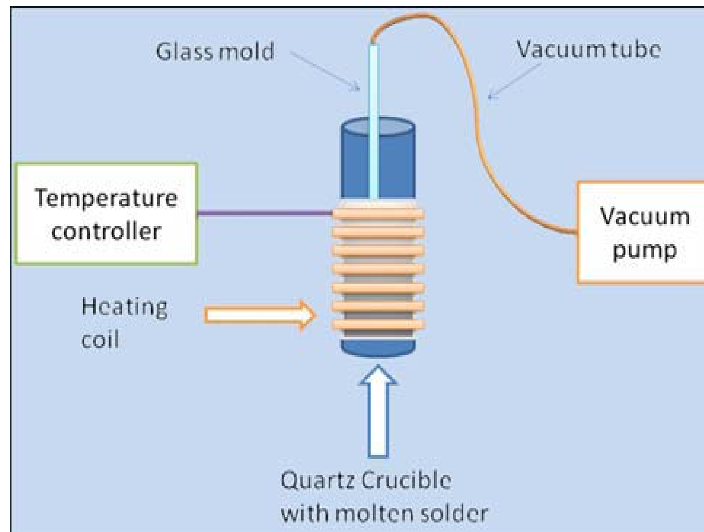

Figure 3.2 Illustration of Specimen Making Procedure

Two different cooling processes, water quenching (fast cooling rate) and reflow oven cooling (controlled cooling rate), were employed to cool the specimens to room temperature for the purpose of observing significant variations in the mechanical behavior and microstructure of the solder alloys. Figure 3.3 shows a typical temperature versus time plot for water quenching of the test specimens. For more controlled cooling, the solder specimens were first cooled by water quenching, and they were sent through a reflow oven (9 zone Heller 1800EXL as shown in Figure 3.4) to remelt the solder and subject them to a prescribed temperature profile. Thermocouples were attached to the glass tubes and the temperature was continuously monitored by a radio-frequency KIC temperature profiling device to ensure that the specimens were formed under the desired temperature profile. Figure 3.5 illustrates the reflow temperature profiles used for the SAC and 63Sn-37Pb solder specimens in this study. These match the profiles used for typical BGA solder joints in SMT assembly.

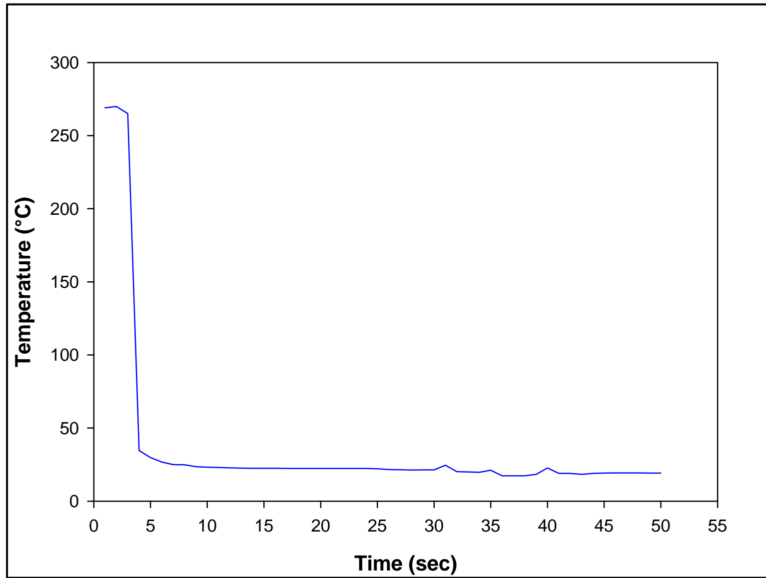

Figure 3.3 Water Quenching Profile

Figure 3.4 Heller 1800EXL Reflow Oven

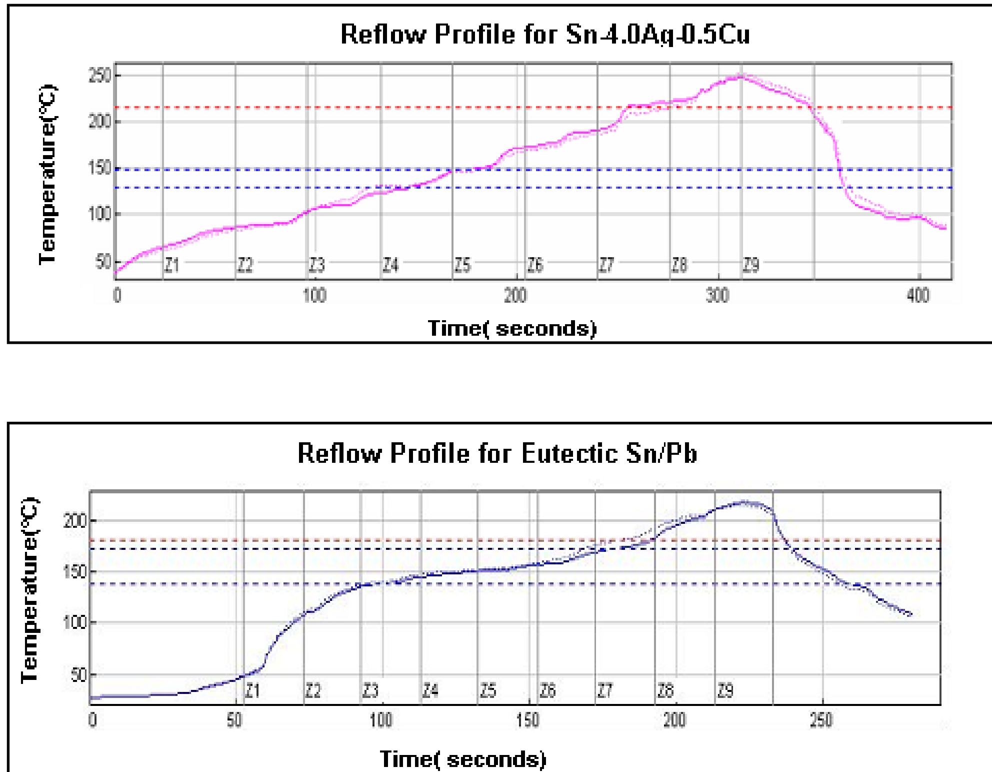

Figure 3.5 Solder Reflow Temperature Profiles

The uniaxial test specimens took their shape within the glass tubes during the solidification process. Specimens were then subjected to various aging conditions. This was accomplished by placing them in ovens set at different temperatures for various durations of time. Before being removed from the glass tubes and mechanically tested, the specimens were inspected by optical microscopy and a micro-focus X-ray system to ensure good quality. Typical test specimens are shown in Figure 3.6.

In this study, the designated dimensions of the test specimens were 80 x 3 x 0.5 mm. The thickness of 0.5 mm was specially chosen to match the height of typical BGA solder balls. Most importantly, the test specimen preparation procedure described above has been proved to be able to repetitively produce high quality specimens with oxidation free surfaces, notch free edges, and uniform dimensions through both water quenching and controlled cooling. Figure 3.7 illustrates the comparison between good (top) and bad specimens (middle and bottom). With carefully designed experimental techniques, flaws and voids in specimen can be effectively eliminated.

(a) Specimens within Glass Tubes

(b) Specimen Removed from the Glass Tube

Figure 3.6 Uniaxial Test Specimens

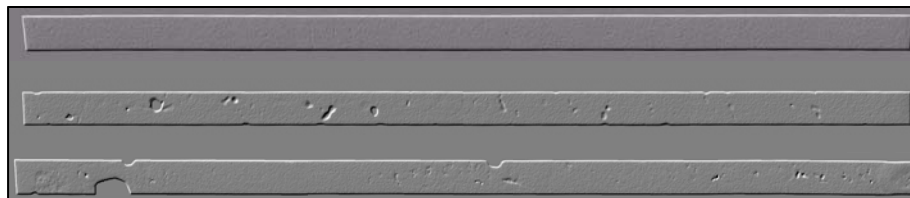

Figure 3.7 X-Ray Inspection of the Test Specimens

3.3 Mechanical Testing and Testing system

All tests in this study were carried out on a multifunctional MT-200 tension/torsion thermo-mechanical test system from Wisdom Technology, Inc. as shown in Figure 3.8. The system is capable of providing an axial displacement resolution of 0.1 microns and a rotation resolution of 0.001°. Testing that can be performed includes tension, shear, creep torsion, bending as well as combinations of these loadings. Cyclic (fatigue) testing can also be conducted at frequencies of up to 5 Hz. A universal 6-axis load cell is employed to simultaneously monitor three axial forces and three moments/torques during tests. Various types of specimens such as solder bars, thin films, solder joints, gold wire, fibers, etc. can be tested on this system. In addition, an attached environmental chamber enables the system to work within a temperature range of approximately -175 °C to 300 °C.

Two major testing modes, uniaxial tension and creep were used to characterize the material properties of solder alloys of interest. In the uniaxial tension tests, forces and displacements were measured and corresponding axial stress and axial strain were calculated from the applied force and measured cross-head displacement using

$$\sigma = \frac{F}{A} \qquad \varepsilon = \frac{\Delta L}{L} = \frac{\delta}{L} \tag{3.1}$$

where σ is the uniaxial stress, ε is the uniaxial strain, F is the measured uniaxial force, A is the original cross-sectional area, δ is the measured crosshead displacement, and L is the specimen gage length that was chosen to be 60 mm in this study. All uniaxial tension tests were conducted at room temperature (T = 25 °C) with a strain rate of $\dot{\varepsilon}$ = 0.001 sec^{-1}.

A typical recorded tensile stress-strain curve for solder with labeled standard material properties is shown in Figure 3.9. This response is nearly perfect elastic-plastic behavior with the exception of a small transition region connecting the elastic and plastic regions.

Figure 3.8 MT-200 Testing System with Environmental Chamber

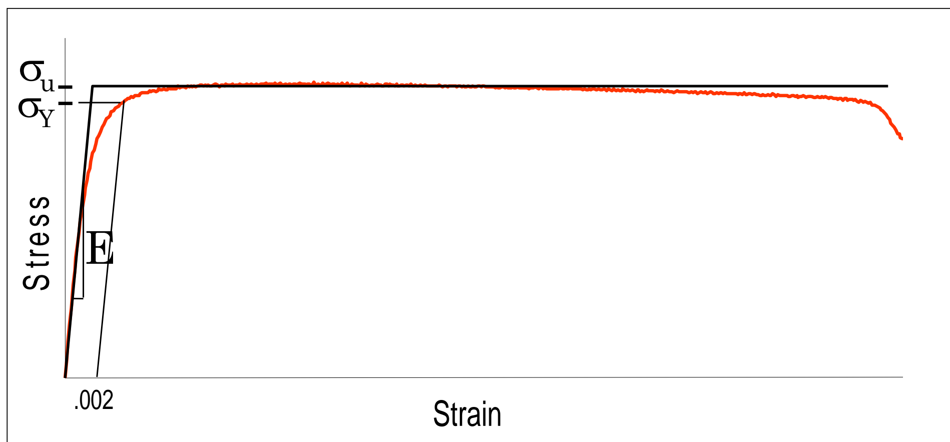

Figure 3.9 Typical Solder Stress-Strain Curve and Labeled Mechanical Properties

The notation "E" is taken to be the effective elastic modulus, which is the initial slope of the stress-strain curve. Due to the viscoplastic nature of solder alloys, this effective modulus will be rate dependent and will approach the true elastic modulus as the testing strain rate approaches infinity. The yield stress (YS) is taken to be the standard 0.2% yield stress (upon unloading, the permanent strain is equal to $\varepsilon = 0.002$) and the ultimate tensile stress σ_u is taken to be the maximum stress recorded in the stress-strain data. As the test progresses after yielding, the accumulated strain increases dramatically and extensive localized necking takes place. Accordingly, the stress level starts to drop and failure becomes imminent at the end of the stress-strain curve.

Creep tests were also carried out on the micro tester system at room temperature (T = 25 °C). The solder specimens were all tested under constant stress level, which was chosen to be 25-50% of the observed UTS of the specific solder alloy. The corresponding load input was calculated using

$$F = \left(\sigma \times W \times T \times 10^3\right) / g \tag{3.2}$$

where F is the input holding force in gram, σ is the chosen stress level for the creep test in MPa, W is the specimen width in mm, T is the specimen thickness in mm, and g is the acceleration of gravity (9.8 N/kg).

All specimens were preconditioned at various aging temperatures (including room temperature and elevated temperatures) for different aging times prior to testing. The specific combination of aging temperature and aging time defined the aging conditions. For the uniaxial tension tests, a total of 10 specimens were tested for each set of aging conditions. A set of averaged temperature dependent mechanical properties (elastic modulus, yield stress, ultimate tensile stress etc.) were then extracted from the results. The 10 individual stress-strain curves for a certain set of aging conditions were fitted by using an empirical model to generate an average stress-strain curve representation to the set of data.

In the creep testing, 4 to 6 specimens were tested for each set of aging conditions, and the creep strain versus time curves were recorded. These curves can be fitted with an empirical creep strain vs. time model to generate an "average" representation of the creep response under the specific aging conditions. For the range of aging conditions considered in this work, the raw creep strain vs. time data in the primary and secondary creep region were found to be well fitted by the four parameter Burger's (spring-dashpot) model:

$$\varepsilon = \varepsilon(t) = k_0 + k_1 t + k_2\left(1 - e^{-k_3 t}\right) \tag{3.3}$$

Based on the results, the "steady state" creep strain rate (k_1 in the model) can be extracted from the secondary region on the creep curves. In practice, this was accomplished by finding the minimum slope value for the observed $\dot{\varepsilon}$ versus t response as shown in Figure 3.10.

3.4 Empirical Modeling of Tensile Stress-Strain Test Results

A set of typical stress-strain curves (10 in the aggregate) for water quenched SAC405 solder alloy tested at T = 25 °C after certain duration of room temperature aging (63 days in this case) is shown in Figure 3.11. Small variations were observed between the various curves due to normal experimental scatter and variability. The obtained tensile curves all exhibit typical elastic-plastic deformation patterns including a linear elastic deformation portion at low strain levels that is characterized by Hooke's law $\sigma = E\varepsilon$ (E: Young's Modulus) plus a nonlinear plastic deformation portion at high stain levels that contains such mechanical properties as yield stress, ultimate tensile strength, and ductility. For this set of data, the curves were very consistent until $\varepsilon \approx 0.02$. After that, necking took place and failure occurs in an unpredictable manner for each specimen.

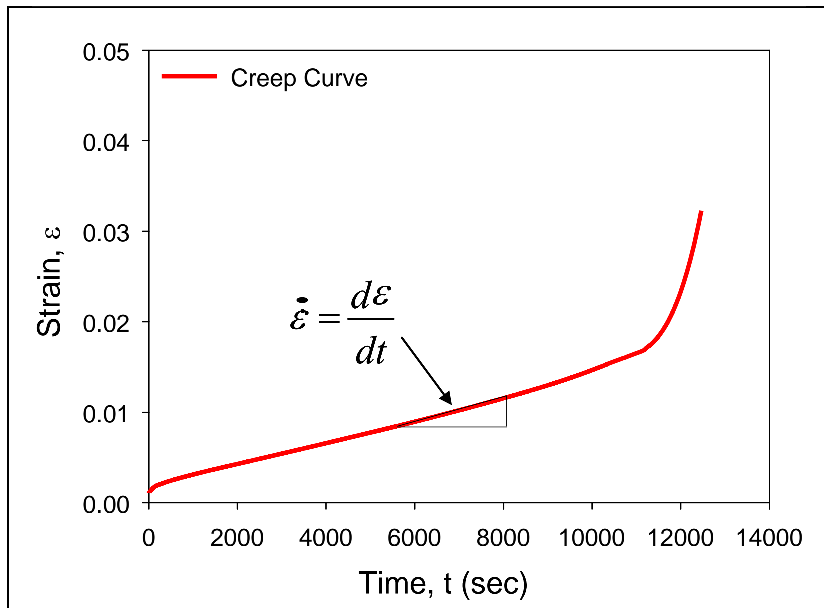

(a) Creep Strain vs. Time Curve

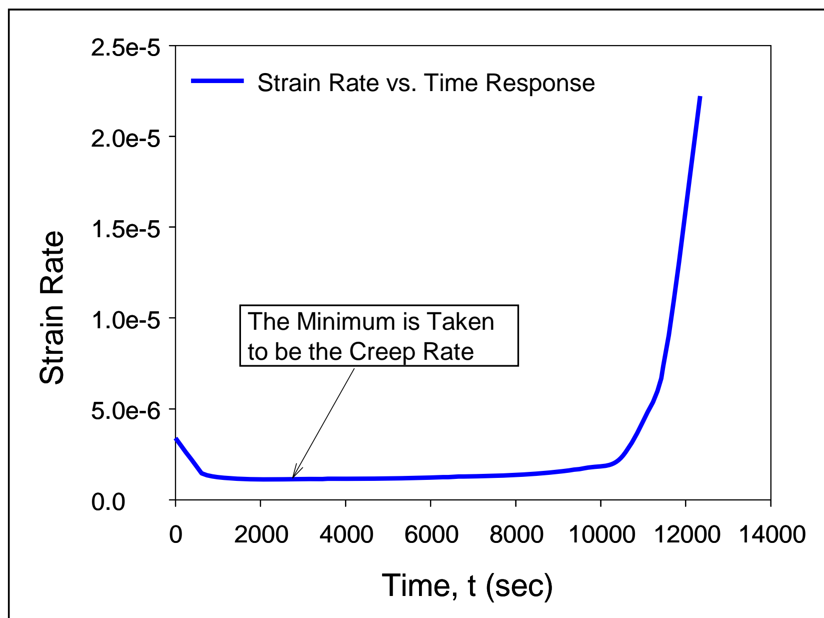

(b) Creep Strain Rate vs. Time Curve

Figure 3.10 Definition of "Steady State" Creep Strain Rate

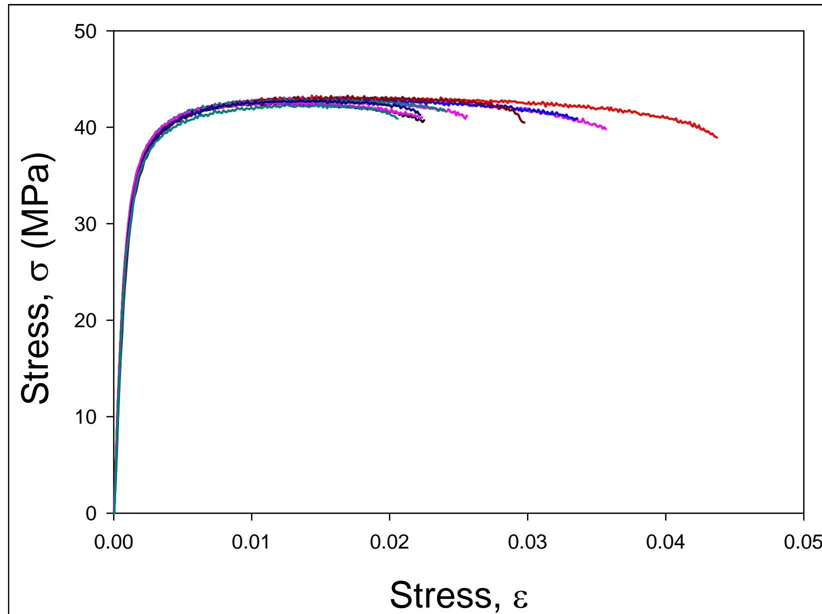

Figure 3.11 A Set of Typical Stress-Strain Curves for Solder

In this study, the analytical focus was placed on the portion of the stress-strain curve before visible necking occurs (typically $\varepsilon < 2\text{-}3\%$ for solders under investigation). Therefore, the stress-strain curves were truncated at a selected strain level prior to necking for the purpose of interpreting the stress-strain behavior of the solder alloys on a statistical basis. The truncated curves, as shown in Figure 3.12 for the raw data in Figure 3.11, satisfactorily preserved the important mechanical property information such as elastic modulus, yield stress and ultimate tensile strength. These truncated curves were quite adequate for mathematical analysis and empirical modeling.

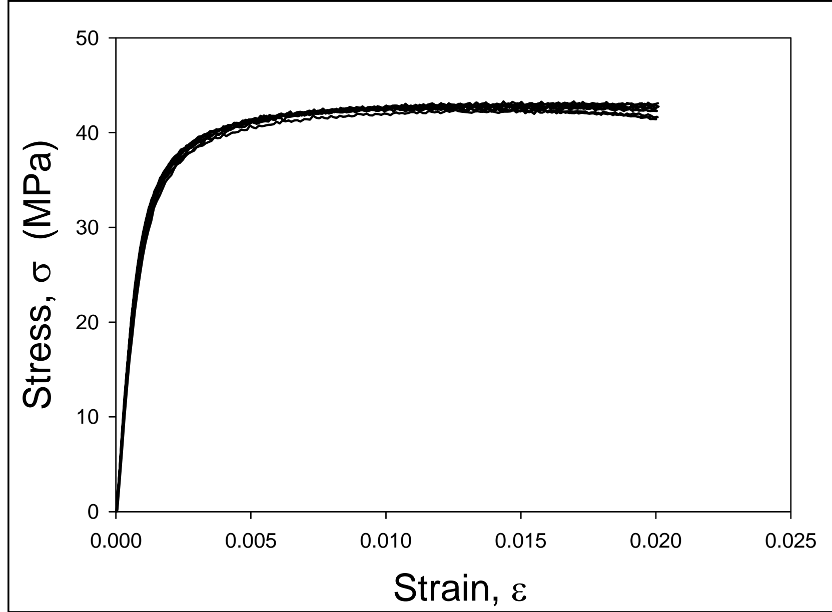

Figure 3.12 Truncated Solder Stress-Strain Curves

A few mathematical models have been used to characterize the stress-strain response of solder alloys [193]. In this study, an empirical mathematical model was developed to fit the truncated stress-strain curves. It consisted of two functions: a Hooke's Law linear model used for extremely small strains ($\varepsilon << 0.0001$), and a four parameter empirical representation called the Weibull model for larger strains:

$$\sigma(\varepsilon) = E\varepsilon \qquad \varepsilon \leq \varepsilon^* \tag{3.4}$$

$$\sigma(\varepsilon) = C_0 - C_1 e^{-C_2 \varepsilon^{C_3}} \qquad \varepsilon \geq \varepsilon^* \tag{3.5}$$

where E is the initial elastic modulus; C_0, C_1, C_2, C_3 are fitting constants to be determined, and ε^* is the strain level where the two functions intersect.

One issue that needs to be noted is the incapability of the Weibull model in describing extremely small strain behavior of a solder alloy. In particular, the slope of the Weibull model will mathematically reach infinity at small strains when $C_3 < 1$. The constant C_0 in the model defines the limiting value of stress at high strains, which is actually the ultimate tensile strength (UTS):

$$C_0 = \sigma_u = UTS \tag{3.6}$$

There are totally 6 constants, E, C_0, C_1, C_2, C_3, and ε^*, that must be determined before the two-function elastic-plastic model can be utilized to fit a set of stress-strain curves. The elastic modulus E was first found as the average value of the initial moduli obtained by fitting the individual truncated stress-strain curves at very small strains using linear regression analyses. Then, a nonlinear regression analysis was performed to simultaneously fit the Weibull model to the same set of truncated stress-strain curves. The 4 material constants C_0, C_1, C_2, C_3 were found by using this fitting approach. Finally, the constant ε^* was determined by solving the nonlinear equation that states the condition under which the two functions (Eq. 3.4 and Eq. 3.5) become equal:

$$\sigma(\varepsilon^*) = E\varepsilon^* = C_0 - C_1 e^{-C_2(\varepsilon^*)^{C_3}} \tag{3.7}$$

After ascertaining the values of the 6 constants for a specific solder alloy under a certain set of aging and test conditions, the empirical model fitting curve can be readily generated (as shown in Figure 3.13). This method can be applied to any set of recorded solder stress-strain curves, and the final fitting curve is an accurate mathematical description of an "average" stress-strain curve to represent the data.

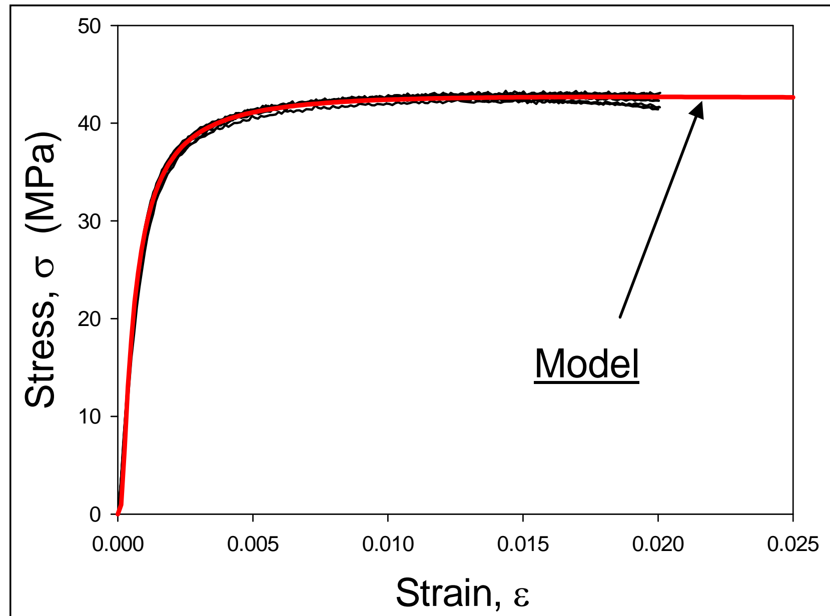

Figure 3.13 Empirical Model Fit to Solder Stress-Strain Curves

3.5 Microstructure Observation

Specimens used for microstructure analysis were mounted in a slow-curing transparent epoxy that took about 24 hours to harden at room temperature. Grinding and polishing were then conducted by hand with regular metallographic rotating polishing disks. Silicon carbide (SiC) sand papers were used for the initial grinding of specimens, and were selected in a sequence of 320, 600, 800, 1000 and 1200 in grit size. Tap water was used during the sand paper grinding for lubrication purposes. The polishing process started with polycrystalline diamond suspension as the abrasive (particle size: 3.0 μm) on woven silk cloth, right after the 1200 SiC sand paper grinding. Final polishing was carried out on a porous neoprene cloth disk by using BUEHLER MasterPrep

polishing suspension as the abrasive (particle size: 0.05 μm). After polishing, the specimen surface was thoroughly cleaned by distilled water in order to remove any residue left in the process. To review the microstructure, chemical etchants were sometimes used, especially for 63Sn-37Pb solder. The formula of the etchant was 5% hydrochloride + 95% methanol (5-8 seconds). It is necessary to point out that the microstructure of solder alloys can evolve rapidly even at room temperature due to aging after solidification. Therefore, specimens must be prepared in a timely manner if one wants to capture the initial microstructure and ensuing microstructure evolution without significant aging effects.

Two microstructure analysis techniques were used in this study, namely, optical microscopy (OM) and scanning electron microscopy (SEM). A Nikon Industrial Microscope ECLIPSE L150/L150A equipped with polarization filters (as shown in Figure 3.14) was used to reveal the morphology of the Sn-based matrix structure. Polarization contrast was used to obtain high quality images. Another optical microscope, an OLYMPUS BX 60 Universal Microscope equipped with Nomarski prism, was used for analyzing solder joint specimens.

The SEM microstructure analyses were carried out on a JEOL JSM-7000F Field Emission Scanning Electron Microscope for the bulk solder studies (as shown in Figure 3.15), and on a Zeiss EVO 50P Scanning Electron Microscope for the solder joint studies. Gold sputter coating was used to ensure good conductivity of the specimens. Furthermore, energy dispersive X-ray spectrometry (EDS/EDX) analysis and electron probe microanalysis (EPMA) were employed to investigate on the chemical composition as well as the distribution of second phases in the solder alloys.

Figure 3.14 Nikon ECLIPSE L150/L150A Optical Microscope

Figure 3.15 JEOL JSM-7000F Field Emission SEM

Chapter 4
Effects of Aging on Mechanical Properties and Microstructure of Lead-free SAC Solder Alloys

4.1 Introduction

It has been widely acknowledged that large discrepancies exist in the current database of measured solder mechanical properties. This issue is mainly caused by variations in the testing procedure such as test specimen geometry and fabrication, testing setup, data acquisition method, and the initial microstructure of the specimens. The variations are further exacerbated by thermal aging.

The microstructure, mechanical response, and failure behavior of solder joints in electronic assemblies are constantly evolving when exposed to isothermal aging and/or thermal cycling environments. The observed material behavior variation during thermal aging/cycling is universally detrimental to reliability and includes reductions in stiffness, yield stress, ultimate strength, and strain to failure, as well as highly accelerated creep.

In this chapter, aging effects on the mechanical properties of a series of SAC solder alloys were examined by performing tensile tests with a full test matrix. The obtained raw stress-strain data were fitted by using the two-function empirical model introduced in Chapter 3 (Eq. 3.4 and 3.5) and mechanical properties such as elastic modulus, yield stress, and UTS were then determined. Microstructure evolution of the SAC alloys was also investigated, and the ensuing influences on the changes of mechanical properties and failure behavior were studied.

4.2 Aging Effects on Stress-Strain Response of SAC Solder Alloys

Uniaxial SAC specimens for tensile testing were prepared by using the casting method and controlled reflow cooling profile described in Chapter 3, followed by up to sixty days of aging at five different aging temperatures (T = 25, 50, 75, 100, and 125 °C). The solders studied included four standard SAC alloys with varying silver content (SAC105, SAC205, SAC305, and SAC405), as well as standard 63Sn-37Pb. Specimens for each alloy were grouped in sets of ten, which were then subjected to a specific set of aging conditions (aging temperature + aging time) prior to testing. The test matrix defined by aging temperature and aging time is listed in Table 4.1. All tensile tests were conducted at room temperature (25 °C) under a constant strain rate $\dot{\varepsilon} = 0.001$.

Figures 4.1-4.4 illustrate the experimentally measured average stress-strain curves for the SAC105, SAC205, SAC305, and SAC405 solder alloys. In each figure, there are five graphs for the five different aging temperatures. In each graph, each individual stress-strain curve represents the empirical model fit to the 10 curves recorded for a certain aging time. The results illustrate the evolution of the stress-strain response as a function of aging. Analogous experiments were also performed with reflowed 63Sn-37Pb eutectic solder specimens for comparison purposes (shown in Figure 4.5).

Table 4.1 Aging Matrix for Stress-Strain Tests

	Aging Temperature				
Aging Time (days)	**25 °C (RT)**	**50 °C**	**75 °C**	**100 °C**	**125 °C**
0	X	X	X	X	X
5	X	X	X	X	X
10	X	X	X	X	X
20	X	X	X	X	X
30	X	X	X	X	X
45	X	X	X	X	X
60	X	X	X	X	X

X: Test Finished, Testing Temperature = R.T., Strain Rate = 0.001/s

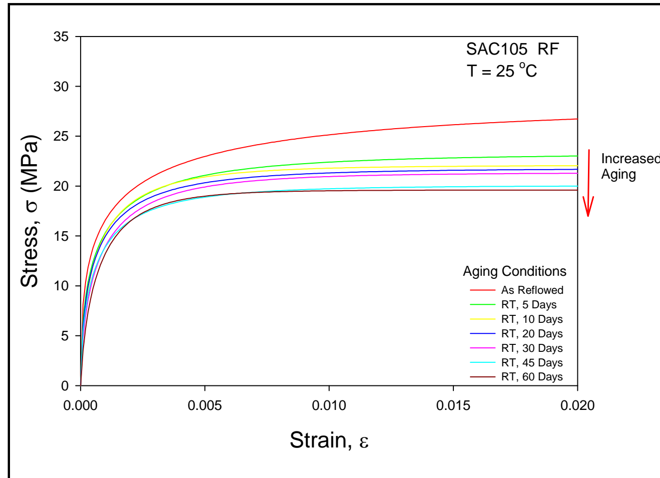

(a) Aging at T = 25 °C

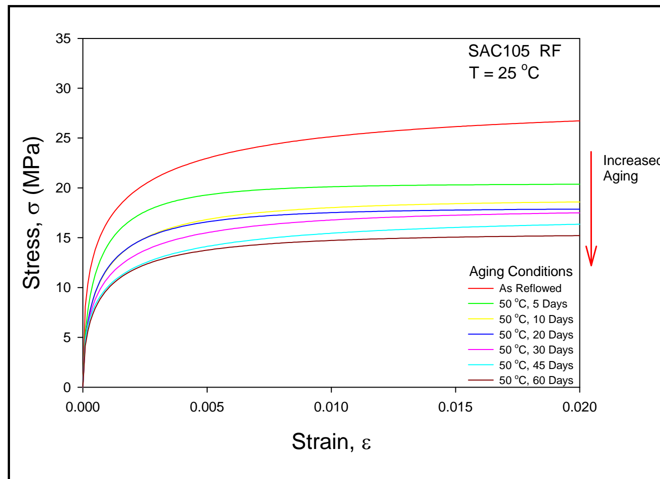

(b) Aging at T = 50 °C

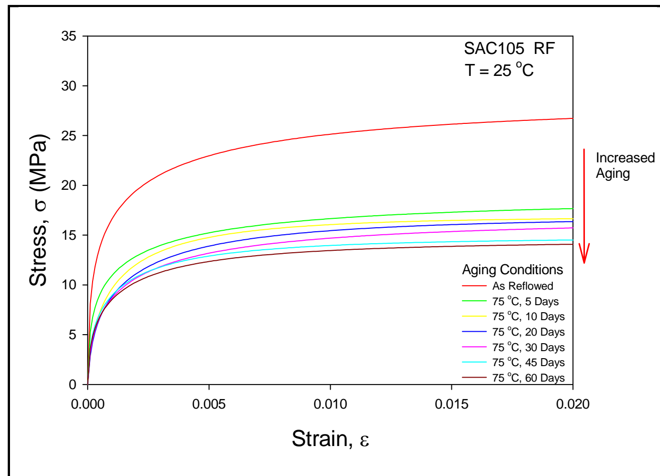

(c) Aging at T = 75 °C

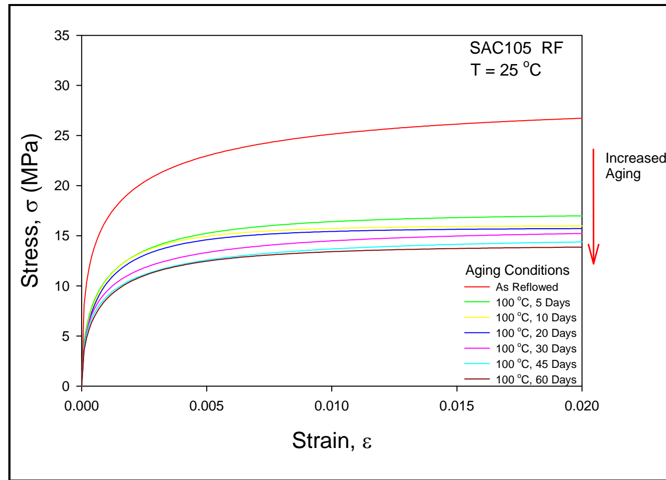

(d) Aging at T = 100 °C

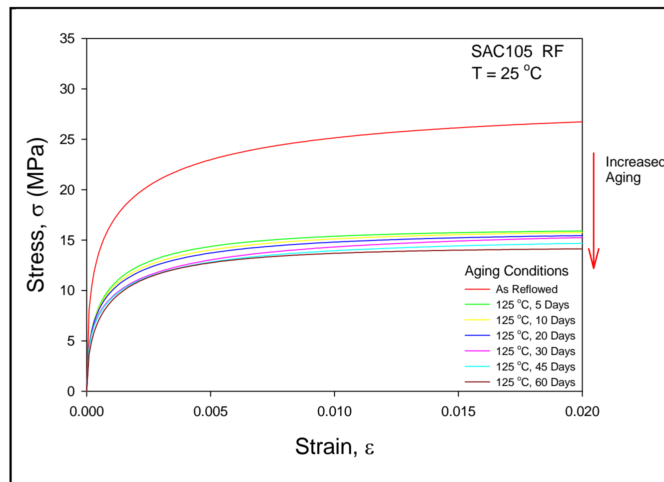

(e) Aging at T = 125 °C

Figure 4.1 Stress-Strain Curves for SAC105 Aged for 0-60 Days

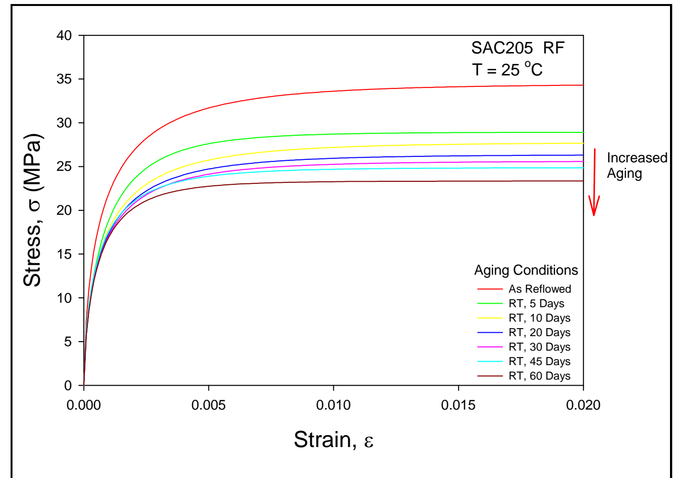

(a) Aging at T = 25 °C

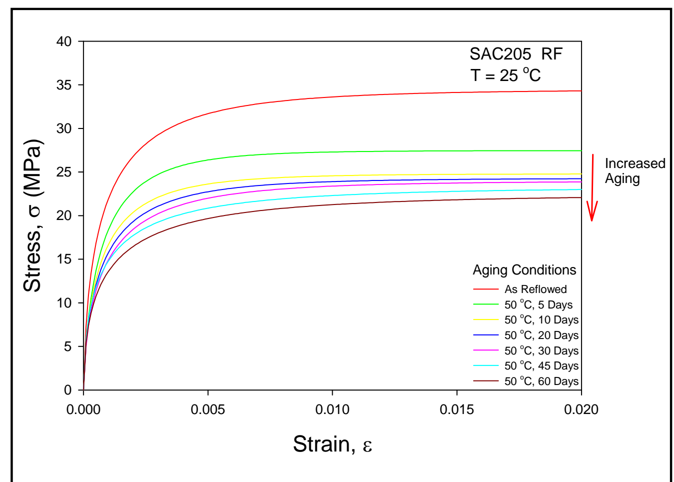

(b) Aging at T = 50 °C

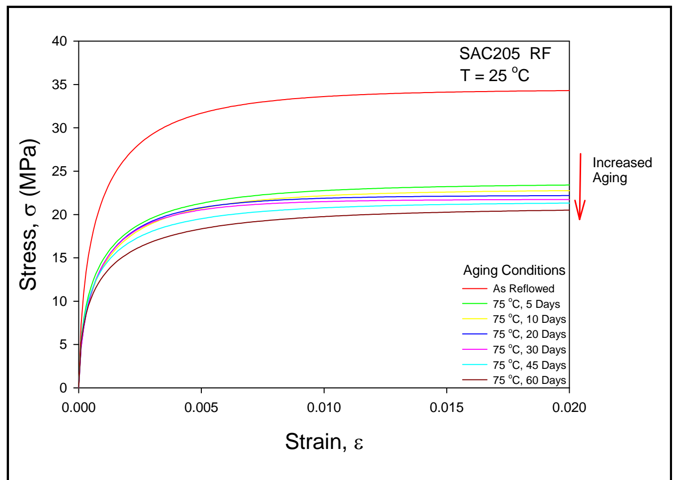

(c) Aging at T = 75 °C

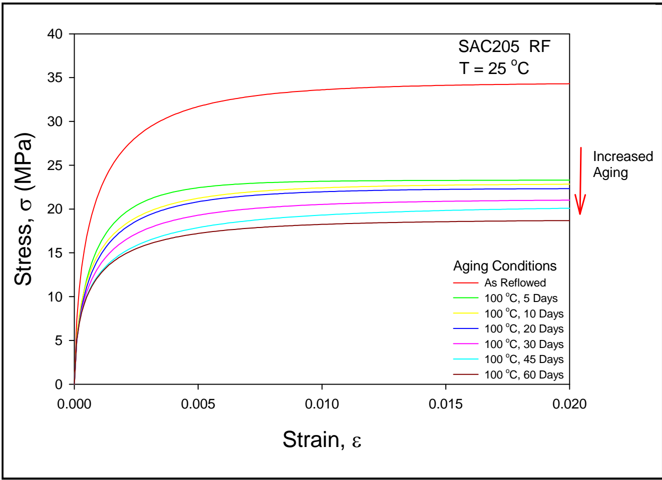

(d) Aging at T = 100 °C

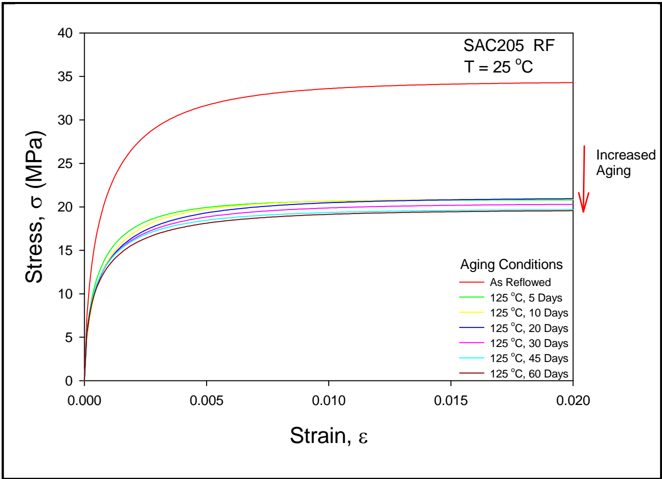

(e) Aging at T = 125 °C

Figure 4.2 Stress-Strain Curves for SAC205 Aged for 0-60 Days

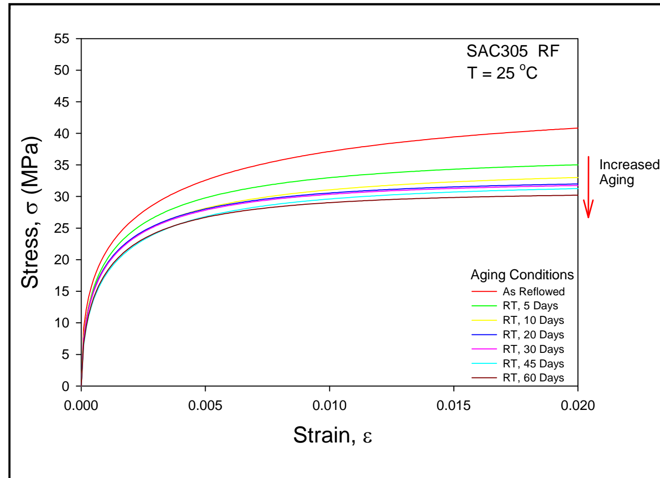

(a) Aging at T = 25 °C

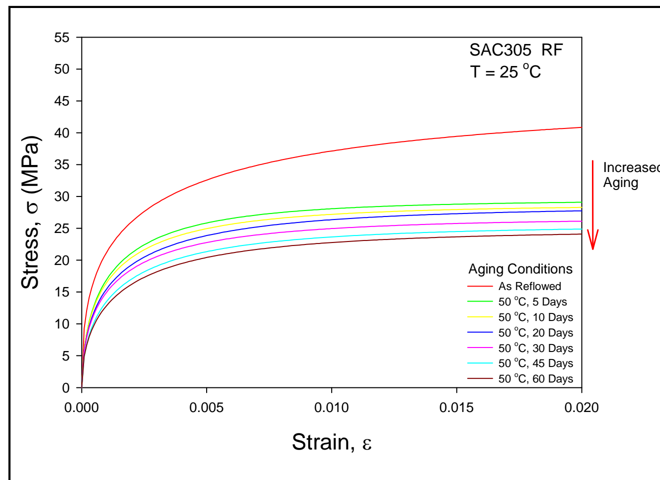

(b) Aging at T = 50 °C

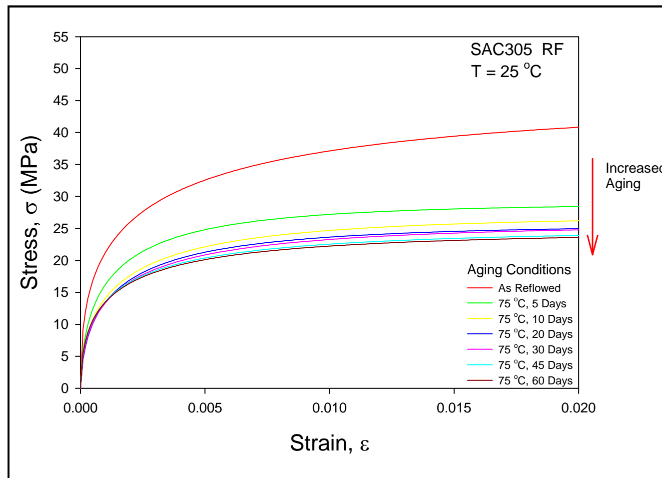

(c) Aging at T = 75 °C

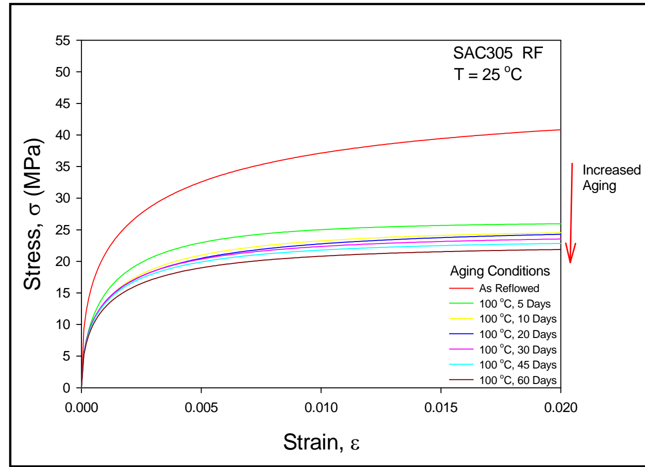

(d) Aging at T = 100 °C

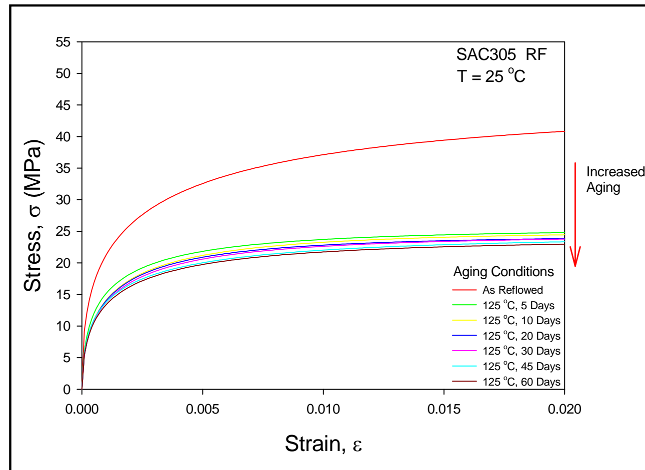

(e) Aging at T = 125 °C

Figure 4.3 Stress-Strain Curves for SAC305 Aged for 0-60 Days

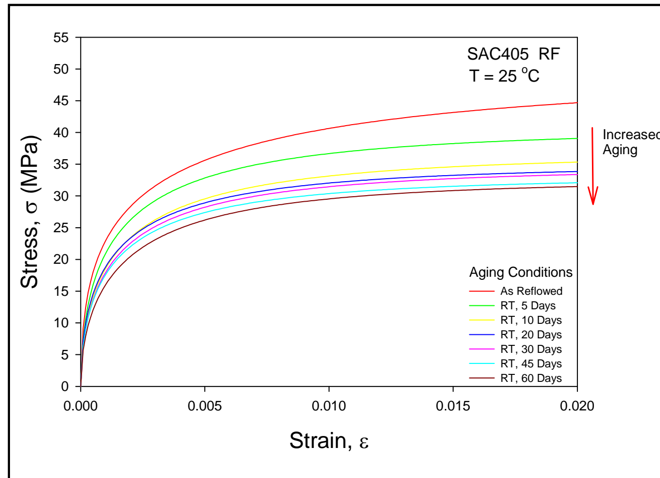

(a) Aging at T = 25 °C

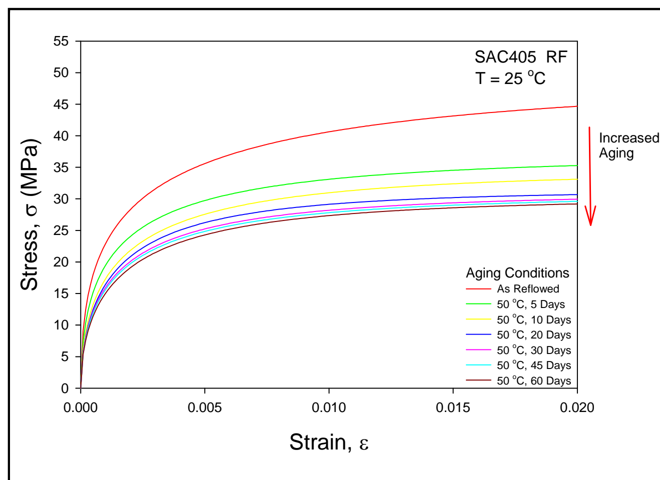

(b) Aging at T = 50 °C

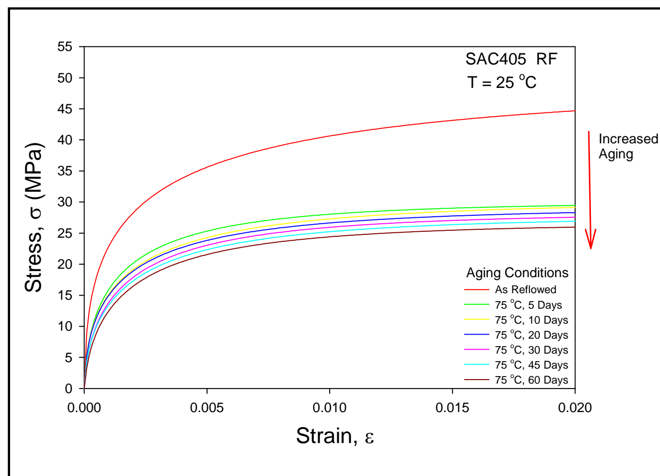

(c) Aging at T = 75 °C

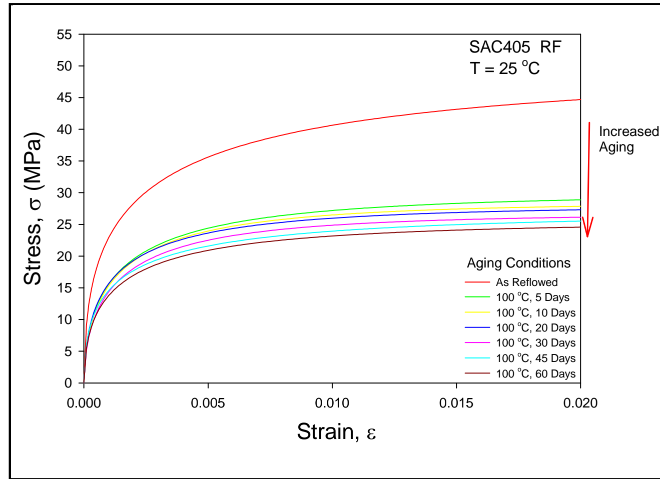

(d) Aging at T = 100 °C

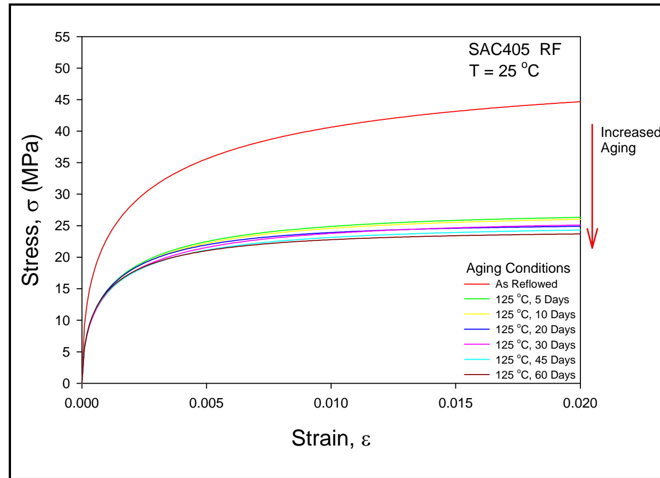

(e) Aging at T = 125 °C

Figure 4.4 Stress-Strain Curves for SAC405 Aged for 0-60 Days

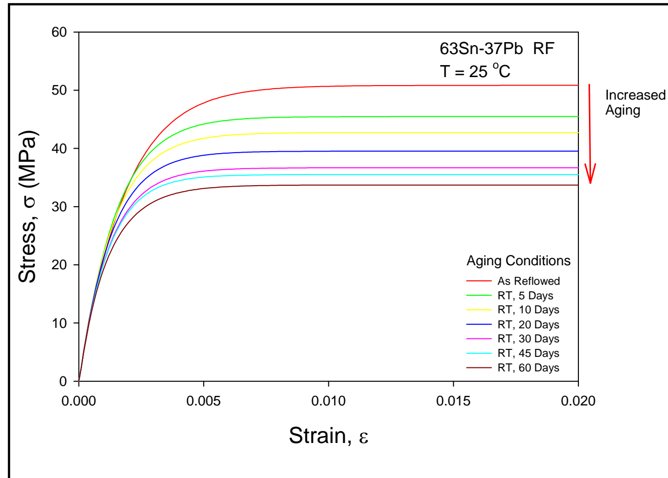

(a) Aging at T = 25 °C

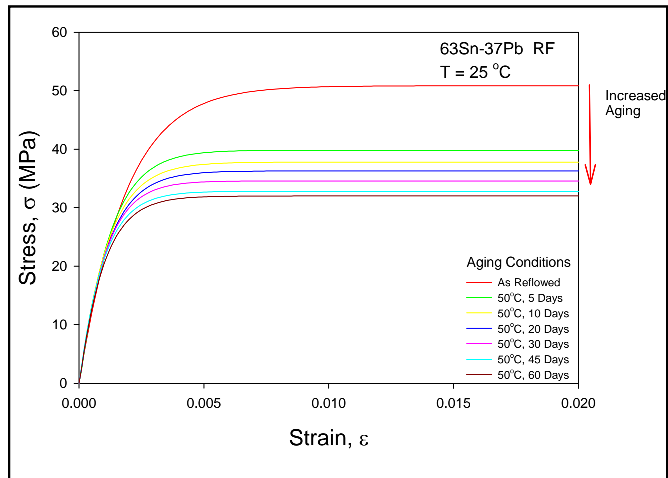

(b) Aging at T = 50 °C

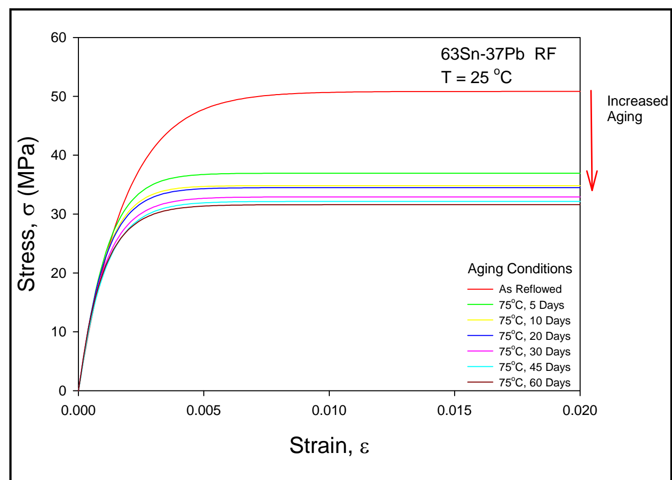

(c) Aging at T = 75 °C

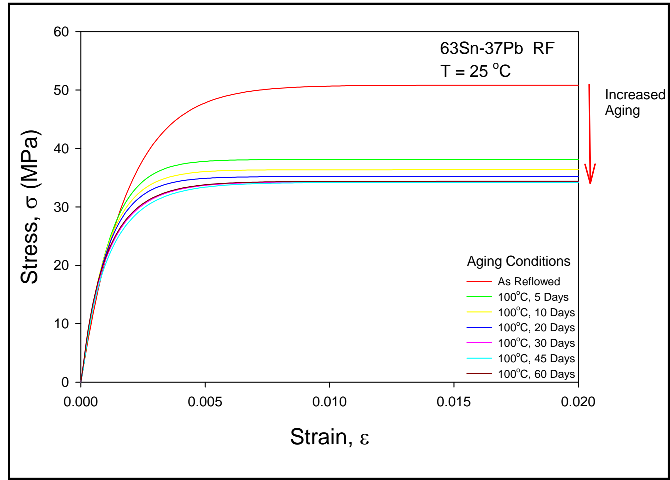

(d) Aging at T = 100 °C

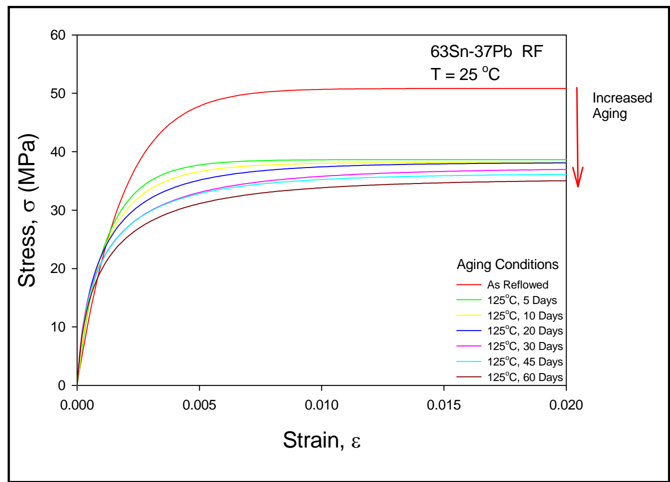

(e) Aging at T = 125 °C

Figure 4.5 Stress-Strain Curves for 63Sn-37Pb Aged for 0-60 Days

4.3 Effects of Aging on Young's Modulus

The elastic modulus for each alloy and set of aging conditions was extracted from the model-fitted stress-strain curves as discussed in Chapter 3. Variations of the modulus as a function of aging time are illustrated in Figures 4.6-4.11 for the various solder alloys at the five aging temperatures. Table 4.2 contains the values of E for the SAC alloys and 63Sn-37Pb after 60-days of aging under different aging temperatures. As-reflowed modulus values that were obtained prior to aging are also shown in the table to demonstrate the magnitude of the aging effects on the elastic modulus of the solder alloys. Several important observations can be made:

(1) For the SAC alloys, the elastic modulus decreased with increasing aging time at all aging temperatures. This trend was represented by a 3-parameter exponential model:

$$E = C_0 + C_1 e^{-C_2 t} \tag{4.1}$$

where C_0 is the modulus value when the aging time reaches infinity ($t \to \infty$); and C_1 and C_2 are fitting constants. Values for these constants are tabulated in Appendix I.

(2) For SAC alloys, the elastic modulus decreased as the aging temperature increased. For higher the silver content in the alloy, the modulus values increased and the degradations decreased as shown in Figure 4.10. For example, after 60-days of aging at 125 °C, the modulus values of SAC105-SAC405 decreased by 48.44%, 36.69%, 33.16%, and 32.34%, respectively, as compared with the as-reflowed values (no aging).

(3) For 63Sn-37Pb, the elastic modulus basically remained constant across the entire aging matrix, and the values can be banded in a narrow range as shown in Figure 4.11.

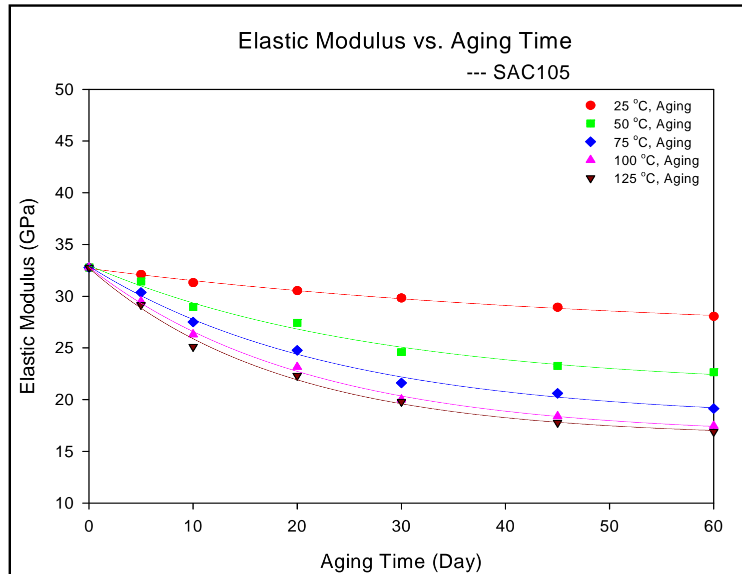

Figure 4.6 Change of Elastic Modulus with Aging for SAC105

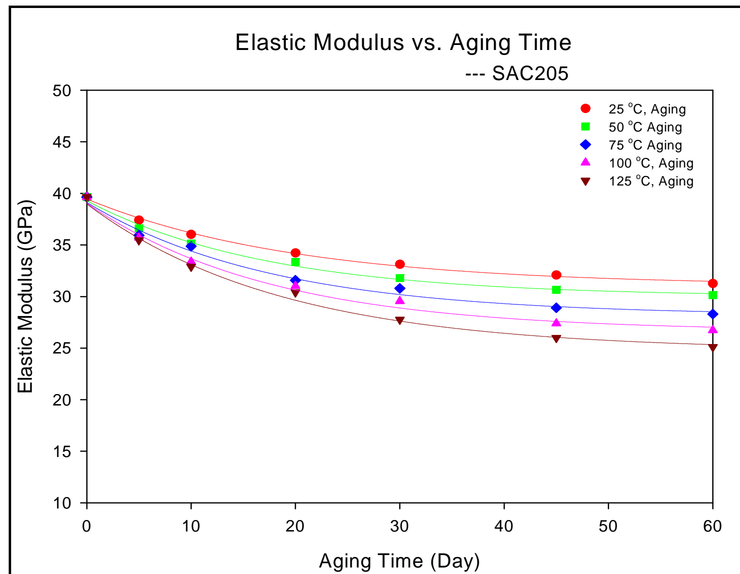

Figure 4.7 Change of Elastic Modulus with Aging for SAC205

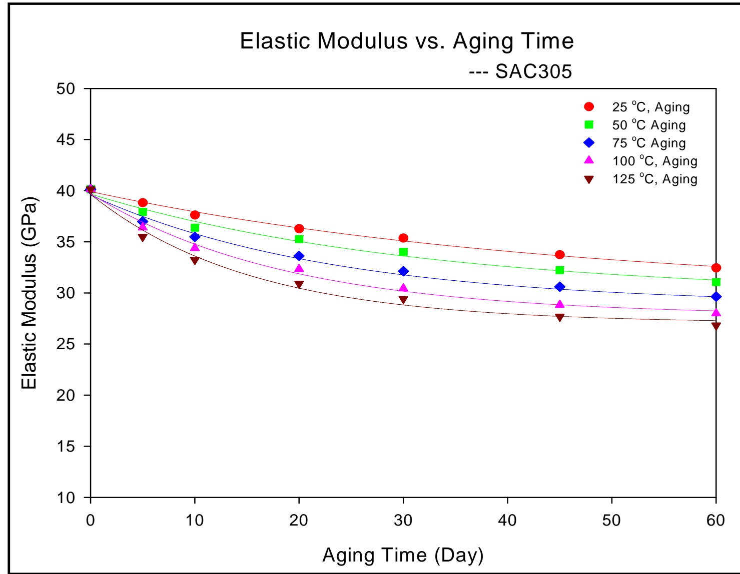

Figure 4.8 Change of Elastic Modulus with Aging for SAC305

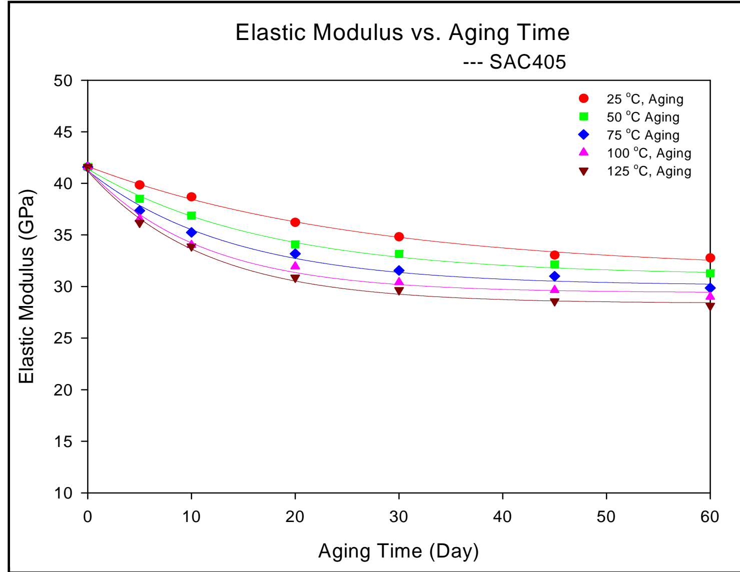

Figure 4.9 Change of Elastic Modulus with Aging for SAC405

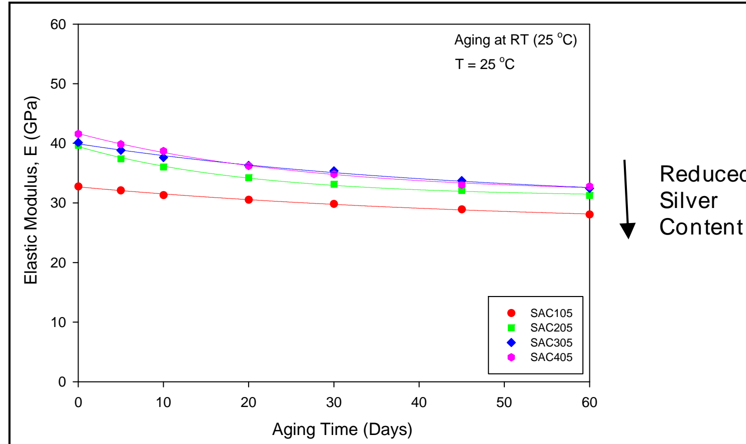

(a) Aging at T = 25 °C

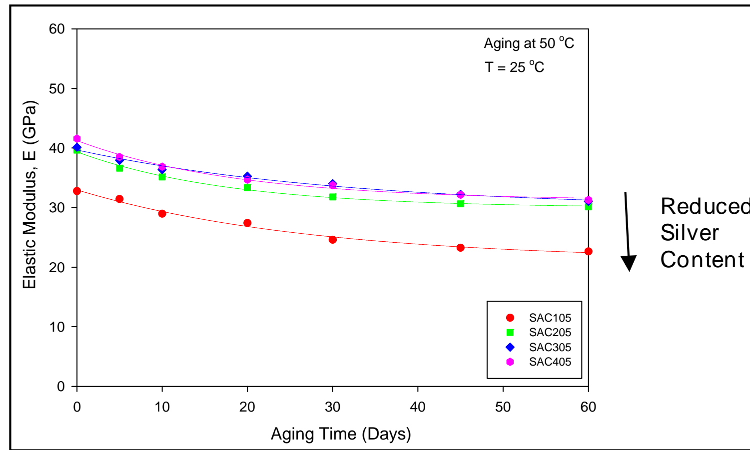

(b) Aging at T = 50 °C

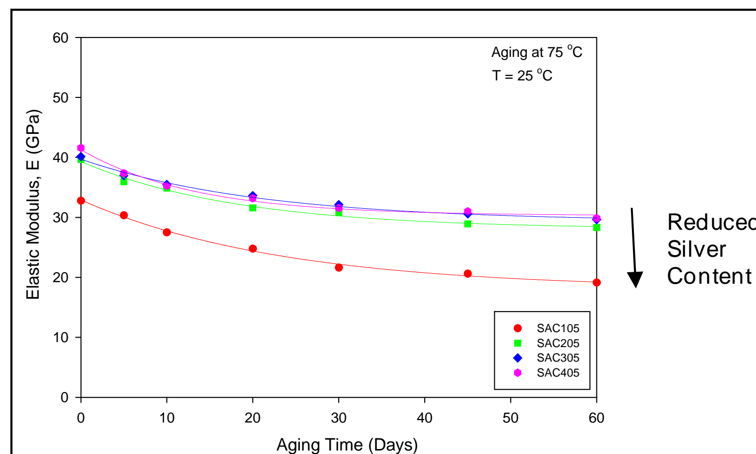

(c) Aging at T = 75 °C

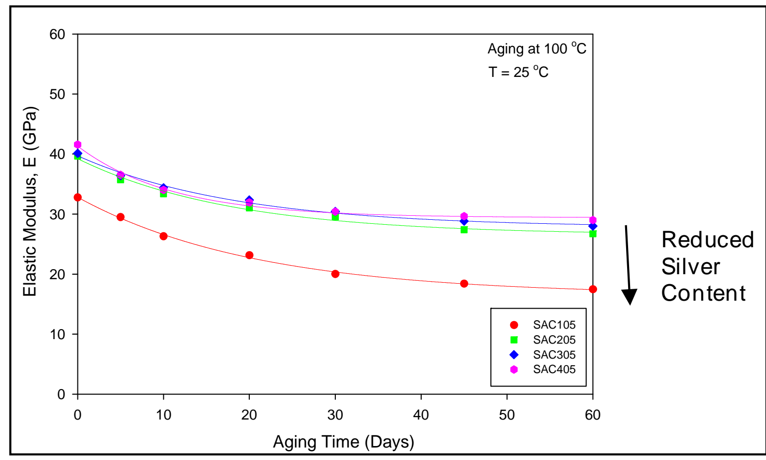

(d) Aging at T = 100 °C

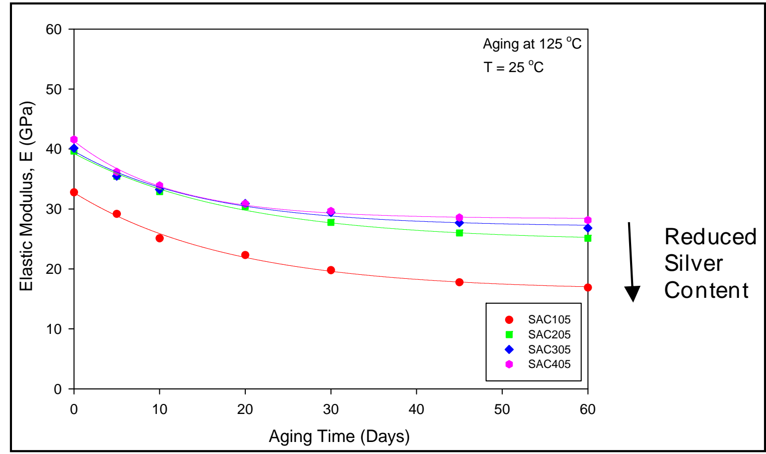

(e) Aging at T = 125 °C

Figure 4.10 Effects of Silver Content on the Evolution of the Elastic Modulus with Aging

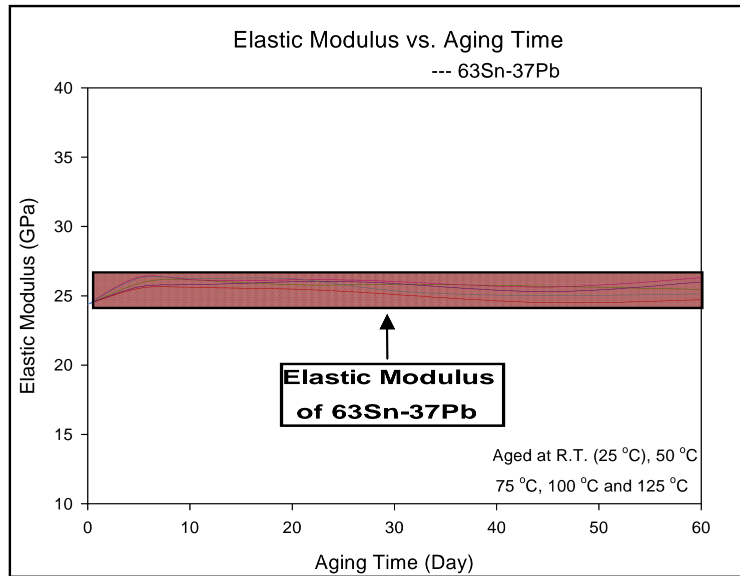

Figure 4.11 Change of Elastic Modulus with Aging for 63Sn-37Pb

Table 4.2 Values of Elastic Modulus after 60-days of Aging

Modulus (GPa)	63Sn-37Pb	SAC105	SAC205	SAC305	SAC405
As Reflowed	24.38	32.77	39.64	40.13	41.58
25 °C	24.72	28.06	31.27	32.45	32.77
50 °C	25.46	22.65	30.13	31.04	31.28
75 °C	25.99	19.13	28.31	29.64	29.86
100 °C	26.31	17.47	26.72	28.00	29.00
125 °C	25.13	16.90	25.10	26.82	28.13

4.4 Effects of Aging on Yield Stress

The yield stress in this study was taken to be the standard 0.2% yield stress σ_{ys} (upon unloading, the permanent strain is equal to ε = 0.002). Values of σ_{ys} were extracted from the solder stress-strain curves shown in Figures 4.1-4.5. Variations of the yield stress as a function of aging time are illustrated in Figures 4.12-4.16 for the various solder alloys at the five aging temperatures. Table 4.3 contains the numeric σ_{ys} values for the SAC alloys and 63Sn-37Pb after 60-days of aging under different aging temperatures. As-reflowed values that were obtained prior to aging are also shown in the table for comparison purposes.

For all of the alloys, the yield stress decreased dramatically with aging time at all aging temperatures. This trend was well fit using a 3-parameter hyperbolic model:

$$\sigma_{ys} = C_0 + \frac{C_1 C_2}{C_2 + t} \tag{4.2}$$

where C_0 is the yield stress value when the aging time approaches infinity ($t \rightarrow \infty$); and C_1 and C_2 are fitting constants. Values for these constants are tabulated in Appendix I.

For the SAC alloys, the higher silver content alloys had higher yield stress after reflow. They also had better resistance to aging, and their yield stresses degraded at a lower rate (see Figure 4.17). For example, after 60-days of aging at 125 °C, the yield stress values for SAC 105 to SAC405 decreased by 49.42%, 45.57%, 44.23%, and 41.84% respectively, as compared to the as reflowed values (no aging).

On the contrary, 63Sn-37Pb showed better aging resistance (34.81% loss in σ_{ys} after 60-days of aging at 125 °C) and also possessed the highest yield stress of all of the solders at the beginning of aging process. This is in agreement with the results of Ma [227].

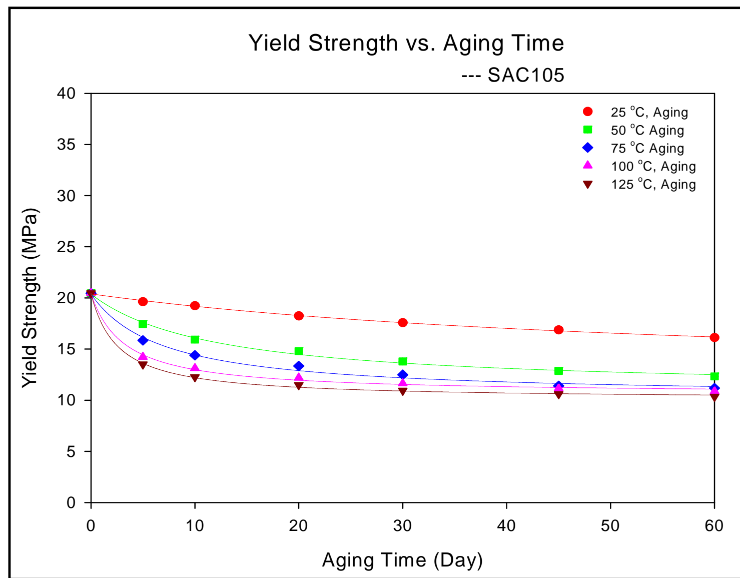

Figure 4.12 Change of Yield Stress with Aging for SAC105

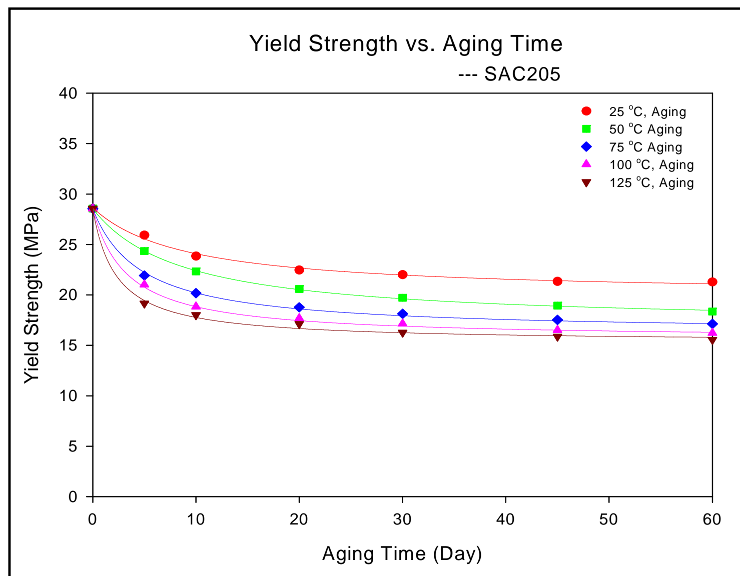

Figure 4.13 Change of Yield Stress with Aging for SAC205

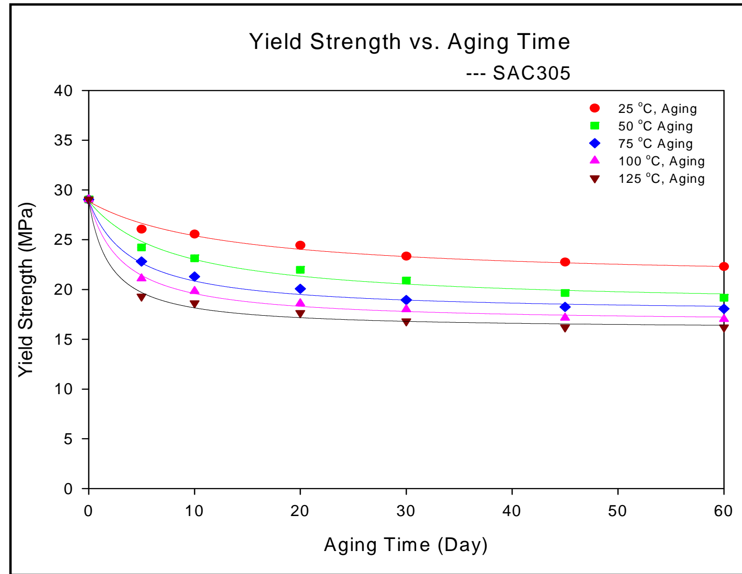

Figure 4.14 Change of Yield Stress with Aging for SAC305

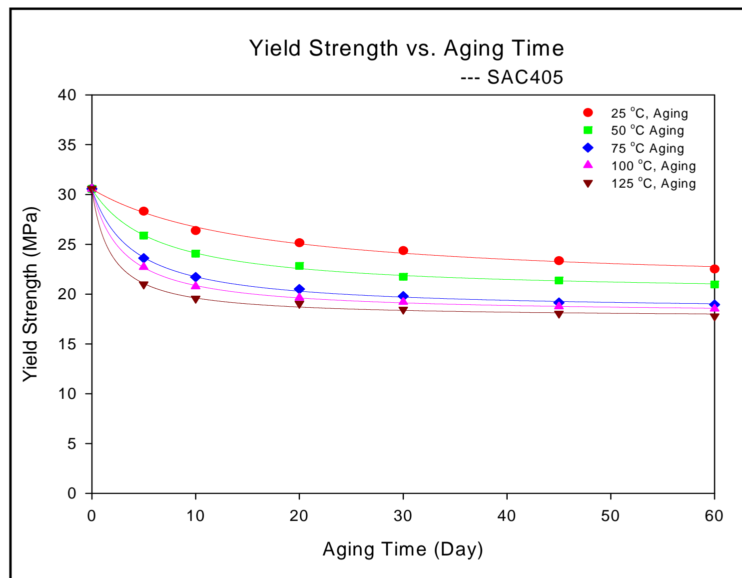

Figure 4.15 Change of Yield Stress with Aging for SAC405

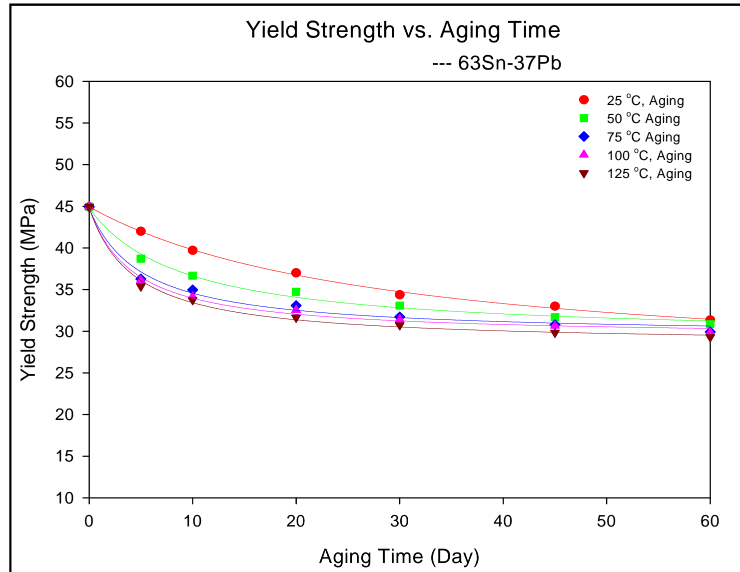

Figure 4.16 Change of Yield Stress with Aging for 63Sn-37Pb

Table 4.3 Values of Yield Stress after 60-days of Aging

σ_{ys} (MPa)	**63Sn-37Pb**	**SAC105**	**SAC205**	**SAC305**	**SAC405**
As Reflowed	44.94	20.45	28.56	29.05	30.56
25 °C	31.35	16.12	21.29	22.31	22.52
50 °C	30.83	12.33	18.35	19.18	20.97
75 °C	29.90	11.18	17.13	18.06	18.94
100 °C	29.82	10.87	16.23	17.02	18.54
125 °C	29.29	10.34	15.55	16.20	17.77

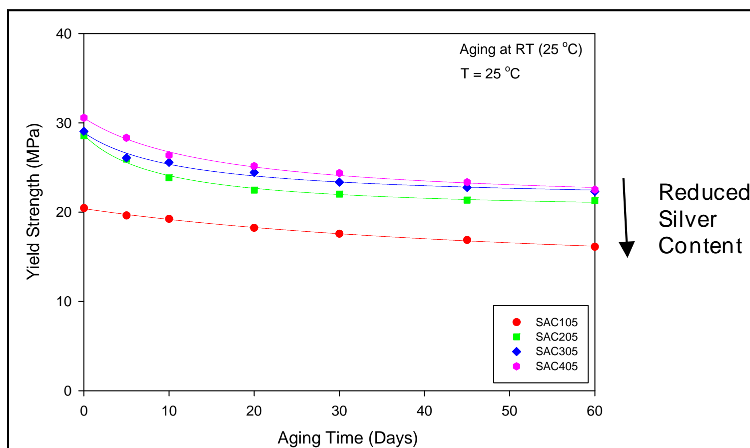

(a) Aging at T = 25 °C

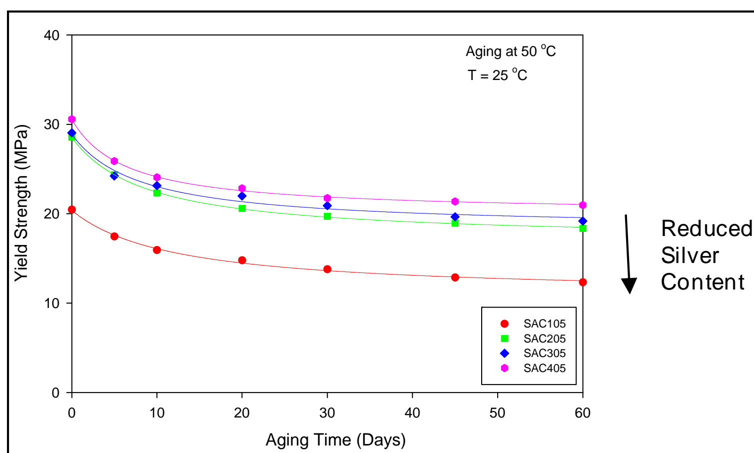

(b) Aging at T = 50 °C

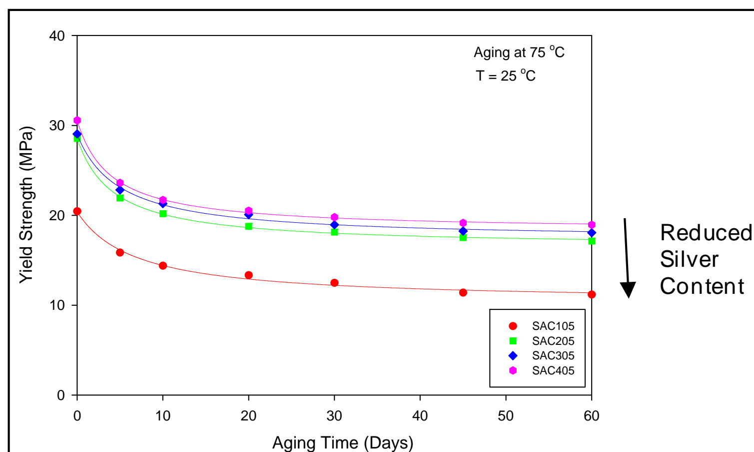

(c) Aging at T = 75 °C

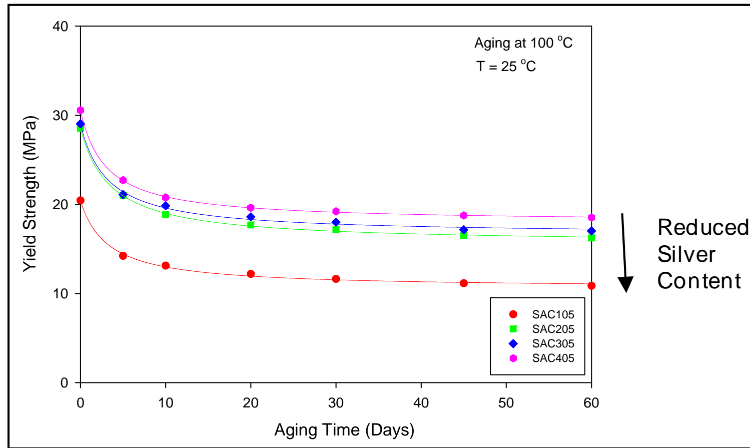

(d) Aging at T = 100 °C

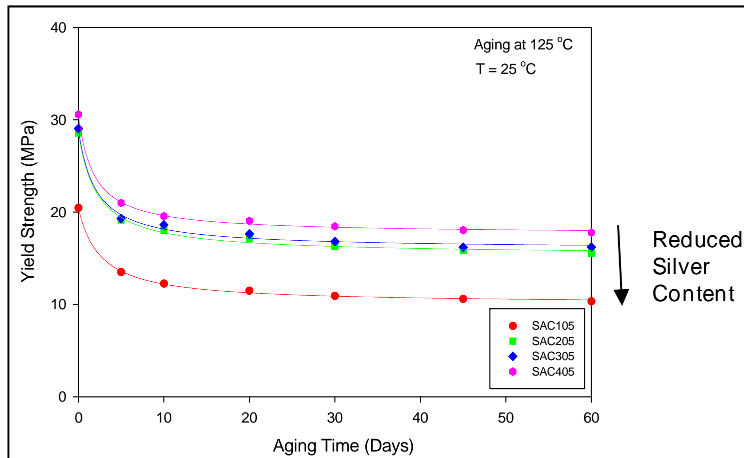

(e) Aging at T = 125 °C

Figure 4.17 Effects of Silver Content on the Evolution of the Yield Stress with Aging

4.5 Effects of Aging on Ultimate Tensile Strength

The ultimate tensile strength (UTS) is the maximum stress level that a material can withstand before failure under uniaxial loading. Similar to earlier sections, variations of the UTS as a function of aging time are illustrated in Figures 4.18-4.22 for the various solder alloys at the five aging temperatures. Table 4.4 contains numeric σ_{uts} values for the SAC alloys and 63Sn-37Pb after 60-days of aging under different aging temperatures. As-reflowed values that were obtained prior to aging are also shown in the table for comparison purposes.

For all of the solders, the UTS decreased with aging in a similar manner as the yield stress. The evolution was again well fit using a 3-parameter hyperbolic model:

$$\sigma_{uts} = C_0 + \frac{C_1 C_2}{C_2 + t} \tag{4.3}$$

where C_0 is the UTS value when the aging time approaches infinity ($t \rightarrow \infty$); and C_1 and C_2 are fitting constants. Values of these constants are tabulated in Appendix I.

As with the yield stress, increased silver content led to higher UTS in the SAC alloys for all aging conditions. After 60-days of aging at 125 °C, it was found that the UTS dropped by up to 44% for the SAC alloys, and only about 30% for 63Sn-37Pb. The influence of silver content on the UTS of the SAC alloys is shown in Figure 4.23.

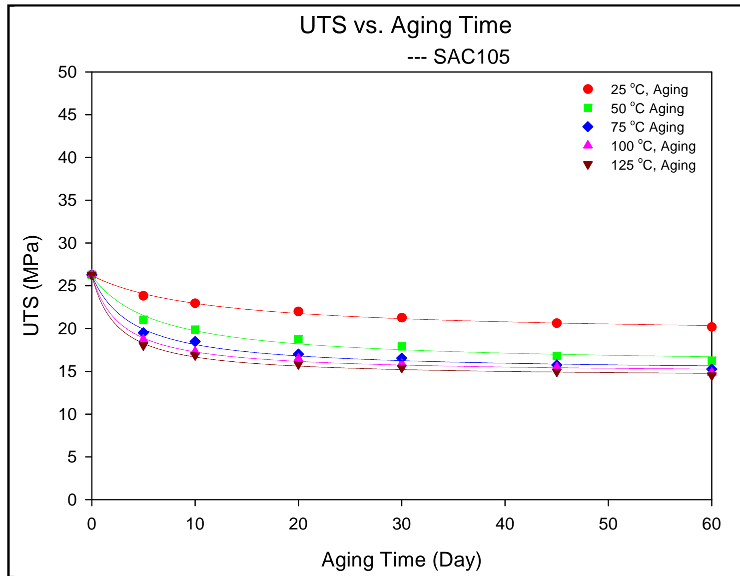

Figure 4.18 Change of UTS with Aging for SAC105

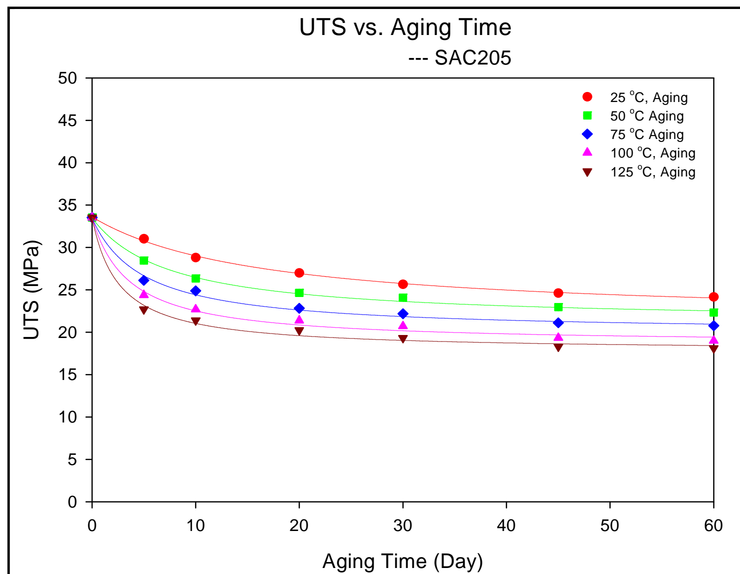

Figure 4.19 Change of UTS with Aging for SAC205

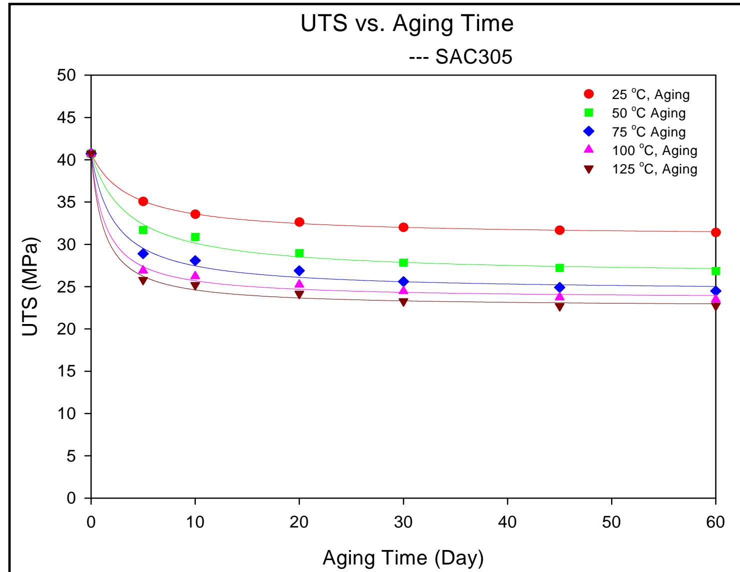

Figure 4.20 Change of UTS with Aging for SAC305

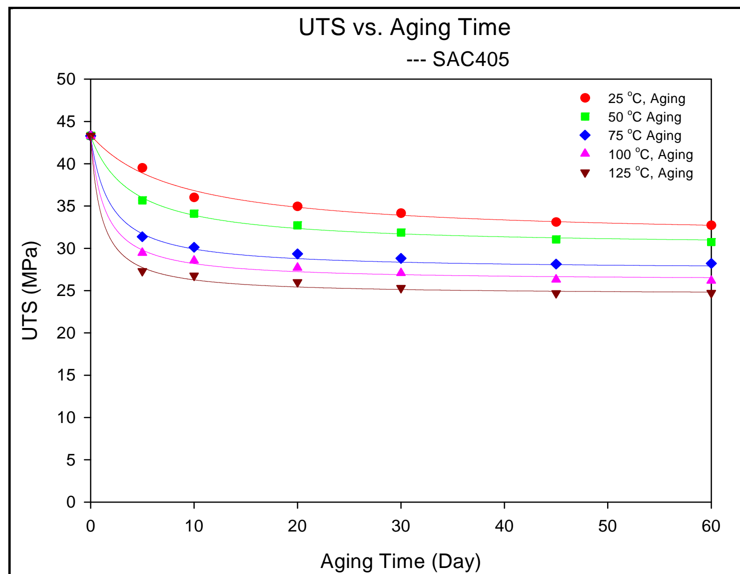

Figure 4.21 Change of UTS with Aging for SAC405

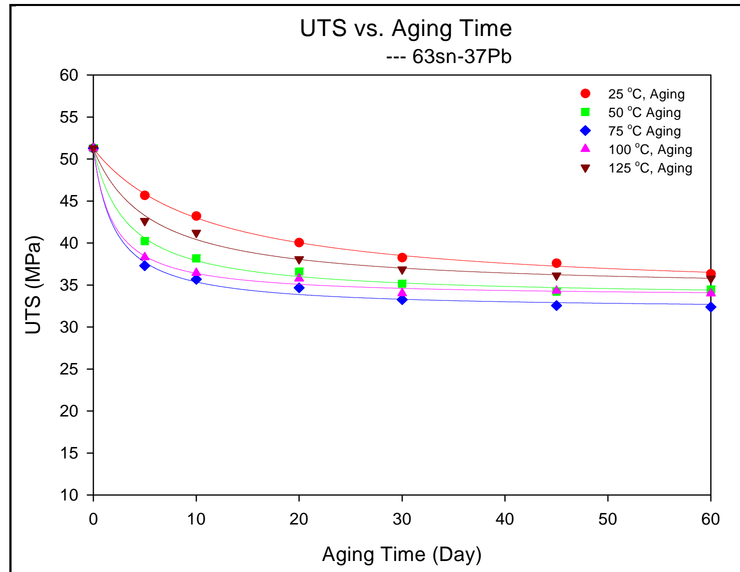

Figure 4.22 Change of UTS with Aging for 63Sn-37Pb

Table 4.4 Values of UTS after 60-days of Aging

σ_{uts} (MPa)	63Sn-37Pb	SAC105	SAC205	SAC305	SAC405
As Reflowed	51.28	26.28	33.53	40.73	43.30
25 °C	36.33	20.18	24.17	31.40	32.72
50 °C	34.45	16.23	22.32	26.82	30.73
75 °C	32.38	15.25	20.77	24.49	28.21
100 °C	34.00	14.84	18.99	23.48	26.17
125 °C	35.77	14.51	18.10	22.74	24.72

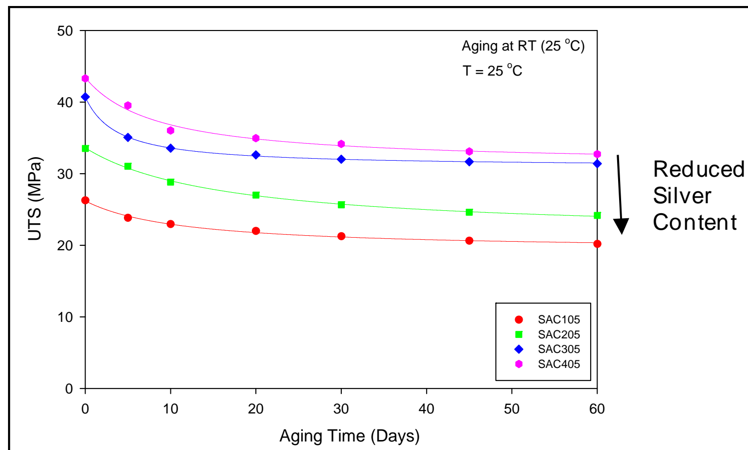

(a) Aging at T = 25 °C

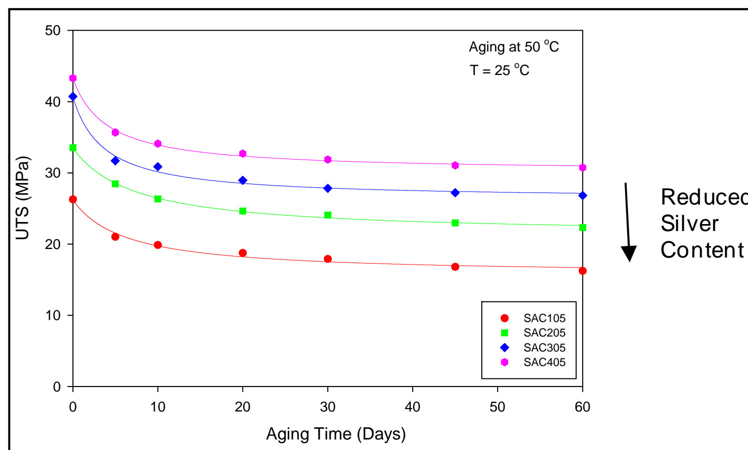

(b) Aging at T = 50 °C

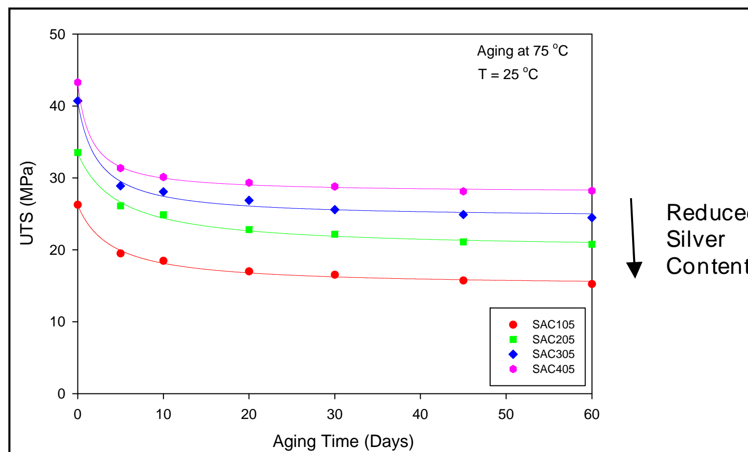

(c) Aging at T = 75 °C

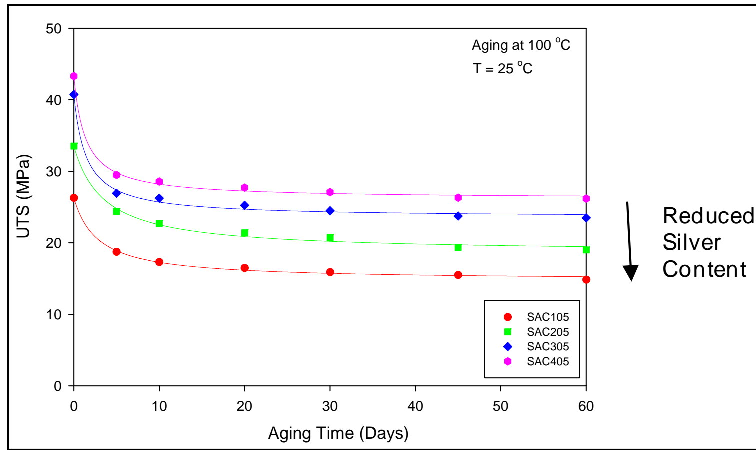

(d) Aging at T = 100 °C

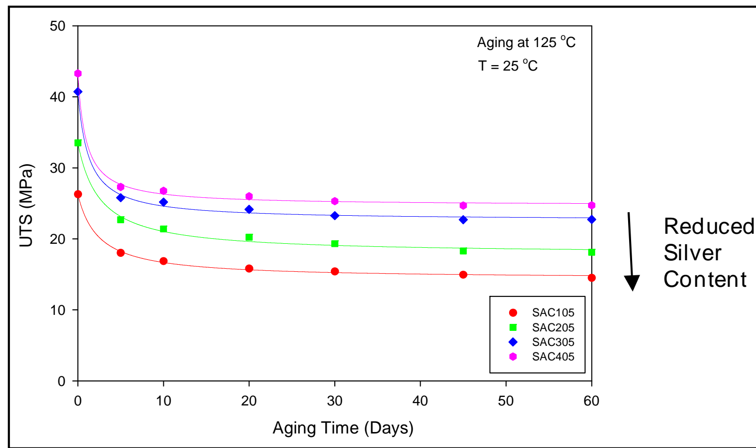

(e) Aging at T = 125 °C

Figure 4.23 Effects of Silver Content on the Evolution of the UTS with Aging

4.6 Microstructure Evolution during Aging

The typical microstructure of the SAC alloys consists of primary dendrites of β-Sn surrounded by a eutectic micro-constituent comprising Ag_3Sn and Cu_6Sn_5 intermetallic particles. Cooling rate and chemical composition are the two major factors in determining the details of the SAC microstructure such as size and distribution of the intermetallic compounds.

In this study, the uniaxial test specimens were first formed in Pyrex glass tubes from liquid solder by using high cooling rate water quenching. Specimens were then recast in a reflow oven and cooled using a prescribed profile with a much lower cooling rate than water quenching. The two different cooling processes, combined with different SAC compositions resulted in significant differences in microstructure. These are shown in Figures 4.24-4.27 for the SAC alloys and in Figure 4.28 for eutectic 63Sn-37Pb.

It can be seen that after quenching, IMC particles are extremely fine and evenly distributed across the β-Sn matrix in all SAC solders. Primary β-Sn dendrites are also very small in size. However, after slower cooling in the reflow oven, IMC particles become much coarser and appear in conglomerates around the β-Sn dendrites.

The chemical composition or Ag content (all SAC alloys had a constant Cu content of 0.5 wt.% in this study) was found to have great effects on the IMC dispersion and Sn dendrite size. The majority of the second phase particles in the SAC alloys are Ag_3Sn IMCs due to the low Cu content. With increase in Ag content, the proportion of the eutectic micro-constituents in relation to the primary β-Sn phase increases, and causes changes in the microstructure. For example, in SAC105 as shown in Figure 4.24(b), large primary β-Sn dendrites exist with a small amount of eutectic present in the intergranular region. In contrast, a rather continuous network around small β-Sn grains was formed by the eutectic micro-constituent in SAC405 as shown in Figure 4.27(b). Generally speaking, higher Ag content SAC alloys have finely dispersed IMCs and fine primary β-Sn dendrites, which results in higher mechanical strength.

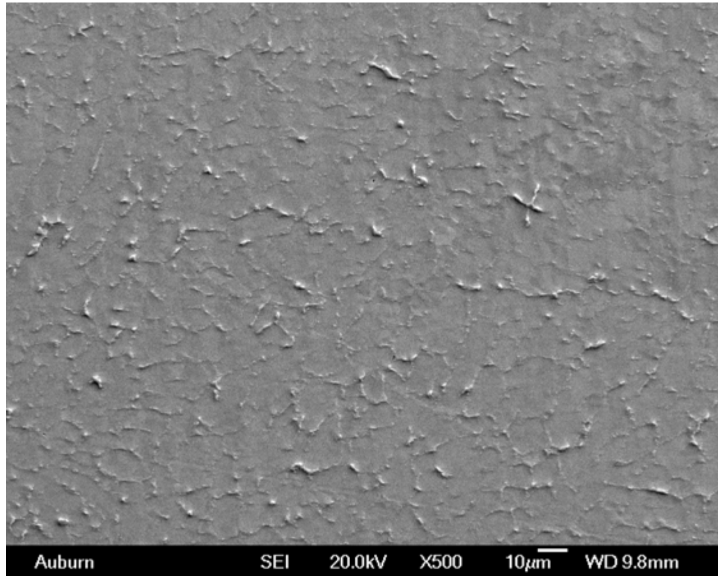

(a) Water Quenched

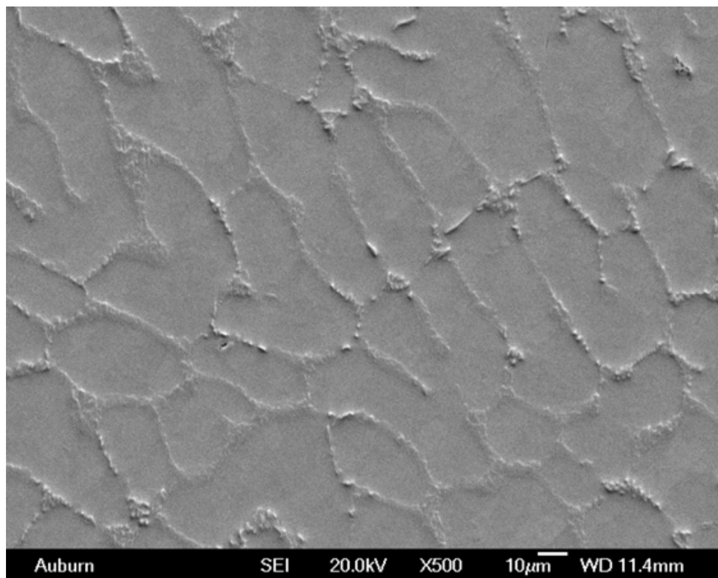

(b) Reflowed (Controlled Cooling)

Figure 4.24 Microstructure of SAC105 Test Specimens (SEM)

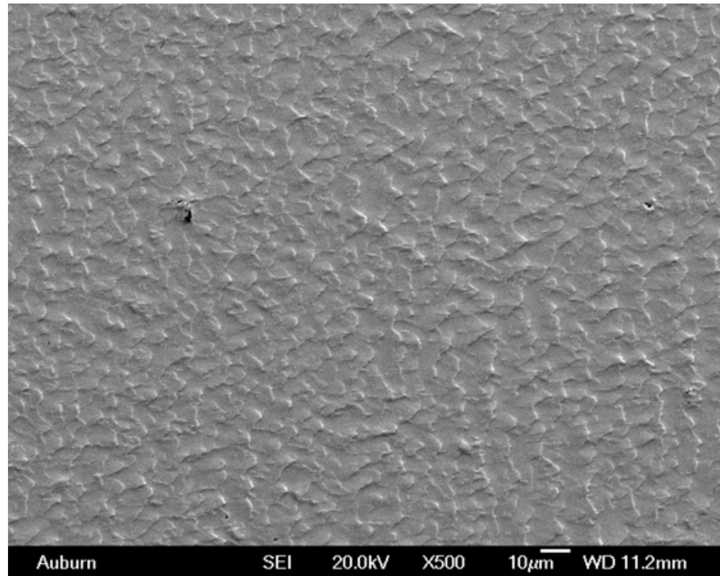

(a) Water Quenched

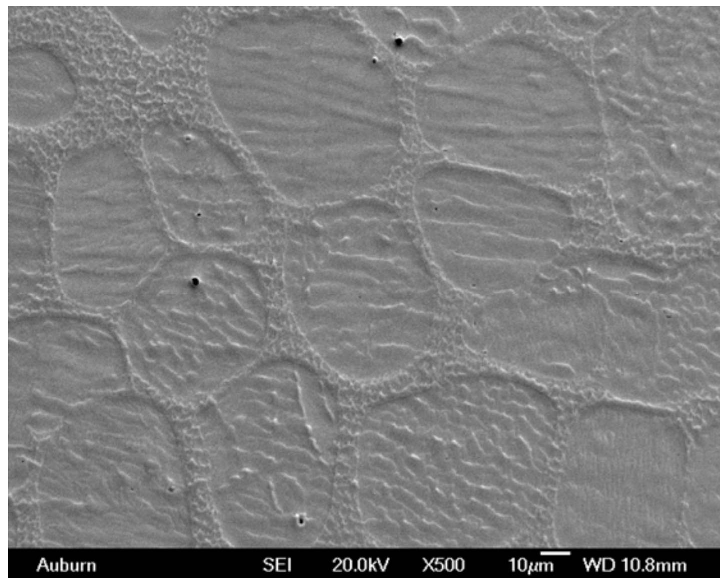

(b) Reflowed (Controlled Cooling)

Figure 4.25 Microstructure of SAC205 Test Specimens (SEM)

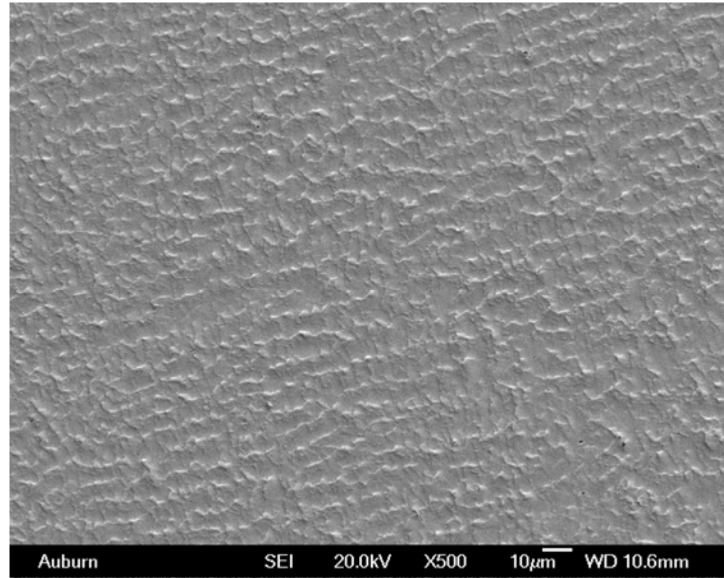

(a) Water Quenched

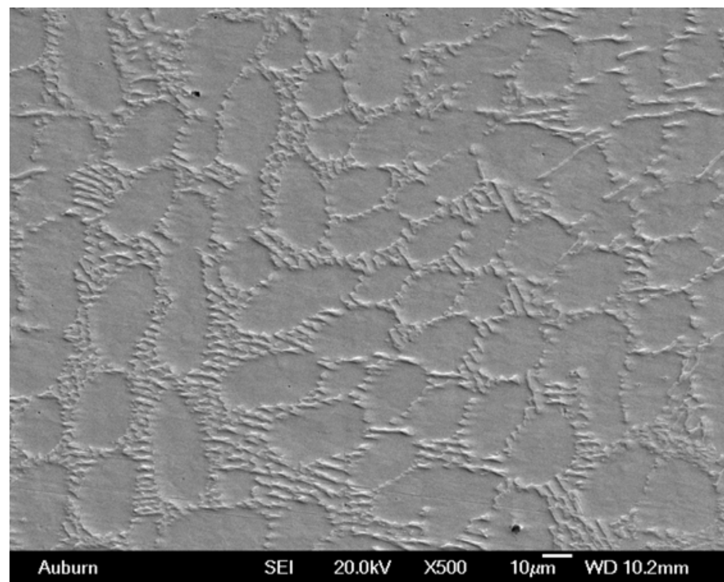

(b) Reflowed (Controlled Cooling)

Figure 4.26 Microstructure of SAC305 Test Specimens (SEM)

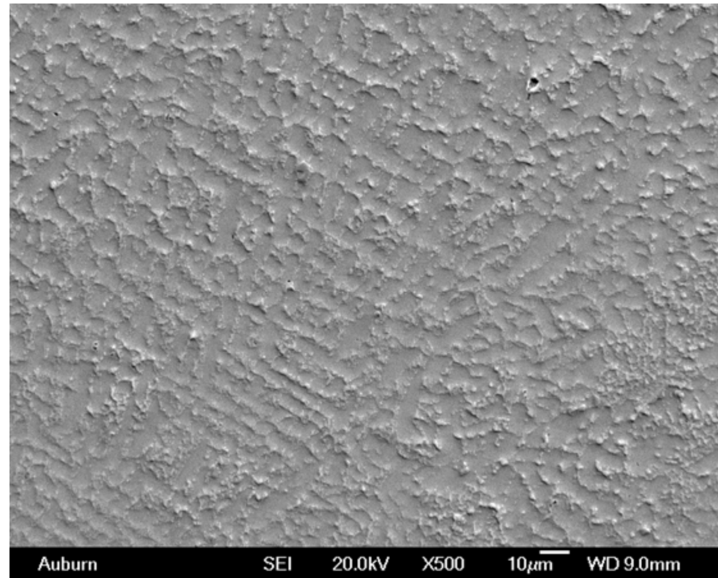

(a) Water Quenched

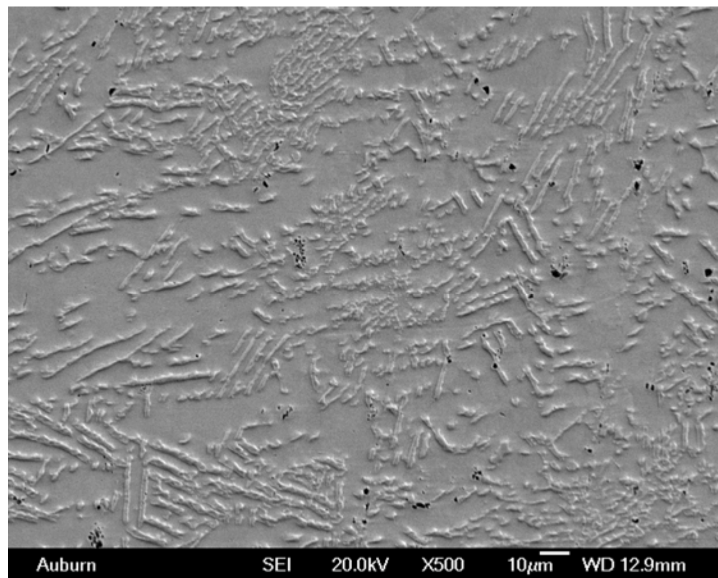

(b) Reflowed (Controlled Cooling)

Figure 4.27 Microstructure of SAC405 Test Specimens (SEM)

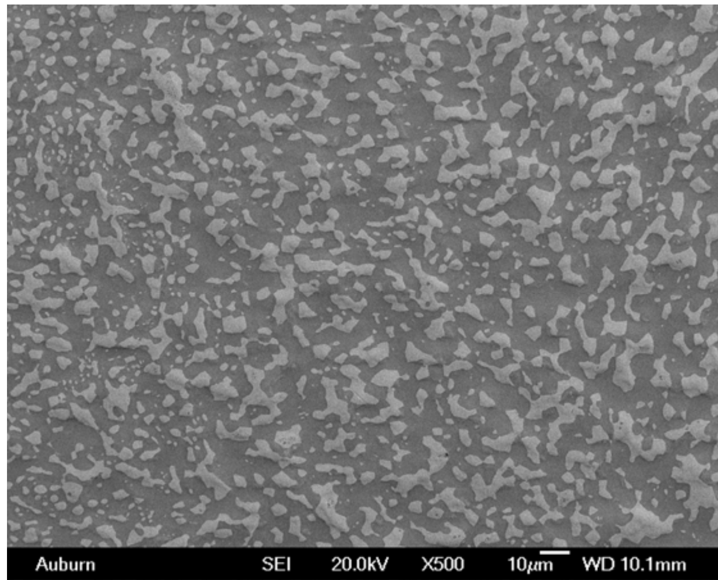

(a) Water Quenched

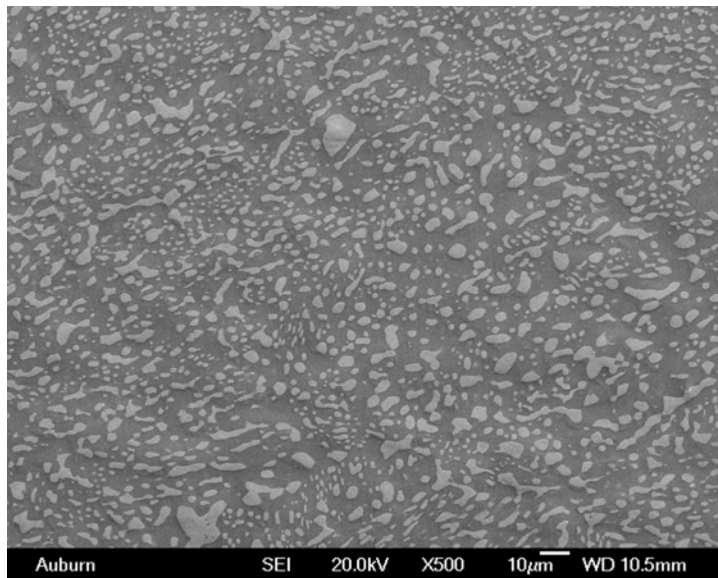

(b) Reflowed (Controlled Cooling)

Figure 4.28 Microstructure of 63Sn-37Pb Test Specimens (SEM)

The microstructure of 63Sn-37Pb in as-water quenched and as-reflowed states are shown in Figures 4.28 (a) and (b). Compared to SAC alloys, there seems to be an opposite mechanism governing the formation of the microstructure. A relatively coarse phase structure was formed in the water quenched specimens after solidification, whereas finer structure was observed in the reflowed specimens. Thus, the extremely fast cooling rate led to a coarser microstructure for 63Sn-37Pb solder. Again, The mechanical behavior corresponded with the microstructure, and coarser microstructure led to lower mechanical properties. Ma [227] observed similar results. He studied the mechanical properties of 63Sn-37Pb with both water quenched and reflowed specimens, and found that the reflowed specimens had superior tensile properties.

Related results were reported by other researchers. Mei [228] and Conrad [229] showed decreased shear strength with increasing cooling rate in their study of 63Sn-37Pb solder joints. They stated that higher cooling rate would yield more refined microstructure but not better mechanical properties for 63Sn-37Pb. They claimed that fine microstructure was more conducive for grain boundary sliding due to the small grain size and increased grain boundary area, so that quickly cooled specimens exhibited lower strength than slow-cooled specimens. This is in stark contrast to SAC solders, in which the interaction of dislocations with Ag_3Sn particles is the dominant deformation mechanism.

After reflow, solder specimens were kept in ovens preset at different temperatures (as listed in Table 4.1) and were subjected to isothermal aging for up to 6 months. Microstructure analysis was conducted after various durations of aging for each solder alloy, in order to keep track of the growth of β-Sn dendrites and evolution of the IMC morphology.

Optical micrographs of SAC105 and SAC405 samples after 6-months of aging at both room temperature (25 °C) and elevated temperature (125 °C) are shown in Figures 4.29 and 4.30. Pictures of as-reflowed specimens (no aging) are also shown in the figures, and were used as baseline references for characterizing aging effects on the solder microstructures.

The basic microstructure of the SAC alloys after reflow consists of β-Sn dendrites and eutectic micro-constituents. SAC405 has smaller IMCs and finer β-Sn dendrites than SAC105 due to its higher Ag content. As aging took place, the microstructure of both alloys started to evolve: the IMC particles conglomerated and grew coarser, and the β-Sn dendrites grew larger with increased aging. After 6 months, the morphology of IMCs changed considerably, especially for alloys aged at high temperature. By carefully examining the images, it was possible to characterize this change in a quantitative way. The number and the average size of IMC particles in the micrographs in Figures 4.29 and 4.30 are shown in Tables 4.5 and 4.6, respectively. Fewer and bigger IMCs are found in the samples subjected to high temperature aging, and this trend was more significant for SAC105. These results agree with the study of Fouassier, et al. on SAC387 [110]. The microstructure evolution of 63Sn-37Pb during aging is shown in Figure 4.31. Notably, the coarsening is more severe for 63Sn-37Pb, even though the mechanical property changes are smaller. The same observation on the microstructure has been made by Allen, et al. [122] and Reinikainen, et al. [123].

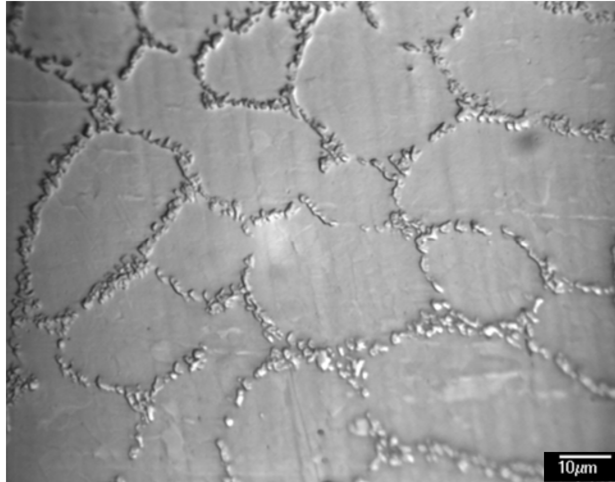

(a) As-reflowed Condition (No Aging)

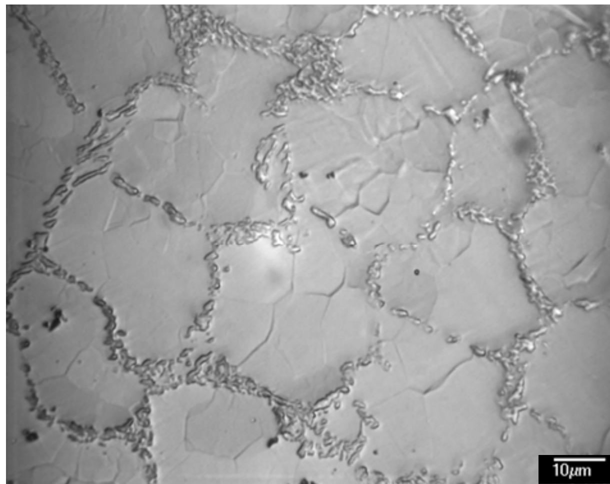

(b) 6-months Aging at 25 °C

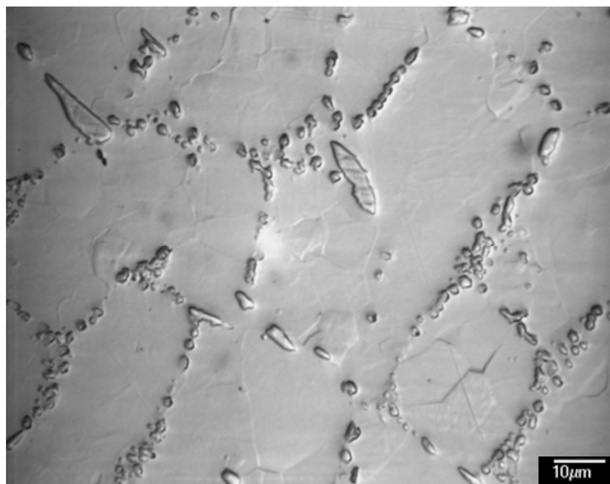

(c) 6-months Aging at 125 °C

Figure 4.29 Microstructure Evolution of SAC105 Microstructure during Aging

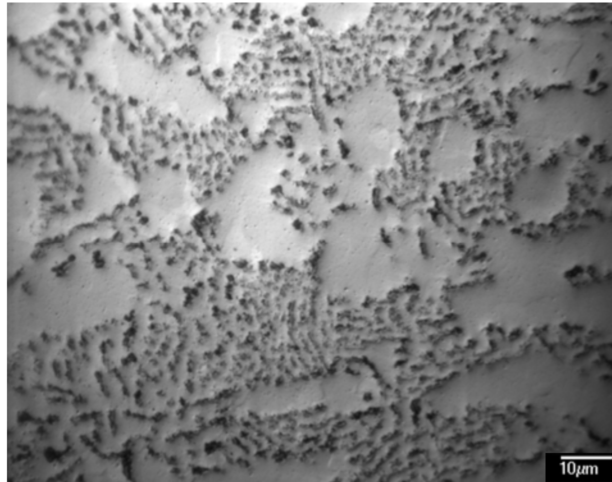

(a) As-reflowed Condition (No Aging)

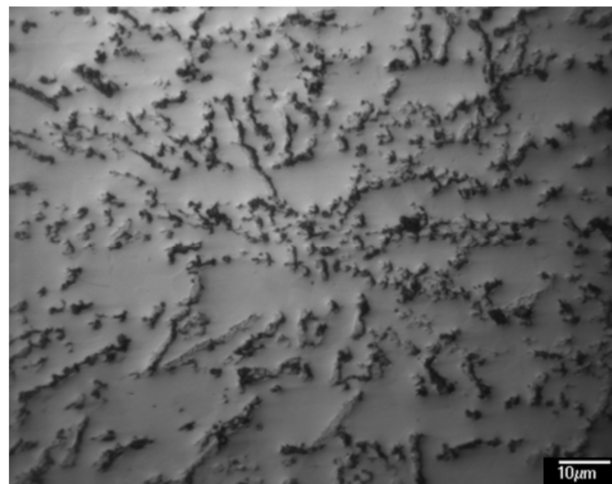

(b) 6-months Aging at 25 °C

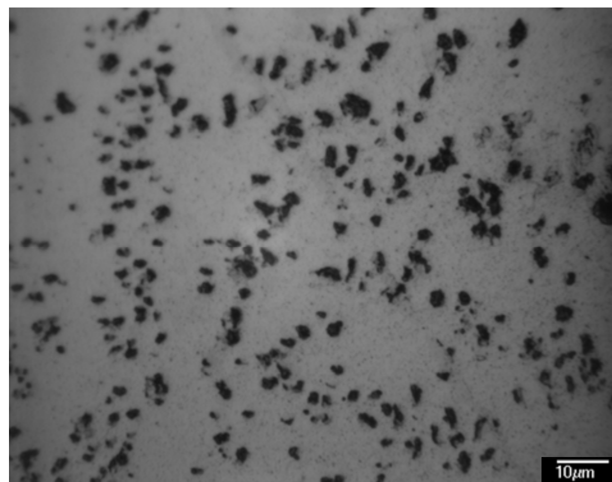

(c) 6-months Aging at 125 °C

Figure 4.30 Microstructure Evolution of SAC405 Microstructure during Aging

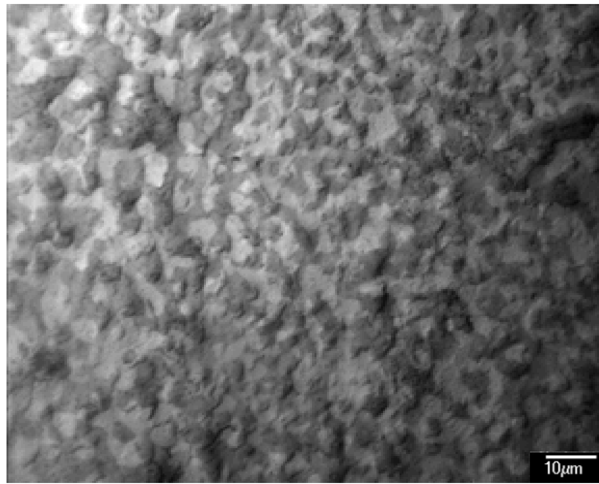

(a) As-reflowed Condition (No Aging)

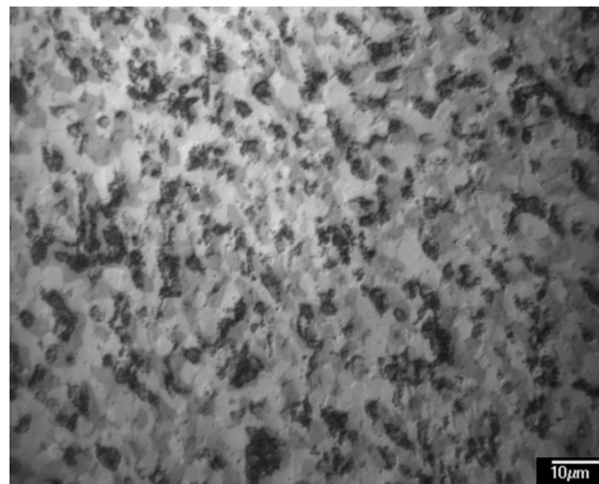

(b) 6-months Aging at 25 °C

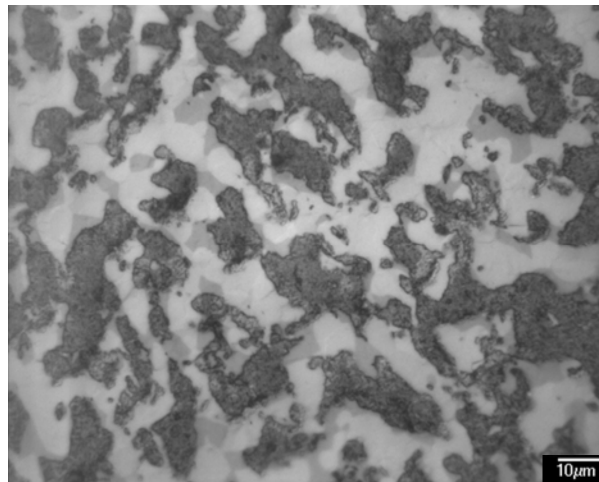

(c) 6-months Aging at 125 °C

Figure 4.31 Microstructure Evolution of 63Sn-37Pb during Aging

Table 4.5 Quantitative Analysis of IMCs in SAC105

	Number of particles	Averaged particle size (μm)
As reflowed condition	373	2.1
25 °C aging (6 months)	306	2.3
125 °C aging (6 months)	167	3.4

Table 4.6 Quantitative Analysis of IMCs in SAC405

	Number of particles	Averaged particle size (μm)
As reflowed condition	528	1.3
25 °C aging (6 months)	442	1.9
125 °C aging (6 months)	319	2.7

4.7 Fractography Analysis of Failed Specimens

Fracture surfaces of the failed tensile specimens were observed using the SEM in order to understand the aging effects on the failure mode of the solder alloys. Images of the failure surfaces for non-aged specimens are shown in Figure 4.32. All solder alloys exhibited typical ductile fracture characteristics. Dimples can be found across the fractured area indicating a transgranular failure mode. Transitions in the failure mode were seen to occur if the specimens were aged prior to testing. Fracture surfaces of failed specimens tested after 60-days aging at room temperature (25 °C) and elevated temperature (100 °C) are shown in Figures 4.33 and 4.34, respectively. With aging, there was a transition from transgranular to intergranular failure (ductile fracture to brittle fracture) in the SAC alloys. This trend was more evident in the SAC alloys with less silver content, or for higher aging temperatures. In contrast, the 63Sn-37Pb specimens showed consistent failure surfaces for all aging conditions. The dimples present in Figures 4.33(e) and 4.34(e) indicated good ductility regardless of aging condition.

4.8 Summary and Conclusions

In this chapter, aging effects on mechanical properties of SAC solder alloys were examined by performing tensile tests with a full test matrix of aging times, aging temperatures and solder alloys. There were 4 SAC alloys with different Ag content and constant Cu content under investigation. Test specimens were preconditioned with isothermal aging for up to 60 days at various temperatures after reflow. Aged specimens were then tested on an MT-200 testing system. For every specific aging condition, i.e. a specific combination of aging time and temperature, 10 specimens were tested and the obtained raw stress-strain data were fitted by

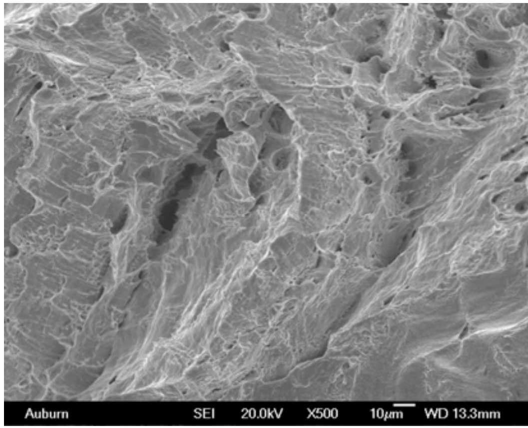

(a) SAC105

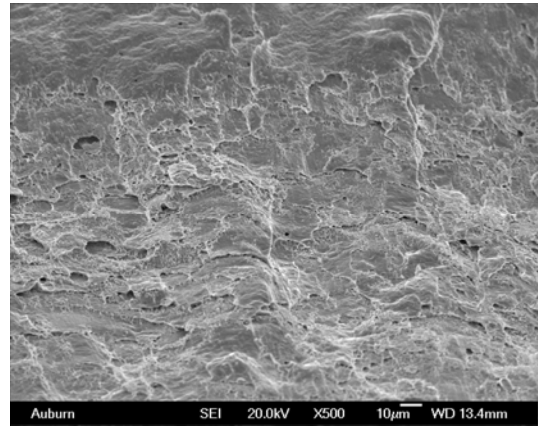

(b) SAC205

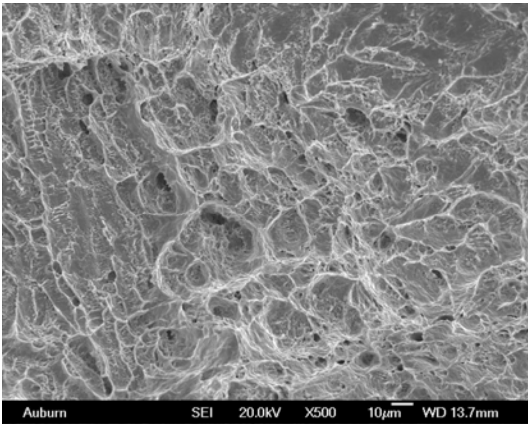

(c) SAC305

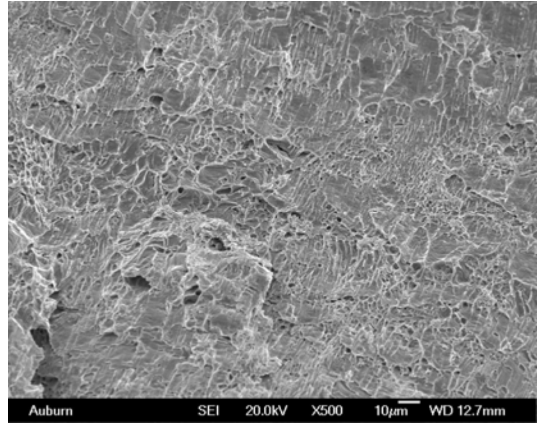

(d) SAC405

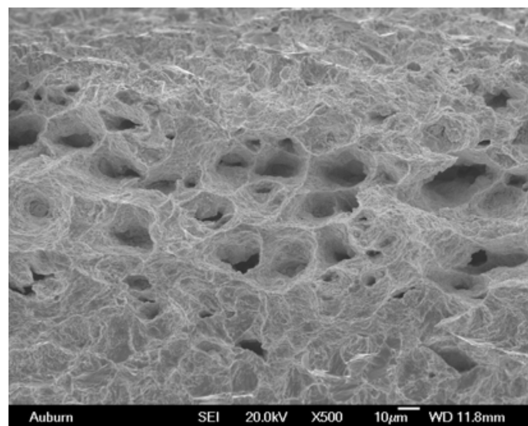

(e) 63Sn-37Pb

Figure 4.32 Fracture Surfaces of the Failed Specimens (No Aging)

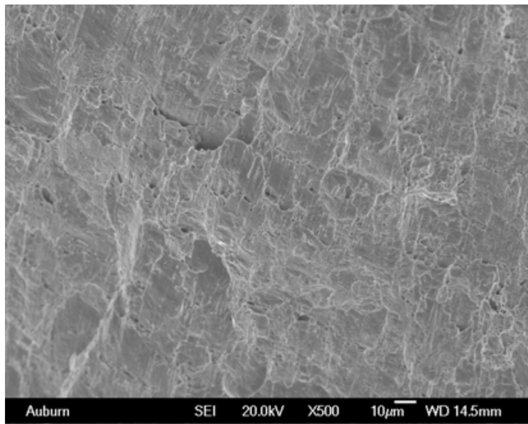

(a) SAC105

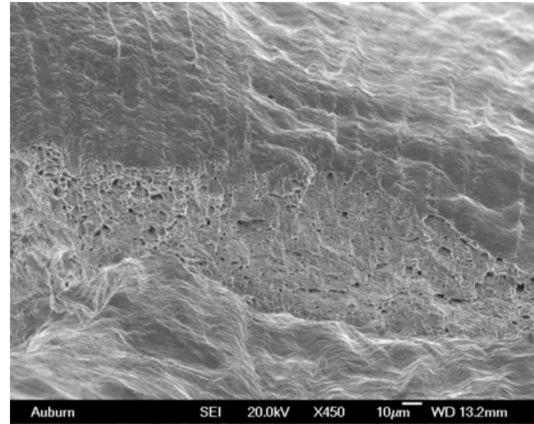

(b) SAC205

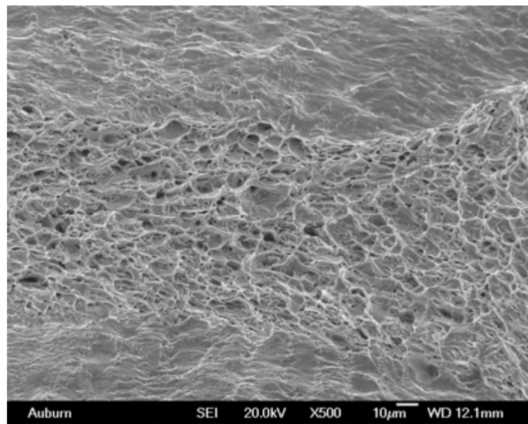

(c) SAC305

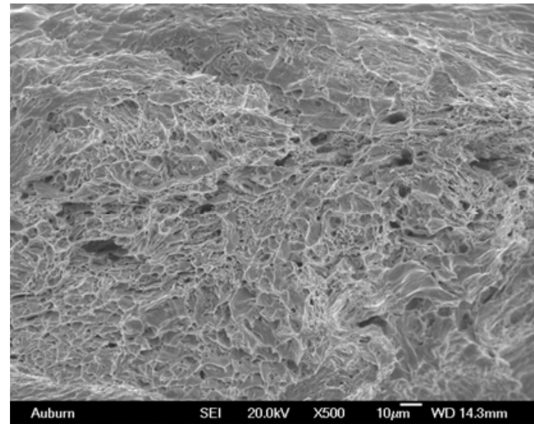

(d) SAC405

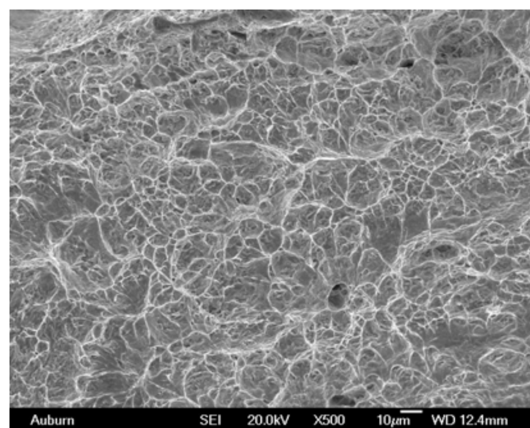

(e) 63Sn-37Pb

Figure 4.33 Fracture Surfaces of the Failed Specimens (60-days Aging at R.T.)

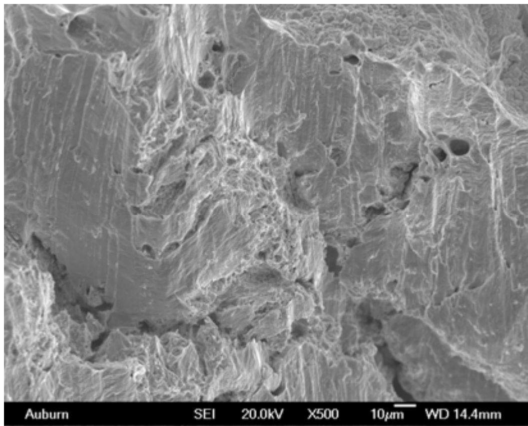

(a) SAC105

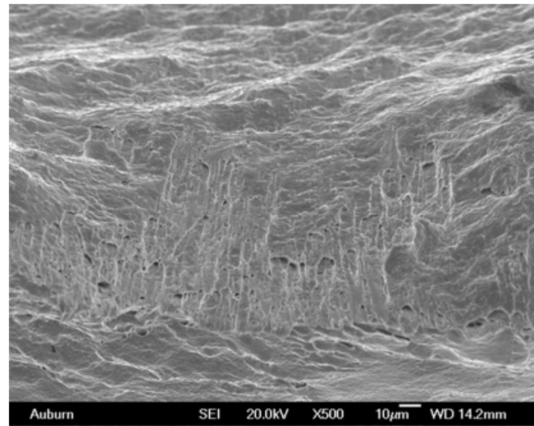

(b) SAC205

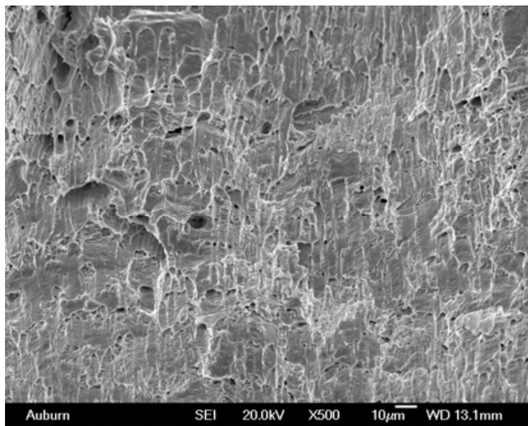

(c) SAC305

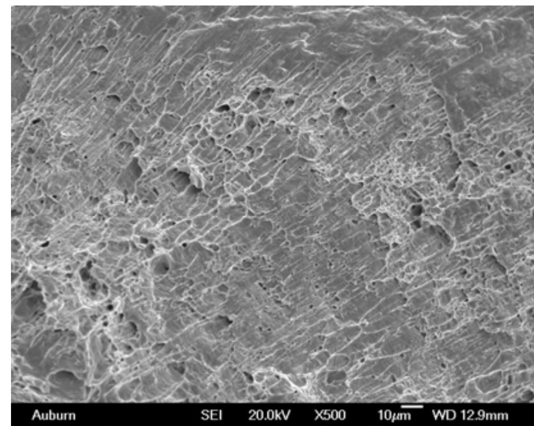

(d) SAC405

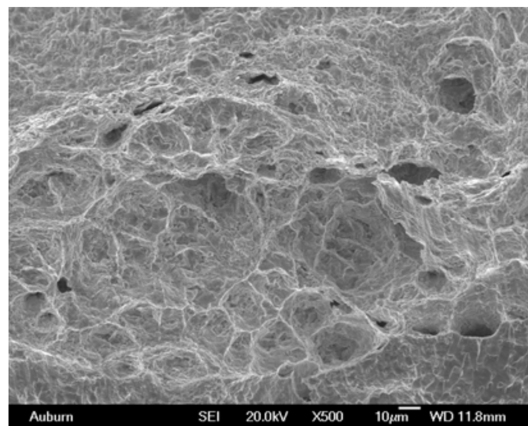

(e) 63Sn-37Pb

Figure 4.34 Fracture Surfaces of the Failed Specimens (60-days Aging at 100 °C)

using a two-function empirical model. The mechanical properties such as elastic modulus, yield stress, and UTS were then determined from the model fitted curve for each SAC alloy. Furthermore, microstructure evolution of the solder alloys due to aging was studied.

The mechanical properties of SAC alloys decreased with increasing aging time and temperature. High Ag content SAC alloys were found to have better aging resistance. The change of elastic modulus was described by a 3-parameter exponential model (Eq. 4.1) for SAC alloys, but the elastic modulus of 63Sn-37Pb basically remained unchanged across the entire aging matrix. The changes of yield stress and UTS of both SAC and 63Sn-37Pb solders were well fit by a 3-parameter hyperbolic model (Eq. 4.2 and Eq. 4.3). Compared with the SAC alloys, 63Sn-37Pb showed better aging resistance and possessed the highest strength values at the beginning of the aging process.

The aging induced microstructure coarsening is the fundamental reason behind the mechanical property deterioration of solder alloys. According to the Hall-Petch equation mentioned in Chapter 2, increasing grain size and phase structure will lead to reduction in tensile strength, i.e. yield stress and UTS. This is because coarsened dendrites and second phase particles in the SAC alloys will lose their effectiveness in blocking dislocation movement due to fewer grain boundaries and weaker precipitation pinning effects. Also, grain size coarsening can cause decrease in the apparent elastic modulus due to increased creep deformations during the measurements, even though the ideal elastic modulus should be relatively independent of microstructure change. For 63Sn-37Pb, the eutectic structure does not contain any second phases, but it also experienced significant loss in its tensile strength. Besides the increase in phase size, the precipitation of β-Sn out of the supersaturated Pb-rich phases during aging is deemed to be another important reason for the softening of the alloy.

Silver content plays an important role in determining the mechanical properties and microstructure evolution of SAC alloys during aging. For the SAC alloys in this study, the difference in microstructure indicates that the Ag content affects the Ag_3Sn IMC dispersion and β-Sn dendrite size. For high Ag content solder alloys, the microstructure has a finely dispersed IMC and fine β-Sn dendrite size, which helps to suppress the plastic deformation of solder alloy and therefore strengthen the material. In general, higher Ag content alloys have better mechanical properties and less changes in microstructure, or greater aging resistance. However, this does not mean high Ag content is the ultimate solution to all the problems encountered in the application of SAC alloys. Low Ag content renders SAC alloys with improved ductility and lowered elastic modulus. Such solders can dissipate more plastic energy, and reduce the dynamic stress transformed from PCB to IMC/solder interface layer so as to improve solder joint drop performance. This advantage had been reported by several researchers [182, 230].

Fractography analysis of failed SAC specimens showed transition in failure mode (from transgranular to intergranular) during aging. In contrast, the dominant failure mode of 63Sn-37Pb remained transgranular and no transition was found in the failed specimens.

Chapter 5
Effects of Aging on the Creep Behavior of Lead-free SAC Solder Alloys

5.1 Introduction

As discussed in the earlier chapters, aging, in terms of both isothermal and thermal cycling, has dramatic effects on the constitutive and failure behavior of solder materials and solder joint interfaces. Also, the acknowledged large discrepancies in the currently available database of measured solder mechanical properties are further exacerbated by thermal aging since the microstructure and material behavior of the specimens used in any single investigation are moving targets that are evolving rapidly even at room temperature. Therefore, the effects of thermal aging on material behavior of solder alloys must be thoroughly understood so that more accurate viscoplastic constitutive models can be developed for solder joint reliability predictions.

In this chapter, aging effects on SAC solder creep behavior were examined by performing creep tests with a full test matrix of aging times, aging temperatures and solder alloys. 63Sn-37Pb was also tested for comparison purpose. Secondary creep strain rate data were obtained from the creep test results, and an empirical exponential model was developed to fit the data points for each alloy and aging temperature.

5.2 Aging Effects on Creep Response of SAC Solder Alloys

Uniaxial specimens were formed for standard SAC solder alloys (SAC105, SAC205, SAC305, and SAC405) using the casting method and controlled reflow cooling profile described in Chapter 3. After solidification, the samples were subjected to up to six months of aging at five different aging temperatures (T = 25, 50, 75, 100, and 125 °C). Specimens for each alloy were

prepared in sets of five. Each set was then subjected to a specific set of aging conditions (aging temperature + aging time). The test matrix defined by aging temperatures and aging times for the creep experiments is listed in Table 5.1. All creep tests were conducted at room temperature (25 °C) and a constant stress level of σ = 15 MPa.

Figures 5.1-5.4 illustrate the recorded creep curves for the SAC105, SAC205, SAC305, and SAC405 solder alloys. In each figure, there are five graphs for the five different aging temperatures. In each graph, the various creep curves are for different aging times, illustrating the evolution of the creep response with duration of aging. For the brevity and clarity of representation, only one of the five available creep curves is shown in each plot for each set of aging conditions. Analogous experiments were also performed with reflowed 63Sn-37Pb eutectic solder specimens for comparison purposes (shown in Figure 5.5).

Table 5.1 Aging Matrix for Creep Tests of SAC Alloys

	Aging Temperature				
Aging Time (months)	**25 °C (RT)**	**50 °C**	**75 °C**	**100 °C**	**125 °C**
0	X	X	X	X	X
0.5	X	X	X	X	X
1	X	X	X	X	X
2	X	X	X	X	X
3	X	X	X	X	X
4	X	X	X	X	X
5	X	X	X	X	X
6	X	X	X	X	X

X: Test Finished, Testing Temperature = 25 °C (R.T.), Stress Level = 15 MPa

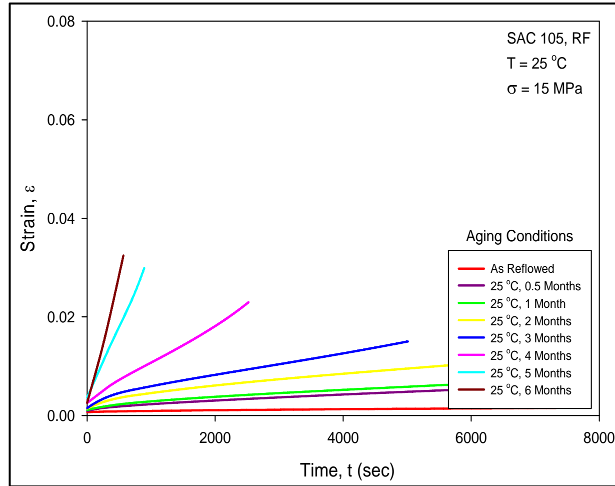

(a) Aging at T = 25 °C

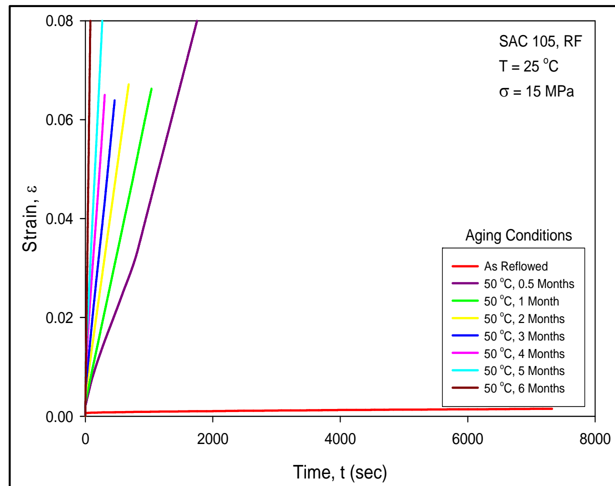

(b) Aging at T = 50 °C

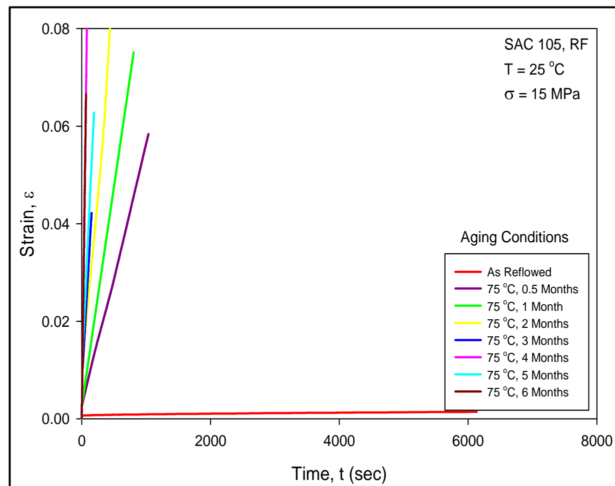

(c) Aging at T = 75 °C

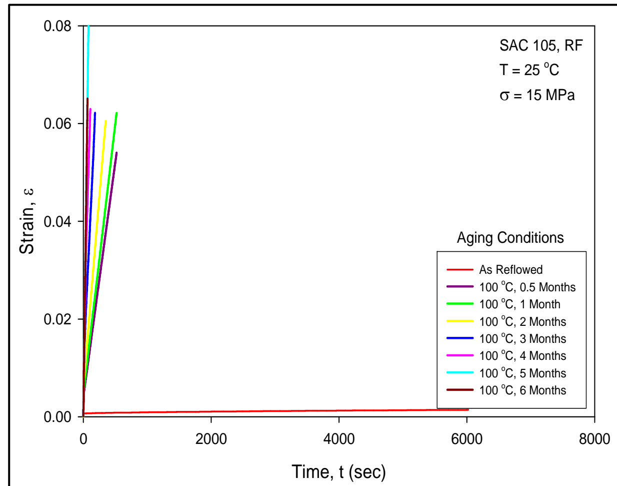

(d) Aging at T = 100 °C

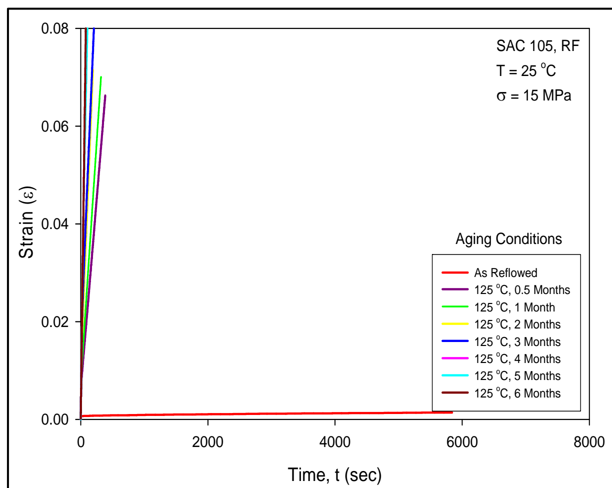

(e) Aging at T = 125 °C

Figure 5.1 Creep Curves for SAC105 Aged for 0-6 Months

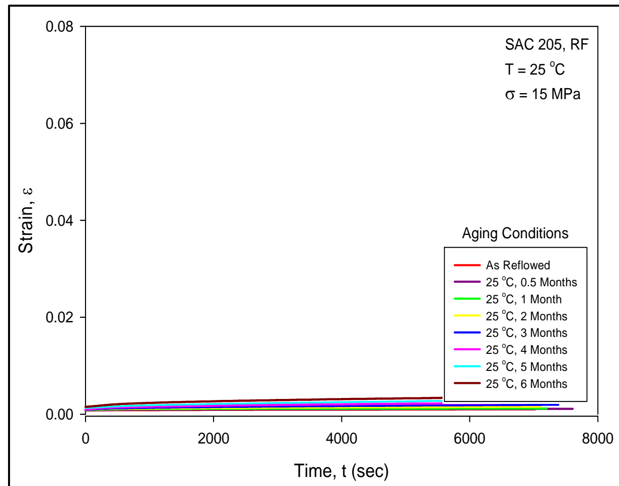

(a) Aging at T = 25 °C

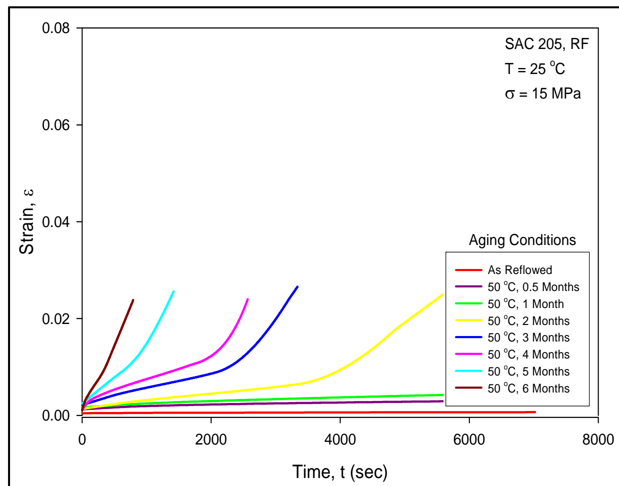

(b) Aging at T = 50 °C

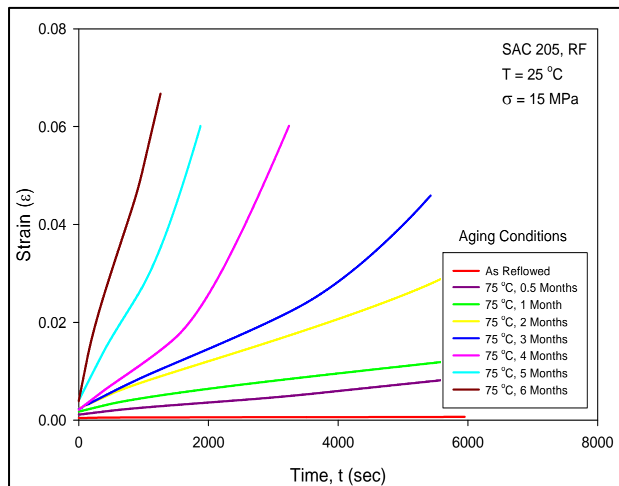

(c) Aging at T = 75 °C

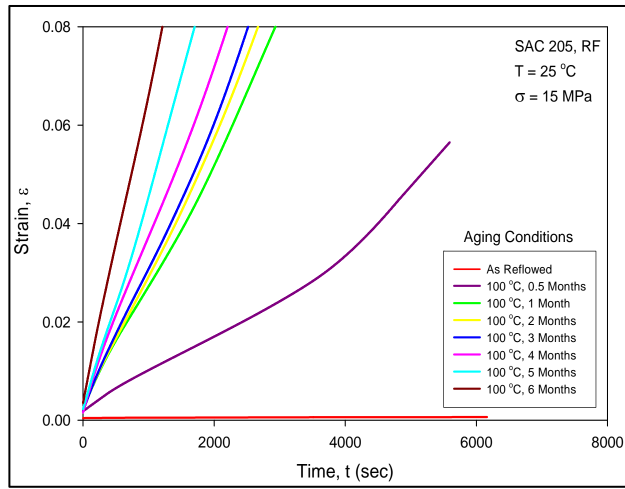

(d) Aging at T = 100 °C

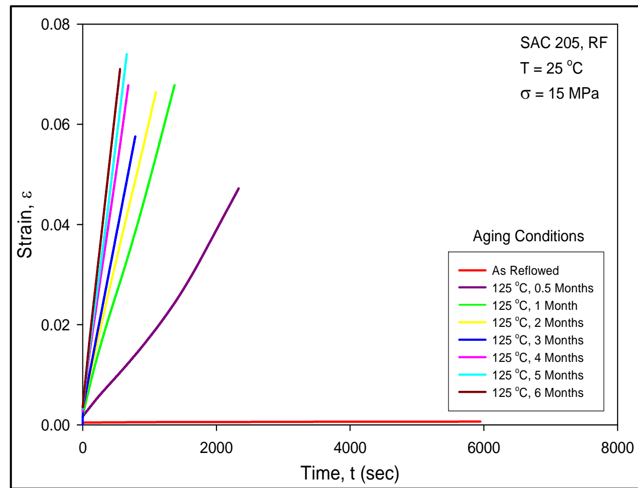

(e) Aging at T = 125 °C

Figure 5.2 Creep Curves for SAC205 Aged for 0-6 Months

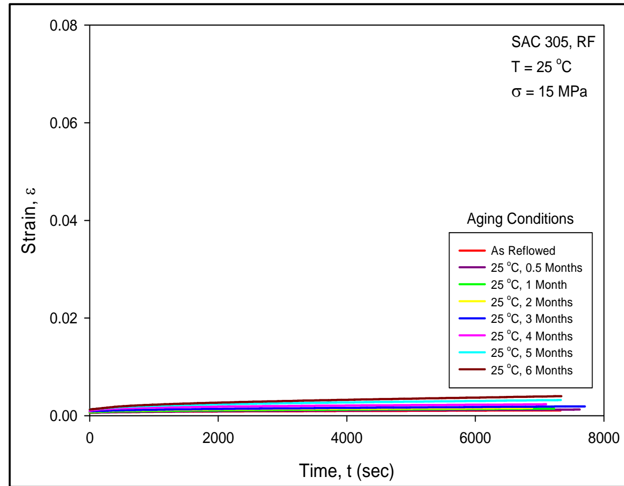

(a) Aging at T = 25 °C

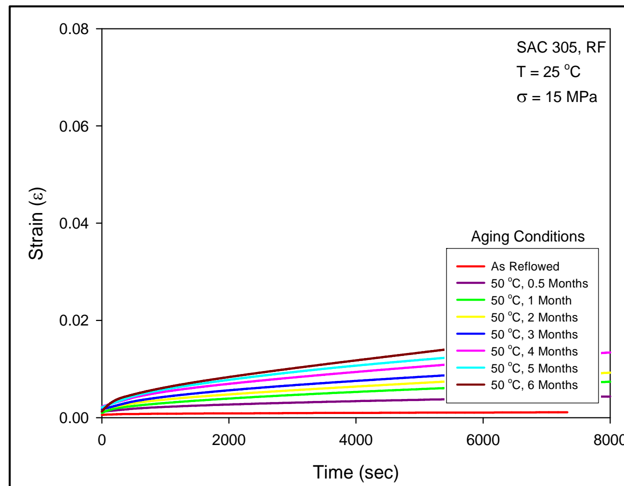

(b) Aging at T = 50 °C

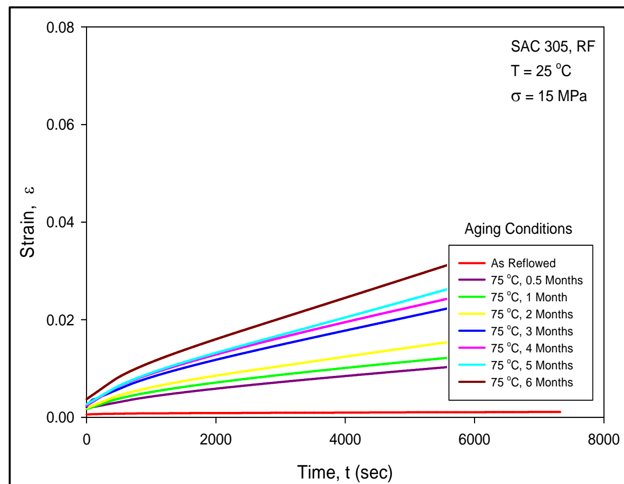

(c) Aging at T = 75 °C

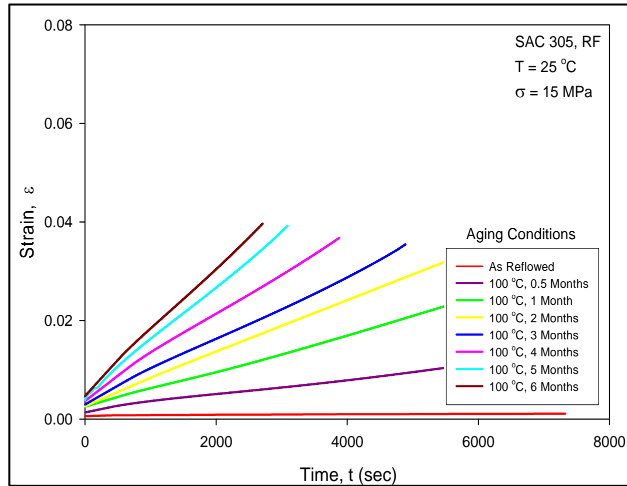

(d) Aging at T = 100 °C

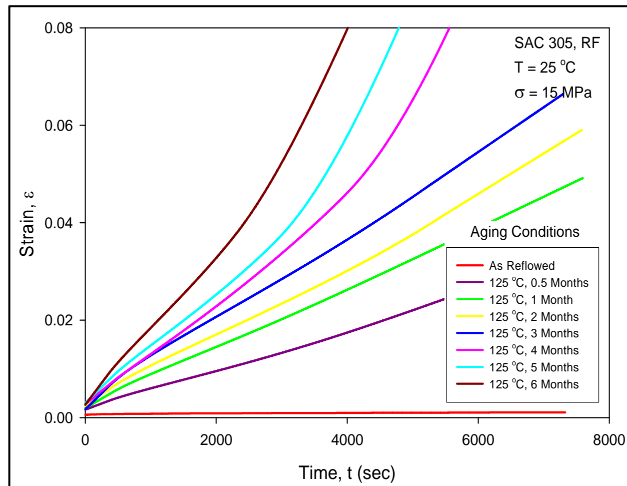

(e) Aging at T = 125 °C

Figure 5.3 Creep Curves for SAC305 Aged for 0-6 Months

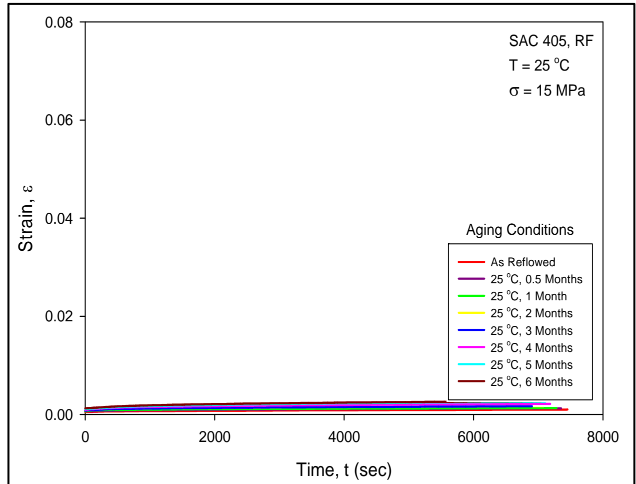

(a) Aging at T = 25 °C

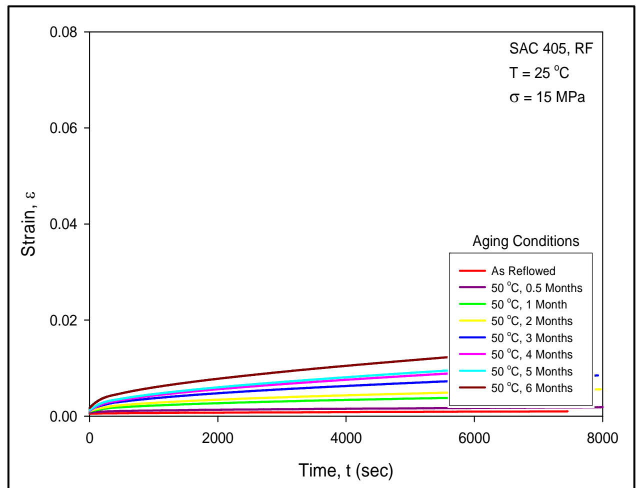

(b) Aging at T = 50 °C

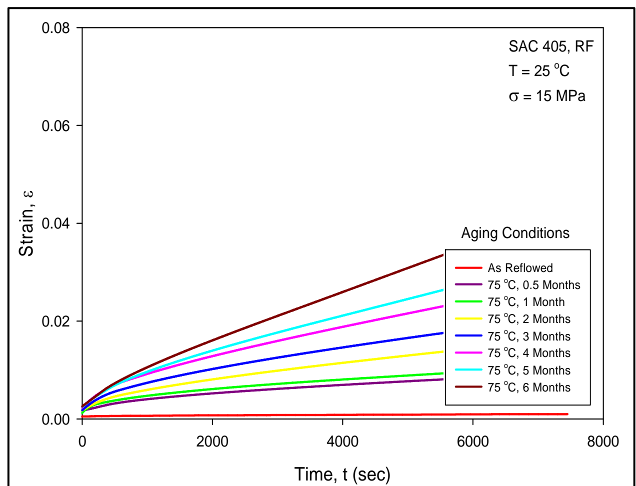

(c) Aging at T = 75 °C

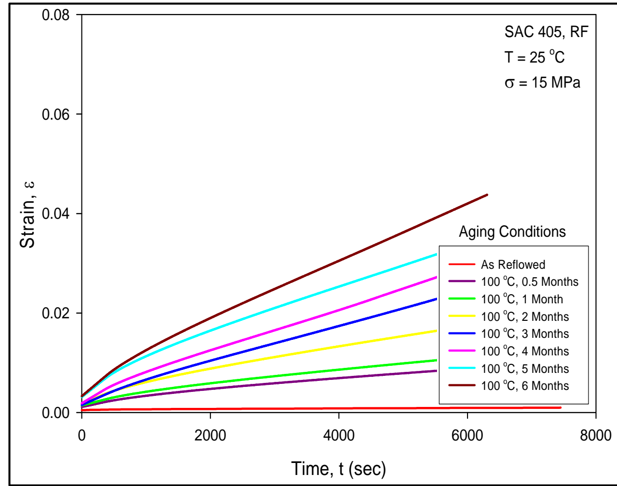

(d) Aging at T = 100 °C

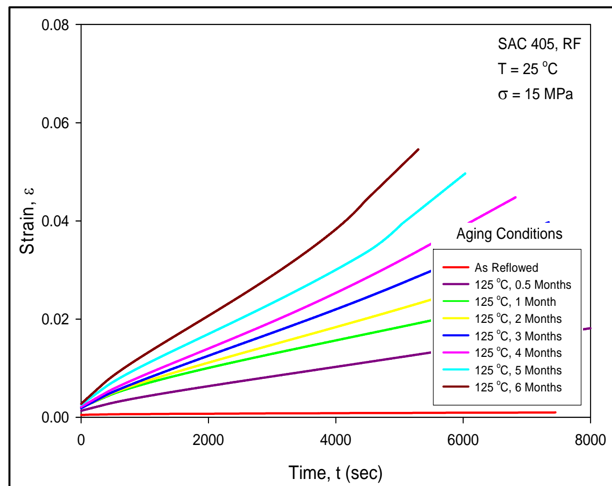

(e) Aging at T = 125 °C

Figure 5.4 Creep Curves for SAC405 Aged for 0-6 Months

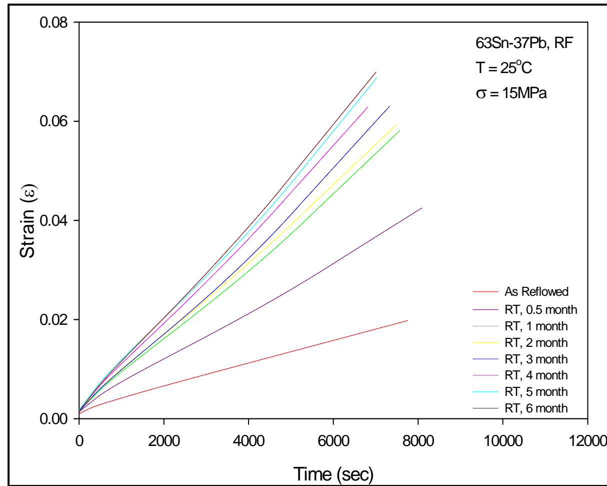

(a) Aging at T = 25 °C

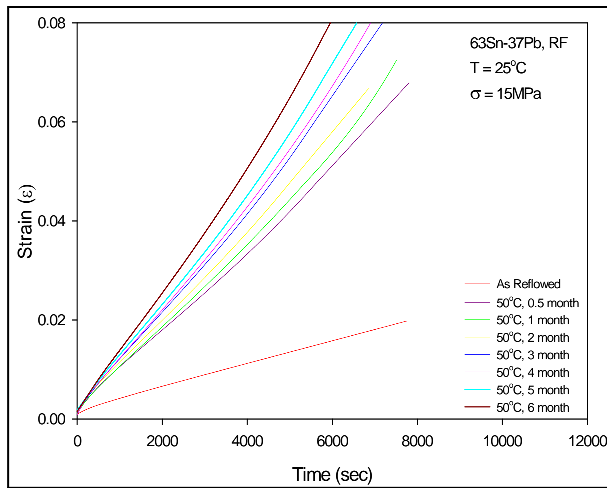

(b) Aging at T = 50 °C

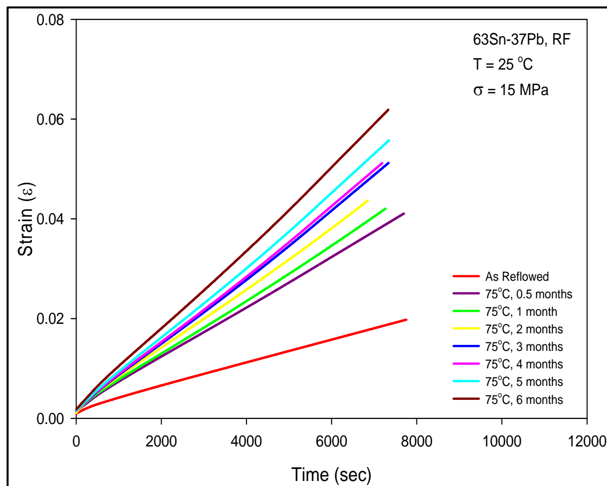

(c) Aging at T = 75 °C

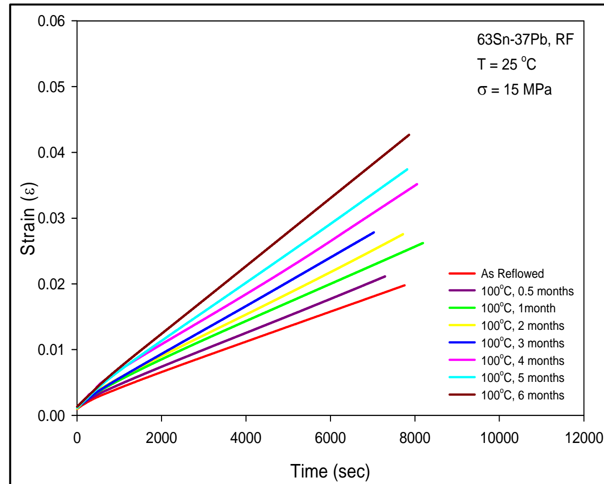

(d) Aging at T = 100 °C

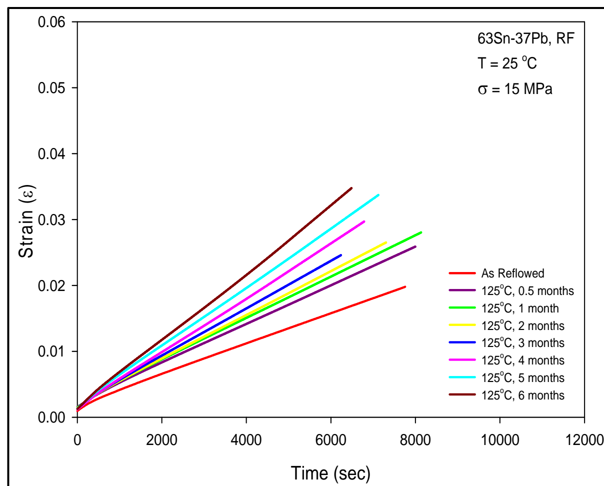

(e) Aging at T = 125 °C

Figure 5.5 Creep Curves for 63Sn-37Pb Aged for 0-6 Months

5.3 Creep Strain Rate Evolution and Modeling with Aging

The effects of aging on solder creep behavior were explored by extracting the secondary creep rates from the raw experimental creep data. The evolution of the creep strain rate with aging was then studied and modeled. An empirical mathematical model was established to perform this function:

$$\dot{\varepsilon} = e^{C_0 + C_1 t + C_2 (1 - e^{-C_3 t})} \tag{5.1}$$

or

$$\log \dot{\varepsilon} = C_0 + C_1 t + C_2 (1 - e^{-C_3 t}) \tag{5.2}$$

where $\dot{\varepsilon}$ is the averaged secondary creep strain rate; t is aging time; and C_0, C_1, C_2 and C_3 are temperature dependent fitting constants.

Figure 5.6 shows an example of the application of the model in Eq. (5.2) to a set of solder aging data, and the significance of the four constants can be visualized. In this graph, each green dot represents the averaged secondary creep strain rate at one specific aging time. Totally, there are 8 data points according to the test matrix in Table 5.1, and they were fitted using the empirical model in Eq. 5.2. Constant C_0 is the intercept of the curve with the vertical log-scale axis on the graph, and therefore is the secondary creep strain rate for no aging. Constant C_1 is the slope of the linear portion on the curve for long aging times. The last two constants C_2 and C_3 jointly govern the position and shape of the transitional region on the curve. Constant C_2 determines the rise of the creep rate during the initial period of aging, before it enters the constant slope region. The values of the four constants are tabulated in Appendix II.

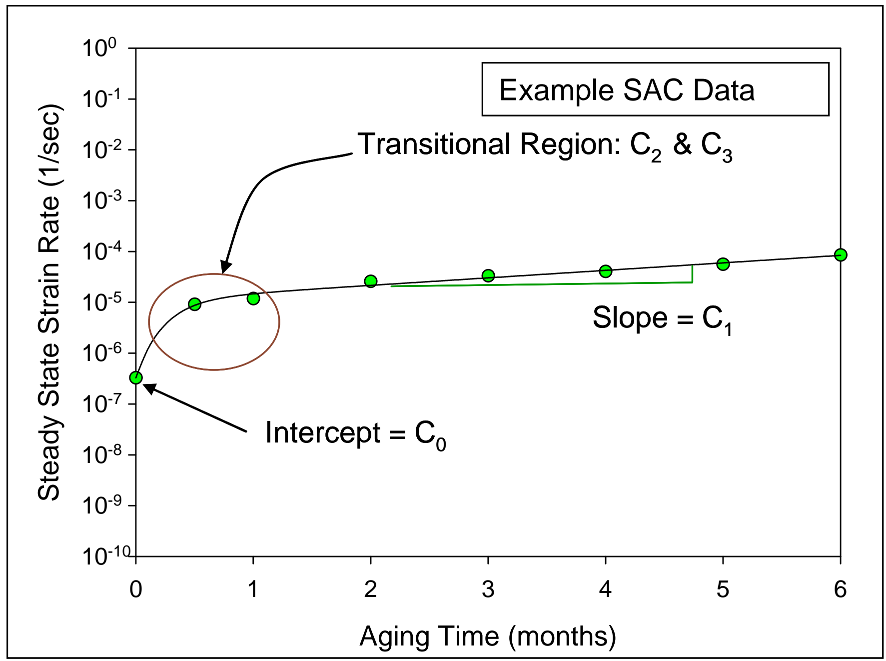

Figure 5.6 Empirical Model for the Creep Strain Rate Evolution

The strain rate evolution data for the various solder alloys are shown in Figures 5.7- 5.11. In each plot, the creep rate variation is illustrated for each of the five aging temperatures. Each data point represents the average creep strain rate measured for the 5 specimens tested at a given set of aging conditions. For each alloy and aging temperature, the data points were fitted with the empirical model in Eq. (5.2), and the model was able to represent the data accurately.

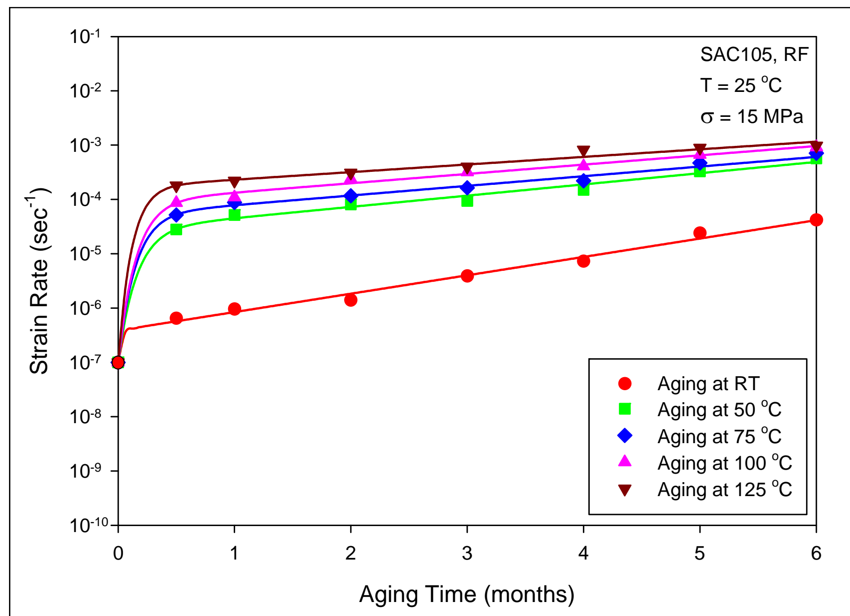

Figure 5.7 Evolution of the Creep Strain Rate with Aging (SAC105)
(Aging at 25, 50, 75, 100 125 °C)

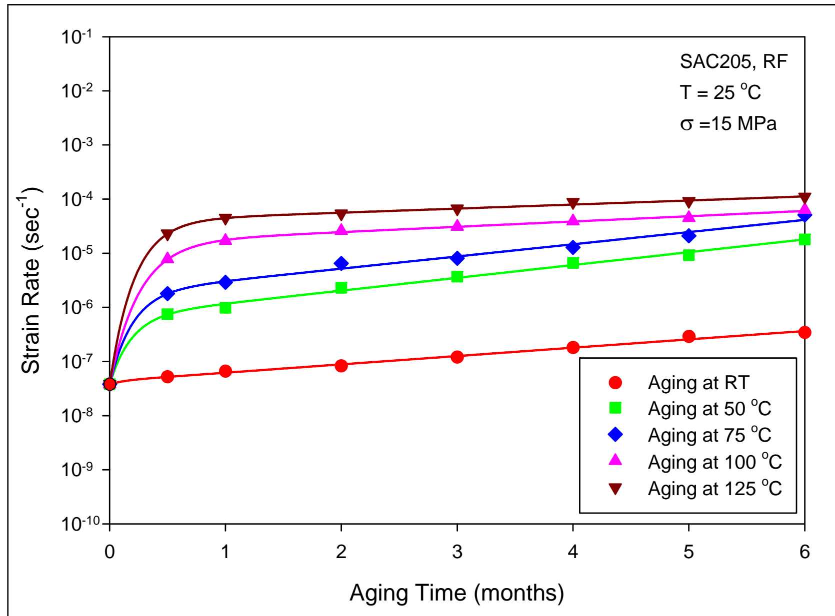

Figure 5.8 Evolution of the Creep Strain Rate with Aging (SAC205)
(Aging at 25, 50, 75, 100 125 °C)

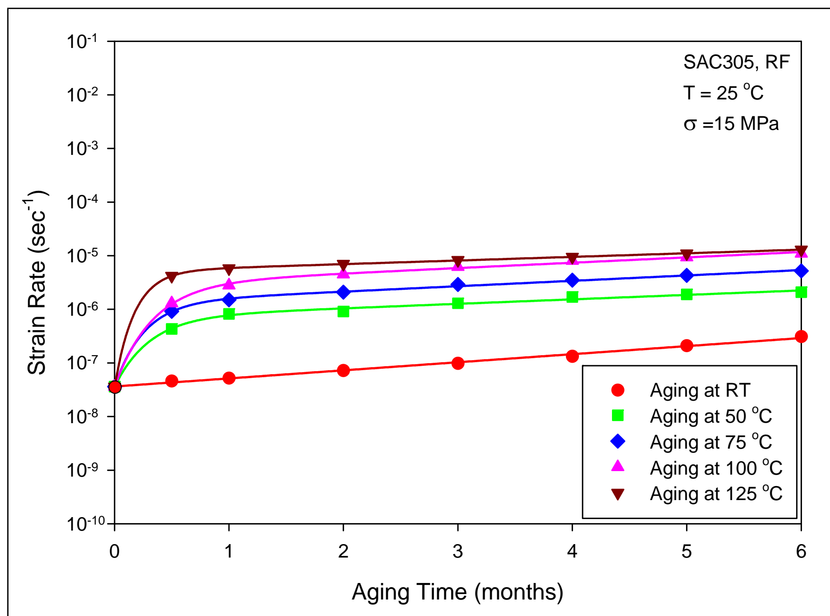

Figure 5.9 Evolution of the Creep Strain Rate with Aging (SAC305)
(Aging at 25, 50, 75, 100 125 °C)

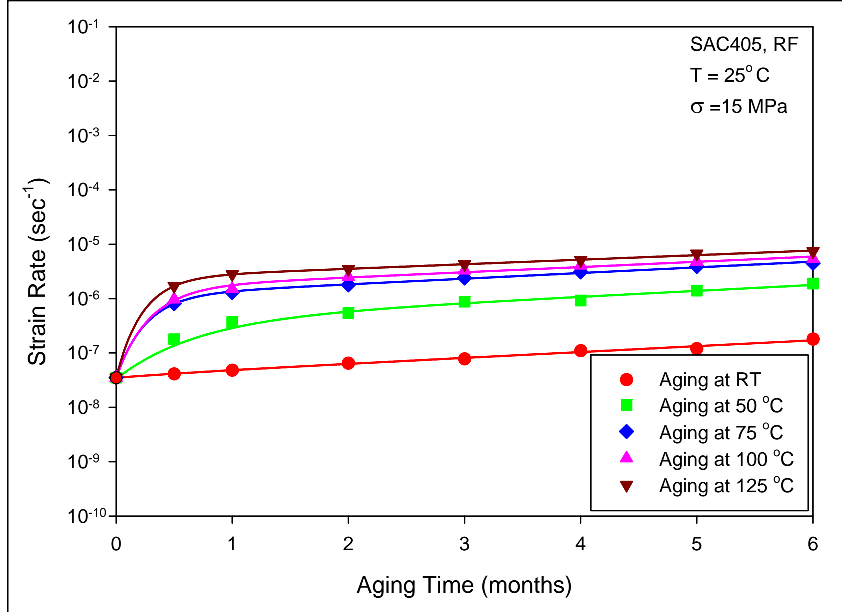

Figure 5.10 Evolution of the Creep Strain Rate with Aging (SAC405)
(Aging at 25, 50, 75, 100 125 °C)

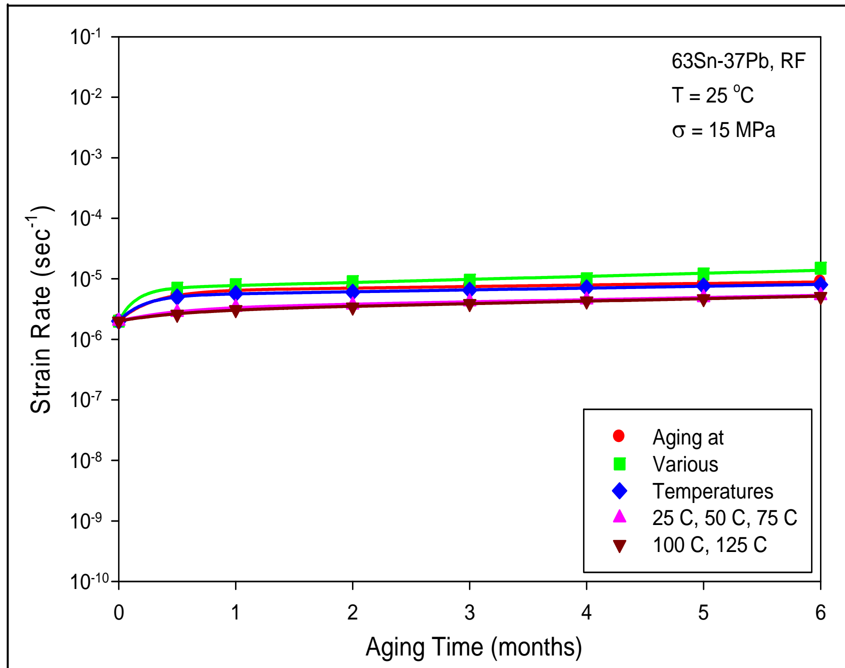

Figure 5.11 Evolution of the Creep Strain Rate with Aging (63Sn-37Pb)
(Aging at 25, 50, 75, 100 125 °C)

From the results in Figures 5.7-5.10, it is apparent that all four of the SAC alloys experience dramatic changes in their creep rate for elevated temperature aging. It is also observed that the functional variations with aging at 50, 75, 100, and 125 °C become approximately parallel with long term aging and are closely spaced. They are significantly separated from the variation occurring with room temperature aging. After the large changes that occur during the first month of aging, the variation of the creep rate (log scale) for all four SAC alloys becomes nearly linear with longer aging times. For the data available currently (up to 6 months of aging), there is no indication that an aging saturation point will be reached where the creep rate stabilizes. This suggests that there will potentially be reliability problems for SAC solder joints subjected to long term exposures at temperatures T > 50 °C.

The measured creep strain rate variations indicate that the effects of aging are much stronger for the lower silver content alloys (SAC105 and SAC205). Considering all of the tests performed so far, the maximum recorded creep strain rate for each alloy was obtained with 6 months aging at 125 °C (most severe aging conditions considered). Table 5.2 contains numerical values of the creep strain rates for non-aged samples, and also the values of the maximum creep strain rates found for the specimens aged for six months at 125 °C. Furthermore, the creep strain rate increases were calculated by taking the ratios of the maximum creep strain rates to the corresponding creep strain rates for the non-aged (as reflowed) materials. These ratios represent the worst cases of the observed creep rate increases with aging. The changes for SAC105 and SAC205 were very large at 9700X and 2895X, respectively. The changes for SAC305 and SAC405 were significantly lower at 361X and 211X, respectively. SAC305 and SAC405 alloys were found to have similar creep-aging behavior. Although a 200-time increase (SAC405) is

still a very large change, the aging effects on the creep response are dramatically reduced when the SAC alloy contains more silver.

Table 5.2 Increases in Creep Strain Rate with Aging

Alloy	Strain Rate (Non-aged)	Strain Rate (After 6 Months Aging at 125 °C)	Increase (Ratio)
SAC105	10.0×10^{-8}	9.7×10^{-4}	9700X
SAC205	3.8×10^{-8}	1.1×10^{-4}	2895X
SAC305	3.6×10^{-8}	0.130×10^{-4}	361X
SAC405	3.5×10^{-8}	0.074×10^{-4}	211X

5.4 Comparison of Aging Effects on SAC Alloys and Eutectic 63Sn-37Pb

The aging induced changes in the creep strain rates of the conventional eutectic 63Sn-37Pb solder were much smaller than the changes observed for the SAC alloys. Figure 5.11 contains the measured creep rate evolution curves for the 63Sn-37Pb solder specimens at the various aging temperatures. The observed creep rates for 63Sn-37Pb are restricted to a very narrow range of values (characterized by the orange band in Figure 5.12) between $\dot{\varepsilon} = 2 \times 10^{-6}$ and $\dot{\varepsilon} = 1.5 \times 10^{-5}$ across the entire test matrix. By superimposing this range on the creep strain rate curves for each SAC alloy, a set of graphical comparisons can be made between the aging effects for the SAC alloys and those for the eutectic 63Sn-37Pb alloy as shown in Figures 5.13-5.16.

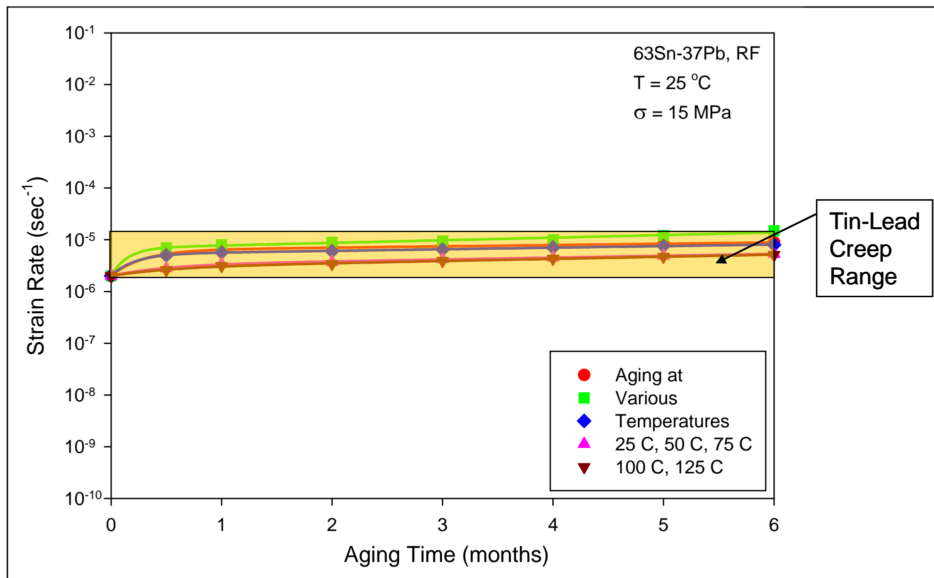

Figure 5.12 Creep Strain Rate Range for 63Sn-37Pb

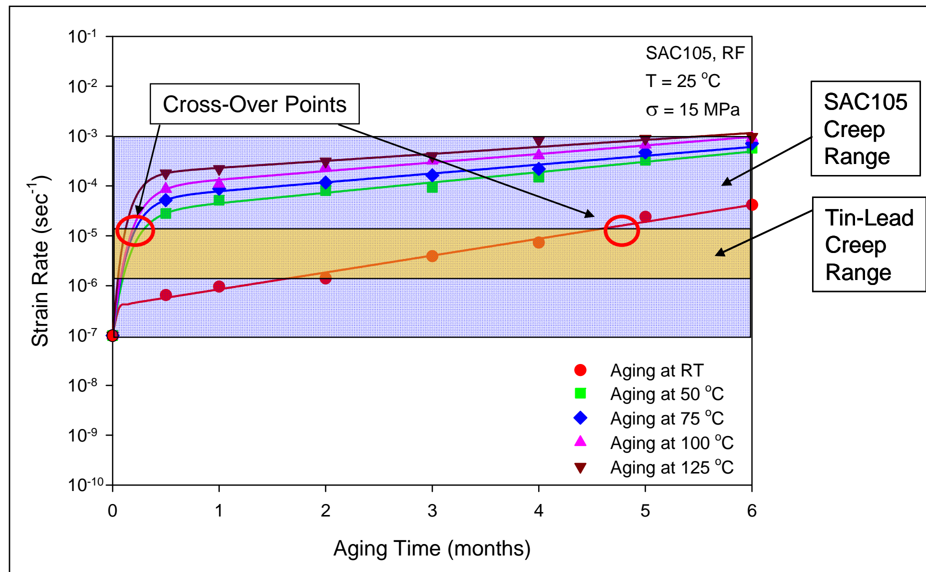

Figure 5.13 Creep Strain Rate Comparison (SAC105 vs. 63Sn-37Pb)

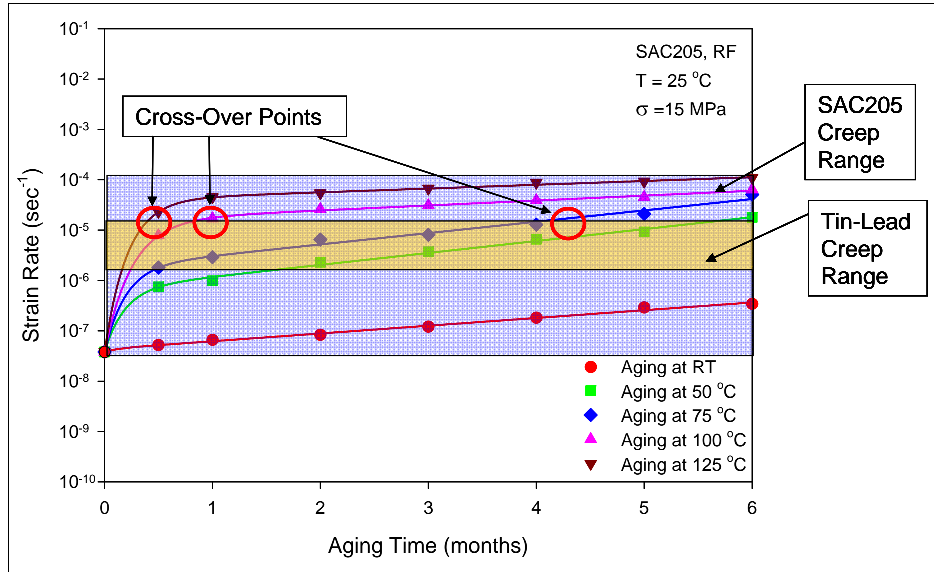

Figure 5.14 Creep Strain Rate Comparison (SAC205 vs. 63Sn-37Pb)

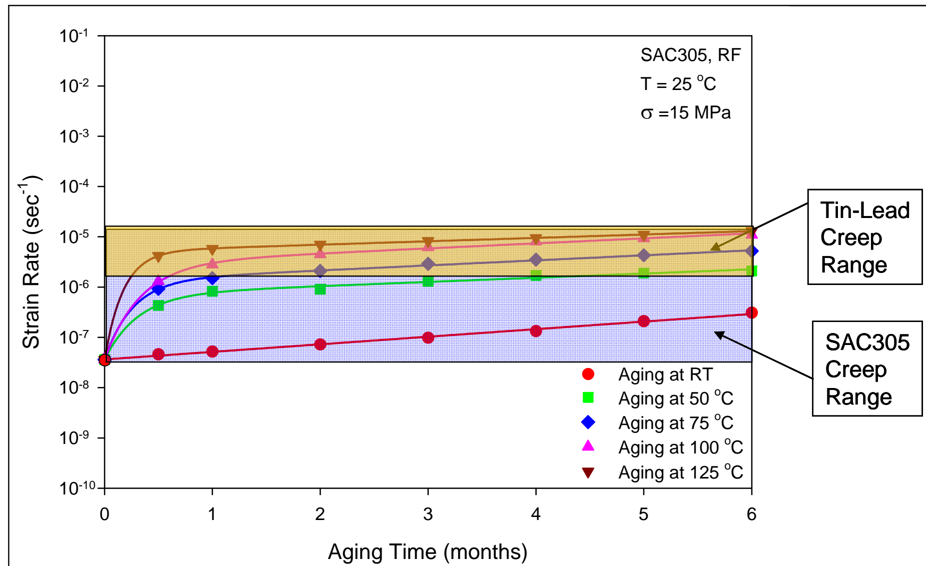

Figure 5.15 Creep Strain Rate Comparison (SAC305 vs. 63Sn-37Pb)

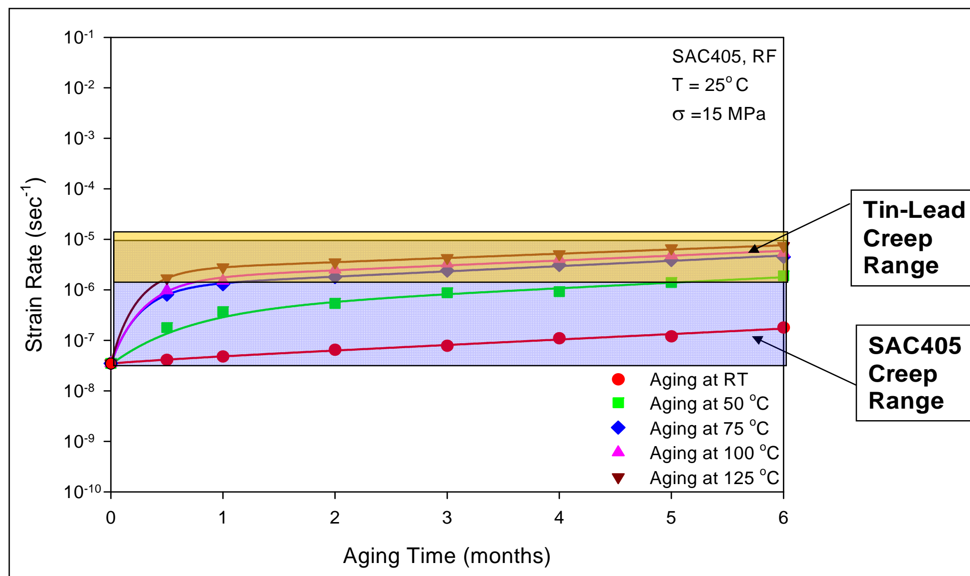

Figure 5.16 Creep Strain Rate Comparison (SAC405 vs. 63Sn-37Pb)

The comparison between SAC105 and 63Sn-37Pb is shown in Figure 5.13. Under the stress level (σ = 15 MPa) chosen for this study, SAC105 started with a much lower creep stain rate before aging effects kicked in. However, as the aging process progressed, the creep rates increased dramatically for SAC105, while they remained relatively small for 63Sn-37Pb. Thus, the creep strain rate curves for SAC105 began to intercept the creep strain rate range of Sn-Pb. After certain periods of time, these curves passed all the way through the Sn-Pb range, so that cross-over points occured on the graph. Once the cross-over occurs, the creep strain rate of SAC105 becomes greater than that of 63Sn-37Pb, and SAC105 has less creep resistance. It is evident on the graph in Figure 5.13 that aging temperature plays the dominant role in the occurrence of the cross-over points. The higher the aging temperature is, the sooner the cross-over will occur. For SAC105 subjected to room temperature aging, this process takes more than 4 months. However, for elevated temperatures aging, it is shortened dramatically to 5-10 days.

This trend also holds true for SAC205 as shown in Figure 5.14. In this case, the cross-over points only occurred at elevated aging temperatures, and took longer to occur. For room temperature aging, there was no cross-over between the evolution curves for SAC205 and 63Sn-37Pb through 6-months of aging. For SAC305 (Figure 5.15) and SAC405 (Figure 5.16), there were no cross-over points within 6 months of aging. However, it appears that given more aging time, these curves will eventually penetrate through the 63Sn-37Pb creep strain range.

Technically speaking, the cross-over points deliver very important information to designers of electronics packages using SAC alloys. Aging effects will deteriorate SAC creep properties so that after certain duration of aging, SAC solder joints will likely be less reliable than analogous Sn-Pb solder joints. The critical factors for aging performance are the aging temperature and chemical composition (silver content) of the alloy.

5.5 Influence of Silver Content on the Creep Strain Rate and Aging Effects

The influences of chemical composition on the mechanical properties of SAC alloys have been investigated in the literature review and Chapter 4. Lowering the silver content of a SAC alloy results in decreases in the mechanical properties. In this section, the effects of silver content on creep performance are explored.

The SAC alloys in this study constituted a series SACN05, N = 1.0, 2.0, 3.0, 4.0 wt.% of silver. All alloys contain the same copper concentration of 0.5 wt.%. In addition, all SAC specimens were prepared by using same reflow profile with identical cooling rate. The creep strain rate data from Figures 5.7-5.10 have been re-organized so that the creep strain rate curves of SACN05 are grouped together for each aging temperature. There are totally 5 plots of this kind as shown in Figures 5.17-5.21.

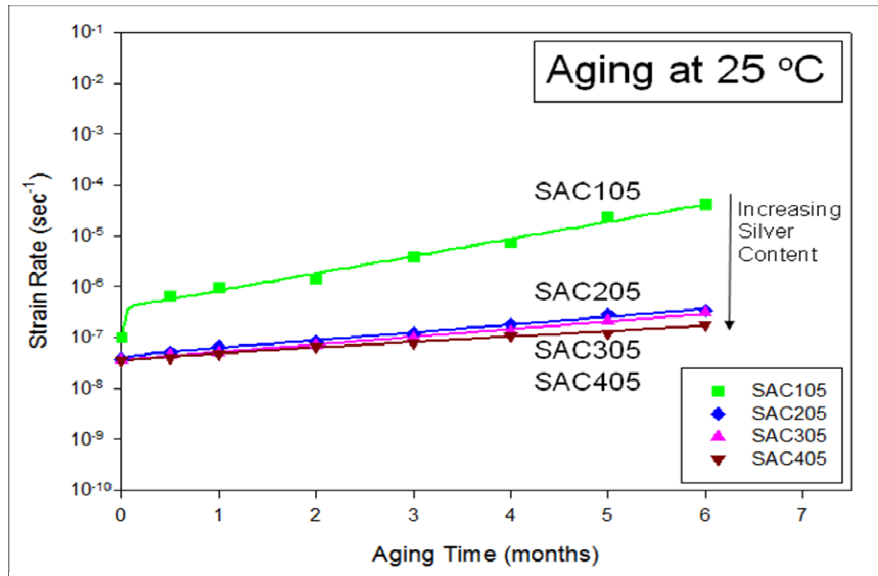

Figure 5.17 SACN05 Creep Rate Comparison (Aging at 25 °C)

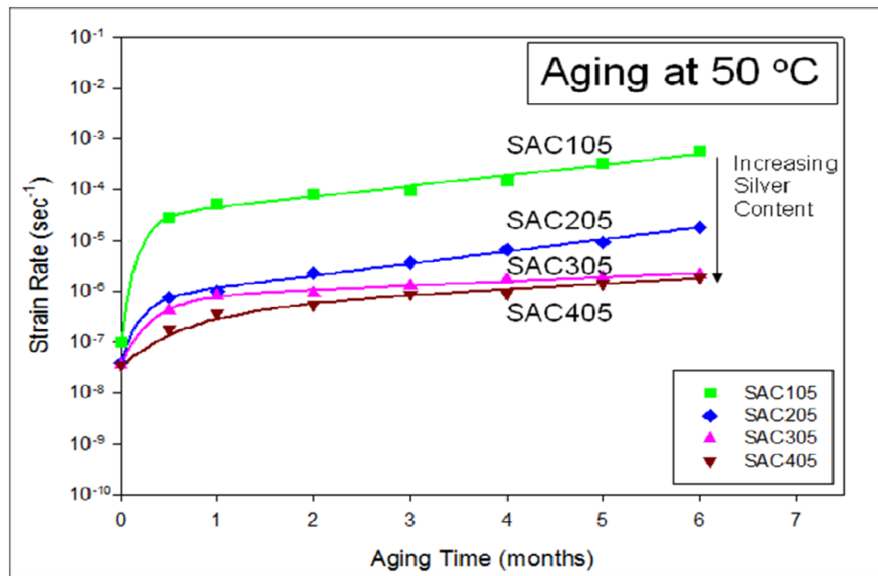

Figure 5.18 SACN05 Creep Rate Comparison (Aging at 50 °C)

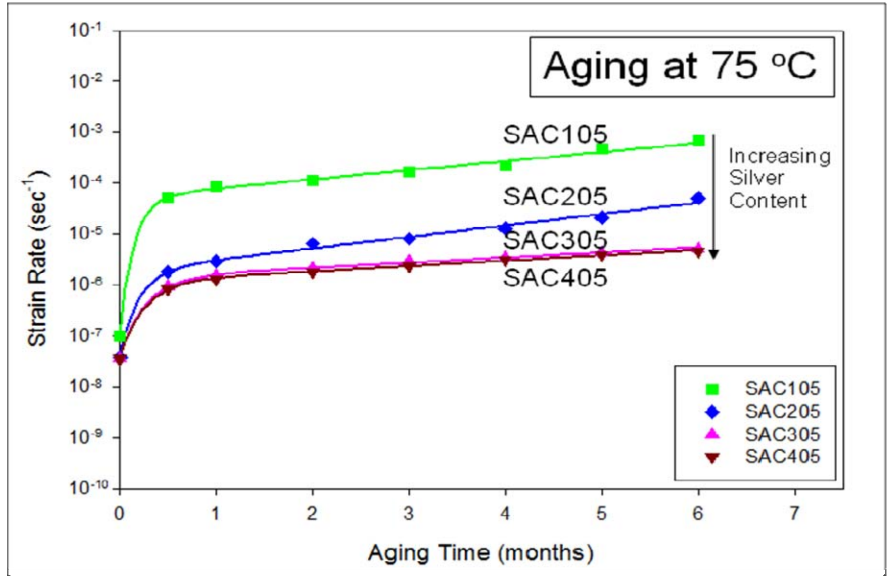

Figure 5.19 SACN05 Creep Rate Comparison (Aging at 75 °C)

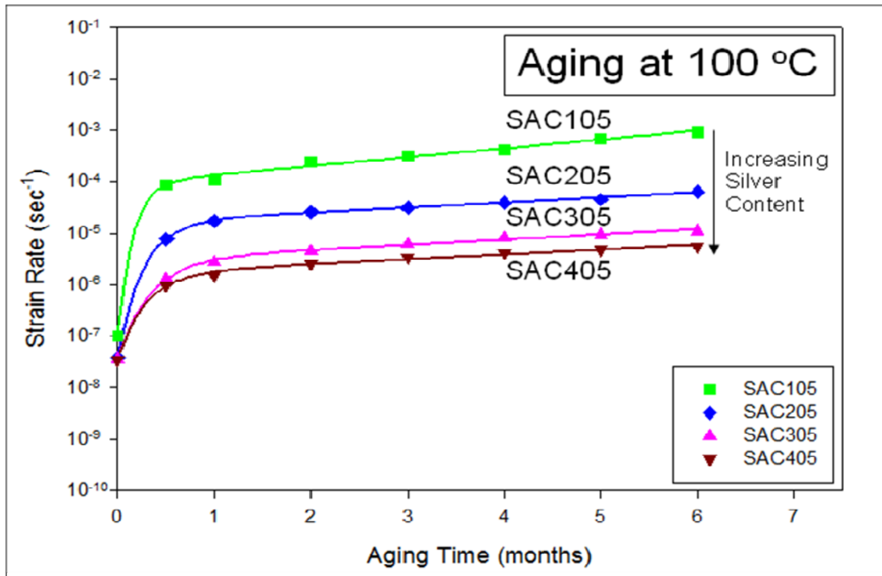

Figure 5.20 SACN05 Creep Rate Comparison (Aging at 100 °C)

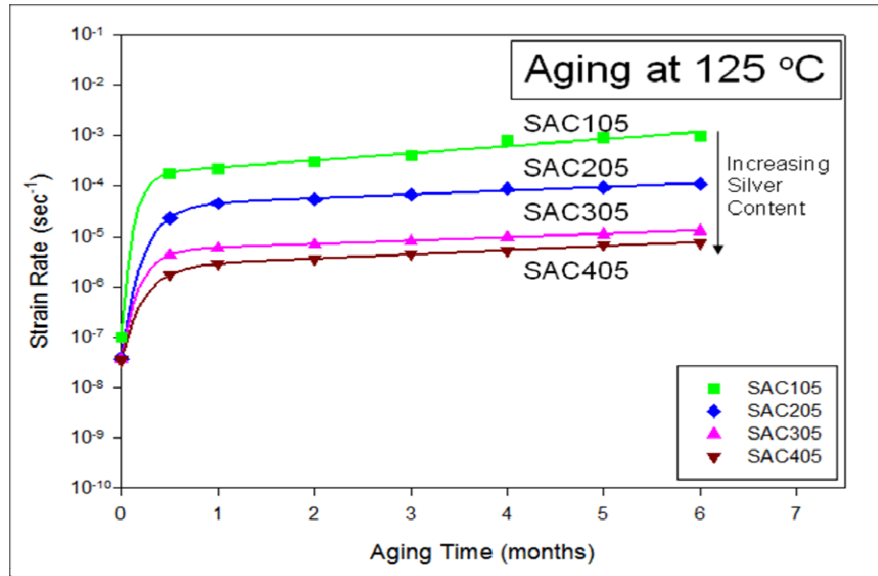

Figure 5.21 SACN05 Creep Rate Comparison (Aging at 125 °C)

Two observations are made from the above graphs:

(1) The creep strain rates of SACN05 for a given applied stress and any given aging temperature and aging time can be ordered by:

$$\dot{\varepsilon}_{SAC105} > \dot{\varepsilon}_{SAC205} > \dot{\varepsilon}_{SAC305} > \dot{\varepsilon}_{SAC405} \quad (5.3)$$

(2) The spread between creep strain rate curves of SACN05 (except for SAC105) becomes larger as the aging temperature increases.

The fundamental cause behind these observations is the difference in silver content. There are two major deformation mechanisms for solder alloys undergoing creep testing: dislocation creep and grain boundary sliding. After reflow, finer and more Ag_3Sn intermetallic compounds will form in the higher silver content SAC alloys. The Ag_3Sn particles, distributed over the Sn matrix, work as pinning sites to block the movement of both dislocations and grain boundaries so as to retard the softening process of creep. Even at higher aging temperatures, despite the

coarsening of IMCs, Ag_3Sn particles in higher silver content SAC alloys still effectively strengthen the material owing to their large number. The overall effect is that higher silver content SAC alloys have lower creep strain rates and are less affected by aging temperature.

Notably, it is not possible to insert the creep rate of 63Sn-37Pb into the creep rate order of SAC alloys stated in the first observation above because of the cross-over points. With no aging, 63Sn-37Pb has the highest creep rate and is on the leftmost side in the expression (5.3). However, after certain durations of aging at elevated temperatures, 63Sn-37Pb has the lowest creep rate and stays at the right of the expression. While the position of 63Sn-37Pb changes, the relative positions of SAC alloys remain fixed.

5.6 Influence of Stress Level on Creep Strain Rate

The magnitude of the applied stress level also has a strong effect on the creep behavior of the solder alloys. In previous sections, a stress level σ = 15 MPa was specified, which is approximately 25%-50% of the observed non-aged UTS values for the various SAC alloys tested. In this section, an additional stress level of σ = 20 MPa was also examined for aging at both 25 °C and 125 °C, with no other changes in the testing conditions and specimen preparation. Only two SAC alloys, SAC305 and SAC405 were used because the chosen stress level exceeded 50% of the non-aged UTS for SAC105 (σ_{uts} = 26 MPa) and SAC205 (σ_{uts} = 34 MPa). Thus, application of σ = 20 MPa to these alloys results in very fast specimen failure. Again, 63Sn-37Pb was tested for comparison purpose. The recorded creep curves for the higher stress level are shown in Figures 5.22-5.24.

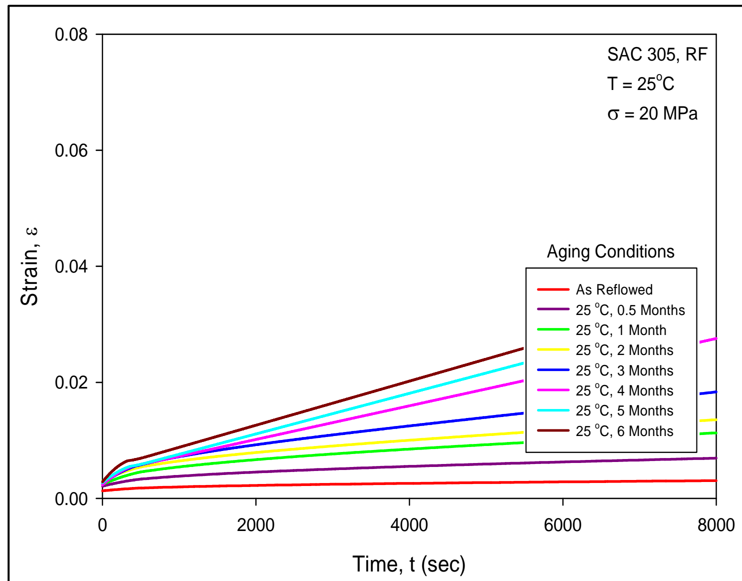

(a) σ = 20 MPa, Aged at 25 °C

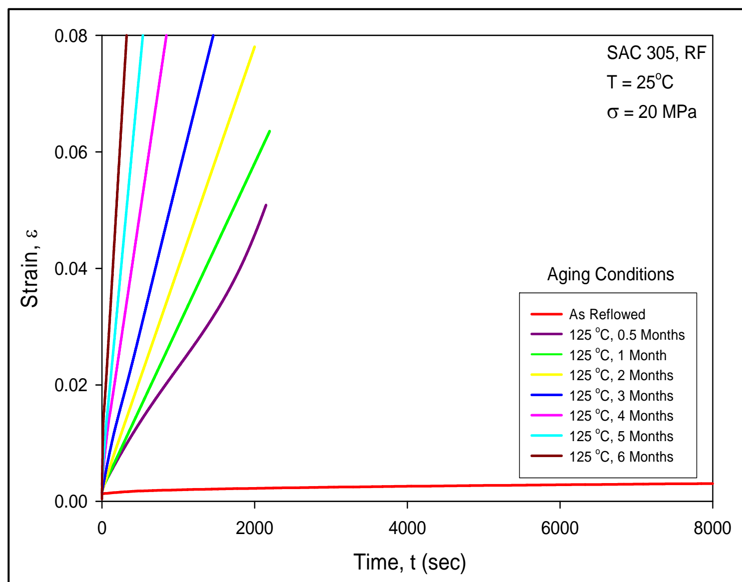

(b) σ = 20 MPa, Aged at 125 °C

Figure 5.22 Creep Curves for SAC305

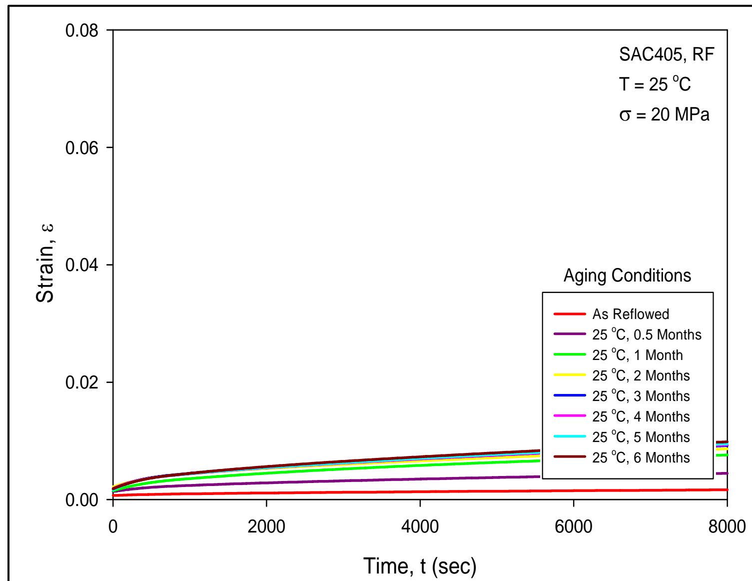

(a) σ = 20 MPa, Aged at 25 °C

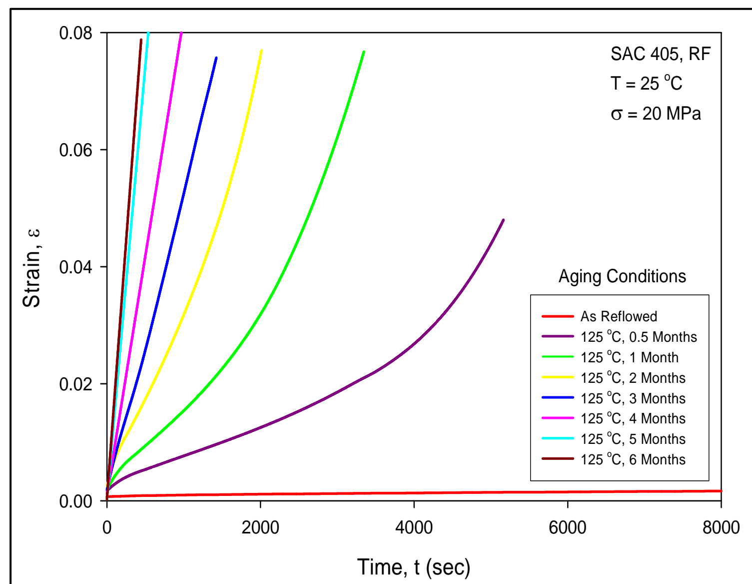

(b) σ = 20 MPa, Aged at 125 °C

Figure 5.23 Creep Curves for SAC405

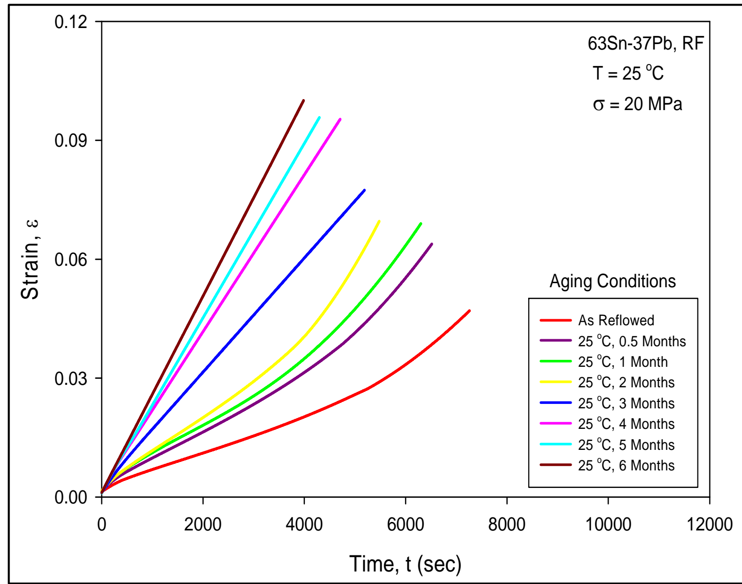

(a) σ = 20 MPa, Aged at 25 °C

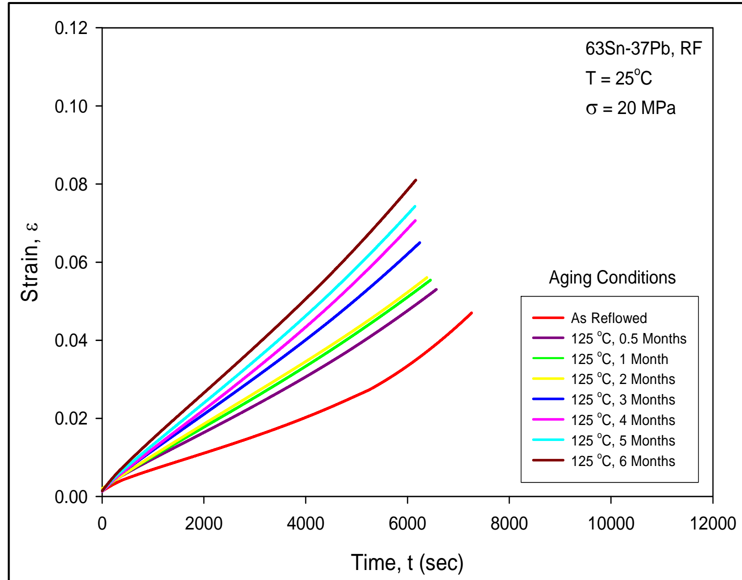

(b) σ = 20 MPa, Aged at 125 °C

Figure 5.24 Creep Curves for 63Sn-37Pb

Specimens aged at 25 °C and 125 °C for up to 6 months were used for studying the influence of stress level on creep behavior of the SAC alloys. The secondary creep strain rates were extracted from the recorded creep curves under σ = 15 MPa and σ = 20 MPa. Comparisons were then made by plotting the creep rates on one graph for each alloy and each aging temperature, as shown in Figures 5.25-5.27.

It was observed that 63Sn-37Pb exhibited limited variation in its creep behavior for both room temperature aging and elevated temperature aging as the stress level increased. This means that 63Sn-37Pb is relatively insensitive to changes of stress level under aging. In contrast, both SAC305 and SAC405 were strongly influenced by the applied stress level. An increase of 5 MPa in stress caused drastic increases in the creep rates of the SAC alloys. The higher the aging temperature was, the more significant the stress level influence became. Hence, the creep behavior of SAC alloys is highly sensitive to the change of stress level, and the influence will be compounded if the aging temperature increases.

More detailed comparisons can be found in Tables 5.3 and 5.4 for the two stress levels, two aging temperatures, and three solder alloys. As the stress level increased from 15 MPa to 20 MPa, the ratio of the creep strain rate after 6-months of aging to the strain rate for no aging increased from 8X to 14X for SAC305, and from 5X to 7X for SAC405 under room temperature aging. More dramatically, under elevated temperature aging, it increased from 361X to 656X for SAC305, and from 211X to 1614X for SAC405. However, this ratio did not change much for 63Sn-37Pb at both aging temperatures.

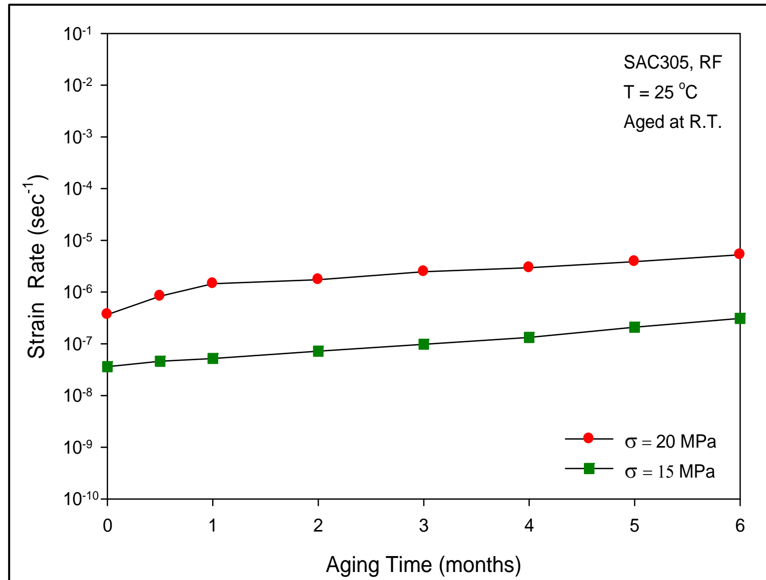

(a) Aging at 25 °C

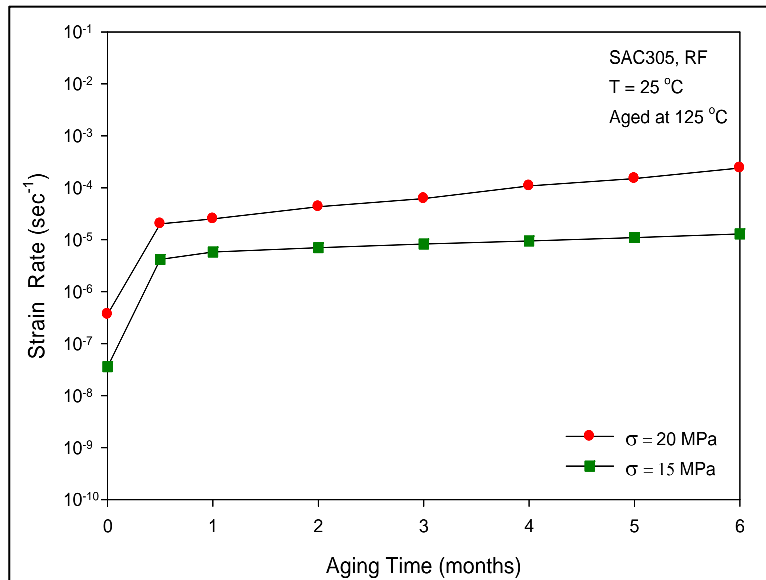

(b) Aging at 125 °C

Figure 5.25 Influence of Stress Level on the Creep Rate of SAC305

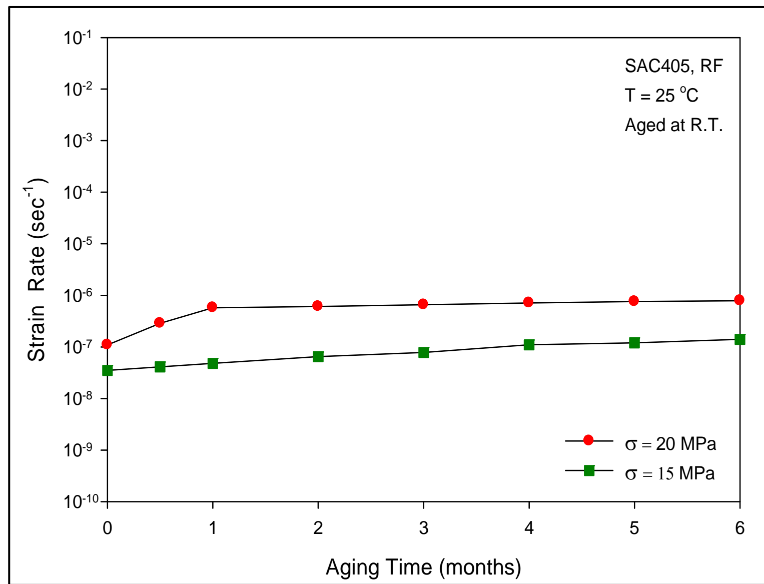

(a) Aging at 25 °C

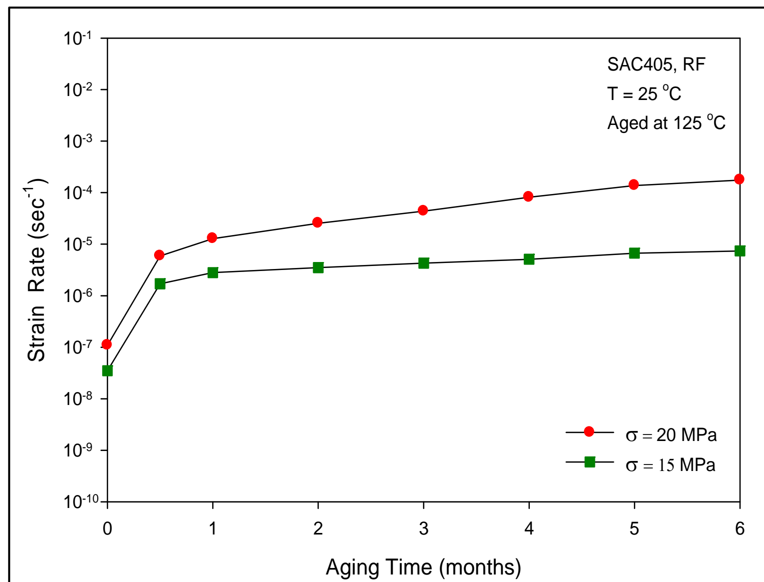

(b) Aging at 125 °C

Figure 5.26 Influence of Stress Level on the Creep Rate of SAC405

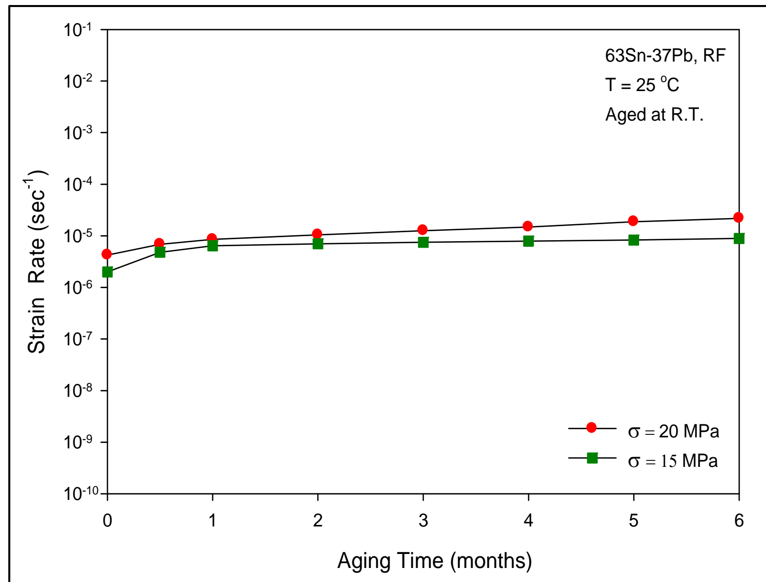

(a) Aging at 25 °C

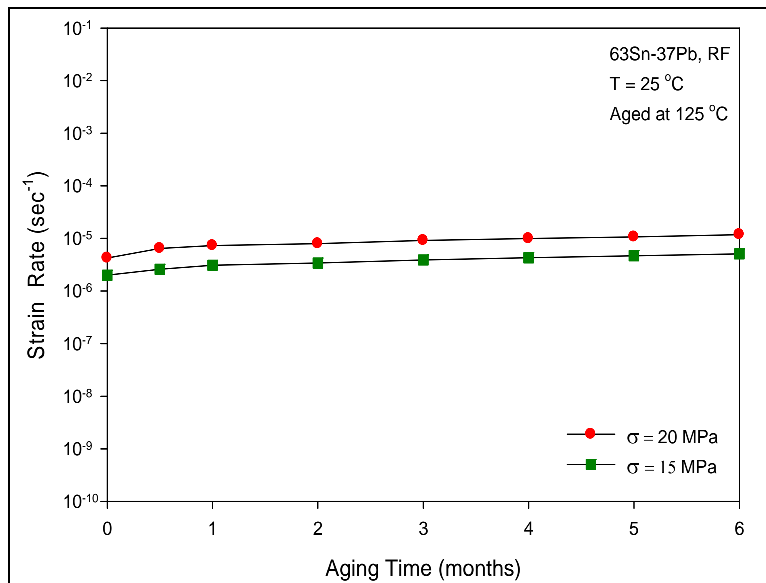

(b) Aging at 125 °C

Figure 5.27 Influence of Stress Level on the Creep Rate of 63Sn-37Pb

Table 5.3 Comparison of Stress Level Influence (R.T. Aging)

Aging at RT	Aging Time (months)	0	1	3	6
63Sn-37Pb	20 MPa	1.00X	2.01X	2.98X	5.18X
	15 MPa	1.00X	3.20X	3.75X	4.45X
SAC305	20 MPa	1.00X	3.95X	6.73X	14.41X
	15 MPa	1.00X	1.44X	2.72X	8.61X
SAC405	20 MPa	1.00X	5.28X	6.02X	7.26X
	15 MPa	1.00X	1.37X	2.23X	5.14X

Table 5.4 Comparison of Stress Level Influence (125 °C Aging)

Aging at 125 °C	Aging Time (months)	0	1	3	6
63Sn-37Pb	20 MPa	1.00X	1.73X	2.17X	2.79X
	15 MPa	1.00X	1.55X	1.95X	2.55X
SAC305	20 MPa	1.00X	62.13X	140.60X	656.68X
	15 MPa	1.00X	161.11X	230.56X	361.11X
SAC405	20 MPa	1.00X	117.43X	401.84X	1614.68X
	15 MPa	1.00X	80.00X	122.86X	211.43X

5.7 Discussion and Conclusions

In this chapter, aging effects on SAC solder creep behavior were examined by performing creep tests with a full test matrix of aging times, aging temperatures, and solder alloys. Four SAC alloys with different silver content and constant copper content were tested, and 63Sn-37Pb was also tested for comparison purposes.

Test specimens were preconditioned by isothermal aging for up to 6 months. Five aging temperatures, from 25 ° to 125 °C with an increment of 25 °C, were used to examine the effects of aging temperature on the creep behavior. Specimens were taken out of the chamber after certain durations of aging, and tested with a constant stress level σ = 15 MPa. For every specific aging condition, i.e. a specific combination of aging time and temperature, 5 specimens were tested and 5 raw creep curves were obtained. Secondary creep strain rate data were then extracted from these creep curves and averaged. An empirical model was used to fit the evolution of the creep strain rate data with aging.

It was found that all SAC alloys experienced dramatic increases in their creep rates for elevated temperature aging (T > 50 °C), and the largest changes occurred during the first month of aging. After 6-months of aging, the creep strain rates were still increasing and showed no sign of aging saturation. This indicates potential reliability problems for SAC solder joints under long term exposures at elevated temperatures. In contrast, the aging induced changes in the creep strain rates of conventional eutectic 63Sn-37Pb solder were much smaller, and could be defined within a very narrow range of values. By comparing this range with the creep strain rate curves for each SAC alloy, much more significant aging effects on creep response of SAC alloys could be seen. The creep strain rates of SAC alloys increased more rapidly with aging. After

certain durations of aging, cross-over points would occur so that the SAC alloys had larger creep strain rates than 63Sn-37Pb solder

Silver content was observed to have considerable influence on SAC creep strain rate and aging effects. Higher silver content SAC alloys had lower creep strain rates and were less affected by aging. For a given applied stress and aging temperature, this observation can be characterized by Eq. (5.3). Finer and more Ag_3Sn particles were formed in higher silver content SAC alloys, and they strengthened the alloys by effectively hindering the movement of dislocation.

Two stress levels were applied to study the influence of stress on the creep behavior of SAC alloys subjected to room temperature and elevated temperature aging. The SAC alloys were strongly influenced by changes in the applied stress during creep, especially for elevated temperature aging. However, 63Sn-37Pb solder exhibited limited variation in its creep behavior for both room temperature and elevated temperature aging as the stress level increased.

Chapter 6
Preparation, Microstructure and Application of Mixed Formulation Solders

6.1 Introduction

The transition from Sn-Pb to Pb-free soldering in electronics manufacturing industry has been in steady progress for many years all over the world. Nonetheless, despite there is a time frame for the completion of this transition (by the year 2010 according to the EU RoHS legislation), many critical issues have not been resolved yet due to the incomplete infrastructure for Pb-free soldering technology and the timing and technical readiness in the various sectors of the electronics manufacturing industry. In the mean time, an interim stage featured by mixed application of Pb-free solder with Pb-coated components and vice-versa has been called in to help with the conversion process and has gained wide acknowledgement within the industry.

However, when Sn-Pb and Pb-free materials and processes are mixed, solder joint reliability problems start to emerge. For example, the mixed application of Sn-Pb and Sn-Ag-Cu solder alloys in area array packages has caused compatibility concerns, which mainly result from the difference in melting temperatures between Sn-Ag-Cu system and Sn-Pb solders. Moreover, at solder joints, the metallurgical reaction of Sn-Ag-Cu and Pb is a secondary alloying process, through which different microstructure may be formed.

In this chapter, seven mixed formulation solders have been formed according to different contents of eutectic 63Sn-37Pb in the mixtures. Their physical properties, microstructure, and application in real solder joints have been extensively investigated and compared.

6.2 Preparation of Mixed Formulation Solders

Pure 63Sn-37Pb and pure SAC305, in the form of small pieces were accurately weighed and mixed together according to the mixing proportions of interest. Then, the mixture was filled into a cylindrical quartz crucible covered with a quartz top that had a hole in the center for introducing stirring rod. The melting process was conducted on a heating stage and protected by inert gas N_2. Finally, the molten mixed formulation solder was rapidly cooled down to room temperature by N_2 gas flow in order to maintain homogeneous microstructure and avoid any possible oxidation of the solder. Mixed formulation solders are named as MIX A-B, where A and B are the weight percentages of pure 63Sn-37Pb and pure SAC305 respectively in the mixture. As an example, solder MIX 30-70 is a mixture of 30 wt.% 63Sn-37Pb and 70 wt.% SAC305. There were totally 5 mixed formulation solders plus 2 pure alloys (63Sn-37Pb and SAC305) prepared in this way and their chemical compositions are listed in Table 6.1.

Table 6.1 Composition of Mixed Formulation Solders (in wt.%)

Solder Type	%Sn	%Pb	%Ag	%Cu
SAC305	96.50	0	3.00	0.50
MIX 10-90	93.15	3.70	2.70	0.45
MIX 30-70	86.45	11.10	2.10	0.35
MIX 50-50	79.75	18.50	1.50	0.25
MIX 70-30	73.05	25.90	0.90	0.15
MIX 90-10	66.35	33.30	0.30	0.05
63Sn-37Pb	63.00	37.00	0	0

6.3 Physical Properties of Mixed Formulation Solders

The variation of physical properties such as melting temperature and pasty range over different mixture ratios of 63Sn-37Pb and SAC305 solder alloys have been examined by DSC analysis (Figure 6.1) and the final results are shown in Figure 6.2-6.3. It can be found that melting temperature of mixture solders initially decreases as the 63Sn-37Pb content increases and levels off beyond 30 wt.%. Furthermore, the melting temperatures of some mixture solders are close to or even lower than that of 63Sn-37Pb. This is a favorable phenomenon due to the concern of temperature effect on electronic packaging process. It also can be seen that the pasty range of mixture solders are wide as mixture composition near pure SAC305 or pure 63Sn-37Pb, then turns narrow rapidly as the composition shifts away from pure alloys and finally reaches low values within content between 30 wt.% and 70 wt.%.

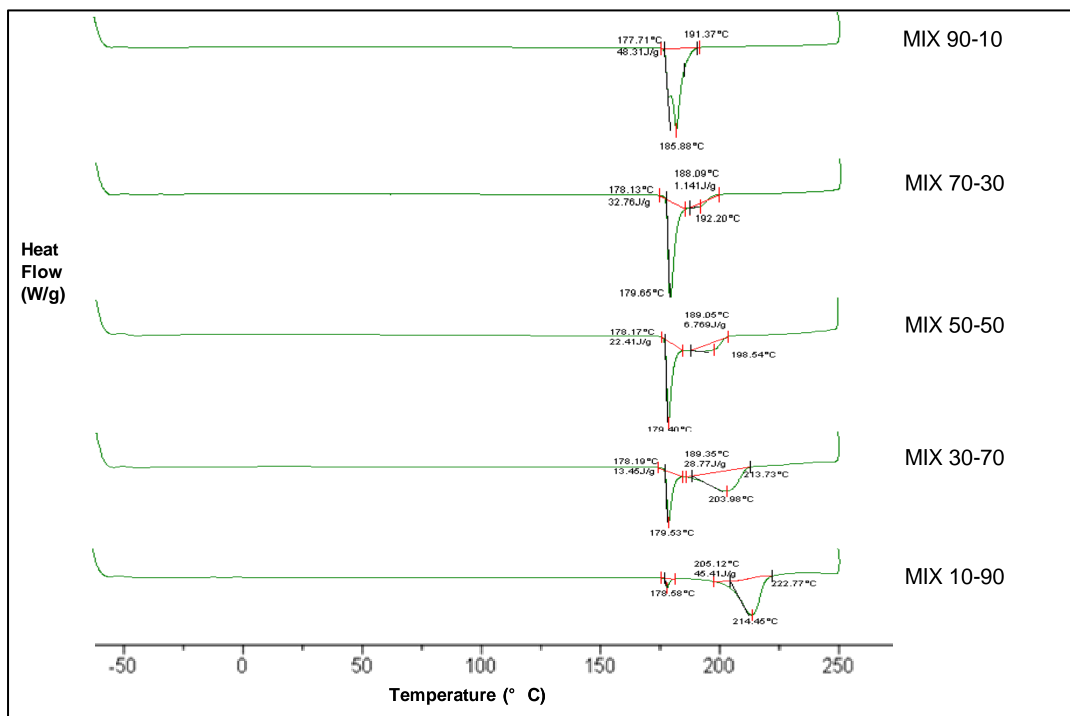

Figure 6.1 DSC Analysis of Mixed Formulation Solders

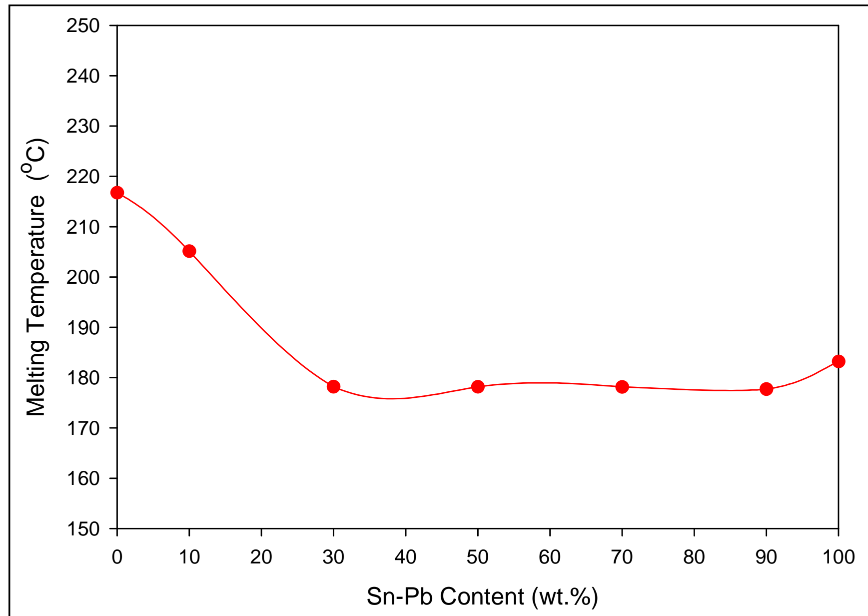

Figure 6.2 Melting Temperature vs. 63Sn-37Pb Content

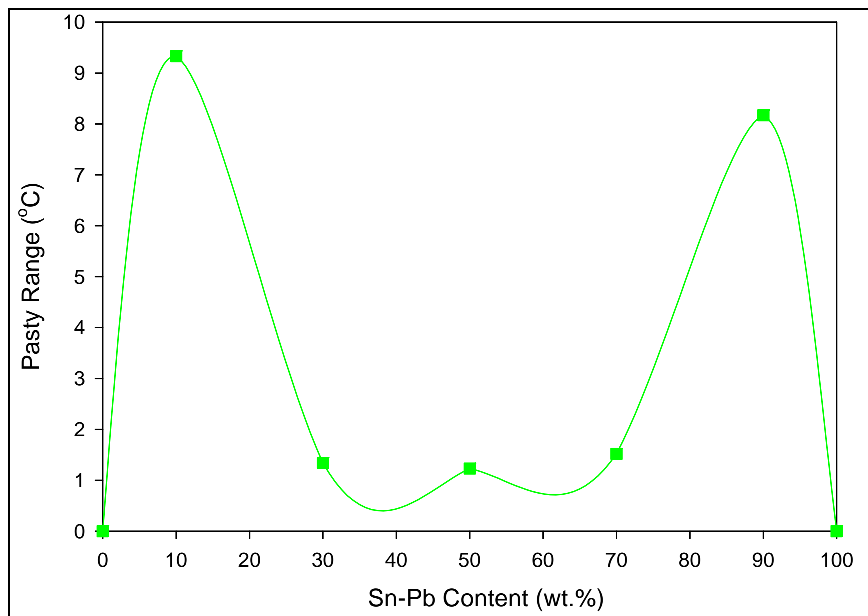

Figure 6.3 Pasty Range vs. 63Sn-37Pb Content

6.4 Microstructure Evolution of Mixed Formulation Solders

The microstructure evolution occurring with different mixture ratios have been evaluated by optical and Scanning Electronic Microscopy. Micrographs in Figure 6.4 demonstrate the microstructure of seven mixed formulations solders recorded at 1000X (OM) and 3500X (SEM). The well-known microstructure of pure SAC 305, i.e. bundles of needle-shaped Ag_3Sn particles distributed on Sn matrix can be found in the first picture of the series. However, as the content of 63Sn-37Pb increases in the mixtures, the Ag_3Sn particles change dramatically into thin and bone-shaped precipitates distributed across the Sn matrix. EDX analysis shown in Figure 6.5 provides such information that these precipitates are rich in Ag and Pb. In addition, elemental solubility listed in Table 6.2 indicates that in Cu-Pb and Ag-Pb binary systems, the elements basically have no solubility in each other at room temperature. Therefore, Pb, which also forms no intermetallic compound with Sn, Ag, and Cu, will be separately present in the mixed formulation solders as Pb-rich phase on the Sn matrix.

As the 63Sn-37Pb content increased from 10% to 90%, the precipitates in the mixed formulation solders evolved from thin bone-shaped to thick bone-shaped to coarse bone-shaped to pie-shaped, and finally, to coarse pie-shaped particles. Eventually, as the 63Sn-37Pb content reached 100%, the typical eutectic structure was observed (last picture in the series). Since mechanical properties are ultimately determined by microstructure, the distinctive microstructure of mixed formulation solders will have dominant effects on their mechanical performance.

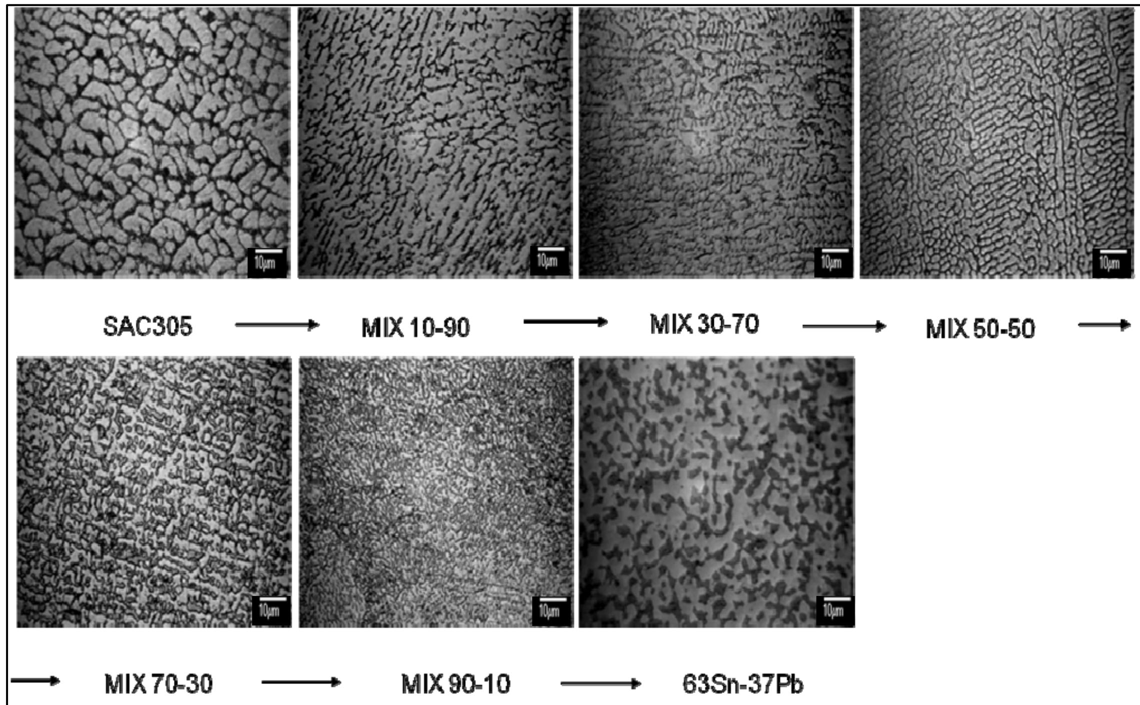

(a) Optical Micrographs

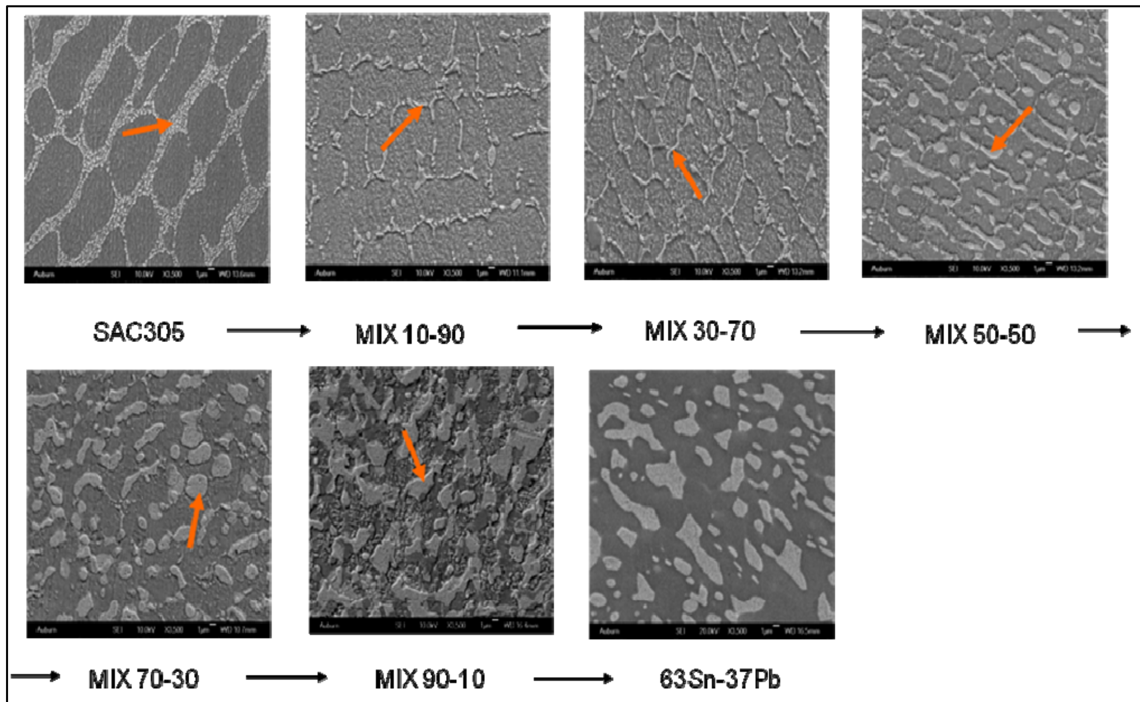

(b) SEM Micrographs (Arrow: EDX spot)

Figure 6.4 Microstructure Evolution of Mixed Formulation Solders

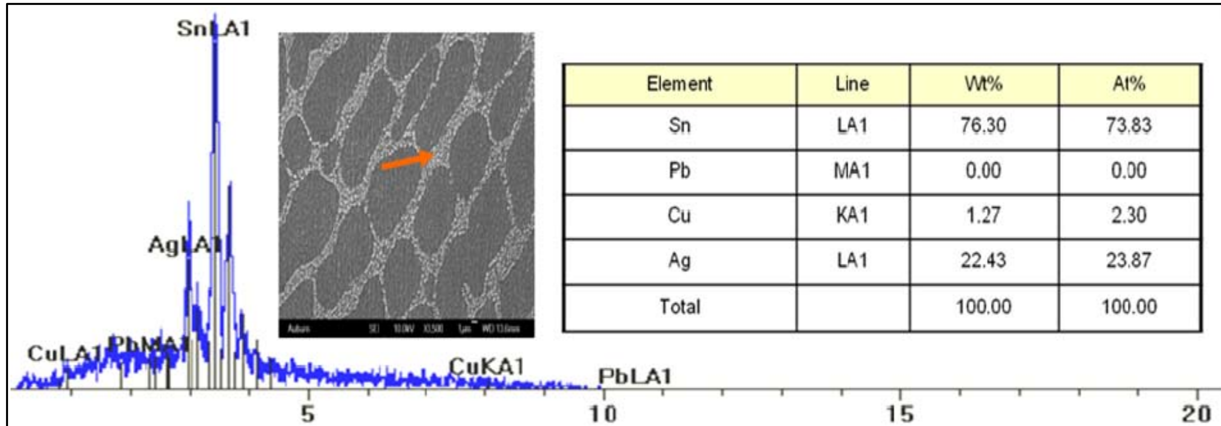

Element	Line	Wt%	At%
Sn	LA1	76.30	73.83
Pb	MA1	0.00	0.00
Cu	KA1	1.27	2.30
Ag	LA1	22.43	23.87
Total		100.00	100.00

(a) SAC305

Microstructure: needle-shaped, Ag_3Sn (white) particles distributed on Sn matrix

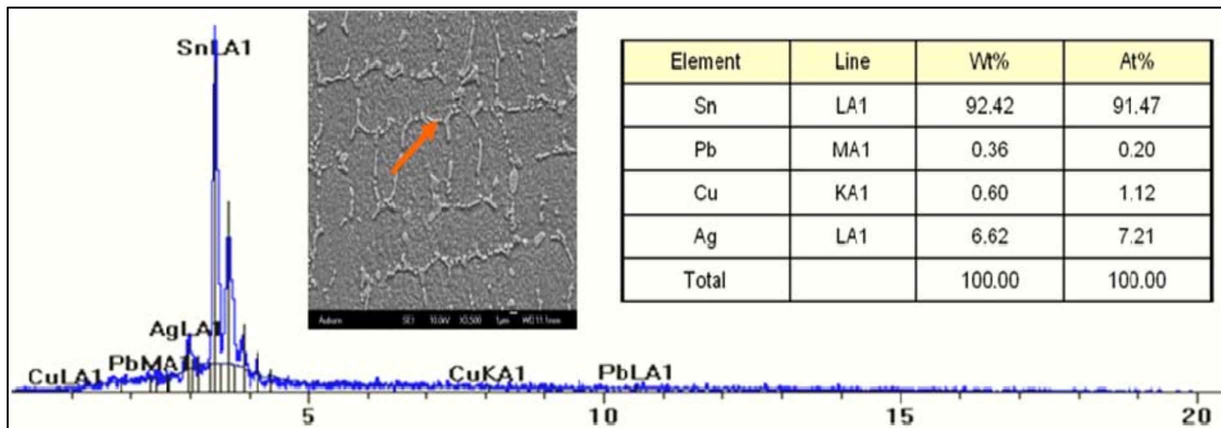

Element	Line	Wt%	At%
Sn	LA1	92.42	91.47
Pb	MA1	0.36	0.20
Cu	KA1	0.60	1.12
Ag	LA1	6.62	7.21
Total		100.00	100.00

(b) MIX 10-90

Microstructure: Ag-rich, thin bone-shaped Precipitates distributed on Sn matrix

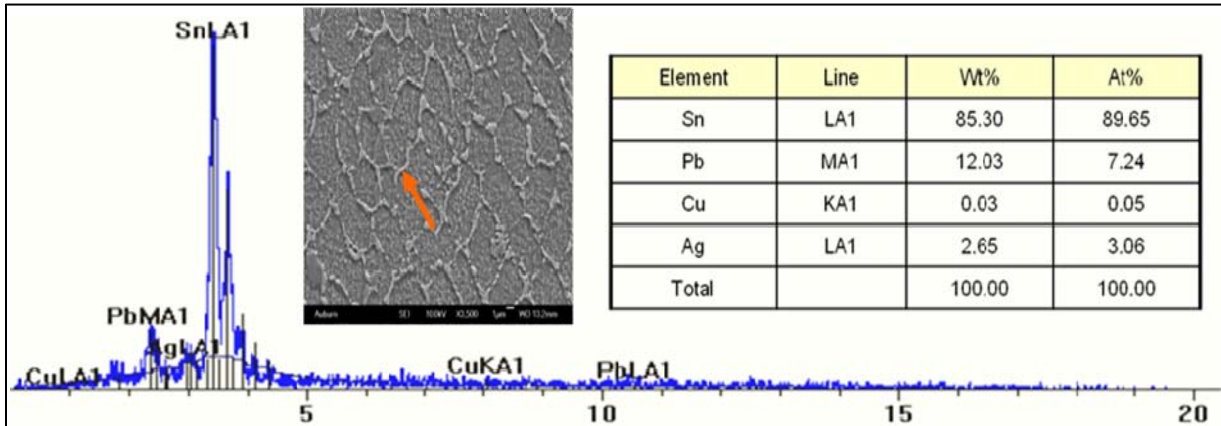

Element	Line	Wt%	At%
Sn	LA1	85.30	89.65
Pb	MA1	12.03	7.24
Cu	KA1	0.03	0.05
Ag	LA1	2.65	3.06
Total		100.00	100.00

(c) MIX 30-70

Microstructure: Pb, Ag-rich, grown bone-shaped precipitates distributed on Sn matrix

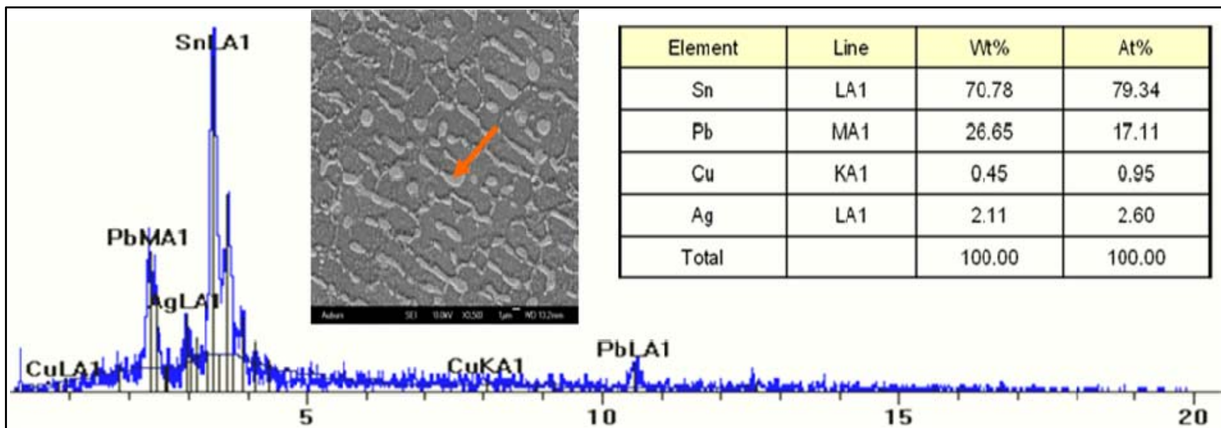

Element	Line	Wt%	At%
Sn	LA1	70.78	79.34
Pb	MA1	26.65	17.11
Cu	KA1	0.45	0.95
Ag	LA1	2.11	2.60
Total		100.00	100.00

(d) MIX 50-50

Microstructure: Pb-rich, coarse bone-shaped precipitates distributed on Sn matrix

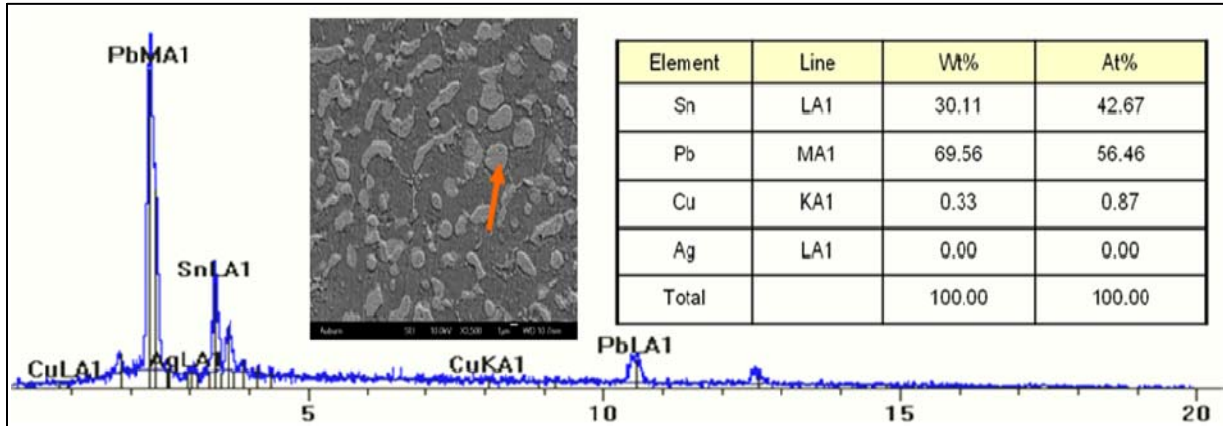

Element	Line	Wt%	At%
Sn	LA1	30.11	42.67
Pb	MA1	69.56	56.46
Cu	KA1	0.33	0.87
Ag	LA1	0.00	0.00
Total		100.00	100.00

(e) MIX 70-30

Microstructure: Pb-rich, pie-shaped precipitates distributed on Sn matrix

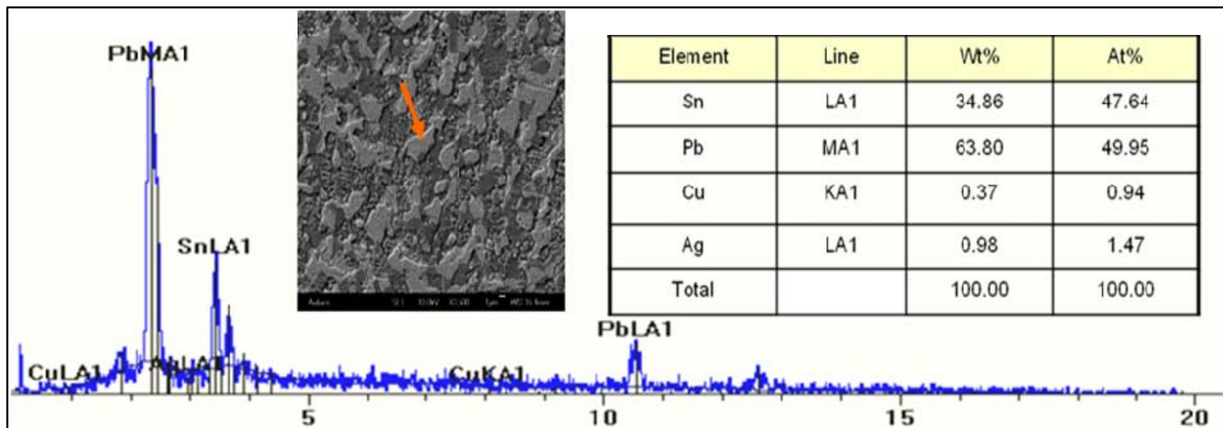

Element	Line	Wt%	At%
Sn	LA1	34.86	47.64
Pb	MA1	63.80	49.95
Cu	KA1	0.37	0.94
Ag	LA1	0.98	1.47
Total		100.00	100.00

(f) MIX 90-10

Microstructure: Pb-rich, coarse pie-shaped precipitates distributed on Sn matrix

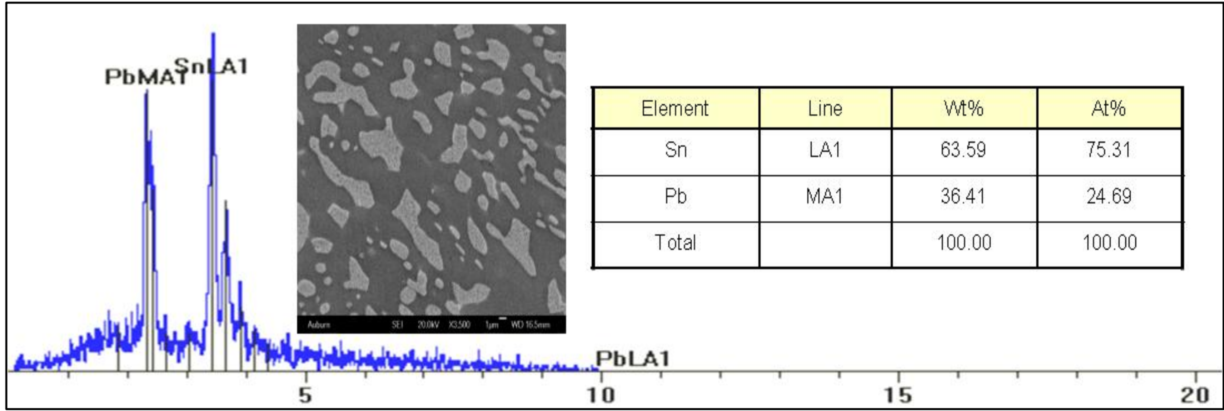

Element	Line	Wt%	At%
Sn	LA1	63.59	75.31
Pb	MA1	36.41	24.69
Total		100.00	100.00

(g) 63Sn-37Pb

Microstructure: Eutectic distribution of Sn and Pb (white) particles

Figure 6.5 EDX Analysis of Mixed Formulation Solders

Table 6.2 Elemental Solubility in Binary System at Room Temperature
(http://www.metallurgy.nist.gov/phase/solder/solder.html)

Sn-Pb Binary System	**Phase**	**Mass% Pb**	**Mass% Sn**
	(Pb)	81.09	18.91
	(Sn)	3.41	96.59
Cu-Pb Binary System	**Phase**	**Mass% Pb**	**Mass% Cu**
	(Pb)	100	0
	(Cu)	0	100
Ag-Pb Binary System	**Phase**	**Mass% Pb**	**Mass% Ag**
	(Pb)	99.90	0.1
	(Ag)	1.43	98.57
Ag-Cu Binary System	**Phase**	**Mass% Cu**	**Mass% Ag**
	(Ag)	8.27	91.73
	(Cu)	92.53	7.47

6.5 Application of Mixed Formulation Solders

As introduced in details in Chapter 1, there are two kinds of assembly compatibility defined by the conditions under which alloys and processes are mixed: “backward compatibility” and “forward compatibility”. Challenge to solder joint reliability arises when the mixed formulation solders between Sn-Pb and Sn-Ag-Cu solder alloys are formed in either of the ways. The currently existing issues mainly result from the 34 °C difference between the eutectic temperature of Sn-Ag-Cu of 217 °C and the eutectic temperature of Sn-Pb of 183 °C.

During reflow soldering, the metallurgical reaction of Sn-Ag-Cu and Sn-Pb may result in different microstructures, which can be fully mixed or only partially mixed. The homogeneity of mixed Sn-Pb and Sn-Ag-Cu structure is driven by Pb diffusion in solder joint and determined by such factors as Pb concentration, peak reflow temperature and time, soldering environment, and Pb-free solder composition. High peak temperature is usually used in reflowing Pb-free solder joints due to its high melting temperature in order to obtain a homogenous microstructure. However, high reflow temperature will cause reliability concerns to the entire packages. Due to the uniqueness of the mixed solder joints, lower peak temperature reflow profile maybe used to achieve solderability, but with uncertainty in microstructure homogeneity at solder joints.

Despite the problems to be solved, the mixed soldering assemblies have been a reality in the electronics manufacturing industry. However, there are a limited number of reports on the evolution of microstructure of the mixed formulation solders formed by conventional Sn-Pb and SAC series Pb-free solders although there is an increasing need for this information.

As further study on mixed formulation solders, the microstructure of real BGA solder joints formed by approximately mixing 50 wt.% Sn-Pb solder and 50 wt.% SAC solder and using different reflow profiles has been investigated and the results are shown in Figure 6.6.

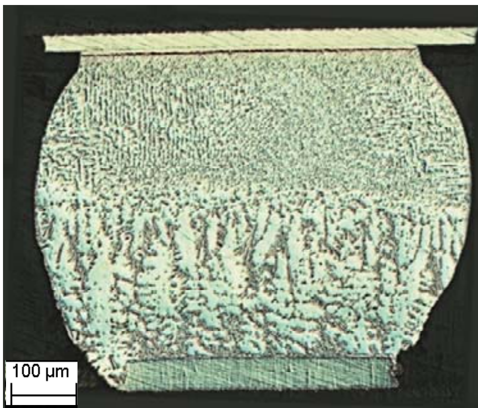

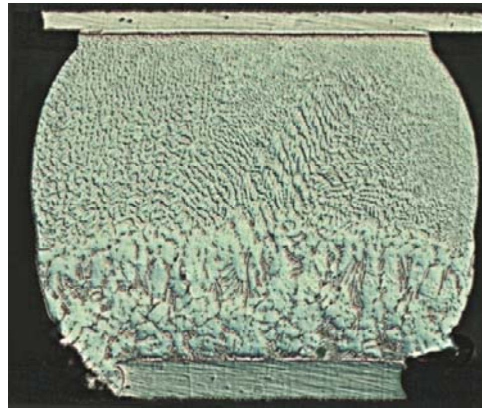

BGA Reflow Profile Description

Reflow Profile	Low-3
Peak (°C)	216
Time above 220 °C (sec)	0
Time above 183 °C (sec)	57

(a) Solder Joints Reflowed with a Peak Temperature of 216 °C

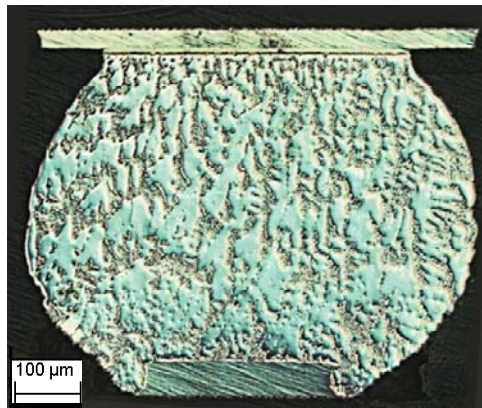

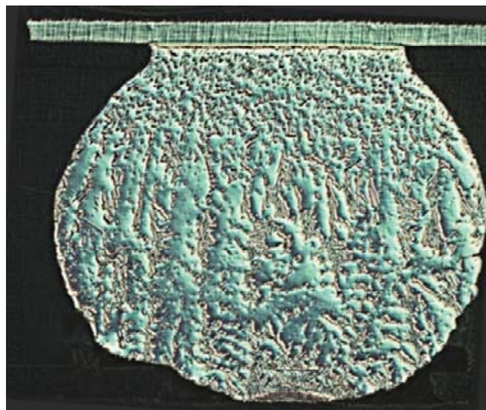

BGA Reflow Profile Description

Reflow Profile	Low-2
Peak (°C)	222
Time above 220 °C (sec)	9
Time above 183 °C (sec)	59

(b) Solder Joints Reflowed with a Peak Temperature of 222 °C

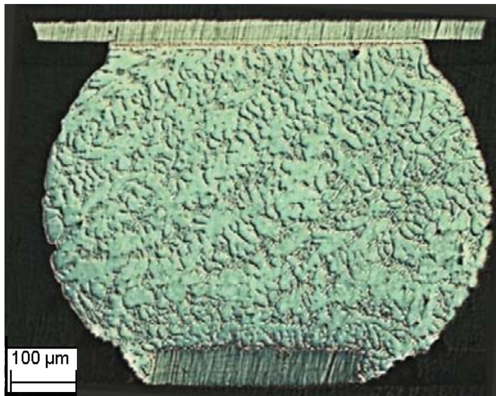

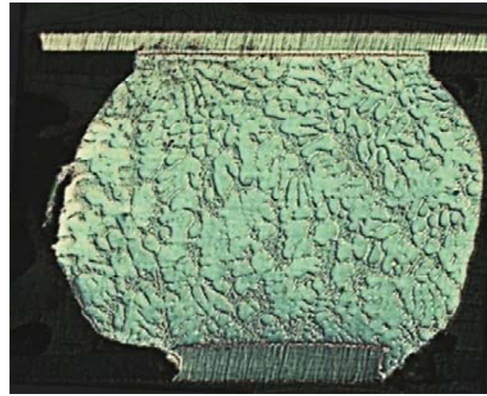

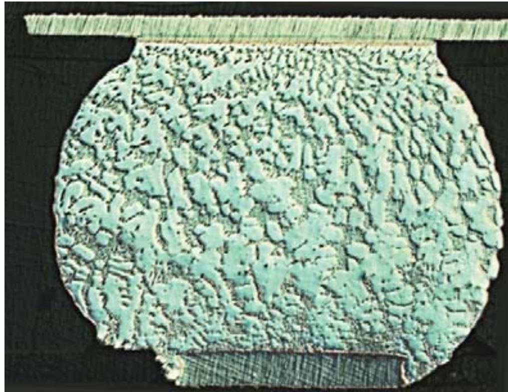

BGA Reflow Profile Description

Reflow Profile	Low-1
Peak (^{o}C)	227
Time above 220 ^{o}C (sec)	15
Time above 183 ^{o}C (sec)	62

(c) Solder Joints Reflowed with a Peak Temperature of 227 °C

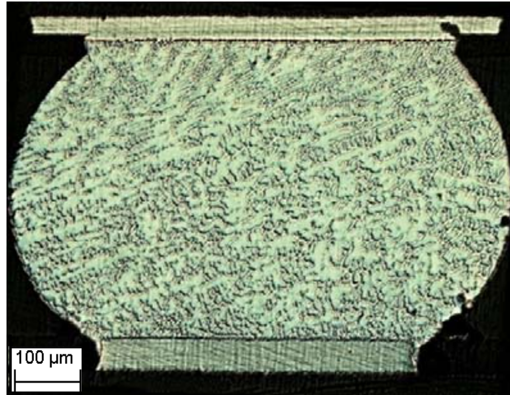

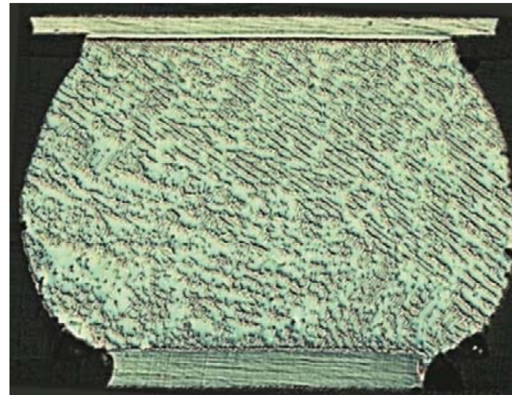

BGA Reflow Profile Description

Reflow Profile	Target
Peak (^oC)	233
Time above 220 ^oC (sec)	22
Time above 183 ^oC (sec)	65

(d) Solder Joints Reflowed with a Peak Temperature of 233 °C

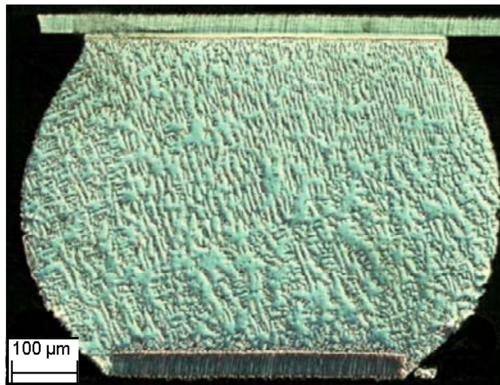

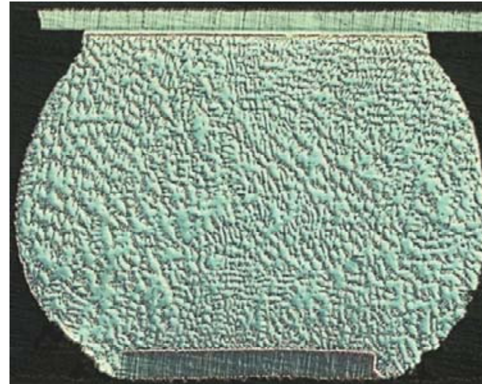

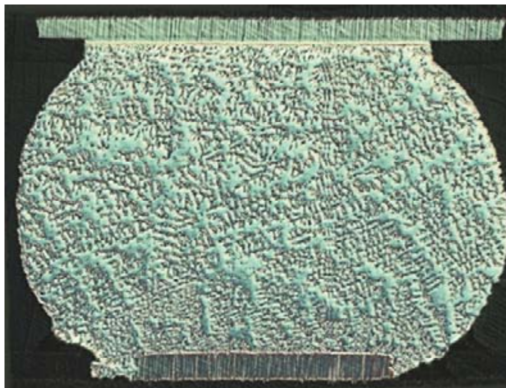

BGA Reflow Profile Description

Reflow Profile	High
Peak (°C)	237
Time above 220 °C (sec)	25
Time above 183 °C (sec)	66

(e) Solder Joints Reflowed with a Peak Temperature of 237 °C

Figure 6.6 Mixed Formulation Microstructure in Real BGA Solder Joints

The BGA solder joints in the study were cut off from 5 identical electronic packages reflowed by using 5 different profiles. In every micrograph above, the 3 solder balls were located at the leftmost, right in the middle and at the rightmost spots respectively on a package for the purposes of eliminating temperature variation at different positions.

The microscope in use (OLYMPUS BX 60) is equipped with a Nomarski prism for differential interference contrast microscopy. The Nomarski prism causes the light rays to come to a focal point outside the body of the prism and allows greater flexibility in image focusing.

The 5 reflow profiles, named as Low-3, Low-2, Low-1, Target, and High, are mainly different in their peak temperatures and dwelling times above the melting points of both Pb-free (≈ 220 °C) and Sn-Pb (≈ 183 °C) solders. It can be found in Figure 6.6 (a)-(e) that the formation of microstructure in solder joints follows such a rule that the higher the reflow peak temperature is, the longer the dwelling times are, the finer and more homogeneous the microstructure will be. Low-3 solder joints have poorly mixed microstructure in which a boundary between Sn-Pb and SAC solders can be clearly seen. By increasing peak temperature from 216 °C to 222 °C, Low-2 solder joints have partially mixed, very coarse microstructure, but the boundary between Sn-Pb and SAC solders no longer exists. Further increasing the peak temperature to 227 °C, Low-1 solder joints have well mixed yet still coarse microstructure. When peak temperature reaches 233 °C, well mixed and fine microstructure occurs in solder joints. Since this is the target microstructure to be achieved, the corresponding reflow profile is called the target reflow profile. Reflow profiles with higher peak temperature and longer dwelling times can also generate fine and homogeneous microstructure (like the one in High solder joints), but it is not necessary to use them when considering solder joint reliability issues caused by thermal damage.

6.6 Discussion and Conclusion

An extensive study on mixed formulation solder alloys has been carried out in this work. 5 mixture solders with different mixing ratios between 63Sn-37Pb and SAC 305 were carefully prepared. The physical properties and microstructure analysis of all 7 solder alloys (including 2 pure solder alloys) has been performed. The application of mixed formulation solder in real electronics package was also investigated.

DSC analysis showed that the melting point of these solders decreased as the 63Sn-37Pb content increased and leveled off beyond 30 wt.%. Pasty range was wide when the composition close to pure SAC 305 or 63Sn-37Pb and turned narrow between 30 wt.% and 70 wt.%.

Microstructure evolved dramatically with the chemical composition. As the 63Sn-37Pb content increased from 10% to 90%, the precipitates in the mixed formulation solders evolved from thin bone-shaped to thick bone-shaped to coarse bone-shaped to pie-shaped, and finally, to coarse pie-shaped particles. Eventually, as the content reached 100%, the typical eutectic structure was observed. EDX analysis indicates that these precipitates are rich in Ag and Pb. Generally speaking, the distinctive microstructure of these mixed formulation solder alloys will play a dominant role in determining their mechanical properties.

Microstructures of BGA solder joints in real electronics packages were observed by using Nomarski optical microscopy. Specimens under investigation were treated with different reflow profiles differing in their peak temperatures and dwelling times above the melting points of both Pb-free and Sn-Pb solders. It is found that the higher the reflow peak temperature is, the longer the dwelling times are, the finer and more homogeneous microstructure will form in the solder joint. Nonetheless, a target reflow profile exists, which takes both homogeneity of microstructure and other aspects of solder joint reliability into consideration.

Chapter 7
Effects of Aging on Mechanical Properties and Creep Behavior of Mixed Formulation Solders

7.1 Introduction

Both benefits and uncertainties involved in the interim stage during the transition from Sn-Pb to Pb-free soldering technology have been extensively investigated. One critical issue that causes contradiction in study is the compatibility between Pb-free solders (especially Sn-Ag-Cu system) and Sn-Pb solders. For example, area array components (BGA/CSP) with SAC solder balls are often assembled to printed circuit boards using traditional 63Sn-37Pb solder paste. Some studies suggest improved reliability of solder joints, whereas others indicate inferior performance. This contradiction primarily roots in the lack of data on the mechanical properties of Sn-Ag-Cu + Pb alloy formed at solder joints.

In this study, seven mixed formulation solders (as defined in Chapter 6) were aged at room (25 °C) and elevated temperatures (100 °C) over various periods of time. For each solder alloy, the mechanical properties such as elastic modulus and strengths were characterized as a function of aging time by conducting tensile tests. The obtained raw stress-strain data were fitted by using the two-function empirical model introduced in Chapter 3 (Eq. 3.4 and 3.5) and mechanical properties were determined from the model fitted curve of mixed formulation solders. Furthermore, aging effects on creep behavior of mixed formulation solders were studied by using the same aging matrix and empirical mathematical creep model described in Chapter 5.

7.2 Aging Effects on Stress-Strain Response of Mixed Formulation Solders

Uniaxial tensile specimens were prepared by using the casting method and water quenching profile (no reflow treatment involved) shown in Chapter 3, followed by up to sixty days aging at room and elevated aging temperatures (T = 25 and 100 °C). Specimens for each alloy were tested in sets of ten, which were subjected to a specific set of aging conditions (aging temperature + aging time) prior to test. A test matrix defined by aging temperature and time for current tensile experiments is listed in Table 7.1. All tensile tests were conducted at room temperature (25 °C) with aged specimens under constant strain rate $\dot{\varepsilon} = 0.001$. Figures 7.1-7.7 illustrate the typical model fitted stress-strain curves of all the seven mixed formulation solders. In each figure, there are two graphs for the two different aging temperatures. On each graph, each individual stress-strain curve represents the result of 10 individual tensile tests on a statistical basis for different aging times, illustrating the evolution of the stress-strain response of mixed formulation solders as a function of aging duration.

Table 7.1 Aging Matrix for Tensile Tests of Mixed Formulation Solders

	Aging Time (days)							
Aging Temperature	As W.Q.	5	10	15	20	30	45	60
25 °C (R.T.)	X	X	X	X	X	X	X	X
100 °C	X	X	X	X	X	X	X	X

X: Test Finished, Testing Temperature = R.T., Strain Rate = 0.001/s

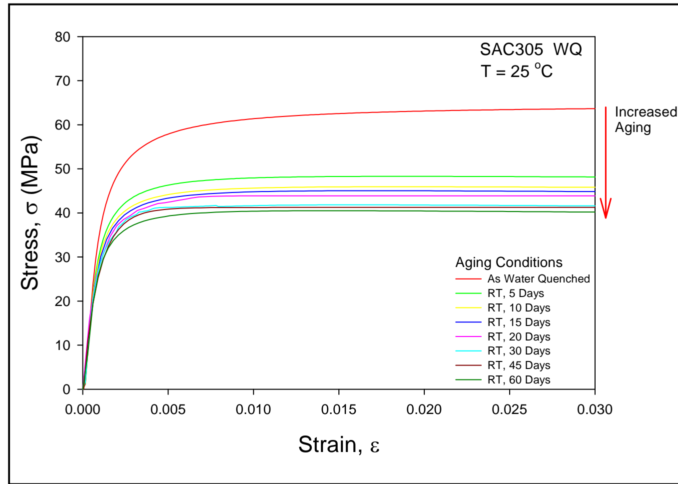

(a) Aging at T = 25 °C

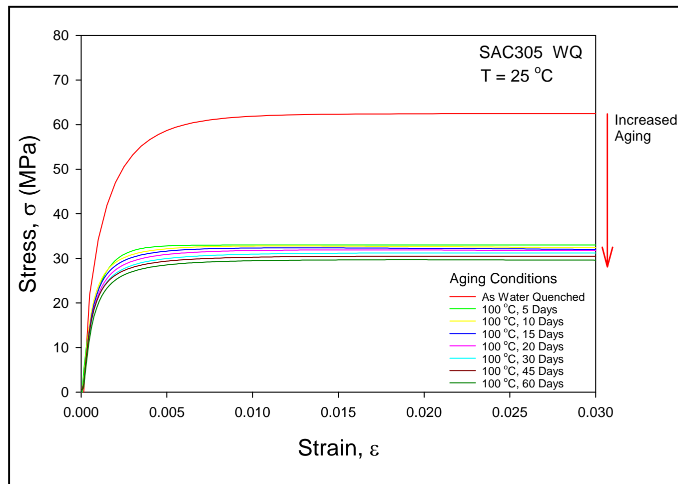

(b) Aging at T = 100 °C

Figure 7.1 Stress-Strain Curves for SAC305 Aged for 0-60 Days

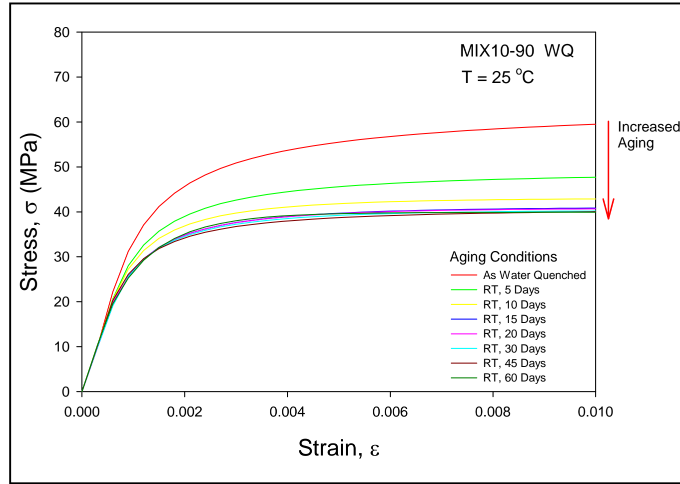

(a) Aging at T = 25 °C

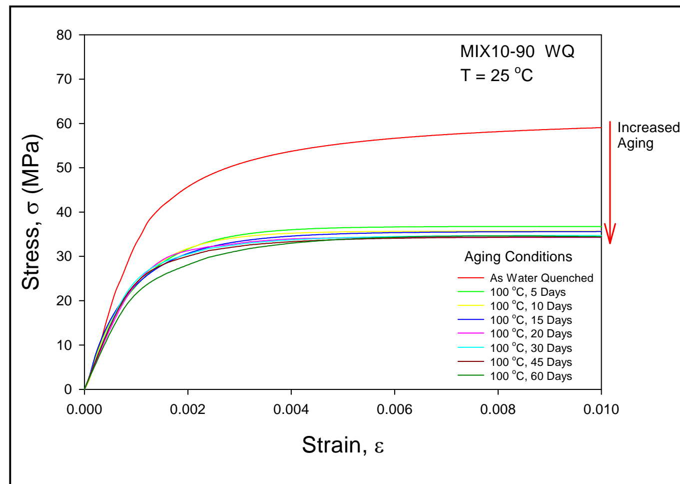

(b) Aging at T = 100 °C

Figure 7.2 Stress-Strain Curves for MIX10-90 Aged for 0-60 Days

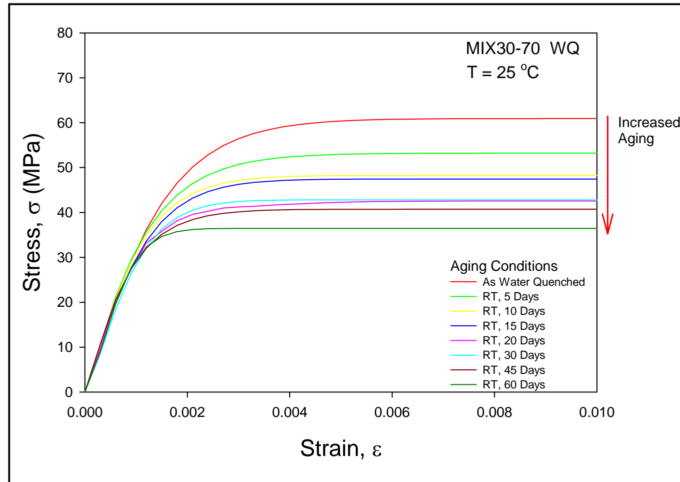

(a) Aging at T = 25 °C

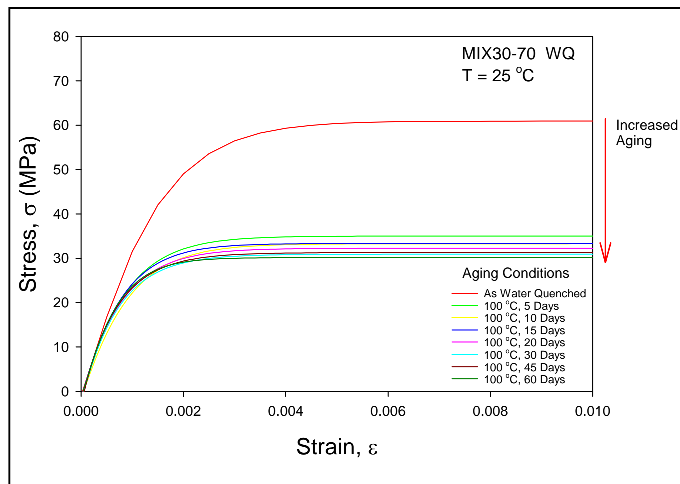

(b) Aging at T = 100 °C

Figure 7.3 Stress-Strain Curves for MIX30-70 Aged for 0-60 Days

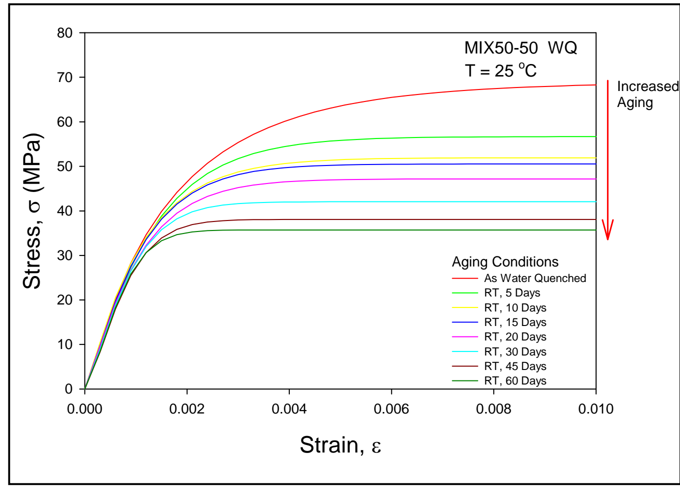

(a) Aging at T = 25 °C

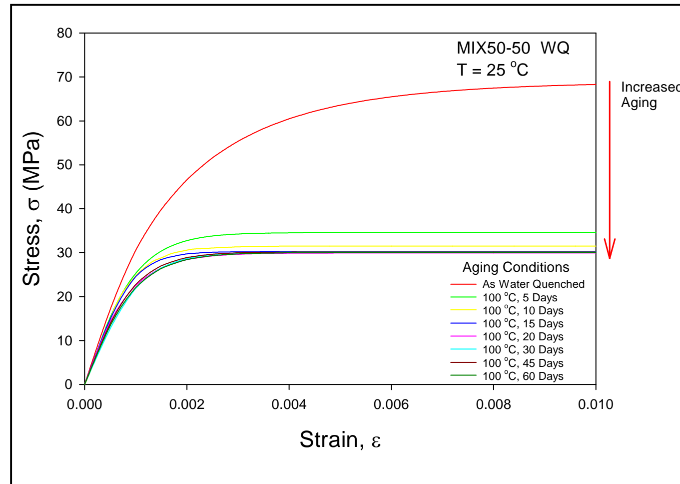

(b) Aging at T = 100 °C

Figure 7.4 Stress-Strain Curves for MIX50-50 Aged for 0-60 Days

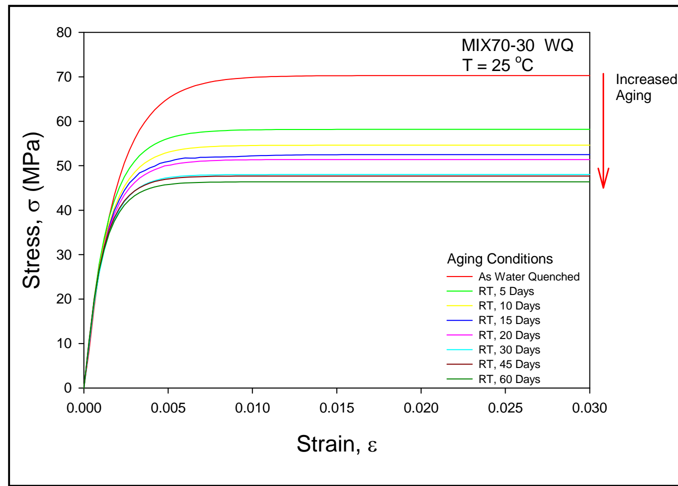

(a) Aging at T = 25 °C

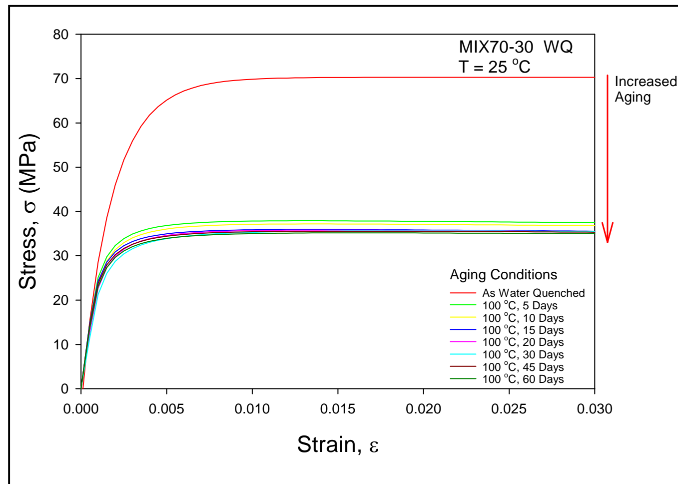

(b) Aging at T = 100 °C

Figure 7.5 Stress-Strain Curves for MIX70-30 Aged for 0-60 Days

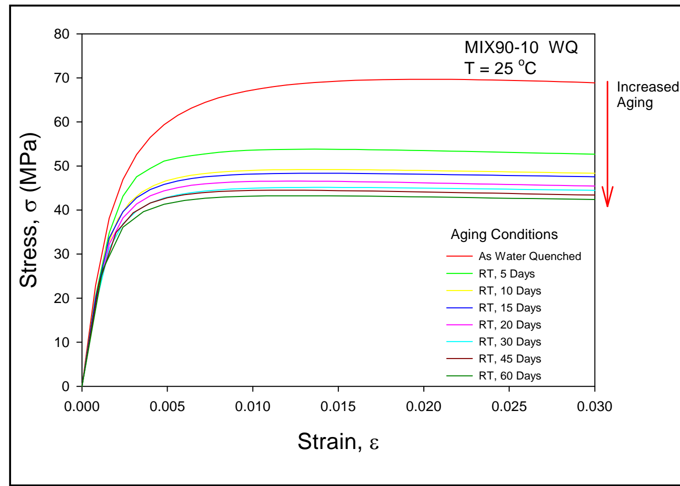

(a) Aging at T = 25 °C

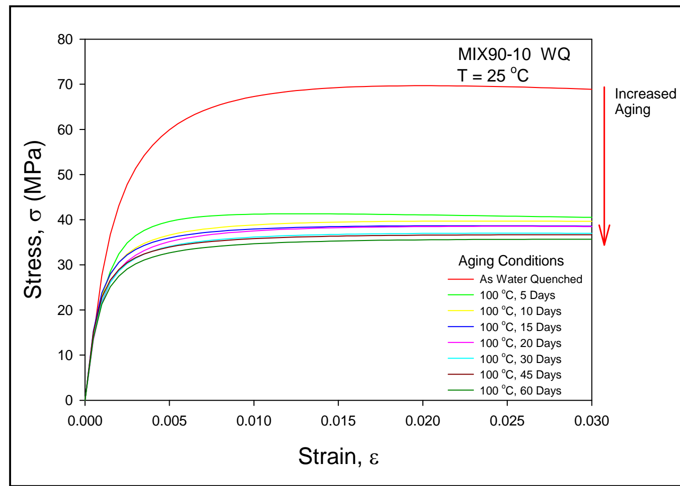

(b) Aging at T = 100 °C

Figure 7.6 Stress-Strain Curves for MIX90-10 Aged for 0-60 Days

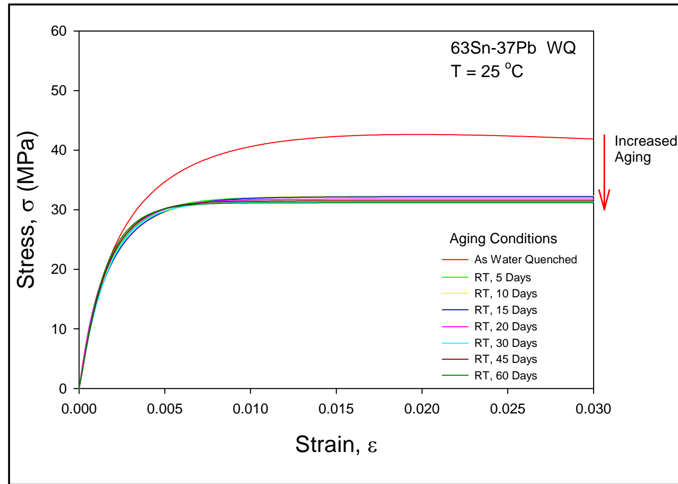

(a) Aging at T = 25 °C

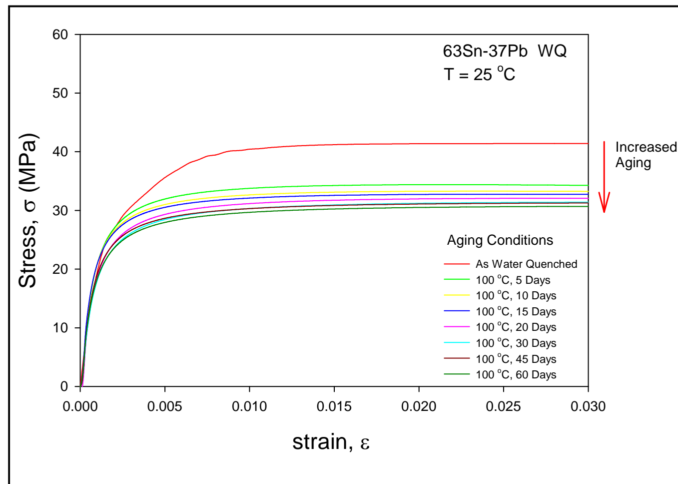

(b) Aging at T = 100 °C

Figure 7.7 Stress-Strain Curves for 63Sn-37Pb Aged for 0-60 Days

7.3 Effects of Aging on Elastic Modulus

Elastic modulus or Young's modulus of mixed formulation solders can be determined from the slope of the elastic portion of the model-fitted stress-strain curves shown in last section.

The variation of elastic modulus with different 63Sn-37Pb content before aging effect set in is shown in Figure 7.8. It can be seen that in the water quenched state, the value of elastic modulus decreased in a linear fashion as 63Sn-37Pb content increased from 0 wt.% to 90 wt.%. Then, the E value experienced a sudden drop all the way down to the value of pure 63Sn-37Pb. However, when aging process took effects, elastic modulus of mixed formulation solders started to change with aging time and aging temperature based on their specific 63Sn-37Pb contents. The change of E values as a function of aging time are illustrated in Figures 7.9-7.10 for all the solder alloys aged at two different aging temperatures.

It can be found that for each individual solder alloy and under certain aging temperature, the elastic modulus basically remained constant over the 60-day period of aging. This constancy indicates that within the given time frame, aging had no strong influence on the elastic modulus. In contrast, the 63Sn-37Pb content played a dominant role in determining the elastic modulus of mixed formulation solders because of the addition of Pb element that resulted in different chemical composition and therefore changed the crystal structure of solder alloys. As consistent with Figure 7.8, the E values of all mixed solders are higher than that of pure 63Sn-37Pb and decrease with increasing 63Sn-37Pb content. Aging temperature has effects on elastic modulus. Under room temperature, almost no change in elastic modulus of each individual solder alloy was observed as aging progressed, but at elevated temperature (100 °C), E values of solder alloys dropped quickly in the first a few days of aging and tended to stabilize within a smaller range. SAC305 and 63Sn-37Pb experienced the most and least change in elastic modulus respectively.

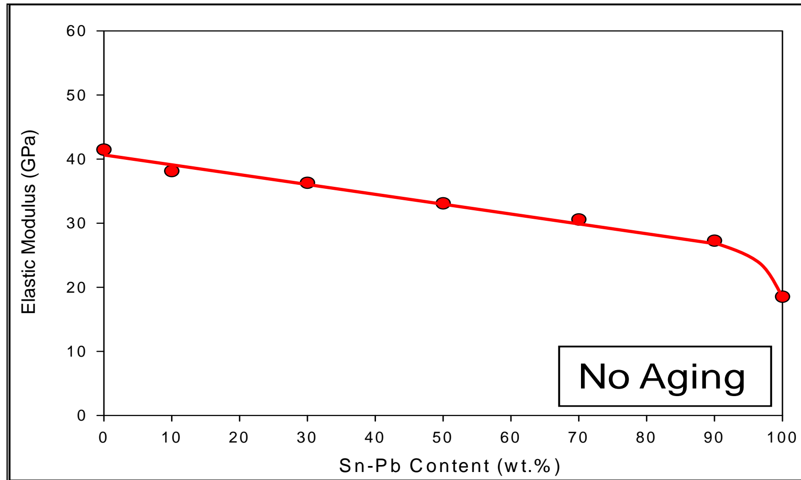

Figure 7.8 Elastic Modulus Variation with 63Sn-37Pb Content

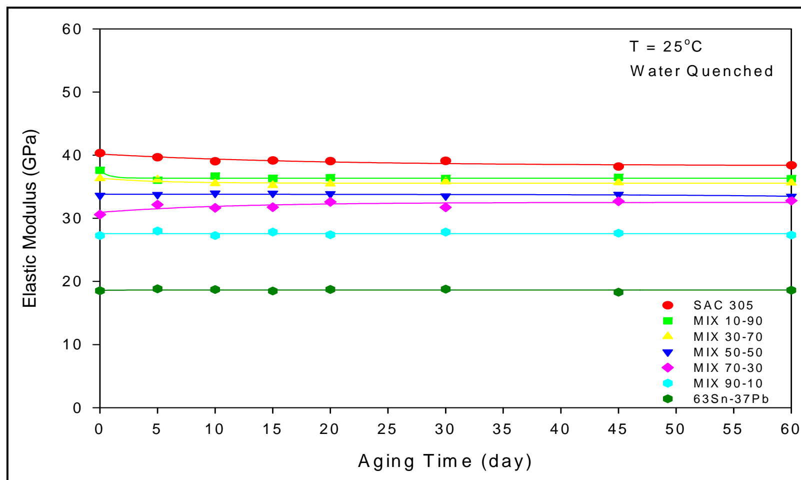

Figure 7.9 Change of Elastic Modulus under R.T. Aging

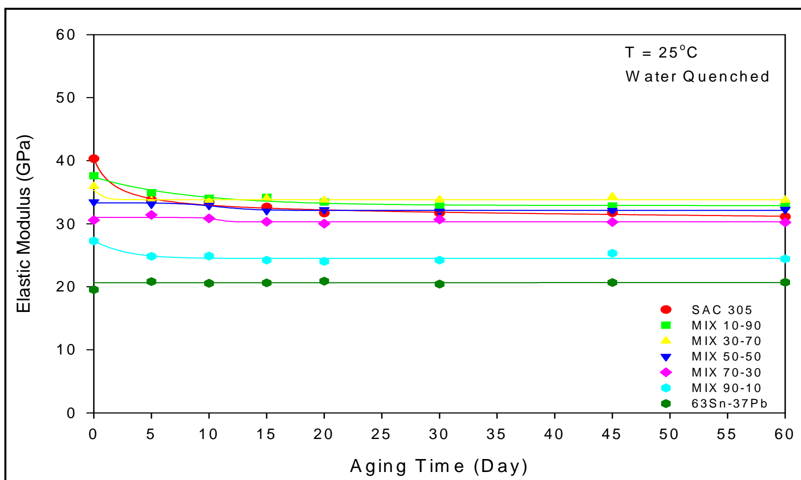

Figure 7.10 Change of Elastic Modulus under 100 °C Aging

7.4 Effects of Aging on Yield Strength

The yield strength of mixed formulation solders is taken to be the standard 0.2% yield stress σ_{ys} (upon unloading, permanent strain $\varepsilon = 0.002$ on the model-fitted stress-strain curves).

The variation of yield strength with different 63Sn-37Pb content under non-aging condition is demonstrated in Figure 7.11. The value of yield strength decreased as 63Sn-37Pb content increased from 0 wt.% to 70 wt.% by following a linear pattern. Beyond this point, the yield strength started to drop quickly and finally reached the lowest value of pure 63Sn-37Pb. When aging effects kicked in, yield strength of each mixed formulation solder changed independently over time based on its specific 63Sn-37Pb content. The changes of yield strength as a function of aging time are illustrated in Figures 7.12-7.13 for all the solder alloys aged at both room and elevated temperatures. It can be seen that aging temperature, time and chemical composition all have significant effects on yield strength of mixed solder alloys.

As aging time increased, the yield strength decreased in a very nonlinear manner. Generally, the yield strength dropped rapidly in the first 5 days of aging and then gradually leveled off. The decreasing rate primarily depended on the content of 63Sn-37Pb in mixtures. Under room temperature, the yield strength of pure 63Sn-37Pb was found to have no significant change over 60 days of aging and the yield strength of MIX 50-50 showed no sign of leveling off until aging after 30 days. Under elevated temperature, it took much less time for the yield strength of mixed formulation solders to stabilize. Meanwhile, the values of yield strength unanimously dropped toward such a level as low as that of pure 63Sn-37Pb. Also, pure SAC 305 (0 wt.% of 63Sn-37Pb) was found to have experienced the maximum loss in yield strength. The peak values occurred at 70 wt.% of 63Sn-37Pb content (MIX 70-30) and 90 wt.% (MIX 90-10) for room temperature and elevated temperature respectively within the given aging time.

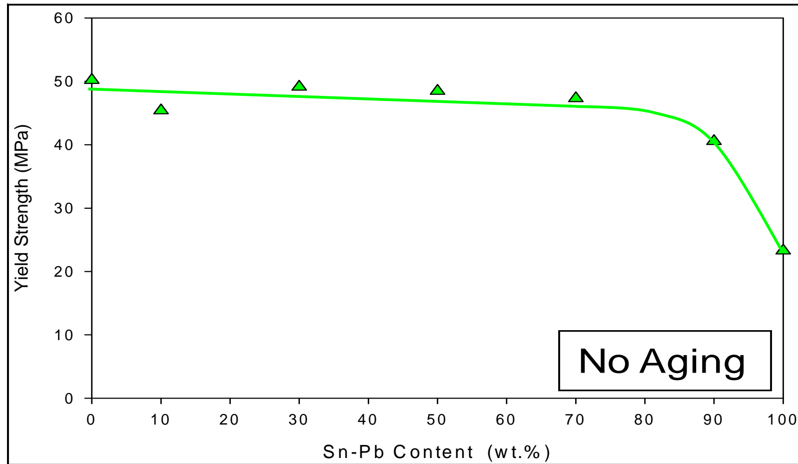

Figure 7.11 Yield Strength Variation with 63Sn-37Pb Content

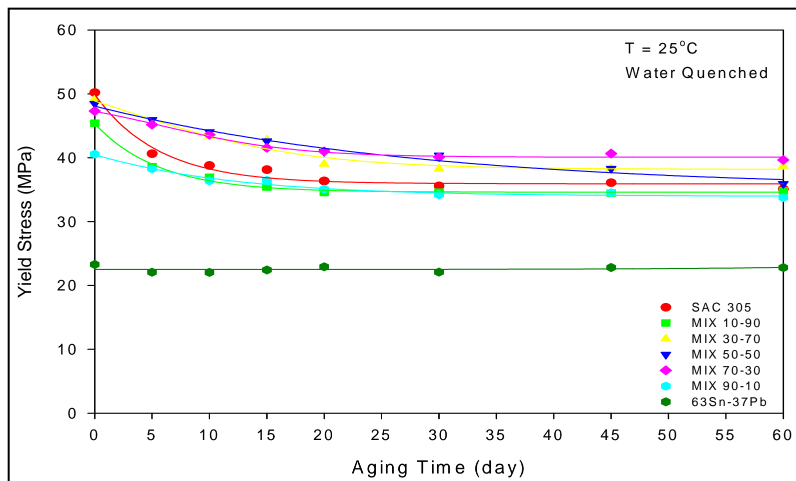

Figure 7.12 Change of Yield Strength under R.T. Aging

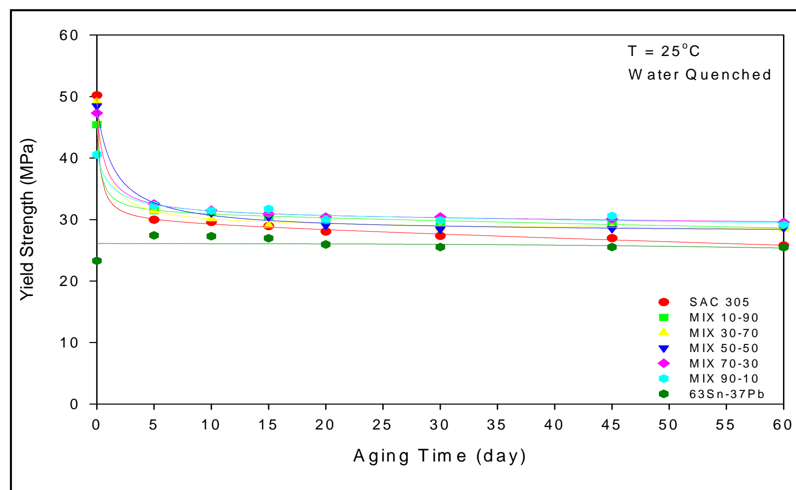

Figure 7.13 Change of Yield Strength under 100 °C Aging

7.5 Effects of Aging on Ultimate Tensile Strength

The ultimate tensile strength (UTS) of mixed formulation solders is defined as the maximum load divided by the initial cross-sectional area of solder specimen. It indicates the maximum stress level that the material can withstand before failure under uniaxial loading.

The variation of UTS with 63Sn-37Pb content without aging is shown in Figure 7.14. Different from the yield strength, the UTS varied nonlinearly as 63Sn-37Pb content changed. The value of UTS decreased from 0 wt.% to about 30 wt.% of 63Sn-37Pb and then started to increase till the content reached 50 wt.%. After that, the UTS relatively maintained constant all the way up to 90 wt.%, but above this point, the UTS dropped quickly and finally down to the lowest value of pure 63Sn-37Pb. However, when aging took effects, the change in UTS of mixed formulation solders presented entire different scenarios due to their specific 63Sn-37Pb contents. The changes of UTS as a function of aging time are illustrated in Figures 7.15-7.16 for all the solder alloys aged at both room and elevated temperatures.

It can be found that aging had significant influences on the UTS of all mixed formulation solders (including pure 63Sn-37Pb) under both room and elevated temperatures. The UTS dropped rapidly in the first 5 days and then gradually stabilized. However, there was exception: The UTS of MIX 50-50 decreased at a much higher rate than other solder alloys and tend not to level off as aged at room temperature. At elevated temperature, similar to yield strength, less time was used for the UTS of mixed formulation solders to stabilize and the values of UTS converged to a narrow range with its lower limits near the UTS value of pure 63Sn-37Pb. Also, pure SAC 305 (0 wt.% of 63Sn-37Pb) experienced the maximum loss in UTS at this temperature. The peak values of UTS occurred at 70 wt.% of 63Sn-37Pb content (MIX 70-30) and 90 wt.% (MIX 90-10) for room and elevated temperature respectively within 60-day aging.

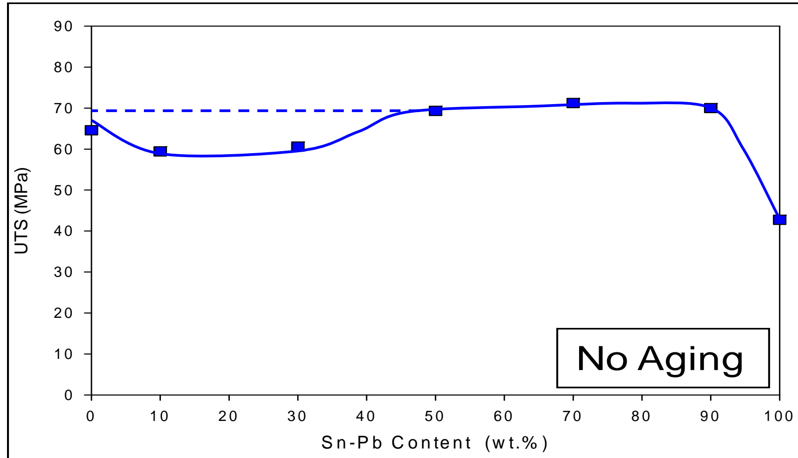

Figure 7.14 UTS Variation with 63Sn-37Pb Content

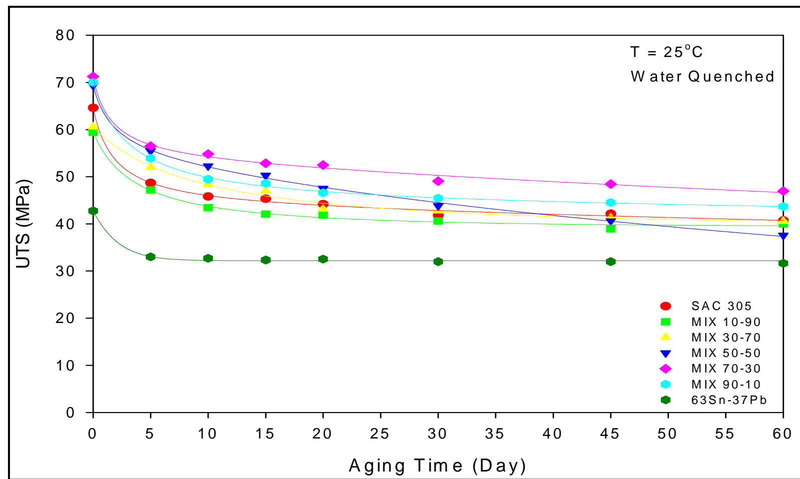

Figure 7.15 Change of UTS under R.T. Aging

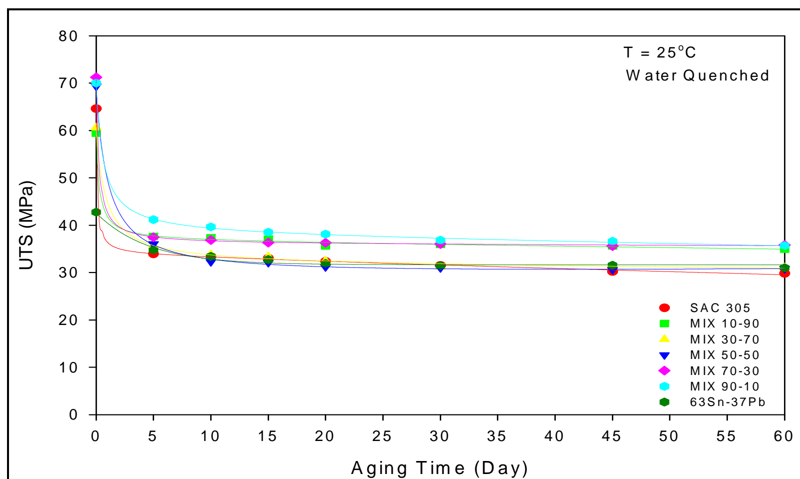

Figure 7.16 Change of UTS under 100 °C Aging

7.6 Fractography Analysis of Failed Specimens

In order to gather more information on the mechanical behavior of mixed formulation solders, fracture surfaces of failed tensile specimens were observed by using SEM to understand the aging effects on the failure mode of these solder alloys.

A series of micrographs of fractured area on failed specimens are shown in Figure 7.17. All specimens were tested immediately after water quenching and before any aging effects set in. It can be found that mixed formulation solders exhibited typical ductile fracture characteristics under non-aging condition and the dimple morphology was greatly influenced by the content of 63Sn-37Pb. The higher the content is, the more dimples can be found across the fractured area, and the more ductile the mixed formulation solder will be.

However, after specimens were aged at certain temperatures for certain period of time, change in failure mode took place. Fracture surfaces of specimens tested after 60-day aging at room temperature (25 °C) and elevated temperature (100 °C) are shown in Figures 7.18 and 7.19. Compared with non-aged specimens, although all solders failed more or less in a ductile way, the transgranular characteristics became less evident in fractured specimens and a trend from ductile fracture to brittle fracture emerged, which was more significant for solder alloys with less 63Sn-37Pb content (except for pure SAC305). Moreover, higher aging temperature seemed to accelerate the transition (from transgranular to intergranular) in failure mode.

Various strain levels were designated on the model-fitted stress vs. strain curves, which defined the degree of deformation before necking and worked as an indicator of solder ductility. For example, the designated strain level for MIX 10-90, 30-70 and 50-50 was 0.01, and 0.03 for other solder alloys. The low value indicated poor ductility and the dominant role played by the content of 63Sn-37Pb in determining the ductility of mixed formulation solders.

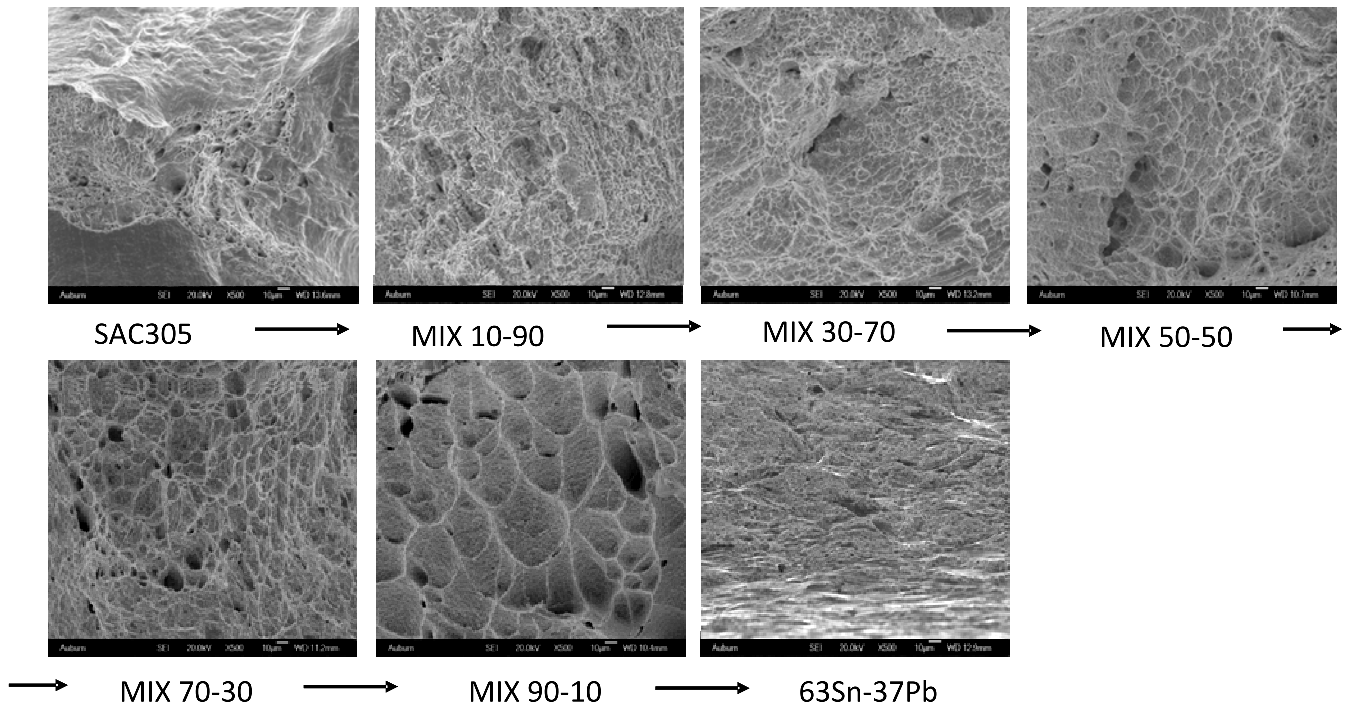

Figure 7.17 Fracture Surface of Failed Tensile Specimens (as Water Quenched)

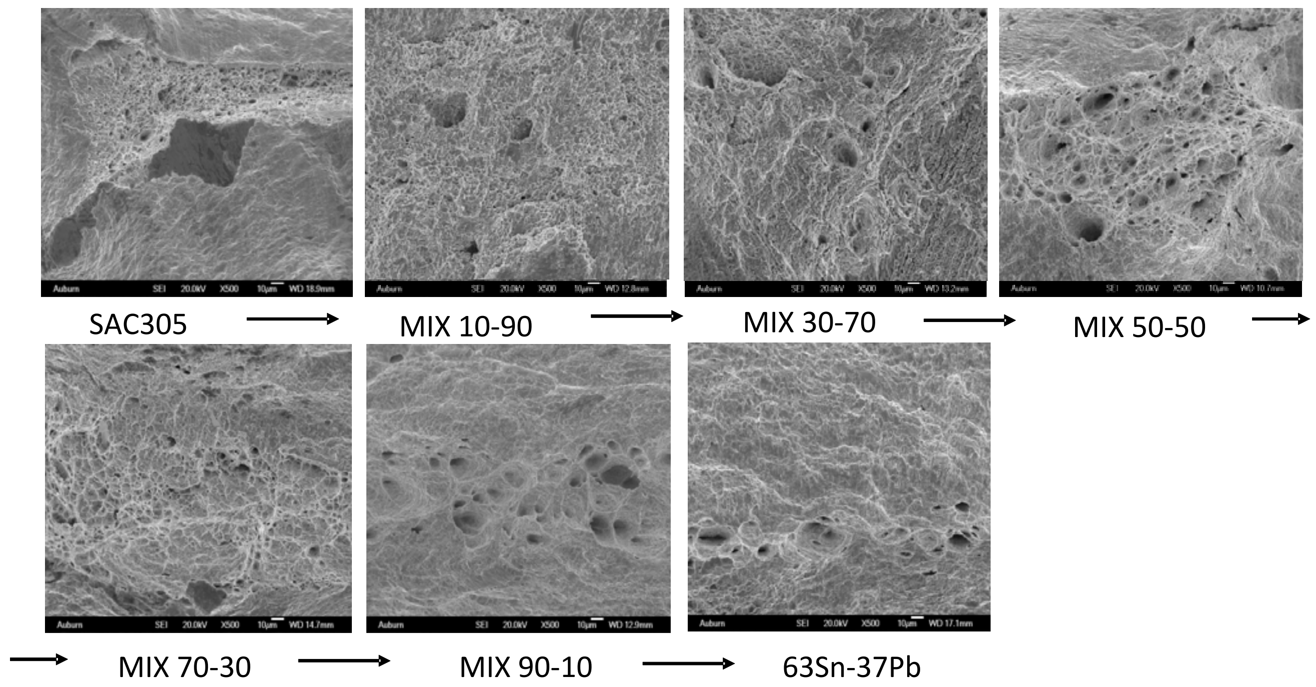

Figure 7.18 Fracture Surface of Failed Tensile Specimens (60-days Aging at R.T.)

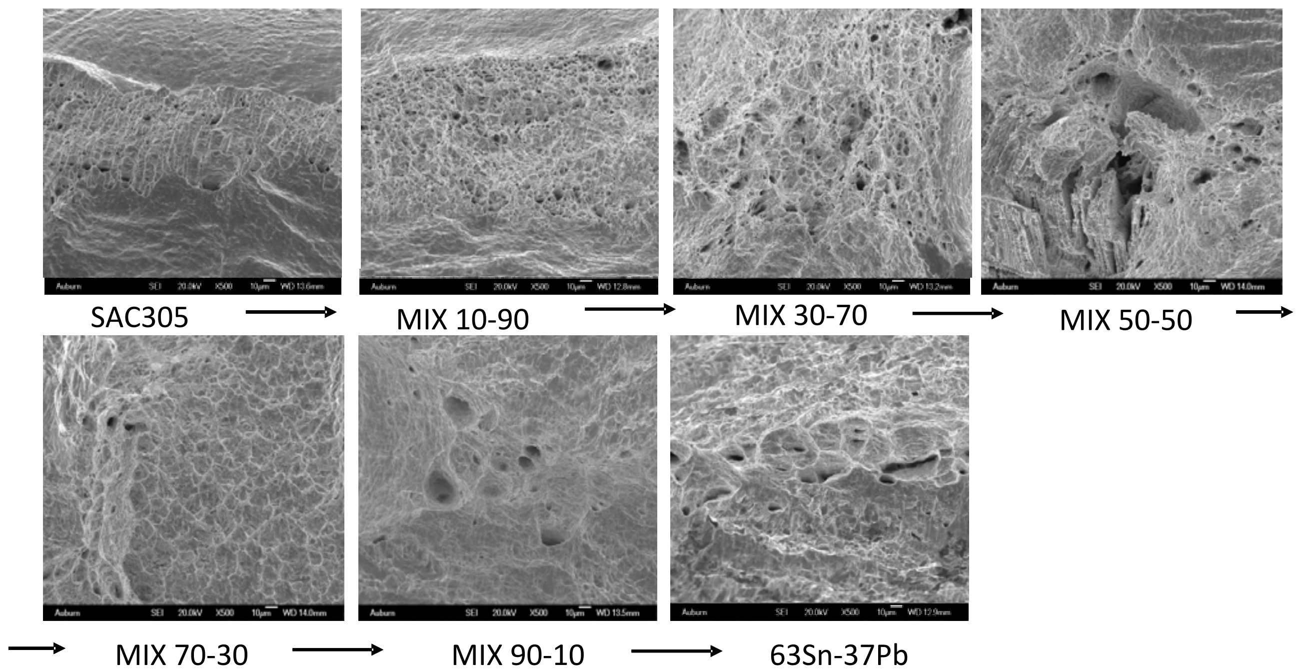

Figure 7.19 Fracture Surface of Failed Tensile Specimens (60-days Aging at 100 °C)

7.7 Effects of Aging on Creep Behavior

Creep tests of mixed formulation solder alloys were carried out at T = 25 °C under constant stress level of 15 MPa. All test specimens were water quenched and then aged at two temperatures for up to 60 days. The aging matrix used is the same as that shown in Table 7.1. The specimens for each alloy were prepared in sets of five, which were then subjected to a specific set of aging conditions (aging temperature and aging time). The typical recorded creep curves for the various solder alloys are illustrated in Figures 7.20-7.26. In each figure, there are two plots for the two different aging temperatures (T = 25 and 100 °C). In each plot, the various creep curves represent tests conducted at different aging times and demonstrate the evolution of the creep response with duration of aging. For brevity and clarity of the presentation, only one of the five available creep curves is shown in each plot for each set of aging conditions.

It can be found that aging temperature has dominant effects on the evolution of creep response of mixed formulation solders. Compared to the dramatic creep evolution for all the solder alloys aged under elevated temperature (100 °C), much less significant creep evolution occurred under room temperature aging (25 °C). Almost no change was observed in the creep behavior of 63Sn-37Pb aged at room temperature, but under the same condition, MIX 90-10 experienced more creep evolution than other mixed formulation solders and SAC305.

The influence of 63Sn-37Pb content is shown in Figure 7.27. Without any aging, the secondary creep strain rate of mixed formulation solders maintained linear until 63Sn-37Pb content went above 70 wt.%. After that, higher content solders had greater secondary creep strain rate, or less creep resistance and finally reached the greatest value of 63Sn-37Pb. When aging took place, under both aging temperatures, same trend was found with all the alloys: relatively constant below 70 wt.% and then rapidly increase in obtained secondary strain rate.

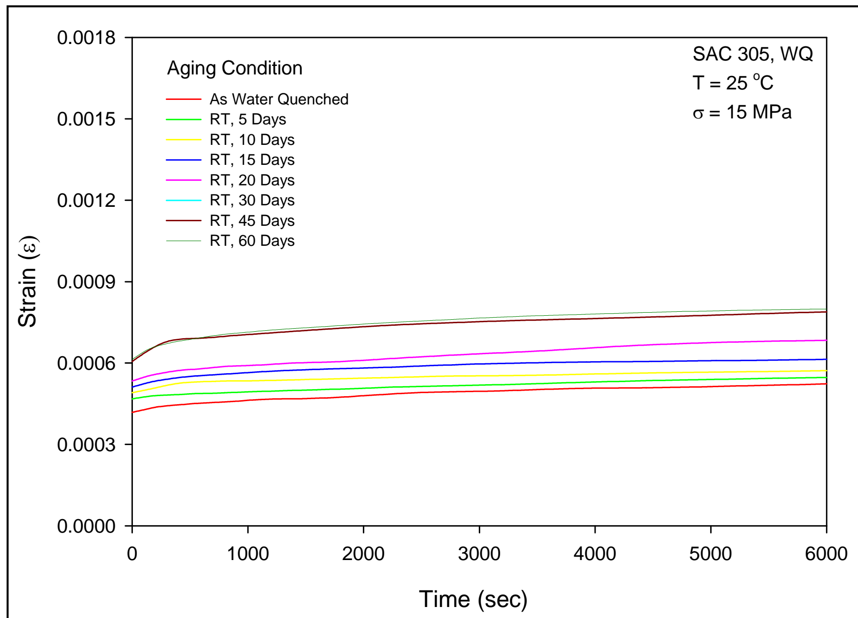

(a) Aging at T = 25 °C

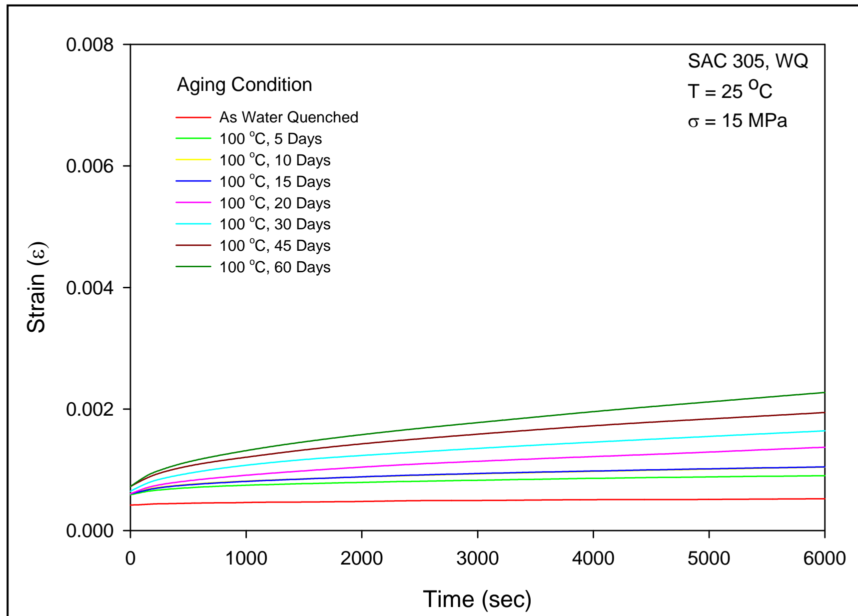

(b) Aging at T = 100 °C

Figure 7.20 Creep Curves for SAC305 for Aging from 0-60 Days

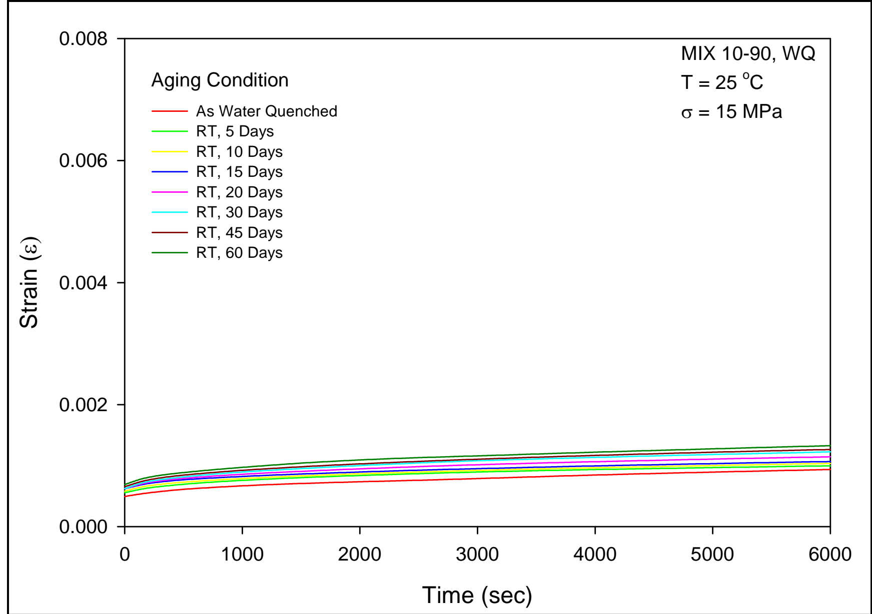

(a) Aging at T = 25 °C

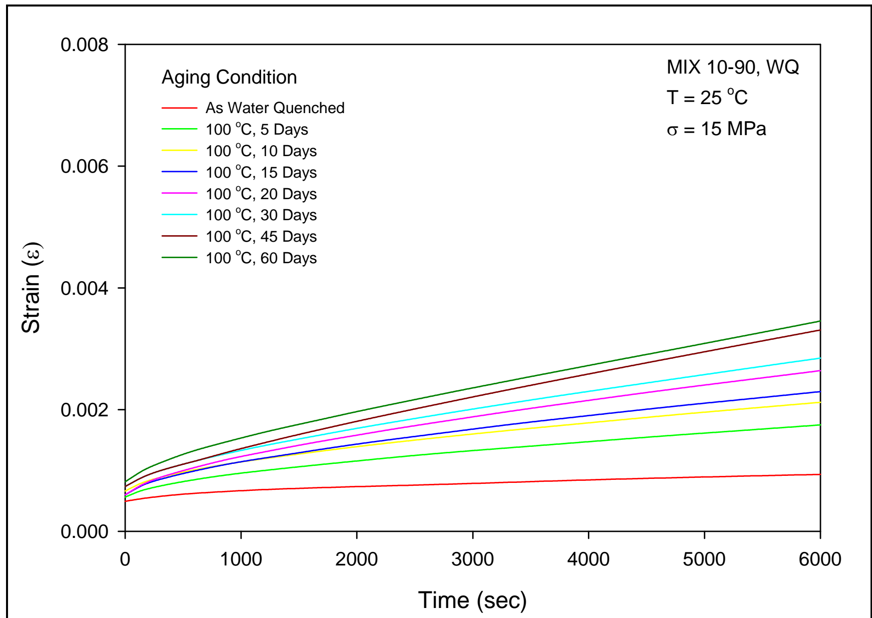

(b) Aging at T = 100 °C

Figure 7.21 Creep Curves for MIX 10-90 for Aging from 0-60 Days

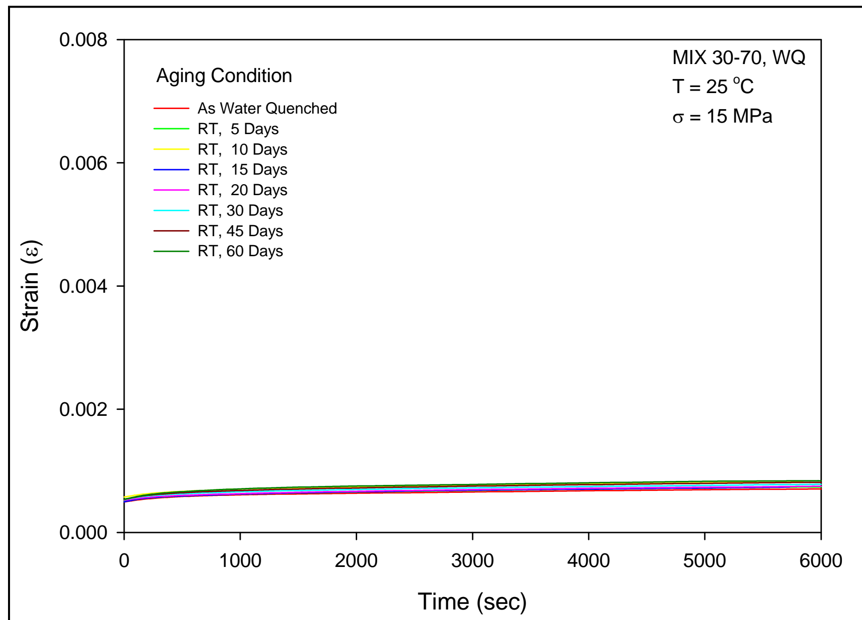

(a) Aging at T = 25 °C

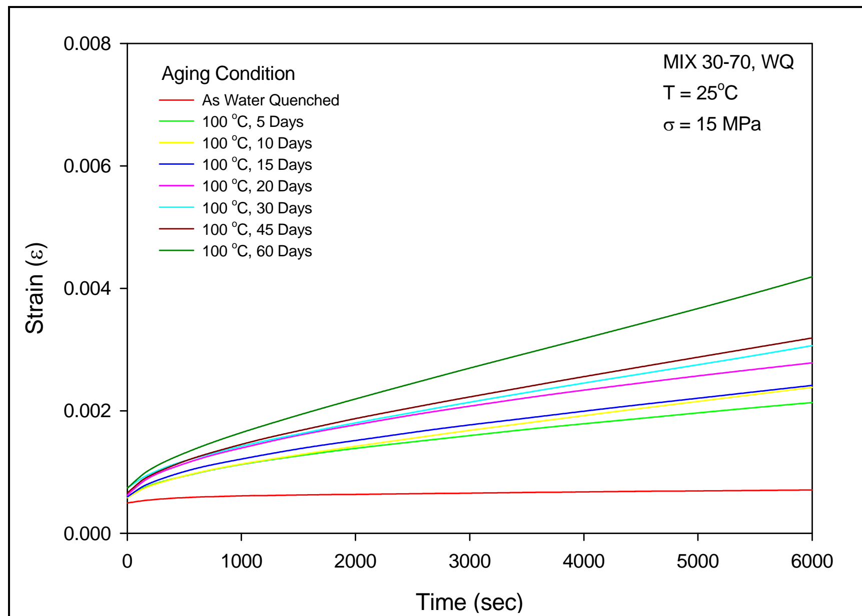

(b) Aging at T = 100 °C

Figure 7.22 Creep Curves for MIX 30-70 for Aging from 0-60 Days

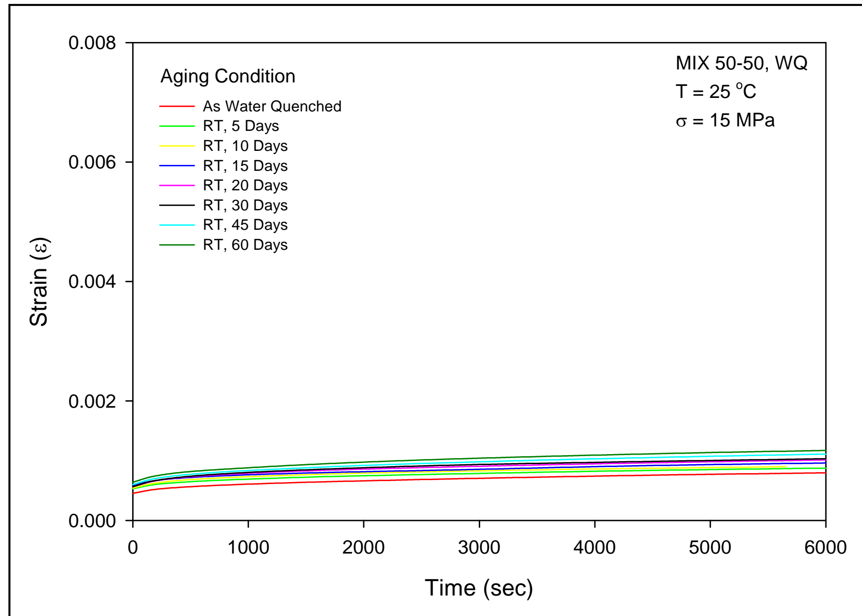

(a) Aging at T = 25 °C

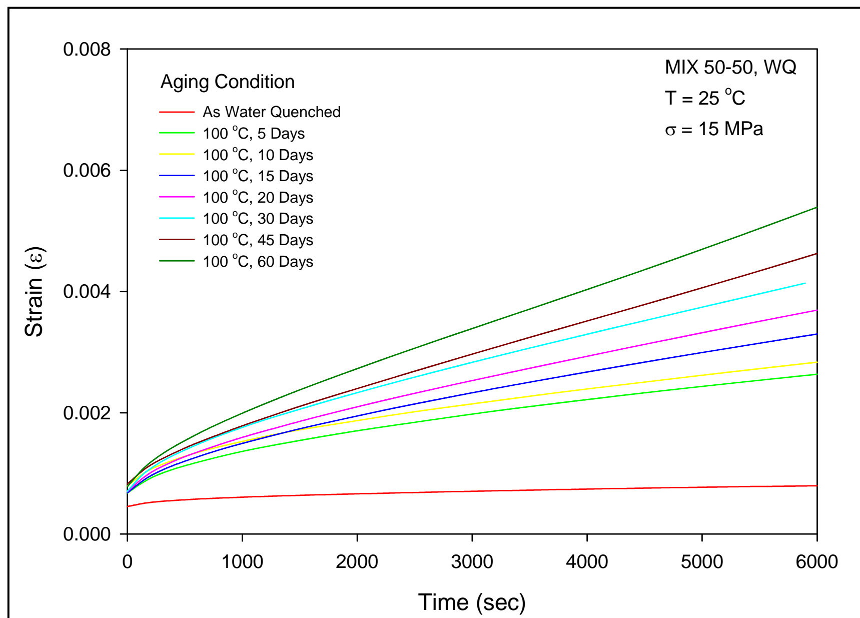

(b) Aging at T = 100 °C

Figure 7.23 Creep Curves for MIX 50-50 for Aging from 0-60 Days

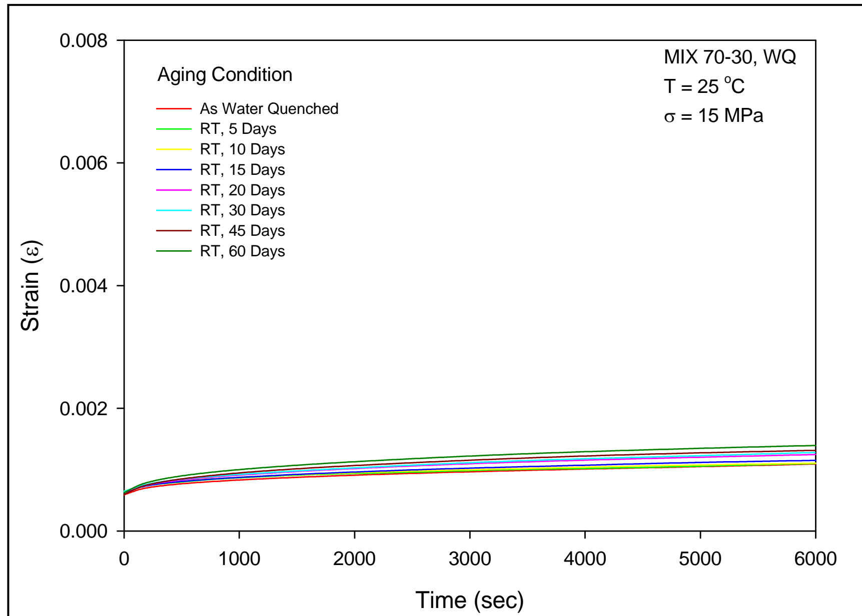

(a) Aging at T = 25 °C

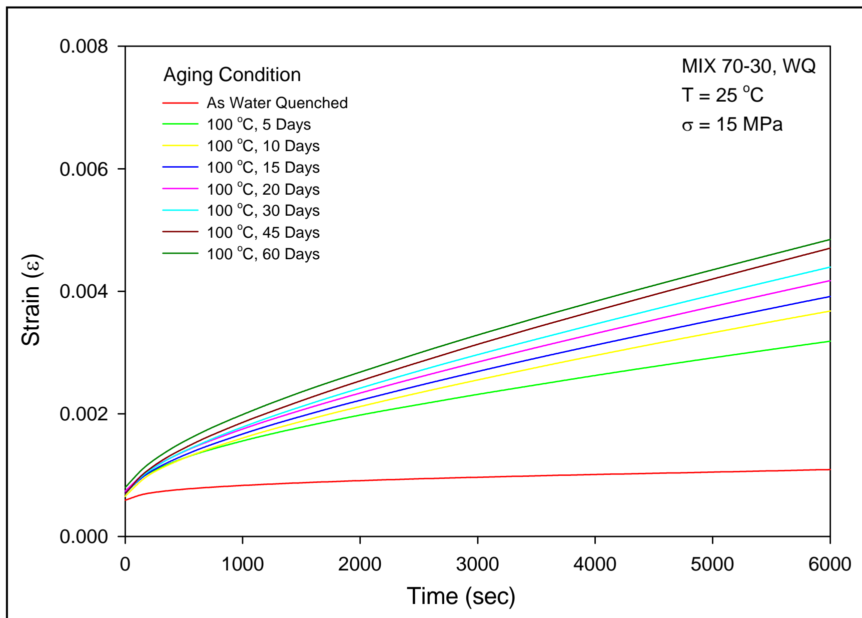

(b) Aging at T = 100 °C

Figure 7.24 Creep Curves for MIX 70-30 for Aging from 0-60 Days

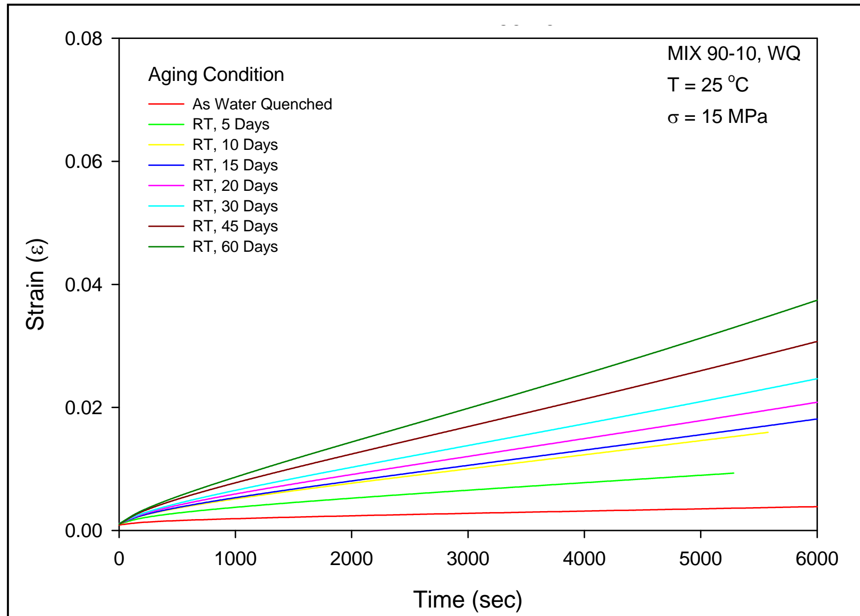

(a) Aging at T = 25 °C

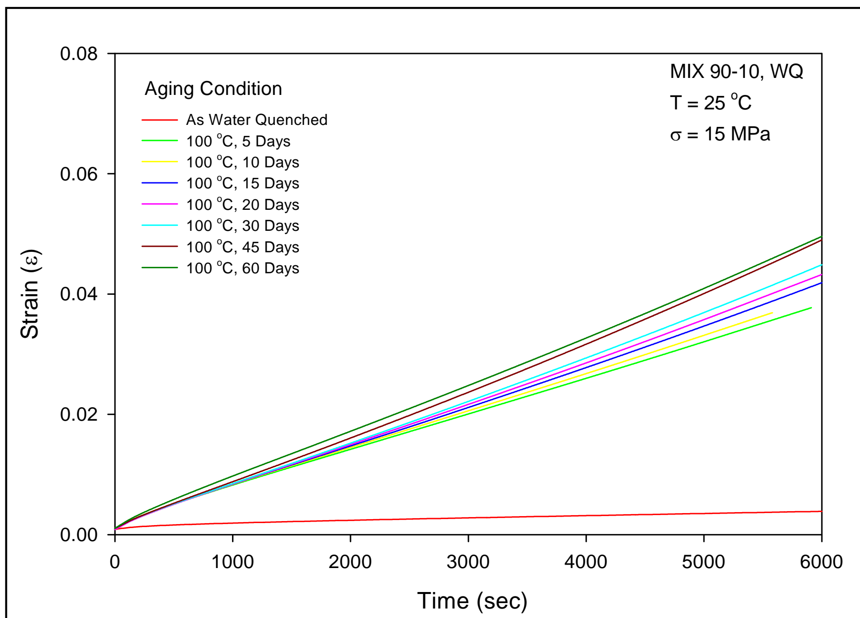

(b) Aging at T = 100 °C

Figure 7.25 Creep Curves for MIX 90-10 for Aging from 0-60 Days

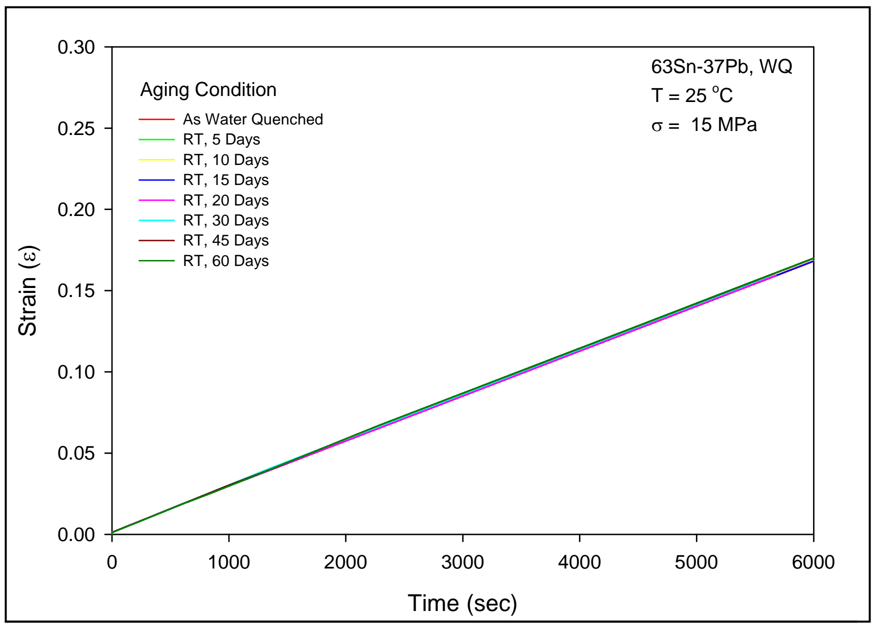

(a) Aging at T = 25 °C

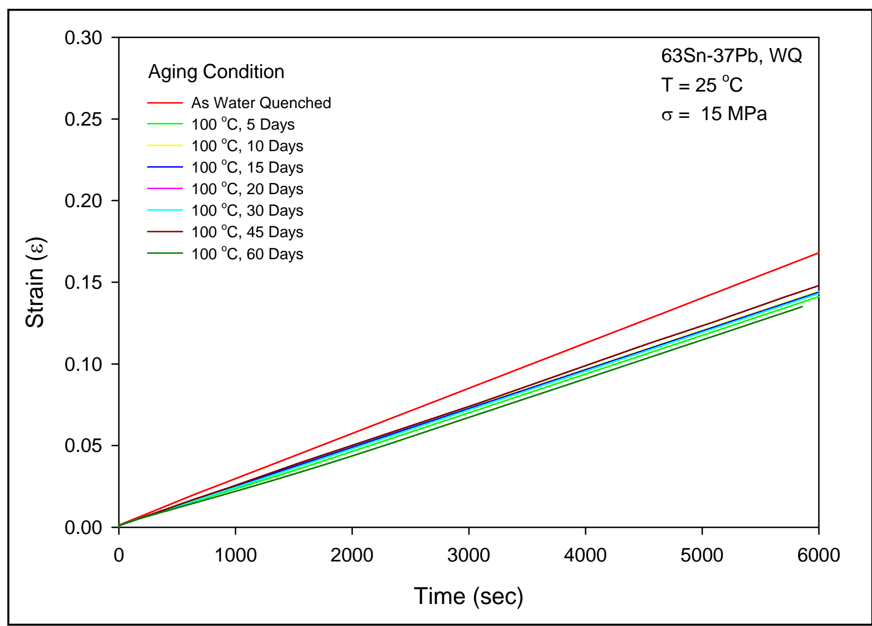

(b) Aging at T = 100 °C

Figure 7.26 Creep Curves for 63Sn-37Pb for Aging from 0-60 Days

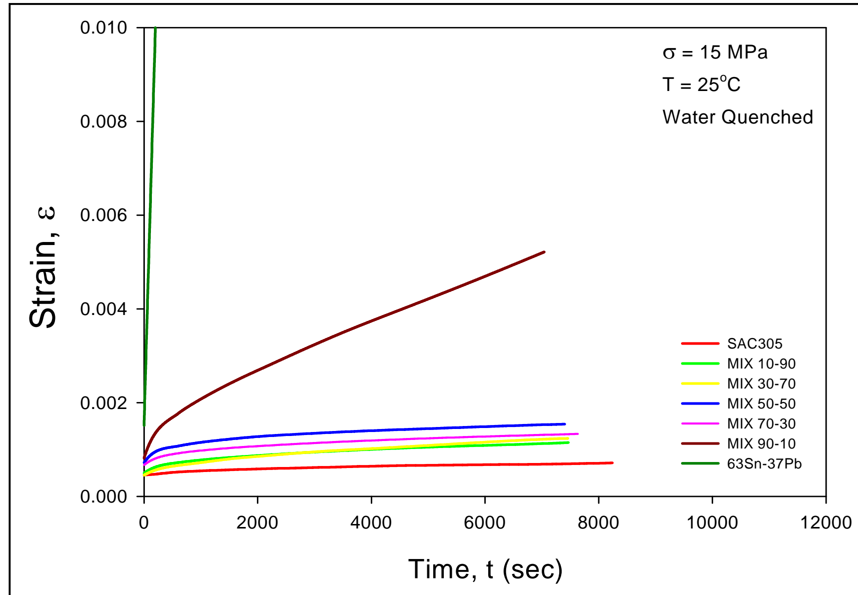

(a) Original Creep Curves (No Aging)

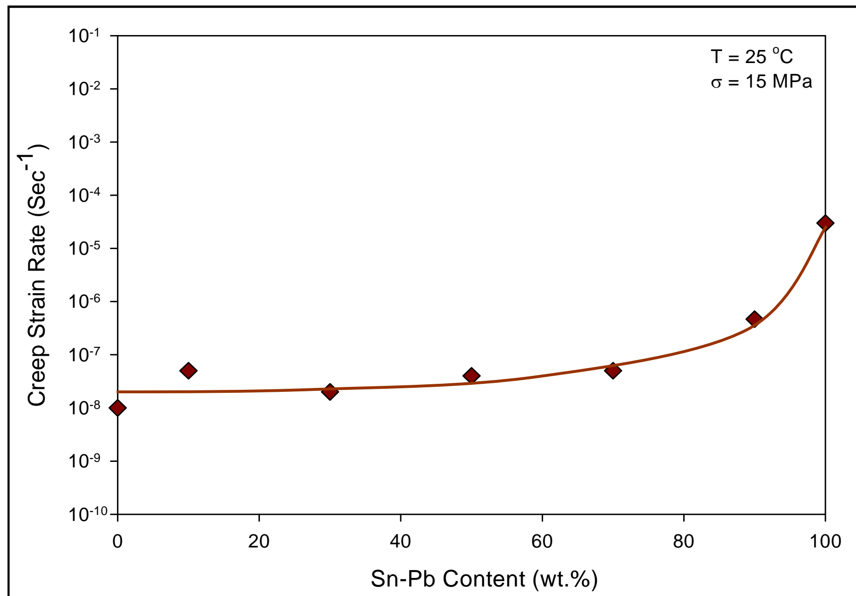

(b) Secondary Creep Strain Rates (No Aging)

Figure 7.27 Evolution of Creep Response with 63Sn-37Pb Content (No Aging)

The effects of aging on the creep behavior of mixed formulation solders can be better seen by plotting the extracted secondary creep rates versus the aging time for each alloy. Based on the empirical mathematical creep model described in Chapter 5 (Eq. 5.1 and 5.2), the evolution of secondary creep strain rate vs. aging time are demonstrated in Figure 7.28 (a) and (b) for room and elevated temperature respectively. On each graph, every single data point represents the averaged creep strain rate of 5 specimens tested at a given set of aging conditions. The four material constants, namely, C_0, C_1, C_2, and C_3 are listed in Appendix III.

It is observed from the Figures that the maximum increase in the creep rate occurred in the first 10 days, after that the strain rate increased in a linear manner for the alloys. Within the 60-day time frame, there was no indication that an aging saturation would be reached when the creep strain rate started to stabilize. Also, the higher the aging temperature was, the faster the alloys would creep. The comparison between the numerical values of the secondary creep strain rates of non-aged specimens and the values of the creep strain rates of the specimens aged for 60 days at 100 °C is shown in Table 7.2, where SAC305 and MIX 30-70 had the greatest change in creep strain rate (27X and 22X) and MIX 10-90 the smallest (only 8.6X).

The creep strain rates of 63Sn-37Pb are found to fall into a very narrow range of values between $\dot{\varepsilon} = 2 \times 10^{-5}$ and $\dot{\varepsilon} = 3 \times 10^{-5}$. However, the aging induced changes in the creep strain rates of other mixed formulation alloys are much larger under the same stress level. At both aging temperatures, the mixed formulation solders and SAC305 began with creep rates much lower than 63Sn-37Pb. As aging progressed, the creep strain rates of these alloys increased continuously. If given enough time (e.g. up to one year), they would approach the creep strain rates of 63Sn-37Pb. By then, they would creep faster and bear less creep resistance than eutectic 63Sn-37Pb, especially for MIX 90-10 due to its high 63Sn-37Pb content.

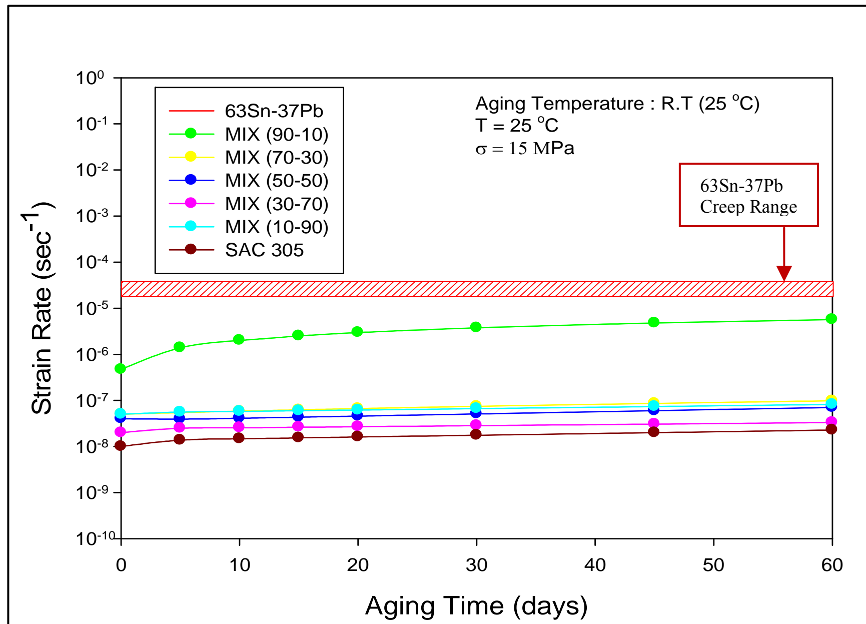

(a) Aging at T = 25 °C

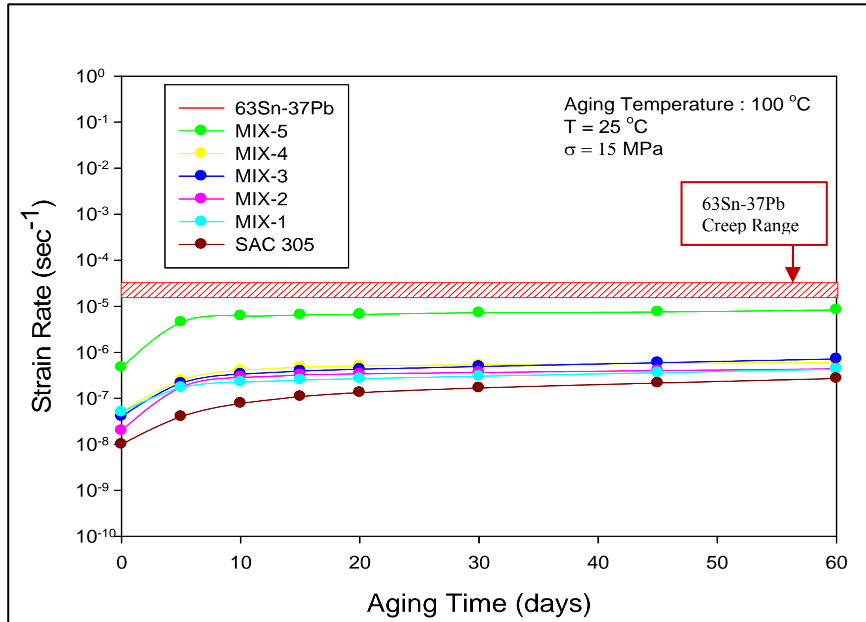

(b) Aging at T = 100 °C

Figure 7.28 Comparison of Creep Strain Rates of Mixed Formulation Solders

Table 7.2 Increase in Creep Strain Rate with Aging (60-days at 100 °C)

Solder	Secondary Strain Rate (with no aging)	Maximum Strain Rate (aging for 60 days at 100 °C)	Increase Ratio
SAC 305	9.98E-09	2.69E-07	27.0X
MIX 10-90	5.00E-08	4.28E-07	8.6X
MIX 30-70	2.00E-08	4.36E-07	21.9X
MIX 50-50	4.01E-08	7.15E-07	17.8X
MIX 70-30	5.00E-08	6.05E-07	12.1X
MIX 90-10	4.67E-07	8.33E-06	17.8X

7.8 Discussion and Conclusions

In this chapter, aging effects on mechanical properties and creep behavior of a series of mixed formulation solder alloys were examined by performing tensile and creep tests with a full aging matrix at two different aging temperatures. There were totally 7 types of mixed formulation solders (including two extreme cases: pure SAC305 and pure 63Sn-37Pb) with different 63Sn-37Pb content under investigation. All test specimens were isothermally aged for up to 60 days at room (25 °C) and elevated (100 °C) temperatures after being water quenched. Then, at different time intervals, aged specimens were tested on the MT-200 testing system with a constant strain rate $\dot{\varepsilon} = 0.001$ for tensile test and a constant stress level $\sigma = 15$ MPa for creep test at ambient temperature. For every specific aging condition, i.e. a specific combination of aging time and temperature, 10 specimens were tensile tested and the obtained raw stress-strain data were fitted by using a two-function empirical mathematic model. The mechanical properties such as elastic modulus, yield strength and UTS were then determined from the model fitted curve for each alloy. Also, for every specific aging condition, 5 specimens were creep tested and the averaged secondary creep strain rates were fitted by using a four-constant empirical mathematic model. The comparison between aging effects on the creep resistance of mixed formulation solders was then conducted based on the model fitted creep strain curves.

The evolution of mechanical properties under the influence of aging exhibited nonlinear pattern to various degrees for different mixed formulation solders. Some general conclusions can be drawn based on the test results and corresponding analysis.

Firstly, as aging time increases, the mechanical strength decreases. It can be found that at both room and elevated temperatures, compared with the relatively stable elastic modulus, yield strength and UTS dropped rapidly in the first a few days of aging and then gradually

leveled off. Elastic modulus, yield strength and UTS of pure 63Sn-37Pb had very limited change over the aging process, especially under room temperature condition. In contrast, pure SAC305 experienced the maximum loss in its mechanical properties with aging.

Secondly, the content of 63Sn-37Pb influences the mechanical properties of mixed formulation solders in a complicated manner. Under room temperature aging, yield strength and UTS decreased as the content of 63Sn-37Pb increased from pure SAC305 all the way to MIX 50-50 and then bounced back up rapidly to its peak values at MIX 70-30. Under elevated temperature (100 °C), similar trends in yield strength and UTS were found with the peak mechanical strength values occurring at MIX 90-10.

Finally, as aging temperature increases, yield strength and UTS of all mixed formulation solders unanimously decreases and the extent of decrease depends on the content of 63Sn-37Pb. Under elevated temperature, it took less time for the mechanical properties to become stabilized, and meanwhile, yield strength and UTS dropped towards a level as low as that of 63Sn-37Pb.

The distinctive microstructure of mixed formulation solders, as shown in Chapter 6, can work as a predictor for the mechanical properties of these alloys. For example, the needle-shaped precipitates in SAC305 play a dual role, i.e. strengthening material as hard precipitations but also causing material failure by providing source and path for crack initiation and propagation. Similarly, the precipitates in mixed solders under MIX 50-50 are more crack source provider than material strengthener due to their bone-like shape and soft particle nature compared with Ag_3Sn in SAC305. In general, this type of precipitate is detrimental to mechanical properties. However, as 63Sn-37Pb content exceeds 50 wt.%, the coarsening process took place and the precipitates changed from bone-shaped particles into pie-shaped particles. Even though these particles are not as strong as that in SAC305, their unique morphology

hinders the formation of crack and retards its spread across the matrix so as to improve the mechanical properties.

Fractography analysis of failed mixed formulation solder specimens showed transition in failure mode (from transgranular to intergranular) during aging. Compared with non-aged specimens that exhibited typical ductile fracture characteristics, all solders failed more or less in a ductile way, but the transgranular characteristics became less evident in fractured specimens and a trend from ductile fracture to brittle fracture emerged, which was more significant for solder alloys with less 63Sn-37Pb content (except for pure SAC305). Moreover, higher aging temperature seemed to accelerate the transition in failure mode.

Analysis of aging effects on creep behavior of mixed formulation solders shows that the maximum change in creep strain rate occurred in the first 10 days of aging, after that the strain rate increased in a linear manner for all the alloys. The higher the aging temperature was, the faster the alloys would creep. Within 60 days, there was no indication of aging saturation when the creep strain rate started to stabilize.

The creep strain rates of 63Sn-37Pb did not vary much under aging and fell into a very narrow range of values. However, the aging induced changes in the creep strain rates of other mixed formulation solders were much larger under the same stress level. At the beginning of aging process, the mixed formulation solders and SAC305 crept much slower than 63Sn-37Pb, but as aging progressed, the creep strain rates of these alloys increased continuously and would end up with much higher values if given enough time. By then, mixed formulation solders would possess less creep resistance and creep faster than eutectic 63Sn-37Pb.

Chapter 8
Conclusions

8.1 Literature Review

Aging has been identified as one of the main causes for the existence of large discrepancies in the property database of soldering materials. Especially given the high homologous temperatures at which solder alloys work, aging affects not only their mechanical properties but also their microstructure. In electronic packages, aging effects take place on bulk solder and solder joints in different ways and to different extent.

The mechanical response of solder joints to external loading can be dramatically different from that of bulk solders under the same aging condition due to the distinctive features that solder joints have such as interfacial intermetallic compounds (interfacial IMCs), fine microstructure and mechanical constraint jointly imposed by substrate and bulk solder. Usually, solder joints have higher strength than bulk solder.

In contrast to the IMC coarsening, coalescing and dispersing in bulk solder, the microstructure evolution of solder joints under aging turns can be much more complicated and requires consideration of such factors as solder bump/solder compositions, the passivation technology or bond-pad metallization in use and the thermal profile of reflow soldering process. The thickness of interfacial IMC layer at solder joints is found to increase by following a square root time law regardless of solder types and substrate surface finishes. Formation of Kirkendall voids can be widely observed in solder joint interface on Cu pad with various surface finishes under solid state thermal aging condition.

To increase the thermal aging resistance of bulk solder and solder joints, metallurgical strengthening approaches, which aim to reinforce not only solder matrix but also matrix/intermetallic interface, are able to offer a solution and can be achieved by adding an alloying element or by using a doping element, e.g. Si, Ti, Cr, Mn, Ni, B or rare earth elements.

The CTE mismatch between the PCB and the IC components generates high mismatch cyclic deformations, which produce complex stress/strain conditions and eventually lead to the failure of solder joints. Therefore, it is necessary to establish reliable constitutive models to describe solder behavior under certain work condition in order to accurately analyze solder joint stress/strain state and predict solder joint life.

The classical elastic-plastic-creep constitutive model consists of four components, namely, elastic, plastic, time-dependent primary (transient) creep, and steady-state creep strain components. Starting from this model, study on constitutive modeling of material behavior of solder alloys has been vastly performed and various stress-strain curve models and constitutive models of creep deformation have been proposed by researchers so far.

Anand viscoplastic model, which was developed for describing the rate-dependent deformation of metals at high temperatures, has been adopted successfully to represent the viscoplastic behavior of solders alloys. This constitutive model unifies both rate-dependent creep behavior and rate-independent plastic behavior occurring concurrently in solder alloys.

Solder joint reliability modeling and life prediction are very important in evaluating the intended application of electronic packages at early stage of product design. Over past two decades, enormous efforts have been taken to study the life prediction of solder joints with different solder alloys and various packaging techniques. As a result, a number of modeling methods have been brought into real application in the electronics packaging industry.

8.2 Specimen Preparation and Experimental Procedures

A unique specimen preparation method is introduced for the purpose of eliminating specimen variation and ensuring microstructure uniformity. Compared with other specimen making approaches, this method has two unique features: (1) Small specimen dimensions that minimize the waste of solder alloys; (2) Net shape technique that requires no further machining operations on specimen.

All solder test specimens are formed in Pyrex glass tubes with high precision rectangular cross-section using an induction melting + vacuum suction specimen preparation system. The typical specimen dimensions are length (80) x width (3) x thickness (0.5) mm. Water quenching and controlled reflow oven cooling are used before aging treatment and test.

Uniaxial tension and creep tests are carried out on a multifunctional tension/torsion thermo-mechanical test system to determine the material properties of solder alloys of interest. Moreover, a two-function empirical mathematical model based on truncated stress-strain curves is developed to characterize the stress-strain response of solder alloys.

Microstructure analysis is conducted on Epoxy potted specimens. Various techniques such as OM, SEM, EPMA, are employed in order to obtain high quality micro-images of solder alloys. Other analytical methods in use are DSC, EDX, etc.

8.3 Aging Effects on Mechanical Properties of SAC Alloys

Aging effects on mechanical properties of SAC solder alloys were examined by performing tensile tests based on a full test matrix of aging time, temperature and solder alloys. The mechanical properties such as Elastic modulus, yield strength and UTS were determined from model fitted curves for each SAC alloy. The microstructure evolution of SAC alloys as

well as its influence on the mechanical properties and failure behavior during aging was studied. Analogous experiments were performed with 63Sn-37Pb specimens for comparison purposes.

The mechanical properties of SAC alloys decreased with increasing aging time and temperature. High Ag content SAC alloys were found to have better aging resistance. The change of elastic modulus can be described by a 3-parameter exponential model (Eq. 4.1) for SAC alloys, but the elastic modulus of 63Sn-37Pb basically remained unchanged across the entire aging matrix and can be characterized by a narrow range. The change of yield strength and UTS of both SAC and 63Sn-37Pb can be depicted by a 3-parameter hyperbolic model (Eq. 4.2 and Eq. 4.3). Compared with SAC, 63Sn-37Pb showed better aging resistance.

The aging induced microstructure coarsening is the fundamental reason behind the mechanical property deterioration of solder alloys. Increase in grain size and phase structure will lead to reduction in tensile strength because coarsened grains and second phase particles will lose their effectiveness in blocking dislocation movement due to fewer grain boundaries and weaker precipitation pinning effect in SAC alloys. For 63Sn-37Pb, the eutectic structure does not contain any second phase, but the solder experienced significant loss in its tensile strength too. The precipitation of β-Sn out of the supersaturated Pb-rich phases during aging is considered to be one important reason for the softening of this alloy.

Silver content plays an important role in determining the mechanical properties and microstructure evolution of SAC alloys during aging. The difference in microstructure indicates that the Ag content affects the Ag_3Sn IMC dispersion and β-Sn grain size. For high Ag content solder alloy, the microstructure has finely dispersed IMC and fine β-Sn grain size, which help to suppress the plastic deformation of solder alloy and therefore strengthen the material. In general, higher Ag content alloys have better mechanical properties and greater aging resistance.

8.4 Aging Effects on the Creep Behavior of SAC Alloys

Aging effects on SAC solder creep behavior were examined by performing creep tests according to a full test matrix of aging time, temperature and solder alloys with different Ag content and constant Cu content. 63Sn-37Pb was also tested for comparison purpose. Secondary creep strain rate data were extracted from original creep curves and averaged for model fitting by using a 4-constant empirical model. The model-fitted curve is called creep strain rate curve.

All SAC alloys experienced dramatic increases in their creep rates for elevated temperature aging ($T > 50$ °C) compared with room temperature aging and large changes occurred during the first month of aging. For the 6-month creep data, creep strain rates maintained increasing trend and showed no sign of aging saturation. In contrast, the aging induced changes in the creep strain rates of the conventional eutectic 63Sn-37Pb solder were much smaller and could be defined within a very narrow range of values. By comparing this range with the creep strain rate curves for each SAC alloy, it could be found that even though 63Sn-37Pb solder crept faster at the beginning of aging, the creep strain rates of SAC alloys increased at much higher rate and after certain duration of aging, cross-over points would occur between creep strain rate curves of SAC alloys and the narrow creep strain rate range of 63Sn-37Pb, indicating worse creep property of SAC alloys from the time forward.

Silver content was observed to have considerable influence on SAC creep strain rate and aging effects. Higher silver content SAC alloy has lower creep strain rate and is less affected by aging. The explanation lies in the finer and more Ag_3Sn particles formed in higher silver content SAC alloys, which can effectively block dislocation movement then strengthen the materials.

According to test results under different stress levels, creep strain rates of SAC alloys were strongly influenced by change in applied stress, especially for elevated temperature aging,

while 63Sn-37Pb exhibited limited variation in its creep behavior as stress level increased. Hence, SAC alloys are more sensitive to change of stress level than 63Sn-37Pb under aging.

8.5 Preparation and Microstructure of Mixed Formulation Solders

Totally, 7 mixture solders with different mixing ratios between 63Sn-37Pb and SAC305 were carefully prepared. DSC analysis showed that the melting point of these solders decreases as the 63Sn-37Pb content increases and levels off beyond 30 wt.%. Pasty range is wide when the composition is close to pure SAC305 or 63Sn-37Pb and narrow between 30 wt.% and 70 wt.%.

Microstructure evolved dramatically with the chemical composition. As the 63Sn-37Pb content increased from 10% to 90%, the precipitates in the mixed formulation solders evolved from thin bone-shaped to thick bone-shaped to coarse bone-shaped to pie-shaped, and finally, to coarse pie-shaped particles. Eventually, as the content reached 100%, the typical eutectic structure was observed. EDX analysis indicates that these precipitates are rich in Ag and Pb. Generally speaking, the distinctive microstructure of these mixed formulation solder alloys will play a dominant role in determining their mechanical properties.

Microstructure of BGA solder joints in real electronics package was observed by using Nomarski optical microscopy. Specimens under investigation were treated with different reflow profiles differing in their peak temperatures and dwelling times above the melting points of both Pb-free and Sn-Pb solders. It is found that the higher the reflow peak temperature is, the longer the dwelling times are, the finer and more homogeneous microstructure will form in the solder joint. Nonetheless, a target reflow profile exists, which takes both homogeneity of microstructure and other aspects of solder joint reliability into consideration.

8.6 Aging Effects on the Tensile and Creep Behavior of Mixed Formulation Solders

The mechanical properties and creep behavior of mixed formulation solders continuously evolved and exhibited nonlinear pattern to various degrees for different mixing ratios under the influence of isothermal aging.

At both room and elevated temperatures, the mechanical strength decreased as aging time increased. Compared with the relatively stable elastic modulus, yield strength and UTS dropped rapidly in the first a few days of aging and then gradually leveled off. Elastic modulus, yield strength and UTS of pure 63Sn-37Pb had very limited change over the aging process, especially under room temperature condition. In contrast, pure SAC305 experienced the maximum loss in its mechanical properties with aging.

The content of 63Sn-37Pb influenced the mechanical properties of mixed formulation solders in a complicated manner. Under room temperature, yield strength and UTS decreased as the content increased from pure SAC305 all the way to MIX 50-50 and then bounced back up rapidly to its peak values at MIX 70-30. Under elevated temperature, similar trends in yield strength and UTS were found with the peak mechanical strength values occurring at MIX 90-10.

As aging temperature increases, yield strength and UTS of all mixed formulation solders unanimously decreases and the extent of decrease depends on the content of 63Sn-37Pb. Under elevated temperature, it took less time for the mechanical properties to become stabilized, and meanwhile, yield strength and UTS dropped towards a level as low as that of 63Sn-37Pb.

Fractography analysis of failed mixed formulation solder specimens showed transition in failure mode (from transgranular to intergranular) during aging. Compared with non-aged specimens that exhibited typical ductile fracture characteristics, all solders failed more or less in a ductile way, but the transgranular characteristics became less evident in fractured specimens

and a trend from ductile fracture to brittle fracture emerged, which was more significant for solder alloys with less 63Sn-37Pb content (except for pure SAC305). Also, higher aging temperature seemed to accelerate the transition in failure mode.

The maximum change in secondary creep strain rate of mixed formulation solders occurred in the first 10 days of aging, after that the strain rate increased in a linear manner for all the alloys. The higher the aging temperature was, the faster the alloys would creep. Within 60 days, there was no indication of aging saturation when the creep strain rate started to stabilize.

The creep strain rates of 63Sn-37Pb did not vary much under aging and fell into a very narrow range of values. However, the aging induced changes in the creep strain rates of other mixed formulation solders were much larger under the same stress level. At the beginning of aging process, the mixed formulation solders and SAC305 crept much slower than 63Sn-37Pb, but as aging progressed, the creep strain rates of these alloys increased continuously and would end up with much higher values if given enough time. By then, mixed formulation solders would possess less creep resistance and creep faster than eutectic 63Sn-37Pb.

References

[1] Rahn, A., The Basics of Soldering, Wiley-Interscience, 1993.

[2] Capillo, C., Surface Mount Technology: Materials, Processes, and Equipment, McGraw-Hill, 1990.

[3] Vianco, T. P., "Development of Alternatives to Lead-bearing Solders," Proceedings of the Technical Program on Surface Mount International, San Jose, CA, 1993.

[4] Reed-Hill, R. E., Physical Metallurgy Principles, PWS Publishing Company, pp. 306-307, 1994.

[5] Wood, E. P., and Nimmo, K. L. "In Search of New Lead-free Electronic Solders," Journal of Electronic Materials, Vol. 23(8), pp. 709-713, 1994.

[6] Jin, S., Frear, D. R., and Foreword, M. J., Journal of Electronic Materials , Vol. 23(8), pp. 691-693, 1994.

[7] Turbini, L. J., Munie, G. C., Bernier, D., Gamalski, J., and Bergman, D. W., "Examining the Environmental Impact of Lead-free Soldering Alternatives," IEEE Transactions on Electronics Packaging Manufacturing, Vol. 24, pp. 4-9, 2001.

[8] Hwang, J. S., Implementing Lead-Free Electronics, McGraw-Hill, 2004.

[9] ASM International, Electronic Material Handbook, Vol. 1: Materials, 1989.

[10] Napp, D., "Lead-free Interconnect Materials for the Electronics Industry," Proceedings of the 27th International SAMPE Technical Conference, pp. 334-337, Albuquerque, NM, 1995.

[11] IPC Roadmap: A Guide for Assembly of Lead-Free Electronics, IPC, Northbrook, IL 2000.

[12] Allenby, B. R., and Ciccarelli, J. P., “An Assessment of the Use of Lead in Electronic Assembly,” Proceedings of Surface Mount International Conference, IEEE, pp. 1-28, San Jose, CA, 1992.

[13] Grusd, A. “Integrity of Solder Joints from Lead-Free Solder Paste,” Proceedings of the Technical Program NEPCON West, pp. 212-221, 1999.

[14] Wassink, K. J. R., and Verguld, M. M. F., Manufacturing Techniques for Surface Mounted Assemblies, Electrochemical Publications Ltd., 1995.

[15] Abtew, M., and Selvaduray, G., "Lead-free Solders in Microelectronics," Materials Science and Engineering: R: Reports, Vol. 27, pp. 95-141, 2000.

[16] Lee, N. C., "Getting Ready for Lead Free Solders," Soldering and Surface Mount Technology, Vol. 9(2), pp. 65-69, 1997.

[17] Karlya, Y., Gagg, C., and Plumbridge, W. J., "Tin Pest in Lead-Free Solders," Soldering and Surface Mount Technology, Vol. 13(1), pp. 39-40, 2000.

[18] Lewis, W. R., "Notes on Soldering," Tin Research Institute, 1961.

[19] Galyon, G. T., and Palmer, L., "The Structure and Kinetics of Tin-Whisker Formation and Growth on High Tin Content Finishes", Handbook of Lead-Free Solder Technology for Microelectronic Assemblies, K. J. Puttlitz and K. A. Stalter, Eds. Marcel Dekker, pp. 851-914, 2004.

[20] Xu, C., Zhang, Y., Fan, C., and Abys, J., "Understanding Whisker Phenomena: The Driving Force for Whisker Formation," Cookson Electronics Report, pp. 94-105, 2002.

[21] Boettinger, W. F., Johnson, C. E., Bendersky, L. A., Moon, K. W., Williams, M. E., and Stafford, G. R., "Whisker and Hillock Formation on Sn, Sn-Cu and Sn-Pb Electrodeposits," Acta Materialia, Vol. 53, pp. 5033-5050, 2005.

[22] Furusawa, A., Suetsugu, K., Yamaguchi, A., and Taketomo, H., "Thermoset Pb-Free Solder Using Heat-Resistant Sn-Ag Paste," National Technical Report, 1997.

[23] McCormack, M., and Jin, S., "Improved Mechanical Properties in New, Pb-Free Solder Alloys," Journal of Electronic Materials, Vol. 23, pp. 715-720, 1994.

[24] Morris, J. J. W., Goldstein, J. L. F., and Mei, Z., "Microstructure and Mechanical Properties of Sn-In and Sn-Bi Solders," Journal of Electronic Materials, pp. 25-27, 1993.

[25] Habassis, H., Rutter, J. W., and Winegard, W. C., "Phase Relationships in Bi-In-Sn Alloy Systems," Materials Science and Technology, Vol. 2, pp. 985-988, 1986.

[26] McCormack, M., Jin, S., Kammlott, G. W., and Chen, H. S., "New Pb-Free Solder Alloy with Superior Mechanical Properties," Applied Physics Letters, Vol. 63(1) pp. 15-17, 1993.

[27] Glazer, J., "Metallurgy of Low Temperature Pb-Free Solders for Electronic Assembly," International Materials Reviews, Vol. 40(2), p. 65-93, 1995.

[28] Hansen, M., and Anderko, K., Constitution of Binary Alloys, Second Edition, Genium Publishing Corporation, 1988.

[29] Abtew, M., and Selvaduray, G., "Lead-Free Solders in Microelectronics," Materials Science and Engineering, Vol. 27, pp. 95-141, 2000.

[30] Lee, N. C., "Lead-Free Soldering—Where the World is Going," Indium Corporation of America Report, Clinton, NY 1999.

[31] Soldertec Report, European Lead-Free Roadmap, 2002.

[32] Sun, F., Hochstenbach, P., Van Driel, W. D., and Zhang, G. Q., "Fracture Morphology and Mechanism of IMC in Low-Ag SAC Solder/UBM (Ni(P)-Au) for WLCSP," Microelectronics Reliability, Vol. 48, pp. 1167-1170, 2008.

[33] Anderson, I., and Harringa, J., "Elevated Temperature Aging of Solder Joints Based on Sn-Ag-Cu: Effects on Joint Microstructure and Shear Strength," Journal of Electronic Materials, Vol. 33, pp. 1485-1496, 2004.

[34] Pang, H. L., Xu, L. H., Shi, X. Q., Zhou, W., and Ngoh, S. L., "Intermetallic Growth Studies on Sn-Ag-Cu Lead-free Solder," Journal of Electronic Materials, Vol. 33(10), pp. 1219-1226, 2004.

[35] Handwerker, C., "NCMS Lead Free Solder Project: A National Program," NEMI Lead Free Solder Meeting, Chicago, IL, 1999.

[36] Nimmo, K., "Alloy Selection," Lead-Free Soldering in Electronics: Science, Technology and Environmental Impact, K. Suganuma, Ed. Marcel Dekker, pp. 61-83, 2004.

[37] Miller, C. M., Anderson, I. E., and Smith, J. F., "A Viable Tin-Lead Solder Substitute: Sn-Ag-Cu," Journal of Electronic Materials, Vol. 23, pp. 595-602, 1994.

[38] Loomans, M. E., and Fine, M. E., “Tin-silver-copper eutectic temperature and composition,” Metallurgical and Materials Transactions A, Vol. 31A, pp. 1155-1162, 2000.

[39] Moon, K. W., Boettinger, W. J., Kattner, U. R., Biancaniello, F. S., and Handwerker, C. A., "Experimental and Thermodynamic Assessment of Sn-Ag-Cu Solder Alloys," Journal of Electronic Materials, Vol. 29, pp. 1122-1136, 2000.

[40] Henderson, D. W., Woods, J. J., Gosselin, T., Bartelo, J., King, D. E., Korhonen, T. M., Korhonen, M. A., Lehman, L. P., Cotts, E. J., Lauro, P., Shih, D. Y., Goldsmith, C., and Puttlitz, K. J. "The Microstructure of Sn in Near-Eutectic Sn–Ag–Cu Alloy Solder Joints and Its Role in Thermomechanical Fatigue," Journal of Materials Research, Vol. 19, pp. 1608-1612, 2004.

[41] Lehman, L. P., Kinyanjui, R. K., Zavalij, L., Zribi, A., and Cotts, E. J., "Growth and Selection of Intermetallic Species in Sn-Ag-Cu No-Pb Solder Systems Based on Pad Metallurgies and Thermal Histories," Proceedings of the 53rd Electronic Components and Technology Conference, pp. 1215–1221, 2003.

[42] Swenson, D., "The Effects of Suppressed Beta Tin Nucleation on the Microstructural Evolution of Lead-Free Solder Joints," Journal of Materials Science: Materials in Electronics, Vol. 18, pp. 39-54, 2007.

[43] Chen, T., and Dutta, I., "Effect of Ag and Cu Concentrations on the Creep Behavior of Sn-Based Solders," Journal of Electronic Materials, Vol. 37, pp. 347-354, 2008.

[44] Korhonen, T. M., Turpeinen, P., Lehman, L., Bowman, B., Thiel, G., Parkes, R., Korhonen, M., Henderson, D., and Puttlitz, K., "Mechanical Properties of Near-Eutectic Sn-Ag-Cu Alloy Over a Wide Range of Temperatures and Strain Rates," Journal of Electronic Materials, Vol. 33, pp. 1581-1588, 2004.

[45] Iting, T., Jung, T. L., Yen, S. F., Chuang, T. H., and Enboa, W., "Identification of Mechanical Properties of Intermetallic Compounds on Lead Free Solder," in Proceedings of the 55th Electronic Components and Technology Conference, pp. 687-691, 2005.

[46] Fields, R. J., and Low, S. R., "Physical and Mechanical Properties of Intermetallic Compounds Commonly Found in Solder Joints," The Metal Science of Joining, pp. 165–174, 1991.

[47] Ganesan, S., and Pecht, M., Lead-Free Electronics, Wiley-Interscience Publication, 2006.

[48] Hua, F., "Pb-Free Solder Challenges in Electronic Packaging and Assembly," Proceedings of the 53rd Electronic Components and Technology Conference, pp. 58-63, 2003.

[49] Nandagopal, N., Zequn, M., and Sue, T., "Microstructure and Thermal Fatigue Life of BGAs with Eutectic Sn-Ag-Cu Balls Assembled at 210 °C with Eutectic Sn-Pb Solder Paste," Proceedings of the 56th Electronic Components and Technology Conference, pp. 875-883, 2006.

[50] Evans, J. L., Mitchell, C., Bozack, M., and Payton, L. N., "Reliability of SAC BGA Using Sn-Pb Paste for Harsh Environment Electronics," SMTA International Conference Proceedings, pp. 365-370, 2005.

[51] Handwerker, C., "Transitioning to Pb-free Assemblies," INEMI Report, 2005.

[52] McCormick, H., Snugovsky, P., and Bagheri, Z., "Mixing Metallurgy: Reliability of SAC Balled Area Array Packages Assembled Using Sn-Pb Solder," SMTA International Conference Proceedings, pp. 425-432, 2006.

[53] Hua, F., Aspandiar, R., Anderson, C., Clemons, G., and Chung, C. K., "Solder Joint Reliability Assesment of Sn-Ag-Cu BGA Components Attached with Eutectic Pb-Sn Solder," Journal of Surface Mount Technology, Vol. 16(1), pp. 34-42, 2003.

[54] Kannabiran, A., Pannerselvam, E. T., and Ramkumar, S. M., "Investigation of the Forward and Backward Compatibility of Solder Alloys with Component Finishes for HASL and OSP PCB Finish," SMTA International Conference Proceedings, pp. 566-570, 2006.

[55] Chatterji, I., "Backward Compatibility, Are We Ready - A Case Study," SMTA International Conference Proceedings, pp. 416-424, 2006.

[56] Zbrzezny, A. R., Snugovsky, P., Lindsay, T., and Lau, R., "Reliability Investigation of Mixed BGA Assemblies," IEEE Transactions on Electronics Packaging Manufacturing, Vol. 29, pp. 211-216, 2006.

[57] Abtew, M., and Kinyanjui, R., "Effect of Inert Atmosphere Reflow and Solder Paste Volume on the Microstructure and Mechanical Strength of Mixed Sn-Ag-Cu and Sn-Pb Solder Joints," SMTA International Conference Proceedings, pp. 74-78, 2006.

[58] Hua, F., Aspandiar, R., Rothman, T., and Anderson, C., "Solder Joint Reliability of Sn-Ag-Cu BGA Components Attached with Eutectic Pb-Sn Solder Paste," SMTA International Conference Proceedings, pp. 246-252, 2003.

[59] Theuss, H., Kilger, T., and Ort, T., "Solder Joint Reliability of Lead-Free Solder Balls Assembled with Snpb Solder Paste," Proceedings of the 53rd Electronic Components and Technology Conference, pp. 331-337, 2003.

[60] Nandagopal, B., Chiang, D., Teng, S., and Thune, P., "Study on Assembly, Rework Process, Microstructures and Mechanical Strength of Backward Compatible Assembly," SMTA International Conference Proceedings, pp. 861-870, 2005.

[61] Sun, F., "Solder Joint Reliability of Sn-Ag-Cu BGA and Sn-Pb Solder Paste," 6th International Conference on Electronic Packaging Technology, pp. 1-6, 2005.

[62] Chung, C. K., Aspandiar, R., Leong, K. F., and Siew, T. C., "The Interactions of Lead (Pb) in Lead-Free Solder (Sn/Ag/Cu) System," Proceedings of the 52nd Electronic Components and Technology Conference, pp. 168-175, 2002.

[63] Hunt, C., Nottay, J., Brewin, A., and Dinsdale, A., "Predicting Microstructure of Mixed Solder Alloy System," NPL Report, 2002.

[64] Bath, J., Hu, L., and Chiang, D., "Reliability Evaluation Of Lead-Free Snagcu Pbga676 Components Using Tin-Lead And Lead-Free Snagcu Solder Paste," SMTA International Conference Proceedings, pp. 891-901, 2005.

[65] Clech, J. P., "Lead-Free and Mixed Assembly Solder Joint Reliability Trends," Proceedings of APEX, Paper S28-3, pp. 1-14, 2004.

[66] Nguyen, J., Geiger, D., Rooney, D., and Shangguan, D., "Reliability Study of Lead-Free Area Array Packages with Tin-Lead Soldering Processes," SMTA International Conference Proceedings, pp. 433-438, 2006.

[67] Pirondi, A., Mechanical Failure in Microelectronic Packaging, Vol. IGF 13, Cassino 27 e 28 Maggio, 1997.

[68] Hertzberg, R. W., Deformation and Fracture Mechanics of Engineering Materials, 4 Ed., John Wiley & Sons, Inc., 1996.

[69] Vianco, P. T., "Fatigue and Creep of Lead-free Solder Alloys: Fundamental Properties," in Lead-Free Solder Interconnect Reliability, D. Shangguan, Ed., ASM International, 2006.

[70] Wiese, S., Schubert, A., Walter, H., Dukek, R., Feustel, F., Meusel, E., and Michel, B., "Constitutive Behavior of Lead-Free Solders vs. Lead-Containing Solders - Experiments on Bulk Specimens and Flip-Chip Joints," Proceedings of the 51st Electronic Components and Technology Conference, pp. 890-902, 2001.

[71] McCabe, R. J., "Athermal and Thermally Activated Plastic Flow in Low Melting Temperature Solders at Small Stresses," Scripta Materialia, Vol. 39, pp. 189-195, 1998.

[72] Hibbeler, R. C., Mechanics Of Materials, 7 Ed., Prentice Hall, 2007.

[73] Lau, J. H., and Pao, Y. H., Solder Joints Reliability of BGA, CSP, Flip-Chip, and Fine Pitch SMT Assemblies, McGraw-Hill, 1997.

[74] Garofalo, F., Fundamentals of Creep and Creep-Rupture in Metals, 2 Ed., Macmillan, 1966.

[75] Kassner, M., and Perez-Prado, M. T., Fundamentals of Creep in Metals and Alloys, Elsevier Science, 2004.

[76] Lea, C., A Scientific Guide to Surface Mount Technology, Electrochemical Publications Ltd., 1988.

[77] Evans, R. W., and Wilshire, B., Creep of Metals and Alloys, Institute of Metals, 1985.

[78] Ashby, M. F., “A First Report on Deformation-Mechanism Maps,” Acta Metallurgica, Vol. 20, pp. 887-897, 1972.

[79] Weertman, J., “Steady-State Creep through Dislocation Climb,” Journal of Applied Physics, Vol. 28, pp. 362-364, 1957.

[80] Coble, R. L., “A Model for Boundary Diffusion Controlled Creep in Polycrystalline Materials,” Journal of Applied Physics, Vol. 34(6), pp. 1679-1682, 1963.

[81] Nabarro, F., "Report of a Conference on Strength of Solids, held at the H.H. Wills Physical Laboratory, University of Bristol," Physical Society, London 1948.

[82] Herring, C., Journal of Applied Physics, Vol. 21, 1950

[83] Ritchie, R. O., "Mechanisms of Fatigue-Crack Propagation in Ductile and Brittle Solids," International Journal of Fracture, Vol. 100, pp. 55-83, 1999.

[84] Stephens, R. I., Metal Fatigue in Engineering, 2 Ed., John Wiley & Sons, Inc., 2001.

[85] Miner, M. A., "Cumulative Damage in Fatigue," Journal of Applied Mechanics, Vol. 12(3), pp. 159-164, 1954.

[86] Kilinski, T. J., Lesniak, J. R., and Sandor, B. I., " Modern Approaches to Fatigue Life Prediction of SMT Solder Joints," Solder Joint Reliability Theory and Applications, J. H. Lau, Ed., Chapter 13, Van Nostrand Reinhold, 1991.

[87] Ma, H., and Suhling, J. C., "A Review of Mechanical Properties of Lead-Free Solders for Electronic Packaging," Journal of Materials Science, Vol. 44, pp. 1141-1158, 2009.

[88] Puttlitz, K. J., and Stalter, K. A., Handbook of Lead-free Solder Technology for Microelectronic Assemblies, Marcel Dekker, 2004.

[89] Nose, H., Masao, S., Yutaka, T., and Hideo, N., "Temperature and Strain Rate Effects on Tensile Strength and Inelastic Constitutive Relationship of Sn-Pb Solders," Journal of Electronic Packaging, Vol. 125, pp. 59-66, 2003.

[90] McCormack, M., and Chen, H. S., "New Lead-Free Sn-Ag-Zn-Cu Solder Alloys with Improved Mechanical Properties," Applied Physics Letters, Vol. 65, pp. 1233-1235, 1994.

[91] Shi, X. Q., Zhou, W., Pang, H. L. J., and Wang, Z. P., "Effect of Temperature and Strain Rate on Mechanical Properties of 63Sn/37Pb Solder Alloy," Journal of Electronic Packaging, Vol. 121, pp. 179-185, 1999.

[92] Pang, J. H. L., Xiong, B. S., Neo, C. C., Mang, X. R., and Low, T. H., "Bulk Solder and Solder Joint Properties for Lead-Free 95.5Sn-3.8Ag-0.7Cu Solder Alloy," Proceedings of the 53rd Electronic Components and Technology Conference, pp. 673-679, 2003.

[93] Pang, J. H. L., Xiong, B. S., and Low, T. H., "Low Cycle Fatigue Models for Lead-Free Solders," Thin Solid Films, Vol. 462-463, pp. 408-412, 2004.

[94] Yeung, B., and Jang, J. W., "Correlation Between Mechanical Tensile Properties and Microstructure of Eutectic Sn-3.5Ag Solder," Journal of Materials Science Letters, Vol. 21, pp. 723-726, 2002.

[95] Kim, K. S., Huh, S. H., and Suganuma, K., "Effects of Cooling Speed on Microstructure and Tensile Properties of Sn-Ag-Cu Alloys," Materials Science and Engineering, Vol. A333, pp. 106 -114, 2002.

[96] Madeni, J. C., Liu, S., and Siewert, T., "Casting of Lead-free Solder Bulk Specimens with Various Solidification Rates," Proceedings of the ASM International Conference, 2002.

[97] Lin, J. K., De Silva, A., Frear, D., Yifan, G., Jin-Wook, J., Li, L., Mitchell, D., Yeung, B., and Zhang, C., "Characterization of Lead-Free Solders and Under Bump Metallurgies for Flip-Chip Package," Proceedings of the 51st Electronic Components and Technology Conference, pp. 455-462, 2001.

[98] Chuang, C. M., Lui, T. S., and Chen, L. H., "Effect of Aluminum Addition on Tensile Properties of Naturally Aged Sn-9Zn Eutectic Solder," Journal of Materials Science, Vol. 37, pp. 191-195, 2002.

[99] Vianco, P. T., Rejent, J. A., and Grant, R., "Development of Sn-Based, Low- Melting Temperature Pb-free Solder Alloys," Transactions of the Japan Institute of Metallurgy, Vol. 45, pp. 765-775, 2004.

[100] Qiang, X., Luu, N., and Armstrong, W. D., "Aging and Creep Behavior of Sn3.9Ag0.6Cu Solder Alloy," Proceedings of the 54th Electronic Components and Technology Conference, pp. 1325-1332, 2004.

[101] Qiang, X., Harold, J. B., and Armstrong, W. D., "Aging Effects on Microstructure and Tensile Property of Sn3.9Ag0.6Cu Solder Alloy," Journal of Electronic Packaging, Vol. 126, pp. 208-212, 2004.

[102] Shohji, I., Yoshida, T., Takahashi, T., and Hioki, S., "Tensile Properties of Sn-Ag Based Lead-Free Solders and Strain Rate Sensitivity," Materials Science and Engineering A, Vol. 366, pp. 50-55, 2004.

[103] Pang, J. H. L., Low, T. H., Xiong, B. S., Luhua, X., and Neo, C. C., "Thermal Cycling Aging Effects on Sn-Ag-Cu Solder Joint Microstructure, IMC and Strength," Thin Solid Films, Vol. 462-463, pp. 370-375, 2004.

[104] Darveaux, R., "Shear Deformation of Lead-Free Solder Joints," Proceedings of the 55th Electronic Components and Technology Conference, pp. 882-893, 2005.

[105] Obaid, A. A., Sloan, J. G., Lamontia, M. A., Paesano, A., Khan, S., and Gillespie, J. W., "Test Method Development to Quantify the In Situ Elastic and Plastic Behavior of 62%Sn-36%Pb-2%Ag Solder Ball Arrays in Commercial Area Array Packages at -40 °C, 23 °C, and 125 °C," Journal of Electronic Packaging, Vol. 127, pp. 483-495, 2005.

[106] Qian, Z., Abhijit, D., Dave, N., and Hector, P., "Systematic Study on Thermo-Mechanical Durability of Pb-Free Assemblies: Experiments and FE Analysis," Journal of Electronic Packaging, Vol. 127, pp. 415-429, 2005.

[107] Rhee, H., Subramanian, K. N., Lee, A., and Lee, J. G., "Mechanical Characterization of Sn-3.5Ag Solder Joints at Various Temperatures," Soldering and Surface Mount Technology, Vol. 15, pp. 21-26, 2003.

[108] Chromik, R., Vinci, R., Allen, S., and Notis, M., "Measuring the Mechanical Properties of Pb-Free Solder and Sn-Based Intermetallics by Nanoindentation," JOM Journal of the Minerals, Metals and Materials Society, Vol. 55, pp. 66-69, 2003.

[109] Lampe, B. T., "Room Temperature Aging Properties of Some Solder Alloys," Welding Journal, Vol. 55, pp. 330s-340s, 1976.

[110] Medvedev, A. S., "Aging of Tin-Lead Solders and Joints Soldered by Them," Metallovedenie i Obrabotka Metallov, No.7, pp. 16-23, 1956.

[111] Fouassier, O., Heintz, J. M., Chazelas, J., Geffroy, P. M., and Silvain, J. F., "Microstructural Evolution and Mechanical Properties of SnAgCu Alloys," Journal Of Applied Physics, Vol. 100, Paper 043519, pp. 1-8, 2006.

[112] Zhang, Q., Dasgupta, A., and Haswell, P., "Isothermal Mechanical Durability of Three Selected PB-Free Solders: Sn3.9Ag0.6Cu, Sn3.5Ag, and Sn0.7Cu," Journal of Electronic Packaging, Vol. 127, pp. 512-522, 2005.

[113] Jones, W. K., Liu, Y., Zampino, M. A., Gonzalez, G., and Shah, M., "A Study on Mechanical Properties of Eutectic and Solid Solution Pb-Sn-Ag Solders from 200 °C to 150 °C " Design and Reliability of Solders and Solder Interconnections, pp. 85-96, 1997.

[114] Lim, T. J., and Lu, W. Y., "Large Scale and Aging Effect on the Mechanical Properties of a 63Sn-37Pb Solder Alloy," Packaging of Electronic and Photonic Devices, ASME, Vol. 28, pp. 203-206, 2000.

[115] Ochoa, F., Williams, J., and Chawla, N., "The Effects of Cooling Rate on Microstructure and Mechanical Behavior of Sn-3.5Ag Solder," JOM Journal of the Minerals, Metals and Materials Society, Vol. 55, pp. 56-60, 2003.

[116] Wei, C., Liu, Y., Gao, Z., Xu, R., and Yang, K., "Effects of Aging on Structural Evolution of the Rapidly Solidified Sn-Ag-Zn Eutectic Solder," Journal of Alloys and Compounds, Vol. 468, pp. 154-157, 2009.

[117] Vianco, P., and Rejent, J., "The Compression Stress-Strain Behavior of Sn-Ag-Cu Solder," JOM Journal of the Minerals, Metals and Materials Society, Vol. 55, pp. 50-55, 2003.

[118] Ma, H., Suhling, J. C., Zhang, Y., Lall, P., and Bozack, M. J. "The Influence of Elevated Temperature Aging on Reliability of Lead Free Solder Joints," Proceedings of the 57th Electronic Components and Technology Conference, pp. 653-668, 2007.

[119] Ma, H., Suhling, J. C., Lall, P., and Bozack, M. J., "Reliability of the Aging Lead-Free Solder Joint," Proceedings of the 56th Electronic Components and Technology Conference, pp. 849-864, 2006.

[120] Mysore, K., Chan, D., Bhate, D., Subbarayan, G., Dutta, I., Gupta, V., Zhao, J., and Edwards, D., "Aging-Informed Behavior of Sn3.8ag0.7cu Solder Alloys," Proceedings of the 11th Intersociety Conference on Thermal and Thermomechanical Phenomena in Electronic Systems, pp. 870-875, 2008.

[121] Plumbridge, W. J., "The Analysis of Creep Data for Solder Alloys," Soldering and Surface Mount Technology, Vol. 15, pp. 92-98, 2003.

[122] Allen, S. L., Notis, M. R., Chromik, R. R., and Vinci, R. P., "Microstructural Evolution in Lead-Free Solder Alloys: Part I. Cast Sn-Ag-Cu Eutectic," Journal of Materials Research, Vol. 19, pp. 1417-1424, 2004.

[123] Allen, S. L., Notis, M. R., Chromik, R. R., and Vinci, R. P., "Microstructural Evolution in Lead-Free Solder Alloys: Part II. Directionally Solidified Sn-Ag-Cu, Sn-Cu and Sn-Ag," Journal of Materials Research, Vol. 19, pp. 1425-1431, 2004.

[124] Reinikainen, T. O., Marjadi, P., and Kivilahti, J. K., "Deformation Characteristics and Microstructural Evolution of SnAgCu Solder Joints," Proceedings of the 6th EuroSimE, pp. 91-98, 2005.

[125] Snugovsky, L., Perovic, D. D., and Rutter, J. W., "Experiments on the Aging of Sn-Ag-Cu Solder Alloys," Powder Metallurgy, Vol. 48, pp. 193-198, 2005.

[126] Darveaux, R., Banerji, K., Mawer, A., and Dody, G., "Reliability of Plastic Ball Grid Array Assembly," Ball Grid Array Technology, McGraw-Hill, 1995.

[127] "Test Methods for Destructive Shear Testing of Ball Bonds," 1991 Annual Book of ASTM Standards, Vol. 10.04, F1269-89, 1991.

[128] Hasegawa, K., Noudou, T., Takahashi, A., and Nakaso, A., "Thermal Aging Reliability of Solder Ball Joint for Semiconductor Package Substrate," Proceedings of the 2001 SMTA International Conference, pp. 1-8, 2001.

[129] Li, L., Jang, J. W., and AUmen, B., "Shear Property and Microstructure Evaluation of Pb-free Solder Bumps under Room Temperature and Multiple Reflow/High Temperature Aging " Proceedings of the International Symposium on Advanced Packaging Materials: Processes, Properties and Interfaces, Tempe, AZ, pp. 347-353, 2001.

[130] Lin, J. K., De Silva, A., Frear, D., Guo, Y., Hayes, S., Jin-Wook, J., Li, L., Mitchell, D., Yeung, B., and Zhang, C., "Characterization of Lead-Free Solders and Under Bump Metallurgies for Flip-Chip Package," Transactions on Electronics Packaging Manufacturing, IEEE, Vol. 25, pp. 300-307, 2002.

[131] Chiu, T. C., Kejun, Z., Stierman, R., Edwards, D., and Ano, K., "Effect of Thermal Aging on Board Level Drop Reliability for Pb-Free BGA Packages," Proceedings of the 54th Electronic Components and Technology Conference, pp. 1256-1262, 2004.

[132] Darveaux, R., and Reichman, C., "Mechanical Properties of Lead-Free Solders," Proceedings of the 57th Electronic Components and Technology Conference, ECTC, pp. 695-706, 2007.

[133] Kumar, P., Dutta, I., Sarihan, V., Frear, D. R., and Renavikar, M., "Effects of Strain Rate and Aging on Deformation and Fracture of Sn-Ag-Cu Solder Joints," Proceedings of the 11th Intersociety Conference on Thermal and Thermomechanical Phenomena in Electronic Systems, pp. 660-667, 2008.

[134] Peng, W., and Marques, M., "Effect of Thermal Aging on Drop Performance of Chip Scale Packages with SnAgCu Solder Joints on Cu Pads," Journal of Electronic Materials, Vol. 36, pp. 1679-1690, 2007.

[135] Lin, C. T., Hsi, C. S., Wang, M. C., Chang, T. C., and Liang, M. K., "Interfacial Microstructures and Solder Joint Strengths of the Sn-8Zn-3Bi and Sn-9Zn-lAl Pb-Free Solder Pastes on OSP Finished Printed Circuit Boards," Journal of Alloys and Compounds, Vol. 459, pp. 225-231, 2008.

[136] Wong, C. K., Pang, J. H. L., Tew, J. W., Lok, B. K., Lu, H. J., and Sun, Y. F., "The Influence of Solder Volume and Pad Area on Sn-3.8Ag-0.7Cu and Ni UBM Reaction in Reflow Soldering and Isothermal Aging," Microelectronics Reliability, Vol. 48, pp. 611-621, 2008.

[137] Lee, S. W. R., Tsui, Y. K., Hunag, X., and Yan, E. C. C., "Effects of Room Temperature Storage Time on the Shear Strength of Pbga Solder Balls", Proceedings of the ASME International Mechanical Engineering Congress and Exposition, pp. 1-4, 2002.

[138] Liang, J., Downes, S., Dariavach, N., Shangguan, D., and Heinrich, S., "Effects of Load and Thermal Conditions on Pb-Free Solder Joint Reliability," Journal of Electronic Materials, Vol. 33, pp. 1507-1515, 2004.

[139] Tsui, Y. K., Lee, S. W. R., and Huang, X., "Experimental Investigation on the Degradation of BGA Solder Ball Shear Strength Due to Room Temperature Aging," Proceedings of the 4th International Symposium on Electronic Materials and Packaging, pp. 478-481, 2002.

[140] Coyle, R. J., Solan, P. P., Serafino, A. J., and Gahr, S. A., "The Influence of Room Temperature Aging on Ball Shear Strength and Microstructure of Area Array Solder Balls," Proceedings of the 50th Electronic Components and Technology Conference, pp. 160-169, 2000.

[141] Koo, J. M., and Jung, S. B., "Effect of Displacement Rate on Ball Shear Properties for Sn-37Pb and Sn-3.5Ag BGA Solder Joints During Isothermal Aging," Microelectronics Reliability, Vol. 47, pp. 2169-2178, 2007.

[142] Suh, M. S., Park, C. J., and Kwon, H. S., "Growth Kinetics of Cu–Sn Intermetallic Compounds at the Interface of a Cu Substrate and 42Sn–58Bi Electrodeposits, and the Influence of the Intermetallic Compounds on the Shear Resistance of Solder Joints," Materials Chemistry and Physics, pp. 95-99, 2008.

[143] Pang, H. L. J., Tan, K. H., Shi, X. Q., and Wang, Z. P., "Microstructure and Intermetallic Growth Effects on Shear and Fatigue Strength of Solder Joints Subjected to Thermal Cycling Aging," Materials Science and Engineering A, Vol. 307, pp. 42-50, 2001.

[144] Li, M., Lee, K. Y., Olsen, D. R., Chen, W. T., Tan, B. T. C., and Mhaisalkar, S., "Microstructure, Joint Strength and Failure Mechanisms of SnPb and Pb-Free Solders in BGA Packages," IEEE Transactions on Electronics Packaging Manufacturing, Vol. 25, pp. 185-192, 2002.

[145] Li, D., Liu, C., and Conway, P., "Microstructure and Shear Strength Evolution of Sn-Ag-Cu Solder Bumps During Aging at Different Temperatures," Journal of Electronic Materials, Vol. 35, pp. 388-398, 2006.

[146] Oliver, J. R., Liu, J., and Lai, Z., "Effect of Thermal Ageing on the Shear Strength of Lead-free Solder Joints," Proceedings of the International Symposium on Advanced Packaging Materials: Processes, Properties and Interfaces, pp. 152-157, 2000.

[147] Liu, C., Paul, C., Li, D., and Michael, H., "Analysis of the Micro-Mechanical Properties in Aged Lead-Free, Fine Pitch Flip Chip Joints," Journal of Electronic Packaging, Vol. 126, pp. 359-366, 2004.

[148] Chilton, A. C., Whitmore, M. A., and Hampshire, W. B., "Fatigue Failure in a Model SMT Joints," Soldering and Surface Mount Technology, Vol. 3, pp. 21-24, 1989.

[149] Pang, J. H. L., Tan, K. H., Shi, X. Q., and Wang, Z. P., "Thermal Cycling Aging Effects on Microstructural and Mechanical Properties of a Single PBGA Solder Joint Specimen," IEEE Transactions on Components and Packaging Technologies, Vol. 24, pp. 10-15, 2001.

[150] Wiese, S., Roellig, M., and Wolter, K. J., "Creep of Eutectic SnAgCu in Thermally Treated Solder Joints," Proceedings of the 55th Electronic Components and Technology Conference, pp. 1272-1281, Vol. 2005.

[151] Wiese, S., and Wolter, K. J., "Creep of Thermally Aged SnAgCu-Solder Joints," Microelectronics Reliability, Vol. 47, pp. 223-232, 2007.

[152] Sigelko, J., Choi, S., Subramanian, K. N., Lucas, J. P., and Bieler, T. R., "Effect of Cooling Rate on Microstructure and Mechanical Properties of Eutectic SnAg Solder Joints with and without Intentionally Incorporated Cu_6Sn_5 Reinforcements " Journal of Electronic Materials, Vol. 28, pp. 1184-1188, 1999.

[153] Zou, H., Zhu, Q., and Zhang, Z., "Growth Kinetics of Intermetallic Compounds and Tensile Properties of Sn–Ag–Cu/Ag Single Crystal Joint," Journal of Alloys and Compounds, Vol. 461, pp. 410-417, 2008.

[154] Morris, J. W., Goldstein, J. L. F. and Mei, Z., "Microstructural Influences on the Mechanical Properties of Solder," The Mechanics of Solder Alloy Interconnects, D. Frear, H. Morgan, S. Burchett, and J. Lau, Eds., Van Nostrand Reinhold, 1994.

[155] Hu, Q., Lee, Z. S., Zhao, Z. I., and Lee, D. L., "Study of Cooling Rate on Lead-free Soldering Microstructure of Sn-3.0Ag-0.5Cu Solder," Proceedings of International Conference on Asian Green Electronics, pp. 156-160, 2005.

[156] Deng, X., Piotrowski, G., Williams, J. J., and Chawla, N., "Influence of Initial Morphology and Thickness of Cu6Sn5 and Cu3Sn Intermetallics on Growth and Evolution during Thermal Aging of Sn-Ag Solder/Cu Joints," Journal of Electronic Materials, Vol. 32, pp. 1403-1413, 2003.

[157] Pandher, R., "Reflow Profile Optimization for Lead-free (SAC) Alloys in BGA Applications," Proceedings of the 8th Electronics Packaging Technology Conference, pp. 708-716, 2006.

[158] Choi, W., Kang, S., and Shih, D., "A Study of the Effects of Solder Volume on the Interfacial Reactions in Solder Joints Using the Differential Scanning Calorimetry Technique," Journal of Electronic Materials, Vol. 31, pp. 1283-1291, 2002.

[159] Zbrzezny, A. R., Snugovsky, P., and Perovic, D. D., "Impact of Board and Component Metallizations on Microstructure and Reliability of Lead-Free Solder Joints", Microelectronics Reliability, Vol. 47, pp. 2205-2214, 2007.

[160] Zeng, K., and Tu, K. N., "Six Cases of Reliability Study of Pb-Free Solder Joints in Electronic Packaging Technology," Materials Science and Engineering: R: Reports, Vol. 38, pp. 55-105, 2002.

[161] Zhong, C. H., and Yi, S., "Solder Ball Failure Mechanisms in Plastic Ball Grid Array Packages," Soldering and Surface Mount Technology, Vol. 14, pp. 40-50, 2002.

[162] Zribi, A., Chromik, R. R., Presthus, R., Teed, K., Zavalij, L., DeVita, J., Tova, J., Cotts, E. J., Clum, J. A., Erich, R., Primavera, A., Westby, G., Coyle, R. L. J., and Wenger, G. M., "Solder Metallization Interdiffusion in Microelectronic Interconnects," IEEE Transactions on Components and Packaging Technologies, Vol. 23, pp. 383-387, 2000.

[163] Ho, C., Zheng, R., Luo, G., Lin, A., and Kao, C., "Formation and Resettlement of $(Au_xNi_{1-x})Sn_4$ in Solder Joints of Ball-Grid-Array Packages with the Au/Ni Surface Finish," Journal of Electronic Materials, Vol. 29, pp. 1175-1181, 2000.

[164] Song, H., Ahn, J., Minor, A., and Morris, J., "Au−Ni−Sn Intermetallic Phase Relationships in Eutectic Pb−Sn Solder Formed on Ni/Au Metallization," Journal of Electronic Materials, Vol. 30, pp. 409-414, 2001.

[165] Arra, M., Shangguan, D., Ristolainen, E., and Lepisto, T., "Effect of Reflow Profile on Wetting and Intermetallic Formation between Sn/Ag/Cu Solder Components and Printed Circuit Boards," Soldering and Surface Mount Technology, Vol. 14, pp. 18-25, 2002.

[166] Choi, S., Bieler, T., Lucas, J., and Subramanian, K., "Characterization of the Growth of Intermetallic Interfacial Layers of Sn-Ag and Sn-Pb Eutectic Solders and Their Composite Solders on Cu Substrate During Isothermal Long-Term Aging," Journal of Electronic Materials, Vol. 28, pp. 1209-1215, 1999.

[167] Roubaud, P., Ng, G., and Henshall, G., "Impact of Intermetallic Growth on the Mechanical Strength of Pb-Free BGA Assemblies," Proceedings of IPC APEX, Paper 23, pp. 1-5, 2001.

[168] Dutta, I., Pan, D., Marks, R. A., and Jadhav, S. G., "Effect of Thermo-Mechanically Induced Microstructural Coarsening on the Evolution of Creep Response of SnAg-Based Microelectronic Solders," Materials Science and Engineering: A, Vol. 410-411, pp. 48-52, 2005.

[169] Wang, F. J., Yu, Z. S., and Qi, K., "Intermetallic Compound Formation at Sn-3.0Ag-0.5Cu-1.0Zn Lead-Free Solder Alloy/Cu Interface During As-Soldered and As-Aged Conditions," Journal of Alloys and Compounds, Vol. 438, pp. 110-115, 2007.

[170] Chou, G. J. S. "Microstructure Evolution of SnPb and SnAg/Cu BGA Solder Joints during Thermal Aging," Proceedings of the 8th International Symposium on Advanced Packaging Materials, pp. 39-46, 2002.

[171] Fan, J. W., Chia-Tai, K., and Ming-Chuen, Y., "Mechanical Characterization of Board-Level 63Sn37Pb and Lead-Free Solder Sphere Attachment on Cu-pad/Ni/Au Surface Finish Substrate," Proceedings of the 5th Electronics Packaging Technology Conference, pp. 712-717, 2003.

[172] Chun, H. S., Yoon, J. W., and Jung, S. B., "Solid-State Interfacial Reactions between Sn-3.5Ag-0.7Cu Solder and Electroless Ni-Immersion Au Substrate during High Temperature Storage Test," Journal of Alloys and Compounds, Vol. 439, pp. 91-96, 2007.

[173] Li, D., Liu, C., and Conway, P. P., "Characteristics of Intermetallics and Micromechanical Properties during Thermal Ageing of Sn-Ag-Cu Flip-Chip Solder Interconnects," Materials Science and Engineering A, Vol. 391, pp. 95-103, 2005.

[174] Peng, W., Monlevade, E., and Marques, M. E., "Effect of Thermal Aging on the Interfacial Structure of SnAgCu Solder Joints on Cu," Microelectronics Reliability, Vol. 47, pp. 2161-2168, 2007.

[175] Salam, B., Ekere, N. N., and Rajkumar, D., "Study of the Interface Microstructure of Sn-Ag-Cu Lead-Free Solders and the Effect of Solder Volume on Intermetallic Layer Formation," Proceedings of the 51st Electronic Components and Technology Conference, pp. 471-477, 2001.

[176] Jin, S., “Developing Lead-free Solders: A Challenge and Opportunity,” Journal of the Minerals, Metals and Materials Society, Vol. 45(7), pp. 20-24, 1993

[177] Anderson, I., and Harringa, J., "Suppression of Void Coalescence in Thermal Aging of Tin-Silver-Copper-X Solder Joints," Journal of Electronic Materials, Vol. 35, pp. 94-106, 2006.

[178] Vaynman, S., Ghosh, G., and Fine, M., "Effects of Palladium and Solder Aging on Mechanical and Fatigue Properties of Tin-Lead Eutectic Solder," Journal of Electronic Materials, Vol. 27, pp. 1223-1228, 1998.

[179] Hao, H., Shi, Y., Xia, Z., Lei, Y., and Guo, F., "Microstructure Evolution of SnAgCuEr Lead-free Solders Under High Temperature Aging," Journal of Electronic Materials, Vol. 37, pp. 2-8, 2008.

[180] Liu, W., and Lee, N. C., "The Effects of Additives to SnAgCu Alloys on Microstructure and Drop Impact Reliability of Solder Joints," JOM Journal of the Minerals, Metals and Materials Society, Vol. 59, pp. 26-31, 2007.

[181] Sousa, I. D., Henderson, D. W., Parry, L., Kang, S. K., and Shih, D. Y., "The Influence of Low Level Doping on the Thermal Evolution of SAC Alloy Solder Joints with Cu Pad Structures," Proceedings of the 56th Electronic Components and Technology Conference, pp. 1454-1461, 2006.

[182] Che, F. X., Luan, J. E., and Baraton, X., "Effect of Silver Content and Nickel Dopant on Mechanical Properties of Sn-Ag-Based Solders," Proceedings of the 58th Electronic Components and Technology Conference, pp. 485-490, 2008.

[183] Ye, L., Lai, Z. H., Liu, J., and ThoÈleÂn, A., "Microstructure Investigation of Sn-0.5Cu-3.5Ag and Sn-3.5Ag-0.5Cu-0.5B Lead-Free Solders," Soldering and Surface Mount Technology, Vol. 13, pp. 16-20, 2001.

[184] Wade, N., Wu, K., Kunii, J., Yamada, S., and Miyahara, K., "Effects of Cu, Ag and Sb on the Creep-Rupture Strength of Lead-Free Solder Alloys," Journal of Electronic Materials, Vol. 30, pp. 1228-1231, 2001.

[185] Law, C. M. T. and Wu, C. M. L. "Microstructure Evolution and Shear Strength of Sn-3.5Ag-RE Lead-free BGA Solder Balls," Proceedings of the Sixth High Density Microsystem Design and Packaging and Component Failure Analysis Conference, pp. 60-65, 2004.

[186] Dudek, M. A., Sidhu, R. S., and Chawla, N., "Novel Rare-Earth-Containing Lead-Free Solders with Enhanced Ductility," JOM Journal of the Minerals, Metals and Materials Society, pp. 57-63, 2006.

[187] Guo, F., Lee, J., Choi, S., Lucas, J., Bieler, T., and Subramanian, K., "Processing and Aging Characteristics of Eutectic Sn-3.5Ag Solder Reinforced with Mechanically Incorporated Ni Particles," Journal of Electronic Materials, Vol. 30, pp. 1073-1082, 2001.

[188] Hsuan, T. C., and Lin, K. L., "Microstructural Evolution of ε-$AgZn_3$ and η-Zn Phases in Sn-8.5Zn-0.5Ag-0.01Al-0.1Ga Solder during Aging Treatment," Journal of Alloys and Compounds, Vol. 469, pp. 350-356, 2009.

[189] Hsuan, T. C., and Lin, K. L., "Effects of Aging Treatment on Mechanical Properties and Microstructure of Sn-8.5Zn-0.5Ag-0.01Al-0.1Ga Solder," Materials Science and Engineering: A, Vol. 456, pp. 202-209, 2007.

[190] Yang, H., Deane, P., Magill, P., and Murty, K. L., "Creep Deformation of 96.5Sn-3.5Ag Solder Joints in a Flip-Chip Package," Proceedings of the 46th Electronic Components and Technology Conference, pp. 1136-1142, 1996.

[191] Pang, J. H. L., Xiong, B. S., and Che, F. X., "Modeling Stress Strain Curves For Lead-Free 95.5Sn-3.8Ag-0.7Cu Solder," Proceedings of the 5th EuroSimE Conference, pp. 449-453, 2004.

[192] Shi, X. Q., Wang, Z. P., Yang, Q. J., and Pang, H. L. J. "Creep Behavior and Deformation Mechanism Map of Sn-Pb Eutectic Solder Alloy," Journal of Engineering Materials and Technology, Vol. 125, pp. 81-88, 2003.

[193] Hwang, J. S., and Koenigsmann, H. J., "Lead-Free Solders for Electronic Packaging and Assembly," Circuit World, Vol. 20, pp. 19-25, 1994.

[194] Xiao, Q., and Armstrong, W., "Tensile Creep and Microstructural Characterization of Bulk Sn3.9Ag0.6Cu Lead-free Solder," Journal of Electronic Materials, Vol. 34, pp. 196-211, 2005.

[195] Qian, Z., Dasgupta, A., and Haswell, P., "Viscoplastic Constitutive Properties and Energy-Partitioning Model of Lead-Free Sn3.9Ag0.6Cu Solder Alloy," Proceedings of the 53rd Electronic Components and Technology Conference, pp. 1862-1868, 2003.

[196] Lau, J., Danksher, W., and Vianco, P., "Acceleration Models, Constitutive Equations, and Reliability of Lead-Free Solders and Joints," Proceedings of the 53rd Electronic Components and Technology Conference, pp. 229-236, 2003.

[197] Pang, J. H. L., Xiong, B. S., and Low, T. H., "Creep and Fatigue Characterization of Lead-Free 95.5Sn-3.8Ag-0.7Cu Solder," Proceedings of the 54th Electronic Components and Technology Conference, pp. 1333-1337, 2004.

[198] Schubert, A., Dudek, R., Auerswald, E., Gollbardt, A., Michel, B., and Reichl, H., "Fatigue Life Models for SnAgCu and SnPb Solder Joints Evaluated by Experiments and Simulation," Proceedings of the 53rd Electronic Components and Technology Conference, pp. 603-610, 2003.

[199] Clech, J. P., "An Extension of the Omega Method to Primary and Tertiary Creep of Lead-Free Solders," Proceedings of the 55th Electronic Components and Technology Conference, pp. 1261-1271, 2005.

[200] Clech, J. P., "An Obstacle-Controlled Creep Model for Sn-Pb and Sn-based Lead-Free Solders," Proceedings of the SMTA International Conference, 2004.

[201] Anand, L., "Constitutive Equations for the Rate-Dependent Deformation of Metals at Elevated Temperatures," Journal of Engineering Materials and Technology, Vol. 104, pp. 12-17, 1982.

[202] Brown, S. B., Kim, K. H., and Anand, L., "An Internal Variable Constitutive Model for Hot Working of Metals," International Journal of Plasticity, Vol. 5, pp. 95-130, 1989.

[203] Zhang, Q., and Dasgupta, A., "Constitutive Properties and Durability of Lead-Free Solders," Lead-Free Electronics, S. Ganesan and M. Pecht, Eds., Wiley-Interscience, pp. 65-137, 2003.

[204] Rodgers, B., Flood, B., Punch, J., and Waldron, F., "Experimental Determination and Finite Element Model Validation of the Anand Viscoplasticity Model Constants for SnAgCu," Proceedings of the 6th EuroSimE Conference, pp. 490-496, 2005.

[205] Chen, X., Chen, G., and Sakane, M., "Prediction of Stress-Strain Relationship with an Improved Anand Constitutive Model for Lead-Free Solder Sn-3.5Ag", IEEE Transactions on Components and Packaging Technologies, Vol. 28, pp. 111-116, 2005.

[206] Amagai, M., Watanabe, M., Omiya, M., Kishimoto, K., and Shibuya, T., "Mechanical Characterization of Sn-Ag-Based Lead-Free Solders," Microelectronics Reliability, Vol. 42, pp. 951-966, 2002.

[207] Pang, J. H. L., Low, P. T. H., and Xiong, B. S., "Lead-Free 95.SSn-3.8Ag-0.7Cu Solder Joint Reliability Analysis For Micro-BGA Assembly," Proceedings of the Ninth Intersociety Conference on Thermal and Thermomechanical Phenomena in Electronic Systems, pp. 131-136, 2004.

[208] Anderson, T., Guven, I., Madenci, E., and Gustafsson, G., "The Necessity of Reexamining Previous Life Prediction Analyses of Solder Joints in Electronic Packages," IEEE Transactions on Components and Packaging Technologies, Vol. 23, pp. 516-520, 2000.

[209] Wang, G. Z., Cheng, Z. N., Becker, K., and Wilde, J., "Applying Anand Model to Represent the Viscoplastic Deformation Behavior of Solder Alloys," Journal of Electronic Packaging, Vol. 123, pp. 247-253, 2001.

[210] Wilde, J., Becker, K., Thoben, M., Blum, W., Jupitz, T., Wang, G., and Cheng, Z. N., "Rate Dependent Constitutive Relations Based on Anand Model for 92.5Pb5Sn2.5Ag Solder," IEEE Transactions on Advanced Packaging, Vol. 23, pp. 408-414, 2000.

[211] Nie, X., Bhate, D., Chan, D., Chen, W., Subbarayan, G., and Dutta, I., "Rate-Dependent Behavior of Sn3.8ag0.7cu Solder Over Strain Rates of 10-6 to 102 s-1," Proceedings of the 11th Intersociety Conference on Thermal and Thermomechanical Phenomena in Electronic Systems, pp. 676-682, 2008.

[212] Pei, M., and Qu, J., "Constitutive Modeling of Lead-Free Solders," Proceedings of the International Symposium on Advanced Packaging Materials: Processes, Properties and Interfaces, pp. 45-49, 2005.

[213] Basaran, C., Zhao, Y., Tang, H., and Gomez, J., "A Damage-Mechanics-Based Constitutive Model for Solder Joints," Journal of Electronic Packaging, Vol. 127, pp. 208-214, 2005.

[214] Yeo, A., Lee, C., and Pang, J. H. L. "Flip-Chip Solder Joint Reliability Analysis Using Viscoplastic and Elastic-Plastic-Creep Constitutive Models," IEEE Transactions on Components and Packaging Technologies, Vol. 29, pp. 355-363, 2006.

[215] Lee, W. W., Nguyen, L. T., and Selvaduray, G. S., "Solder Joint Fatigue Models: Review and Applicability to Chip Scale Packages," Microelectronics Reliability, Vol. 40, pp. 231-244, 2000.

[216] Ng, H. S., Tee, T. Y., Goh, K. Y., Luan, J. E., Reinikainen, T., Hussa, E., and Kujala, A., "Absolute and Relative Fatigue Life Prediction Methodology for Virtual Qualification and Design Enhancement of Lead-Free BGA," Proceedings of the 55th Electronic Components and Technology Conference, pp. 1282-1291, 2005.

[217] Che, F. X., and Pang, J. H. L., "Thermal Fatigue Reliability Analysis for PBGA with Sn-3.8Ag-0.7Cu Solder Joints," Electronics Packaging Technology Conference, pp. 787-792, 2004.

[218] Chen, X., Lin, Y., Liu, X., and Lu, G. Q., "FEM Analysis with Cyclic Visco-Plasticity for Solder Bumped Flip-Chip Packaging," Proceedings of the Fifth International Conference on Electronic Packaging Technology, ICEPT, pp. 282-287, 2003.

[219] Yutaka, T., Hideo, N., Hiroki, Y., and Masao, S., "A Strain Rate Ratio Approach for Assessing Creep-Fatigue Life of 63Sn-37Pb Solder Under Shear Loading," Journal of Electronic Packaging, Vol. 127, pp. 407-414, 2005.

[220] Syed, A., "Accumulated Creep Strain and Energy Density Based Thermal Fatigue Life Prediction Models for SnAgCu Solder Joints," Proceedings of the 54th Electronic Components and Technology Conference, pp. 737-746, 2004.

[221] Classe, F. C., and Sitaraman, S. K., "Asymmetric Accelerated Thermal Cycles: An Alternative Approach to Accelerated Reliability Assessment of Microelectronic Packages," Proceedings of the Fifth Conference on Electronics Packaging Technology, pp. 81-89, 2003.

[222] Pang, J. H. L., and Low, T. H., "Modeling Thermal Cycling and Thermal Shock Tests for FCOB," Proceedings of the Eighth Intersociety Conference on Thermal and Thermomechanical Phenomena in Electronic Systems, pp. 987-992, 2002.

[223] Pitarresi, J. M., Sethuraman, S., Nandagopal, B., and Primavera, A., "Reliability Modeling of Chip Scale Packages," Proceedings of the 26th International Electronics Manufacturing Technology Symposium, pp. 60-69, 2000.

[224] Wang, J., Peng, W., and Ren, W., "Power Amplifier (PA) Transistors Fatigue Life Prediction under Thermo-Mechanical Cyclic Loading," Proceedings of the 7th EuroSime Conference, pp. 1-8, 2006.

[225] Choi, S., Subramanian, K., Lucas, J., and Bieler, T., "Thermomechanical Fatigue Behavior of Sn-Ag Solder Joints," Journal of Electronic Materials, Vol. 29, pp. 1249-1257, 2000.

[226] Ma, H., "Constitutive Models of Creep for Lead-Free Solders," Journal of Materials Science, Vol. 44, pp. 3841-3851, 2009.

[227] Ma, H., Characterization of Lead-Free Solders for Electronic Packaging, Ph.D. Dissertation, Auburn University, Auburn, AL, 2007.

[228] Mei, Z., “Effects of Cooling Rate on Mechanical Properties of Near-Eutectic Tin-Lead Solder Joint,” Journal of Electronic Materials, Vol. 20, pp. 599-608, 1991.

[229] Conrad, H., “Influence of Microstructure Size on the Plastic Deformation Kinetics, Fatigue Crack Growth Rate, and Low-Cycle Fatigue of Solder Joints,” Journal of Electronic Materials, Vol. 28, p. 1062-1070, 1999.

[230] Suh, D., Kim, D. W., Liu, P., Kim, H., Weninger, J. A., Kumar, C. M., Prasad, A., Grimsley, B. W., and Tejada, H. B., "Effects of Ag Content on Fracture Resistance of Sn-Ag-Cu Lead-Free Solders Under High-Strain Rate Conditions," Materials Science and Engineering: A, Vol. 460-461, pp. 595-603, 2007.

Appendix I

Empirical Models Used in Curve Fitting of Solder Mechanical Properties:

(1) Elastic Modulus:

$$E = C_0 + C_1 e^{-C_2 t}$$

(2) Yield Strength:

$$\sigma_{ys} = C_0 + \frac{C_1 C_2}{C_2 + t}$$

(3) UTS:

$$\sigma_{uts} = C_0 + \frac{C_1 C_2}{C_2 + t}$$

Model Constants for SAC105

Elastic Modulus	C_0 (GPa)	C_1 (GPa)	C_2 (Day^{-1})
25 °C	26.17	6.52	0.0199
50 °C	21.10	11.87	0.0365
75 °C	18.07	14.83	0.0426
100 °C	16.51	16.30	0.0481
125 °C	16.39	16.33	0.0541

Yield Strength	C_0 (MPa)	C_1 (MPa)	C_2 (Day)
25 °C	12.02	8.38	59.38
50 °C	10.92	9.45	12.06
75 °C	10.36	10.02	6.79
100 °C	10.59	9.84	3.22
125 °C	10.08	10.36	2.58

UTS	C_0 (MPa)	C_1 (MPa)	C_2 (Day)
25 °C	19.24	6.95	11.36
50 °C	15.71	10.47	6.27
75 °C	14.93	11.31	3.94
100 °C	14.74	11.53	2.81
125 °C	14.37	11.90	2.40

Model Constants for SAC205

Elastic Modulus	C_0 (GPa)	C_1 (GPa)	C_2 (Day^{-1})
25 °C	31.05	8.41	0.0496
50 °C	29.94	9.42	0.0563
75 °C	28.05	11.26	0.0546
100 °C	26.51	12.72	0.0553
125 °C	24.62	14.65	0.0521

Yield Strength	C_0 (MPa)	C_1 (MPa)	C_2 (Day)
25 °C	19.95	8.69	9.07
50 °C	17.01	11.54	8.79
75 °C	16.51	12.04	4.28
100 °C	15.62	12.93	3.53
125 °C	15.36	13.18	2.23

UTS	C_0 (MPa)	C_1 (MPa)	C_2 (Day)
25 °C	21.41	12.19	16.51
50 °C	21.28	12.21	7.33
75 °C	20.04	13.42	4.82
100 °C	18.62	14.86	3.55
125 °C	17.85	15.65	2.56

Model Constants for SAC305

Elastic Modulus	C_0 (GPa)	C_1 (GPa)	C_2 (Day^{-1})
25 °C	29.77	9.90	0.0316
50 °C	29.29	10.41	0.0473
75 °C	27.76	11.95	0.0533
100 °C	27.76	11.95	0.0534
125 °C	27.03	12.61	0.0651

Yield Strength	C_0 (MPa)	C_1 (MPa)	C_2 (Day)
25 °C	21.22	7.68	11.72
50 °C	18.31	10.59	8.03
75 °C	17.29	11.71	4.94
100 °C	16.61	12.42	3.17
125 °C	15.99	13.04	1.99

UTS	C_0 (MPa)	C_1 (MPa)	C_2 (Day)
25 °C	30.92	9.81	3.73
50 °C	26.31	14.36	3.64
75 °C	24.43	16.27	2.28
100 °C	23.54	17.18	1.43
125 °C	22.59	18.13	1.25

Model Constants for SAC405

Elastic Modulus	C_0 (GPa)	C_1 (GPa)	C_2 (Day^{-1})
25 °C	31.49	10.15	0.0377
50 °C	31.28	10.14	0.0617
75 °C	30.29	11.07	0.0755
100 °C	29.42	11.92	0.0904
125 °C	28.37	12.95	0.0873

Yield Strength	C_0 (MPa)	C_1 (MPa)	C_2 (Day)
25 °C	20.69	9.86	15.92
50 °C	20.03	10.52	6.38
75 °C	18.28	12.27	3.94
100 °C	17.99	12.57	2.96
125 °C	17.63	12.93	1.82

UTS	C_0 (MPa)	C_1 (MPa)	C_2 (Day)
25 °C	31.22	12.19	8.55
50 °C	30.17	13.09	3.98
75 °C	27.93	15.36	1.53
100 °C	26.15	17.14	1.35
125 °C	24.68	18.61	0.95

Model Constants for 63Sn-37Pb

Elastic Modulus	C_0	C_1	C_2
25 °C	Model cannot be applied due to the near constant modulus values across the entire aging matrix.		
50 °C			
75 °C			
100 °C			
125 °C			

Yield Strength	C_0 (MPa)	C_1 (MPa)	C_2 (Day)
25 °C	24.96	19.98	28.79
50 °C	29.16	15.62	9.18
75 °C	29.36	15.48	4.91
100 °C	29.29	15.59	4.29
125 °C	28.62	16.27	4.03

UTS	C_0 (MPa)	C_1 (MPa)	C_2 (Day)
25 °C	33.76	17.48	11.18
50 °C	33.46	17.78	3.33
75 °C	32.05	19.21	2.08
100 °C	33.53	17.74	1.91
125 °C	34.35	16.85	5.62

Appendix II

Empirical Mathematical Model Used in Creep Curve Fitting:

$$\log\dot{\varepsilon} = C_0 + C_1 t + C_2(1 - e^{-C_3 t})$$

<u>Note</u>: The units of C_0, C_1, C_2, and C_3 are chosen so that $\dot{\varepsilon}$ is in sec^{-1} and t is in months.

Model Constants for (R.T.) 25 ºC Aging

Constants	**63Sn-37Pb**	**SAC105**	**SAC205**	**SAC305**	**SAC405**
C_0	-13.12	-16.12	-17.09	-17.13	-17.17
C_1	0.0583	0.7795	0.3546	0.3654	0.2481
C_2	1.14	1.36	0.14	13.70	0.0989
C_3	3.53	37.41	8.36	2.42	1.37

Model Constants for 50 ºC Aging

Constants	63Sn-37Pb	SAC105	SAC205	SAC305	SAC405
C_0	-13.12	-16.12	-17.09	-17.13	-17.17
C_1	0.1161	0.4764	0.5453	0.1919	0.2490
C_2	1.24	5.64	2.89	2.98	2.49
C_3	6.83	6.37	5.33	3.28	1.46

Model Constants for 75 ºC Aging

Constants	63Sn-37Pb	SAC105	SAC205	SAC305	SAC405
C_0	-13.12	-16.12	-17.09	-17.13	-17.17
C_1	0.0704	0.4091	0.5189	0.2314	0.2402
C_2	0.97	6.26	3.88	3.62	3.48
C_3	4.75	6.87	5.17	3.91	4.01

Model Constants for 100 ºC Aging

Constants	63Sn-37Pb	SAC105	SAC205	SAC305	SAC405
C_0	-13.12	-16.12	-17.09	-17.13	-17.17
C_1	0.0819	0.3948	0.2251	0.2298	0.2212
C_2	0.49	6.81	6.03	4.41	3.80
C_3	2.05	6.61	3.97	3.02	3.55

Model Constants for 125 ºC Aging

Constants	63Sn-37Pb	SAC105	SAC205	SAC305	SAC405
C_0	-13.12	-16.12	-17.09	-17.13	-17.17
C_1	0.0942	0.3224	0.1728	0.1555	0.1929
C_2	0.38	7.42	6.96	4.96	4.23
C_3	1.86	8.80	4.78	5.78	4.51

Appendix III

Empirical Mathematical Model Used in Creep Curve Fitting:

$$\log \dot{\varepsilon} = C_0 + C_1 t + C_2 (1 - e^{-C_3 t})$$

Note: The units of C_0, C_1, C_2, and C_3 are chosen so that $\dot{\varepsilon}$ is in sec^{-1} and t is in months.

Model Constants for the Creep Strain Rate vs. Aging Time Curves (25 °C)

Solder	C_o	C_1	C_2	C_3
SAC305	-18.42	0.0086	0.31	0.46
MIX 10-90	-16.74	0.0070	0.01	0.00
MIX 30-70	-17.54	0.0052	-0.07	0.00
MIX 50-50	-17.03	0.0011	-0.01	0.40
MIX 70-30	-16.81	0.0076	0.23	0.04
MIX 90-10	-14.57	0.0161	1.56	0.19
63Sn-37Pb	-10.45	0.0003	0.02	0.07

Model Constants for the Creep Strain Rate vs. Aging Time Curves (100 °C)

Solder	C_o	C_1	C_2	C_3
SAC305	-18.41	0.0152	2.37	0.16
MIX 10-90	-16.78	0.0117	1.41	0.33
MIX 30-70	-17.73	0.0061	2.71	0.31
MIX 50-50	-17.03	0.0127	2.12	0.29
MIX 70-30	-16.96	0.1237	2.40	7.64
MIX 90-10	-14.65	0.0027	2.67	0.41
63Sn-37Pb	-10.45	0.0012	-0.44	0.56